Boson stars, baby universes and wormholes in a modified gravity scenario

By
Andreu Sales Masó Ferrando

VNIVERSITAT DE VALÈNCIA

Programa de Doctorat en Física - 3126
Departament de Física Teòrica

PhD Thesis
November 2023

Advisors:
Gonzalo Olmo Alba
Nicolás Sanchis Gual

Author's Declaration

I declare that the work presented in this thesis was carried out in accordance with the requirements of the University's Regulations and Code of Practice for Research Degree Program.

The contents of this thesis are based on the following papers:

[1] **A. Masó-Ferrando**, N. Sanchis-Gual, J. A. Font and G. J. Olmo, "Boson stars in Palatini $f(\mathcal{R})$ gravity," *Class. Quant. Grav.* vol. 38, no.19, p.194003, Sep 2021.

[2] **A. Masó-Ferrando**, N. Sanchis-Gual, J. A. Font and G. J. Olmo, "Birth of baby universes from gravitational collapse in a modified-gravity scenario," *JCAP*, vol. 06, p. 028, Jun 2023.

[3] R. B. Magalhães, **A. Masó-Ferrando**, G. J. Olmo and L. C. B. Crispino, "Asymmetric wormholes in Palatini $f(\mathcal{R})$ gravity: Energy conditions, absorption and quasibound states," *Phys. Rev. D*, vol. 108, p. 024063, Jul 2023.

[4] **A. Masó-Ferrando**, N. Sanchis-Gual, J. A. Font and G. J. Olmo, "Numerical evolutions of boson stars in Palatini $f(\mathcal{R})$ gravity," arXiv:gr-qc/2309.14912, Sep 2023.

[5] R. B. Magalhães, **A. Masó-Ferrando**, F. Bombacigno, G. J. Olmo and L. C. B. Crispino, "Echoes from bounded universes," arXiv:gr-qc/2310.03727, Oct 2023.

The text presented here should be understood as a dissertation submitted to the University of Valencia as required to obtain the degree of Doctor of Philosophy in Physics.

Except where indicated by specific reference in the text, this is the candidate's own work, done in collaboration with, and with the assistance of, the candidate's supervisors and collaborators. Any views expressed in the thesis are those of the author.

València, November 2023
Andreu S. Masó Ferrando

Contents

Preface

The absence of a well-established theory concerning gravity and its behavior at high energies demands a global effort to construct a viable quantum theory for the gravitational field. The complexity of this issue calls for a multidisciplinary approach, that incorporates a wide range of viewpoints, from sophisticated mathematical tools and statistical techniques to ambitious experiments. A deep understanding of our fundamental theories, their capabilities and limitations, as well as an improvement of the main roads in them are essential steps towards achieving the ultimate goal, the development of a satisfactory theory that combines gravity and quantum physics. This PhD thesis is situated within this context, with particular emphasis on investigating the existence and properties of exotic compact objects resembling black holes.

In the last decade, we have witnessed significant technological advancements that have transformed the direct observation of extremely compact astrophysical objects into a reality. This has highlighted that the black holes predicted by Einstein's General Theory of Relativity are consistent with observations. However, given that the current precision of gravitational wave observatories and very long baseline radio astronomy observatories, such as the LIGO-Virgo-KAGRA collaboration and the Event Horizon Telescope, is not sufficient to unequivocally confirm the Kerr hypothesis—which stands that all black holes in the Universe are described by the Kerr metric—it becomes necessary to consider alternative explanations that allow us to confront the data with potential deviations from General Relativity. These deviations are expected both for theoretical considerations linked to quantum gravity and for phenomenological reasons related to the potential existence of sources of dark matter and energy.

These sources are crucial to justify the standard cosmological model and the growth of large-scale structures.

Exploring alternatives beyond General Relativity is challenging, primarily due to technical complexities, as equations become highly intricate and, analytical and numerical methods are not developed or optimized beyond General Relativity. Obtaining analytical solutions that accurately depict compact objects is, in itself, a formidable challenge. Moreover, the endeavor to extract gravitational wave profiles for studying the merger processes of these compact objects, in order to extract characteristic information from these theories, presents an even greater challenge.

Recently, alternative gravity theories that are likely to have an optimal analytical and numerical treatment have been characterized. By formulating gravity theories in metric-affine-type manifolds where the gravitational Lagrangian is an arbitrary function of traces of the Ricci tensor and the metric, it is possible to establish a correspondence between the solution space of General Relativity and these theories. This facilitates discovering solutions and studying their dynamical properties within these alternative theories by solving similar problems within the framework of General Relativity.

Furthermore, among the wide range of exotic compact objects detailed in the literature that could potentially exhibit characteristics similar to black holes, boson stars occupy a prominent role. Unlike conventional stars, predominantly composed of fermionic matter, boson stars are formed by bosonic particles and described by scalar or vector fields. Consequently, when referring to boson stars we do not refer to a unique singular entity but instead to an entire family of astronomical objects which depend on the specific boson that constitutes them.

It can be found in the literature that boson stars have a significant potential to mimic part of the phenomenology of black holes, as they share multiple similarities in various observational aspects. Due to all these effects and with the aim of maintaining simplicity in the resulting equations at an acceptable level, we will dedicate our study to the conjunction between boson stars and alternatives to the General Theory of Relativity.

Derived from the outcomes of this study and driven by curiosity and the will to explore the boundaries of established gravitational scenarios, we will also delve into the concept of wormholes—a topological phenomenon widely popularized by science fiction. This concept allows for the identification of two spatially separated regions connected by a sort of spacetime *tunnel*. The foundational principles underlying these objects and the observable consequences they entail can offer valuable insights in our quest to deepen our understanding of the constraints governing gravitational models.

The thesis is structured into two distinct parts. The first part, encompassing Chapters 1 through 5, delves into the exploration of boson stars within the framework of modified gravity. In Chapter 1, we introduce the reader to the concept of boson stars, while Chapter 2 provides an overview of modified gravity theories. In Chapter 3, we put together the notions acquired from the preceding chapters, studying boson stars in a modified gravity scenario. Chapter 4 inquires deeper into our study by performing numerical evolutions to the boson stars described in the previous chapter. This first part culminates with Chapter 5, where we investigate the gravitational collapse of the aforementioned boson stars.

The second part comprises three chapters. Chapter 6 introduces the reader to the concept of wormhole, while Chapter 7 explores various observational aspects of an asymmetric Reissner-Nordström thin-shell wormhole. The final chapter, Chapter 8, introduces a novel line element describing an asymmetric Ellis-type wormhole with a bounded areal radius. Within this chapter, we further explore various observational implications associated with this unique wormhole configuration.

Throughout the thesis, we use Greek indices $\alpha, \beta, \ldots$ when referring to spacetime indices, while Latin indices $i, j, \ldots$ are used for spatial indices. Symmetric and anti-symmetric tensors are represented using parentheses and brackets, respectively. Unless stated otherwise we use a system of natural units in which $c = G = \hbar = 1$. Any additional conventions employed will be explicitly mentioned in the text.

Part I.

Boson Stars and Modified Gravity

Chapter 1.

Boson stars

1.1. Overview

When discussing boson stars, the first image that may come to mind is that of an object of astrophysical proportions. Nevertheless, the origin of these entities can be traced back to a longstanding debate about the fundamental nature of particle-like entities.

In the 1950s, John Wheeler delved into the Newtonian notion of a *body* and aimed to build a self-gravitating and divergence-free entity. The conventional representation of three-dimensional objects as bodies moving along geodesics implies an idealization where a nonzero mass is concentrated at a single one-dimensional point. Consequently, this implies the occurrence of metric singularities at the location of the object. Wheeler succeeded in creating an object that was free of singularities and could fulfill the role of bodies within the framework of General Relativity [6]. These objects are characterized by a smooth, classical electromagnetic field coupled to gravity, which adopts a closed circular toroidal form with a high concentration of energy. The gravitational attraction associated with the field energy sustains this configuration. Wheeler named these entities *geons*, an abbreviation derived from the phrase *gravitational-electromagnetic entity*. Unfortunately, these objects were found

to be unstable over time due to the gradual leakage of field energy, leading to their dissolution [7, 8].

Subsequently, in 1968, Kaup expanded upon Wheeler's concept of geon by replacing the electromagnetic field with a complex massive scalar field, giving rise to what he named as *Klein-Gordon geon* [9], which is now commonly referred as *boson star*. Kaup semiclassically coupled the complex scalar field to gravity, where matter is treated as a quantum field while its energy-momentum tensor is calculated classically, and gravity is described by General Relativity. A year after Kaup's work, Ruffini and Bonazzola [10] quantized a real scalar field and discovered that the same energy-momentum tensor, as well as the same field equations, were obtained when analyzing a macroscopic system.

The existence of these solutions had to satisfy Derrick's theorem [11], which establishes that a regular, localized, time-independent scalar field cannot possess stability and, consequently, cannot exist. This restriction is avoided by adopting a harmonic ansatz for the complex scalar field. As a result, we are presented with a non-static oscillating scalar field that gives rise to a boson star within a static spacetime. The boson star itself represents a stationary soliton-like solution.

A boson star can be understood as a collection of particles that follow the dynamics dictated by the Klein-Gordon equation, and therefore, it exhibits a dispersive behavior. To ensure stability, the presence of a confining mechanism becomes crucial. This confinement mechanism arises from the mass μ associated with the field, which generates a potential barrier. Consequently, boson stars can be regarded as macroscopic self-gravitating Bose-Einstein condensates.

Given that boson stars can be regarded as macroscopic quantum states, it is possible to apply the Heisenberg uncertainty principle to estimate their maximum mass. Assuming that the boson star is confined within a radius $\Delta x = R$ and possesses a maximum momentum of $\Delta p = \mu c$, where μ represents the mass of the constituent particle, the uncertainty principle, $\Delta x \Delta p \geq \hbar$, can

be expressed as,

$$\mu c R \geq \hbar \quad . \tag{1.1}$$

To determine the maximum mass, we consider that it tends towards the Schwarzschild mass, leading to $R = 2GM_{\max}/c^2$. Consequently, we find

$$M_{\max} = \frac{1}{2}\frac{\hbar c}{G\mu} = \frac{1}{2}\frac{M_{\rm Pl}^2}{\mu} \quad , \tag{1.2}$$

where $M_{\rm Pl}^2 \equiv \hbar c/G$ is the Planck mass. As has been calculated, the mass of a boson star exhibits an inverse relationship with the mass of the constituent scalar field particle. Thus, from this perspective, the mass and size of a boson star can vary across atomic and astrophysical scales, depending on the mass of the constituent boson. Furthermore, the inclusion of a self-interacting term in the field's potential may introduce variations in the mass of the bosonic star [12].

The extensive range of mass scales exhibited by boson stars stands as a significant motivation for their study. These objects could potentially represent astrophysical entities, particularly since experimental observations have yet to definitively rule out the existence of exotic compact objects and determine the true nature of dark matter. Moreover, investigating boson stars can contribute to our understanding of the compact objects abundances and mass spectrum observed by the gravitational wave observatories LIGO-Virgo [13, 14], exemplified by the intriguing case of GW190521 [15], which has been proposed to arise from the head-on collision of two Proca stars [16], that are the vectorial cousins of scalar boson stars [17]. This exemplifies the profound implications of gravitational wave interferometers in raising questions about the nature and origins of merged compact objects (see [18–20]).

In addition to their potential astrophysical significance, boson stars have the capacity to surpass galactic sizes. This scales combined with the fact that they only interact gravitationaly, positions them as plausible candidates for

serving as dark matter halos that explain the observed flat rotation curves of spiral galaxies [21–23].

Beyond the question of whether boson stars actually exist, their large compactness, approaching those of black holes, along with the absence of horizons and the simplicity of the model provide motivation for studying these objects. Such investigations offer valuable insights into the behavior of gravity in the strong-field regime.

The investigation of boson stars offers notable advantages in comparison to the study of neutron stars or other fermionic stars. Unlike neutron stars, boson stars do not possess a sharply defined stellar surface, resulting in the avoidance of discontinuities in the equations governing their dynamics. On the other hand, fermionic stars matter is typically described as a perfect fluid which needs an equation of state to be fully determined and are subject to hydrodynamical equations. Consequently, the dynamic study of this kind of stars needs the intrincate analysis of turbulence and shock formation. Such, considerations are not needed in the study of bosonic stars.

Lastly, it is crucial to address the choice of fundamental particle that serves as the building block for the bosonic material constituting the star. Currently, the Higgs boson is the only particle within the Standard Model of particles that potentially fulfills this role, possessing a mass of 125 GeV/c^2. However, to form a boson star with a mass equivalent to that of the Sun, a constituent boson with a mass lighter than 10^{-19} GeV/c^2 is required. To find such particles we will have to look in *Beyond Standard Model* theories, with special mention to those incorporating the axion particle [24].

1.2. Static boson stars: the Einstein-Klein-Gordon system

In order to obtain a boson star, we shall start by describing the action of the system. To do so, we couple a massive complex scalar field to the General Theory of Relativity. The action for the system is given by

$$S = \int d^4x\sqrt{-g}\left(\frac{R}{2\kappa} + \mathcal{L}_{\mathcal{M}}\right) \quad . \tag{1.3}$$

Where, $\kappa = 8\pi$, g is the determinant of the metric tensor $g_{\alpha\beta}$ and R is the Ricci curvature scalar defined as $R = g^{\alpha\beta}R_{\alpha\beta}$. The Ricci tensor $R_{\alpha\beta}$ is calculated using the Levi-Civita connection $\Gamma^{\rho}_{\ \alpha\beta}$ [25], and it is given by

$$R_{\alpha\beta} = \partial_\beta\Gamma^{\rho}_{\ \alpha\rho} - \partial_\rho\Gamma^{\rho}_{\ \alpha\beta} + \Gamma^{\sigma}_{\ \alpha\rho}\Gamma^{\rho}_{\ \sigma\beta} - \Gamma^{\sigma}_{\ \alpha\beta}\Gamma^{\rho}_{\ \sigma\rho} \quad . \tag{1.4}$$

With the Levi-Civita connection expressed using its Christoffel symbols

$$\Gamma^{\alpha}_{\ \beta\gamma} = \frac{g^{\alpha\rho}}{2}\left(\partial_\gamma g_{\rho\beta} + \partial_\beta g_{\rho\gamma} - \partial_\rho g_{\beta\gamma}\right) \quad . \tag{1.5}$$

The first term of the above action Eq. (1.3) is the Einstein-Hilbert action and is the responsible for describing gravity dynamics in the context of the theory of General Relativity. The second term is the matter Lagrangian, in this case, the Lagrangian of a massive complex scalar field coupled to gravity, that reads

$$\mathcal{L}_{\mathcal{M}} = -\frac{1}{2}\left[g^{\alpha\beta}\partial_\alpha\Phi^*\partial_\beta\Phi + V(|\Phi|^2)\right] \quad . \tag{1.6}$$

Here, Φ is a complex scalar field and with an asterisk (*) we denote its complex conjugate. $V(|\Phi|^2)$ is the potential associated to this scalar field. By applying the principle of least action and performing variations with respect to the metric tensor $g^{\alpha\beta}$, we obtain the Einstein field equations

$$R_{\alpha\beta} - \frac{1}{2}g_{\alpha\beta}R = \kappa T_{\alpha\beta} \quad , \tag{1.7}$$

$$T_{\alpha\beta} = \frac{1}{2}\left[\partial_\alpha \Phi^* \partial_\beta \Phi + \partial_\alpha \Phi \partial_\beta \Phi^*\right] - \frac{1}{2} g_{\alpha\beta}\left[g^{\rho\sigma}\partial_\rho \Phi^* \partial_\sigma \Phi + V(|\Phi|^2)\right] \quad , \tag{1.8}$$

where $T_{\alpha\beta}$ represents the energy-momentum tensor.

Varying the action with respect to the field yields the Klein-Gordon equations

$$\left(\Box + \frac{dV}{d|\Phi|^2}\right)\Phi = 0 \quad , \tag{1.9}$$

$$\left(\Box + \frac{dV}{d|\Phi|^2}\right)\Phi^* = 0 \quad , \tag{1.10}$$

where $\Box \coloneqq (1/\sqrt{-g})\,\partial_\alpha\left(\sqrt{-g}g^{\alpha\beta}\partial_\beta\right)$ is the d'Alembertian operator.

One can observe the symmetry exhibited by the matter Lagrangian Eq. (1.6) under global $U(1)$ transformations $\Phi \to \Phi e^{ia}$, where a is a constant. According to Noether's theorem, this symmetry implies the existence of a conserved 4-current, which reads

$$\begin{aligned} J^\alpha &= \frac{\partial \mathcal{L}_\mathcal{M}}{\partial\left(\partial_\alpha \Phi\right)}\delta\Phi + \frac{\partial \mathcal{L}_\mathcal{M}}{\partial\left(\partial_\alpha \Phi^*\right)}\delta\Phi^* \\ &= \frac{i}{2} g^{\alpha\beta}\left(\Phi^* \partial_\beta \Phi - \Phi \partial_\beta \Phi^*\right) \quad . \end{aligned} \tag{1.11}$$

By integrating the time-like component of the 4-current, J^0, over spatial coordinates, we obtain the Noether charge

$$N = \int J^0 \sqrt{-g} dx^3 \quad . \tag{1.12}$$

Following the approach of Ruffini and Bonazzola [10], we identify N as the total number of bosonic particles.

As mentioned earlier, in order to satisfy Derrick's theorem, we adopt the harmonic ansatz for the scalar field

$$\Phi(\boldsymbol{r},t) = \phi(\boldsymbol{r})e^{i\omega t} \quad . \tag{1.13}$$

Since we require the spacetime to be static, despite the time-dependence of the complex scalar field, for the case of spherical symmetry, we can introduce the line element in Schwarzschild-like coordinates (also known as polar-areal coordinates)

$$ds^2 = -\mathcal{A}(r)^2dt^2 + \mathcal{B}(r)^2dr^2 + r^2d\theta + r^2\sin\theta^2d\varphi^2 \quad , \tag{1.14}$$

where $\mathcal{A}$ and $\mathcal{B}$ are two real metric functions.

We implement the harmonic and spherically symmetric ansatz into the Einstein and Klein-Gordon equations, Eq. (1.7), Eq. (1.9) and Eq. (1.10), respectively. The only remaining task is to specify the field potential $V(|\Phi|^2)$. For our purposes, we consider a free massive complex scalar field, leading to the potential

$$V\left(|\Phi|^2\right) = \mu^2\Phi^*\Phi \quad , \tag{1.15}$$

where μ is a constant representing the mass of the constituent boson. Following the approach of [26,27] we write the Einstein-Klein-Gordon system of differential equations:

$$\frac{\partial_r\mathcal{B}}{\mathcal{B}} = \frac{1-\mathcal{B}^2}{2r} + \frac{\kappa r}{4}\left[\mathcal{B}^2\mu^2\phi^2 + \omega^2\phi^2\frac{\mathcal{B}^2}{\mathcal{A}^2} + \psi\right] \quad , \tag{1.16}$$

$$\frac{\partial_r\mathcal{A}}{\mathcal{A}} = \frac{\mathcal{B}^2-1}{r} + \frac{\partial_r\mathcal{B}}{\mathcal{B}} + \frac{\kappa r}{4}\left[-2\mathcal{B}^2\mu^2\phi^2\right] \quad , \tag{1.17}$$

$$\partial_r\psi = -\psi\left(\frac{2}{r} + \frac{\partial_r\mathcal{A}}{\mathcal{A}} - \frac{\partial_r\mathcal{B}}{\mathcal{B}}\right) - \omega^2\phi\frac{\mathcal{B}^2}{\mathcal{A}^2} + \mathcal{B}^2\mu^2\phi \quad , \tag{1.18}$$

where we define $\psi = \partial_r \phi$. Eq. (1.16) is obtained from the tt component of the Einstein equation, while Eq. (1.17) is obtained from the rr component. The third equation, Eq. (1.18), follows from the Klein-Gordon Eq. (1.9).

In order to solve the system, we need to specify appropriate boundary conditions. In the case we are considering, we impose asymptotic flatness, which means that far away from the boson star, the spacetime should be flat and asymptotically approach Minkowski spacetime. This can be expressed as

$$\mathcal{B}(\infty)^2 = 1 \quad , \quad \mathcal{A}(\infty)^2 = 1 \quad , \tag{1.19}$$

$$\phi(\infty) = 0 \quad , \quad \psi(\infty) = 0 \quad . \tag{1.20}$$

At the origin, we impose regularity, requiring that all functions are smooth at $r = 0$.

$$\partial_r \mathcal{B}|_{r=0} = 0 \quad , \quad \partial_r \mathcal{A}|_{r=0} = 0 \quad , \tag{1.21}$$

$$\partial_r \phi|_{r=0} = 0 \quad , \quad \partial_r \psi|_{r=0} = 0 \quad . \tag{1.22}$$

By introducing these four conditions into the Einstein-Klein-Gordon system, we obtain

$$\mathcal{B}(0) = 1 \quad , \quad \mathcal{A}(0) = \mathcal{A}_0 \quad , \tag{1.23}$$

$$\phi(0) = \phi_0 \quad , \quad \psi(0) = 0 \quad , \tag{1.24}$$

where α_0 and ϕ_0 are constants.

It is worth introducing the concept of the Misner-Sharp mass [28], which serves as a geometrical measure of the total mass enclosed within a given radius of a spherically symmetric object in an asymptotically flat spacetime. For our numerical simulations, we will utilize the expression of the Misner-Sharp mass

evaluated at the maximum radial value of our finite grid as an approximate measure of the total mass of the boson star. Its expression is

$$M = \frac{r_{\max}}{2}\left(1 - \frac{1}{\mathcal{B}(r_{\max})^2}\right) \quad . \tag{1.25}$$

By combining this expression with the number of particles, we introduce the notion of binding energy E_b, which arises naturally

$$E_b = M - N\mu \quad . \tag{1.26}$$

The sign of the binding energy will determine the fate of unstable models, leading to either their migration to stable configurations or the dispersion of the bosonic star.

At this stage, we are set to solve the Einstein-Klein-Gordon system numerically, utilizing the given boundary conditions. It is important to note that only one parameter remains free, namely, the central density of the scalar field $\phi(r = 0) \equiv \phi_0$. The remaining parameters, $\mathcal{A}_0$ and ω, are determined by the condition of asymptotic flatness once ϕ_0 is chosen. For a given ω, there exists a set of n discrete eigenvalues that satisfies this condition. As n increases also does the number of radial nodes of ϕ. Here, we will focus on the nodeless $n = 0$ case, known as the ground state or fundamental family.

In Figure 1.1, we have depicted the radial profile of the solved functions with $\phi_0 = 0.07$. The value obtained for the frequency is $\omega/\mu = 0.863$ with an associated mass of $M = 0.632 M_{\rm Pl}/\mu$. We can now observe more clearly some properties of the boson star that were previously mentioned. The solution represents a localized lump of scalar field, lacking a definite surface. The radial profile of the scalar field density, ϕ, exhibits a smooth decrease from its maximum point at $r = 0$, gradually approaching zero density asymptotically. Due to the absence of a well-defined surface, the radius of a boson star is typically defined as the radial value of a sphere that encloses 99% of the mass. It is noteworthy that the boson star radius is scaled by the mass of the constituent boson, implying that a lighter boson results in a larger star.

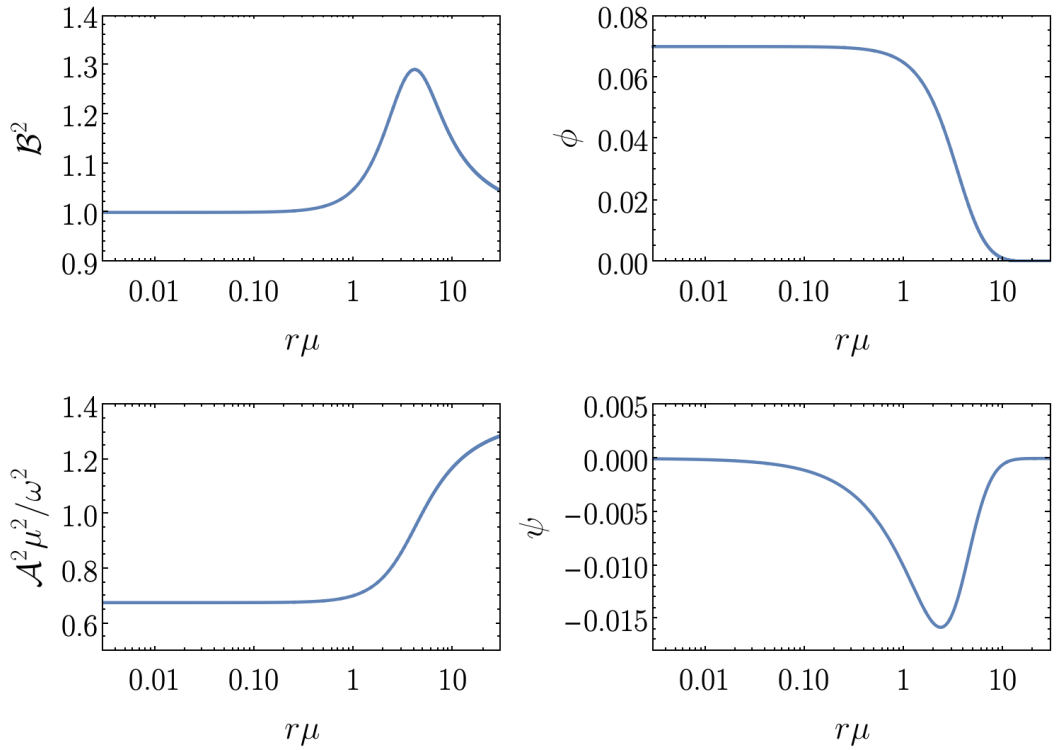

Figure 1.1.: Radial profiles of the metric and scalar field functions.

Moreover, the radial profiles of the metric functions demonstrate that this solution does not possess a horizon. Then, the solution is everywhere regular and asymptotically flat.

Now, solving the Einstein-Klein-Gordon system for a collection of ϕ_0, we obtain the results shown in the top pannel of Figure 1.2. The figure displays the mass of each configuration as a function of the central scalar field ϕ_0 and the frequency ω. Notably, there exists a maximum mass $M_{\max} \approx 0.633 M_{\rm Pl}^2/\mu$, corresponding to a central scalar field value of $\phi_0 \approx 0.08$. Increasing the value of the central scalar field beyond this point does not lead to an increase in the mass of the boson star, in fact, the mass decreases. Consequently, there exists an upper limit to the mass spectrum that boson stars can exhibit, beyond which no static configuration can exist, in analogy with the Chandrasekhar mass limit

for white dwarfs. The following sections will demonstrate that configurations to the left of the maximum mass are stable, while those to the right are unstable.

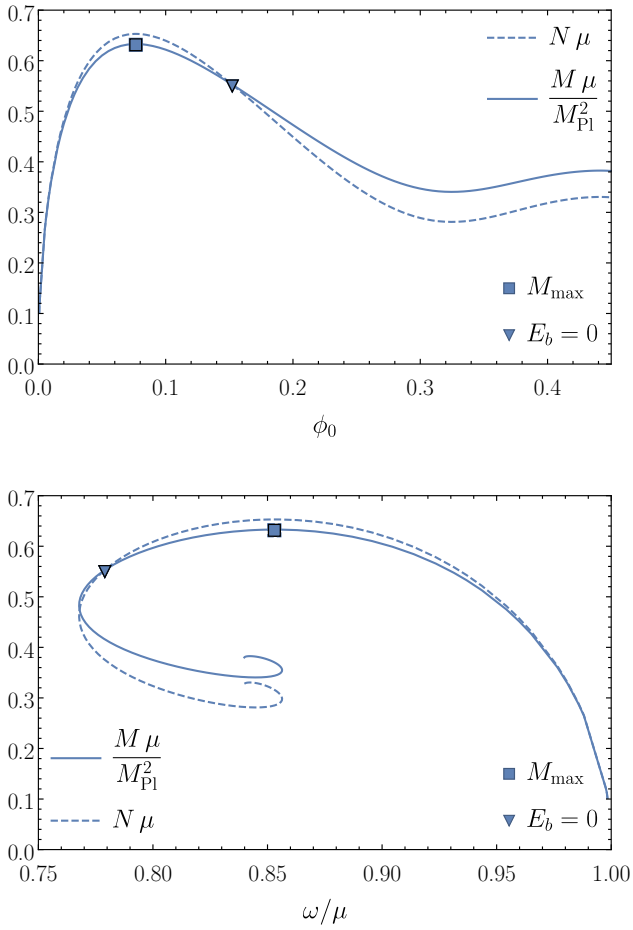

Figure 1.2.: Existence curves of spherically symmetric boson stars, obtained by solving Eq. (1.16)-Eq. (1.18). The upper panel displays with a solid line the Misner–Sharp mass against the central value of the scalar field ϕ_0 while the dashed line represents the number of particles against the same parameter. Mass and particle number are also plotted in the bottom panel against the frequency of the scalar field ω in units of μ. Square symbols indicate the maximum values of the mass, inverted triangles the values where the binding energy changes sign.

In the bottom panel of Figure 1.2, we observe the characteristic spiral behavior displayed by boson star solutions. This implies that boson stars exist within a finite range of frequencies, indicating that only oscillations with sufficient frequency can prevent gravitational collapse, yet not excessively energetic, which would cause dispersion. Notice that boson stars exist only for frequencies $\omega < \mu$.

The underlying cause for the large masses that boson stars have, despite being composed of light bosons, is the elevated particle occupation number, as depicted by the dashed lines in Figure 1.2. We highlight in the mentioned figure the values at which the binding energy undergoes a change in sign using inverted triangles. Finally, the relation between the occupation number and the mass will determine the fate of the time evolution of the boson star.

1.3. Numerical Relativity

It would be of high interest to find analytical solutions of time-dependent boson stars in General Relativity. However, the inherent complexity associated with the fundamental nature of General Relativity makes this goal extremely difficult. The Einstein field equations constitute a system of ten coupled and nonlinear partial differential equations in four dimensions. When written in fully expanded form in a general coordinate system, these equations involve thousands of terms. Consequently, exact solutions of the Einstein equations are only known in cases with high symmetry, either in space or in time. These solutions typically involve spherical or axial symmetry, static or stationary configurations, as well as homogeneous and/or isotropic scenarios. If the goal is to investigate systems of astrophysical relevance characterized by strong and dynamic gravitational fields exhibiting minimal or no symmetry, exact solutions to the field equations become inherently impossible to obtain.

Furthermore, Einstein's theory unifies the concepts of *space* and *time* into the concept of spacetime. This unification represents one of the most significant

achievements of the theory, offering a fundamentally different perspective on gravity compared to Newtonian physics. Gravity is now understood as a manifestation of the geometry of spacetime. Consequently, discussing *space* and *time* separately loses its significance. However, when attempting to time evolve the static configurations obtained in the previous section, the concept of spacetime difficults our aim, as we cannot directly evolve dynamically initial data as we would in Hamiltonian physics.

Numerical Relativity [29, 30] emerged in the 1960s [31] as an attempt to develop numerical methods that discretize the spacetime and solve Einstein's field equations using computational algorithms. By approximating spacetime continuum with a discrete grid, Numerical Relativity facilitates the simulation of gravitational phenomena. Initially, the limited computational resources available constrained simulations to highly symmetric and relatively simple scenarios. However, the advancement of powerful computers in recent decades has significantly expanded the capabilities of Numerical Relativity, enabling researchers to address more intricate problems within the realm of General Relativity, such as the dynamics of rotating stars, black holes, and gravitational collapse. This progress aligns with the emergence of advanced gravitational wave detectors, which use the templates obtained from the Numerical Relativity simulations to look for signals in their data.

1.3.1. The 3+1 formalism and the ADM equations

Our goal is to decouple the concepts of *space* and *time* in order to make predictions of initial data sets. Given appropriate initial and boundary conditions, one should be able to predict the evolution of the gravitational field in the future, this is known as the Cauchy problem for General Relativity. The first attempt to describe General Relativity in terms of a three-dimensional space plus one-dimensional time decomposition, or as it is more commonly known *3+1 decomposition*, was carried out by Darmoise in the 1920s [32], followed by Lichnerowicz and Choquet-Bruhad [33–37]. In 1962 Arnowitt, Deser, and Misner published their work [38], which introduced an approach that laid the

foundation for the field of Numerical Relativity. The approach, named after them, is called the *ADM formalism*.

The first step is foliating the spacetime manifold $\mathcal{M}$, equipped with a metric tensor $g_{\mu\nu}$. To do so, we have to consider that events of the spacetime can be time ordered. By introducing the time parameter t, we can slice the spacetime into spatial 3-hypersurfaces (Cauchy surfaces) that correspond to constant global time and label them accordingly with the value of t. The collection of these slices, denoted as Σ_t, does not intersect and covers the entire manifold $\mathcal{M}$. The normal vector to each hypersurface is given by $\nabla_\mu t$, which must be a one-form pointing in a timelike direction as it represents the gradient of a time coordinate. Its norm is expressed as

$$g^{\mu\nu}\nabla_\mu t \nabla_\nu t = -\frac{1}{\alpha^2} \quad , \tag{1.27}$$

where α denotes the lapse function, which is always positive. Next, we define the unit vector normal to the hypersurfaces as

$$n^\mu \equiv -\alpha g^{\mu\nu}\nabla_\nu t \quad , \tag{1.28}$$

where the minus sign has been chosen in such a way that the normal vector points in the direcction of growing t. From the definition, it is obvious that $n^\mu n_\mu = -1$.

The induced metric on every hypersurface Σ_t is defined as

$$\gamma_{\mu\nu} \equiv g_{\mu\nu} + n_\mu n_\nu \quad . \tag{1.29}$$

By contracting either with the spatial projector operator γ^μ_ν or with the time projector operator $N^\mu_\nu \equiv -n^\mu n_\nu$, tensors can be decomposed into purely spatial components (on the hypersurface Σ_t) and purely temporal components (orthogonal to Σ_t). To express the Einstein field equations in a 3+1 form, we need to project the tensors involved onto the hypersurfaces. Let us begin with

the covariant derivative, which defines the curvature tensor

$$D_\alpha A^\beta_{\ \delta} = \gamma^\rho_{\ \alpha}\gamma^\beta_{\ \sigma}\gamma^\tau_{\ \delta}\nabla_\rho A^\sigma_{\ \tau} \quad , \tag{1.30}$$

where $A^\beta_{\ \delta}$ represents any tensor. This covariant derivative is compatible with the induced metric $D_\alpha \gamma^\beta_{\ \delta} = 0$, which fixes a Levi-Civita 3-connection

$${}^{(3)}\Gamma^\alpha_{\beta\delta} = \frac{1}{2}\gamma^{\alpha\mu}\left(\partial_\delta\gamma_{\mu\beta} + \partial_\beta\gamma_{\mu\delta} - \partial_\mu\gamma_{\beta\delta}\right) \quad . \tag{1.31}$$

The Ricci curvature tensor on the hypersurface Σ_t, also known as the intrinsic curvature, is then defined as

$${}^{(3)}R^\alpha_{\beta\gamma\delta} = {}^{(3)}\Gamma^\alpha_{\beta\delta,\gamma} - {}^{(3)}\Gamma^\alpha_{\beta\gamma,\delta} + {}^{(3)}\Gamma^\mu_{\beta\delta}\,{}^{(3)}\Gamma^\alpha_{\mu\gamma} - {}^{(3)}\Gamma^\mu_{\beta\gamma}\,{}^{(3)}\Gamma^\alpha_{\mu\delta} \quad . \tag{1.32}$$

Similarly, we can introduce the concept of extrinsic curvature, which quantifies the change of the normal vector to a hypersurface under parallel transport between two points on that hypersurface. It provides information about the curvature of the hypersurface Σ_t within the manifold. The extrinsic curvature is denoted as

$$K_{\alpha\beta} = -\gamma_\alpha^{\ \mu}\gamma_\beta^{\ \nu}\nabla_{(\mu}n_{\nu)} \quad . \tag{1.33}$$

Alternatively, it can be expressed as the Lie derivative of the induced metric along the normal vector,

$$K_{\alpha\beta} = -\frac{1}{2}\mathcal{L}_n\gamma_{\alpha\beta} \quad . \tag{1.34}$$

At this stage, one might consider the natural evolution vector to be the normal vector n^μ. However, this assumption is incorrect since the foliation is characterized by the one-form $\nabla_\mu t$, and the normal vector n^μ is not its dual. Specifically, $n^\mu\nabla_\mu t = -\alpha g^{\mu\nu}\nabla_\mu t\nabla_\nu t = \alpha^{-1}$. To address this, we introduce a

vector defined as

$$t^\mu = \alpha n^\mu + \beta^\mu \quad , \tag{1.35}$$

which is dual to the foliation characterizing one-form,

$$t^\mu \nabla_\mu t = \alpha n^\mu \nabla_\mu t + \beta^\mu \nabla_\mu t = 1 \quad . \tag{1.36}$$

Here, β^μ represents the shift vector, which is purely spatial. The lapse function α, determines the proper time interval between two hypersurfaces, while the shift vector indicates the spatial coordinate displacement relative to the normal vector, as depicted illustratively in Figure 1.3.

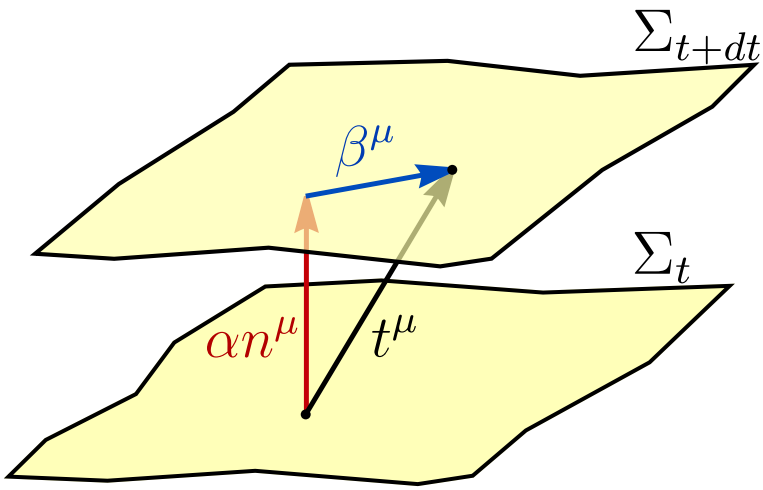

Figure 1.3.: Representation of two adjacent 3-hypersurfaces, Σ_t and Σ_{t+dt}. It is also displayed the definition of the evolution vector t^μ, in terms of the normal vector n^μ, and the shift vector β^μ.

Using that $\alpha\mathcal{L}_n = \mathcal{L}_t - \mathcal{L}_{\vec{\beta}}$, we can rewrite the definition of extrinsic curvature as a Lie derivative of the induced metric along the normal vector Eq. (1.34) as

$$\mathcal{L}_t\gamma_{\mu\nu} = -2\alpha K_{\mu\nu} + \mathcal{L}_{\vec{\beta}}\gamma_{\mu\nu} \quad . \tag{1.37}$$

This is the evolution equation for the induced metric. Let us write here the explicit expression for the Lie derivative acting on a scalar, a vector and a tensor, respectively

$$\mathcal{L}_{\vec{u}}\vartheta = u^\mu\partial_\mu\vartheta \quad , \tag{1.38}$$

$$\mathcal{L}_{\vec{u}}v^\alpha = u^\mu\partial_\mu v^\alpha - v^\mu\partial_\mu u^\alpha \quad , \tag{1.39}$$

and

$$\mathcal{L}_{\vec{u}}B^{\alpha\beta} = u^\mu\partial_\mu B^{\alpha\beta} - B^{\mu\beta}\partial_\mu u^\alpha - B^{\alpha\mu}\partial_\mu u^\beta \quad . \tag{1.40}$$

We can perform three kinds of projections on the Einstein's field equations: onto the hypersurface, mixed and normal projection. Respectively

$$\gamma^\alpha{}_\mu\gamma^\beta{}_\nu\left(R_{\alpha\beta} - \frac{1}{2}g_{\alpha\beta}R - \kappa T_{\alpha\beta}\right) = 0 \quad , \tag{1.41}$$

$$\gamma^{\mu\alpha}n^\beta\left(R_{\alpha\beta} - \frac{1}{2}g_{\alpha\beta}R - \kappa T_{\alpha\beta}\right) = 0 \quad , \tag{1.42}$$

$$n^\alpha n^\beta\left(R_{\alpha\beta} - \frac{1}{2}g_{\alpha\beta}R - \kappa T_{\alpha\beta}\right) = 0 \quad . \tag{1.43}$$

After some algebraic manipulations, these projections lead to the evolution equation for the extrinsic curvature

$$\begin{aligned}\mathcal{L}_t K_{\mu\nu} = &- D_\mu D_\nu \alpha + \alpha \left({}^{(3)}R_{\mu\nu} - 2K^\beta_{\ \nu} K_{\mu\beta} + K K_{\mu\nu} \right) \\ &-\kappa\alpha \left(S_{\mu\nu} - \frac{1}{2}\gamma_{\mu\nu}\left(S - \rho\right) \right) + \mathcal{L}_{\vec{\beta}} K_{\mu\nu} \quad ,\end{aligned} \tag{1.44}$$

the momentum constraint equation

$$\mathcal{M} \equiv D_\nu K^\nu_{\ \mu} - D_\mu K - \kappa j_\mu = 0 \quad , \tag{1.45}$$

and the Hamiltonian constraint equation

$$\mathcal{H} \equiv {}^{(3)}R + K^2 - K_{\mu\nu}K^{\mu\nu} - 2\kappa\rho = 0 \quad . \tag{1.46}$$

Where source terms, that are projections of the energy-momentum tensor, are defined as

$$\rho = n^\alpha n^\beta T_{\alpha\beta} \quad , \tag{1.47}$$

$$j_\mu = \gamma_\mu^{\ \alpha} n^\beta T_{\alpha\beta} \quad , \tag{1.48}$$

$$S_{\mu\nu} = \gamma^\alpha_{\ \mu}\gamma^\beta_{\ \nu} T_{\alpha\beta} \quad , \tag{1.49}$$

and $S = S^\mu_{\ \mu}$. It can be shown that the evolution of the constraint equations preserves the constraints if they are initially satisfied.

Up to this point, all calculations have been performed in a tensorial way, without specifying a vector basis x^μ. Let us choose the coordinate basis. We require three basis vectors to be spacelike, satisfying $n_\mu (e_j)^\mu = 0$. We choose the evolution timelike vector t^μ as the time-basis vector, given by $t^\mu = (e_0)^\mu$. With these choices, the Lie derivative along the vector t corresponds to the partial derivative with respect to time, i.e., $\mathcal{L}_t = \partial_t$. Purely spacelike vectors

will be expressed with a null temporal component, for example, the shift vector $\beta^\mu = (0, \beta^i)$.

From the definition of the time vector t^μ, it follows that the (future-oriented) unit normal timelike vector of each hypersurface is $n^\alpha = (1/\alpha, -\beta^i/\alpha)$, and its dual is $n_\alpha = (-\alpha, 0, 0, 0)$.

The contravariant components of the metric are calculated with the previous assumptions and recalling the definition of the induced metric Eq. (1.29),

$$g^{\mu\nu} = \begin{pmatrix} -1/\alpha^2 & \beta^i/\alpha^2 \\ \beta^i/\alpha^2 & \gamma^{ij} - \beta^i\beta^j/\alpha^2 \end{pmatrix} \quad . \tag{1.50}$$

Similarly, the covariant components are

$$g_{\mu\nu} = \begin{pmatrix} -\alpha^2 + \beta_i\beta^i & \beta_i \\ \beta_i & \gamma_{ij} \end{pmatrix} \quad . \tag{1.51}$$

The system formed by the six evolution equations for the induced metric Eq. (1.37) plus six evolution equations for the extrinsic curvature Eq. (1.44) plus the momentum constraint Eq. (1.45) and the Hamiltonian constraint Eq. (1.46), form the so-called ADM system of equations. They define a 3+1 projection of the Einstein field equations, and provide a numerical framework to compute solutions for General Relativity. However, in practice, the ADM formalism is found to be of little utility because it crashes rapidly. The main reason for this failure is that there is an ambiguity in the definition of the evolution equation for the extrinsic curvature, Eq. (1.44).

In the original work by Arnowitt, Deser, and Misner, they obtained a slightly different equation for the evolution of the extrinsic curvature, which included an additional term proportional to the Hamiltonian constraint, $\mathcal{H}$. One may think that this would not be a huge problem since they are physically equivalent. It should be noted that the constraint is preserved in time if it is satisfied initially, and thus, adding this null term should not affect the evolution of the

extrinsic curvature. However, in numerical simulations, the initial conditions are typically provided as numerical approximations rather than exact solutions. Due to the fact that there are second derivatives of the metric, written in the Ricci scalar R, adding the Hamiltonian constraint results in the alteration of the system of differential equations and becomes a weakly hyperbolic system. Consequently, the system is considered an ill-posed Cauchy problem, leading to an unreliable evolution in numerical computations.

1.3.2. The BSSN formulation

In order to overcome the limitations that the ADM system exhibits, in the decade of 1990s, a reformulation of the system was presented by Baumgarte and Shapiro [39] and Shibata and Nakamura [40] (BSSN). This formalism, incorporates additional parameters and equations into the system, aiming to create a strongly hyperbolic system of differential equations that yield a well-posed Cauchy problem.

The spatial metric is written in terms of a conformal metric $\hat{\gamma}_{ij}$, defined by a conformal factor ψ, which is chosen in such a way that the determinant of conformal metric is $\hat{\gamma} = 1$. It reads as

$$\hat{\gamma}_{ij} = \psi^{-4}\gamma_{ij} \quad , \tag{1.52}$$

$$\psi = \gamma^{1/12} \quad . \tag{1.53}$$

Where γ is the determinant of γ_{ij}. Within the BSSN formalism, the extrinsic curvature is decomposed into its trace K and its conformal trace-free part

$$K = \gamma^{ij}K_{ij} \quad , \tag{1.54}$$

$$\hat{A}_{ij} = \psi\left(K_{ij} - \frac{1}{3}\gamma_{ij}K\right) \quad . \tag{1.55}$$

The additional variables introduced are the conformal connection functions, which can be expressed as

$$\hat{\Gamma}^i = \hat{\gamma}^{jk}\hat{\Gamma}^i{}_{jk} \quad . \tag{1.56}$$

Here, $\hat{\Gamma}^i{}_{jk}$ are the Christoffel symbols of the conformal metric.

In contrast to the ADM formalism, which relies on the induced metric γ_{ij} and the extrinsic curvature K_{ij} as variables, the BSSN formalism employs 17 variables: $\hat{\gamma}_{ij}$, ψ, K, A_{ij} and $\hat{\Gamma}^i$. As they have been presented above, in equations Eq. (1.52)-Eq. (1.56).

Our objective now is to rewrite the evolution equations of the ADM system using these new variables. After some algebraic manipulation, we arrive at the following expressions

$$\partial_t \hat{\gamma}_{ij} = \mathcal{L}_{\vec{\beta}}\,\hat{\gamma}_{ij} - 2\alpha\hat{A}_{ij} \quad , \tag{1.57}$$

$$\partial_t \psi = \mathcal{L}_{\vec{\beta}}\psi - \frac{1}{6}\psi\alpha K \quad , \tag{1.58}$$

$$\partial_t \tilde{A}_{ij} = \mathcal{L}_{\vec{\beta}}\tilde{A}_{ij} + \psi^{-4}\left[-D_iD_j\alpha + \alpha R_{ij}\right]^{\mathrm{TF}} + \alpha\left(K\tilde{A}_{ij} - 2\tilde{A}_{ik}\tilde{A}^k{}_j\right), \tag{1.59}$$

$$\partial_t K = \mathcal{L}_{\vec{\beta}}\partial_m K - D_iD^i\alpha + \alpha\left(\tilde{A}_{ij}\tilde{A}^{ij} + \frac{1}{3}K^2\right), \tag{1.60}$$

$$\begin{aligned}\partial_t \hat{\Gamma}^i =& \mathcal{L}_{\vec{\beta}}\hat{\Gamma}^i - 2\hat{A}^{ij}\partial_j\alpha + 2\alpha\left(\hat{\Gamma}^i{}_{jk}\hat{A}^{kj} - \frac{2}{3}\hat{\gamma}^{ij}\partial_j K - \hat{\gamma}^{ij}S_j + 6\hat{A}^{ij}\partial_j(\ln\psi)\right)\\ &- \partial_j\left(\beta^l\partial_l\hat{\gamma}^{ij} - 2\hat{\gamma}^{m(j}\partial_m\beta^{i)} + \frac{2}{3}\hat{\gamma}^{ij}\partial_l\beta^l\right) \quad ,\end{aligned} \tag{1.61}$$

where $^{\mathrm{TF}}$ in Eq. (1.59) denotes the trace-free part of the expression inside the brackets.

Having performed these calculations, we are now presented with a system of 17 evolution equations Eq. (1.57)-Eq. (1.61), accompanied by the previous 4 constraint equations Eq. (1.45)-Eq. (1.46). Collectively, these equations form the BSSN system,the formulation used in most current 3+1 Numerical Relativity codes, which serves as the foundation for numerical computations in General Relativity.

1.3.3. Gauge conditions

As the reader may have noticed, the BSSN system, as well as the underlying Einstein equations, do not provide any information regarding the specific form or evolution of the lapse function α and the shift vector β^i. These variables are *gauge variables* which we have freedom to chose. There are infinite options when choosing the gauge condition. Depending on the physical system that we are evolving numerically, we will have to choose a gauge condition that facilitates or even allows us to perform our simulations.

For clarity, let us start by computing the acceleration of Eulerian observers

$$\begin{aligned} a_\mu =& n^\nu \nabla_\nu n_\mu = n^\nu \nabla_\nu(-\alpha \nabla_\mu t) = -n^\nu \nabla_\nu \alpha \nabla_\mu t - n^\nu \alpha \nabla_\nu \nabla_\mu t \\ =& - n^\nu \nabla_\nu \alpha \nabla_\mu t - n^\nu \alpha \nabla_\mu \nabla_\nu t = \frac{1}{\alpha} n^\nu n_\mu \nabla_\nu \alpha - n^\nu \alpha \nabla_\mu \left(-\frac{n_\nu}{\alpha}\right) \\ =& \frac{1}{\alpha} n^\nu n_\mu \nabla_\nu \alpha + n^\nu \nabla_\mu n_\nu - \frac{1}{\alpha} n^\nu n_\nu \nabla_\mu \alpha \\ =& \frac{1}{\alpha}\left(n^\nu n_\mu \nabla_\nu \alpha - \nabla_\mu \alpha\right) = \frac{1}{\alpha} \gamma^\nu_{\ \mu} \nabla_\nu \alpha = \frac{1}{\alpha} D_\mu \alpha \\ =& D_\mu \ln \alpha \quad . \end{aligned} \tag{1.62}$$

From here follows the relation between the acceleration of Eulerian observers and the lapse function.

First, we must chose a suitable lapse function α, commonly referred to as choosing a *slicing condition*, as it determines the manner in which the manifold is foliated into slices. The most straightforward option is to set $\alpha = 1$, known as geodesic slicing, where the proper time of Eulerian observers (coordinate system) coincides with the coordinate time t. However, this choice gives rise to some issues. The acceleration of Eulerian observers is null, pointing that they follow geodesics. While this would not pose a problem for simulating an empty void, the purpose of employing the BSSN formalism is to simulate astrophysical scenarios, where matter is present and the spacetime geometry is non-flat. In such cases, observers move in diverse directions and may eventually collide, leading to the existence of multiple coordinate systems at a given point. Consequently, geodesic slicing is not widely used.

Instead, adopting a *maximal slicing* proves to be more advantageous. In maximal slicing, the volume elements $v \equiv \nabla_\mu n^\mu = -K$ are maintained constant, preventing Eulerian observers from intersecting one another. This condition is accomplished by requiring that Eq. (1.60) remains constant. The equation that governs the evolution of the lapse function is then expressed as the following elliptic equation

$$D_i D^i \alpha = \alpha \left(\tilde{A}_{ij} \tilde{A}^{ij} + \frac{1}{3} K^2 \right). \tag{1.63}$$

maximal slicing also possesses the feature of being a *singularity-avoiding slicing*, which is particularly useful when studying the gravitational collapse of an object into a black hole. During the formation of a black hole, a singularity appears at its center, making it desirable for the slicing condition to avoid these points. With maximal slicing, the lapse function collapses to zero at the center of the black hole (see Figure 1.4). Consequently, long simulations of black holes can be successfully conducted.

The only disadvantage that maximal slicing has is the computational effort that it requires, as numerically solving elliptic equations is usually a computationally demanding task. In 1995, a new family of slicing conditions called

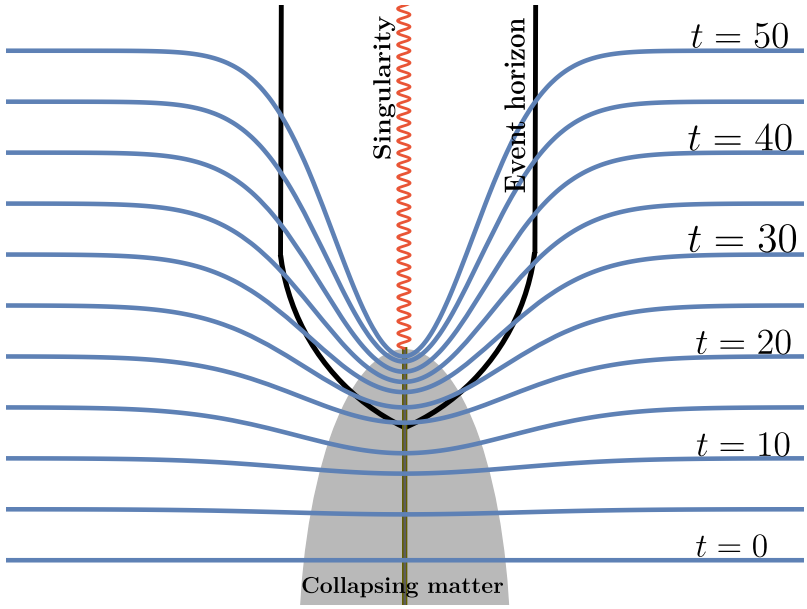

Figure 1.4.: Diagram illustrating the gravitational collapse of a star.The lapse function exhibits a decreasing trend towards the center of the configuration. This decrease effectively enables the slices (depicted as blue lines) to avoid the singularity.

Bona-Massó slicing was introduced [41]

$$\partial_t \alpha - \mathcal{L}_{\vec{\beta}} \alpha = -\alpha^2 f(\alpha) K \quad . \tag{1.64}$$

Here, $f(\alpha)$ is an arbitrary function. Specifically, choosing $f(\alpha) = 2/\alpha$ yields a slicing condition that possesses the same advantages as maximal slicing but with reduced computational requirements. When this specific form of $f(\alpha)$ is employed, the slicing condition is referred to as *1+log slicing*, as the lapse function takes on this form after solving the above equation. In practice, *1+log slicing* is implemented as

$$\partial_t \alpha = \mathcal{L}_{\vec{\beta}} \alpha - 2\alpha K \quad . \tag{1.65}$$

For many systems, it is sufficient to set the shift vector to null, as it has been proven to be a favorable choice in some cases. However, in certain scenarios, it is desirable to counteract the distortion and dragging effects caused by the energy-momentum tensor in spacetime. Various proposals have been made to define an appropriate shift vector, such as the *minimal distortion shift*. This shift vector choice aims to minimize the distortion tensor $\Sigma_{ab}\Sigma^{ab}$ under variations of β^i. The deformation and distortion tensors are defined as:

$$\Theta_{ab} = \frac{1}{2}\gamma^{\mu}_{\ a}\mathcal{L}_t\hat{\gamma}_{\mu b} \quad , \tag{1.66}$$

$$\Sigma_{ab} = \Theta_{ab} - \frac{1}{3}\hat{\gamma}_{ab}\Theta^{i}_{\ i} \quad . \tag{1.67}$$

Similar to the lapse function, this shift selection is effective but can be further optimized in terms of computational cost. This leads us to the *Gamma-driver* shift condition, which is defined as

$$\partial_t\beta^i = \frac{3}{4}\alpha B^i \quad , \tag{1.68}$$

$$\partial_t B^i = \partial_t\hat{\Gamma}^i - \eta B^i \quad , \tag{1.69}$$

where B^i is an auxiliary variable and η is a positive constant.

The *1+log condition* for the lapse function and the *Gamma-driver* condition for the shift vector are typically the most widely used choices in the field of Numerical Relativity. In this study, we will employ these conditions as well.

1.4. Dynamical boson stars

After familiarizing ourselves with the computational procedure for the time evolution of an astrophysical scenario, we are ready to apply it to our specific

case of interest, namely, a boson star [42]. Applying the conditions considered in Section 1.2 for the boson star, such as spherical symmetry, to the 3+1 formalism of Numerical Relativity, leads to the following form of the line element

$$\begin{aligned} ds^2 = &- (\alpha^2 - \beta^r \beta_r) dt^2 + 2\beta_r dr dt \\ &+ e^{4\chi(t,r)} \left(a(t,r) dr^2 + r^2 b(t,r) d\Omega^2 \right) \quad . \end{aligned} \tag{1.70}$$

Where $d\Omega^2 = d\theta^2 + \sin^2\theta d\varphi^2$ is the spherical sector, $a(t,r)$ and $b(t,r)$ are the conformal metric components, and $\chi(t,r)$ is a conformal factor.

Correspondingly, the equations of motion for the scalar field are derived by reformulating the Klein-Gordon equation in terms of the following two first-order variables

$$\Psi := \partial_r \Phi \quad , \tag{1.71}$$

$$\Pi := n^\alpha \partial_\alpha \Phi = \frac{1}{\alpha} \left(\partial_t \Phi - \beta^r \Psi \right) \quad . \tag{1.72}$$

By introducing these variables, the equations of motion for the scalar field can be expressed as

$$\partial_t \Phi = \beta^r \partial_r \Phi + \alpha \Pi \ , \tag{1.73}$$

$$\partial_t \Psi = \beta^r \partial_r \Psi + \Psi \partial_r \beta^r + \partial_r \left(\alpha \Pi \right) \ , \tag{1.74}$$

$$\begin{aligned} \partial_t \Pi = &\ \beta^r \partial_r \Pi + \frac{\Psi}{a e^{4\chi}} \partial_r \alpha + \alpha K \Pi - \alpha \mu^2 \Phi \\ + &\ \frac{\alpha}{a e^{4\chi}} \left[\partial_r \Psi + \Psi \left(\frac{2}{r} - \frac{\partial_r a}{2a} + \frac{\partial_r b}{b} + 2\partial_r \chi \right) \right] \end{aligned} \tag{1.75}$$

During the time evolution of these functions, solved using a second-order Partially Implicit Runge-Kutta method (PIRK) [43–45], we need to specify a stress-energy tensor and its 3+1 projections. For the specific case at hand, the corresponding stress-energy tensor is given by Eq. (1.8) with the potential Eq. (1.15). The projections are performed using the unit normal vector n^α and the induced metric $\gamma^{\alpha\beta}$, as shown in Eq. (1.47)-Eq. (1.49). The matter

source terms appearing in the BSSN evolution equations Eq. (1.57)-Eq. (1.61) are defined as follows:

$$\rho = \frac{1}{2}\left[\Pi^2 + \frac{\Psi^2}{ae^{4\chi}} + \mu^2\Phi^2\right] \quad , \tag{1.76}$$

$$S_a = \frac{1}{2}\left[\Pi^2 + \frac{\Psi^2}{ae^{4\chi}} - \mu^2\Phi^2\right] \quad , \tag{1.77}$$

$$S_b = \frac{1}{2}\left[\Pi^2 - \frac{\Psi^2}{ae^{4\chi}} - \mu^2\Phi^2\right] \quad , \tag{1.78}$$

$$j_r = \frac{1}{2}\left[\frac{1}{ae^{4\chi}}\left(\Pi\Psi^* + \Pi^*\Psi\right)\right] \quad . \tag{1.79}$$

Here, we have introduced the notation $S_a \equiv S^r_{\ r}$ and $S_b \equiv S^\theta_{\ \theta} \equiv S^\varphi_{\ \varphi}$.

We take as initial condition the static solutions found in Section 1.2. These solutions are formulated in polar-areal coordinates, so a coordinate transformation to isotropic coordinates is necessary to perform the time evolution in our particular numerical code, called `NADA1D` [45] that assumes spherical symmetry and employs spherical isotropic coordinates. Thus, we set $\Phi(t=0,r)$, $\Psi(t=0,r)$ and $\Pi(t=0,r)$. Also, the conformal factor has been determined by the coordinate change. Following Ref. [46], we have to ask the initial conformal spatial metric to be flat, $\hat{\gamma}(t=0) = x^4 \sin^2\theta$, which sets the initial metric components, $a(0,r) = b(0,r) = 1$.

As discussed in Section 1.2, the fate of the boson star strongly depends on its initial parameters. Referring to the top pannel of Figure 1.2, we find that boson stars with initial configurations to the left of the maximum mass configuration exhibit stability, while those to the right of this point are unstable.

1.4.1. Stable models

Consider an initial configuration of a boson star characterized by the following parameters:

$\Phi_0(t=0)$	ω	M	E_B
0.02	0.95419	0.47514	-0.00679

We have introduced $\Phi_0(t) \equiv \Phi(t, r=0)$ for the central value of the scalar field.

Figure 1.5 illustrates the magnitude of the central value of the scalar field $\Phi_0(t)$ over time in the given scenario. The plot reveals that the scalar field does not strictly fulfills the assumption of being time-independent; instead, it exhibits oscillations over time due to the numerical error associated with the discretization of the grid. However, the plot also demonstrates that the

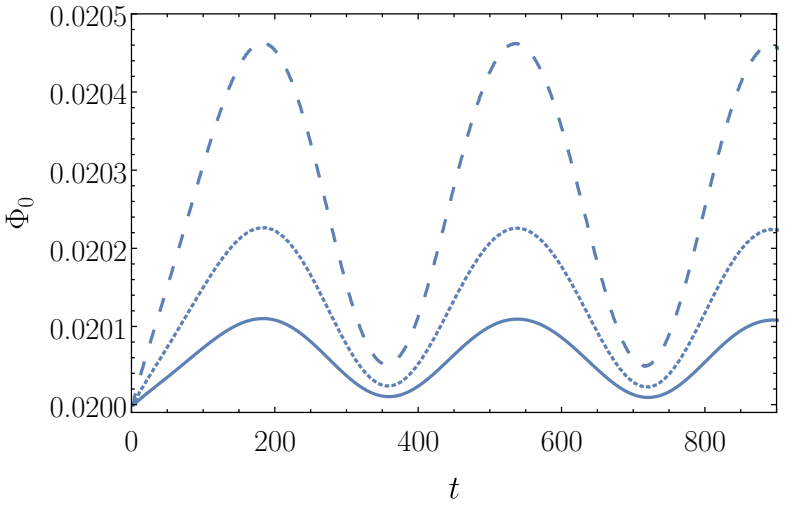

Figure 1.5.: Time evolution of the central value of the scalar field for a stable boson star for three different grid resolutions. We used a dashed line to plot the result with base resolution, a dotted line for double resolution and a solid line for quadruple resolution.

numerical calculations approach the time-independent outcome at the continuum level with second-order convergence. The rest of the evolved functions show the same trend as the one shown by the scalar field, they oscillate with frequency ω.

The fundamental frequency of oscillation for the scalar field is determined through a Fourier Transform analysis. Remarkably, the analysis reveals that this frequency aligns with the value of ω determined by the initial data.

1.4.2. Unstable models

Let us now investigate the behavior of boson stars whose initial parameters lie to the right of the maximum mass configuration, corresponding to the unstable branch, and possess negative binding energy. Its initial parameters are:

$\Phi_0(t=0)$	ω	M	E_B
0.1	0.82296	0.62180	-0.01775

Numerical investigations [42] have demonstrated that these models inevitably undergo gravitational collapse, leading to the formation of a Schwarzschild black hole. However, under certain perturbations, these models can also transition to the stable branch of equilibrium configurations [47, 48]. Specifically, if the only perturbation affecting the initial data is due to discretization errors, the models undergo a migration process towards the stable branch. Conversely, when a slightly larger perturbation is included in the initial data, the models collapse and form black holes.

A migrating boson star transforms into a different boson star configuration, maintaining the same mass but residing in the stable branch of equilibrium configurations. Consequently, the central scalar field of the star exhibits a smaller value. For instance, Figure 1.6 illustrates the migration of a boson star, depicting its movement from an initial central scalar field value of $\Phi_0(t=0) = 0.1$ to a final value of $\Phi_0 \approx 0.06$. Remarkably, this final value corresponds precisely

to the scalar field at which a stable boson star with the same mass is obtained (Figure 1.2). The corresponding Fourier Transform analysis points towards the same direction, showing that after the migration the frequency of the boson star is the one of the configuration with the same mass as the original but located in the stable branch.

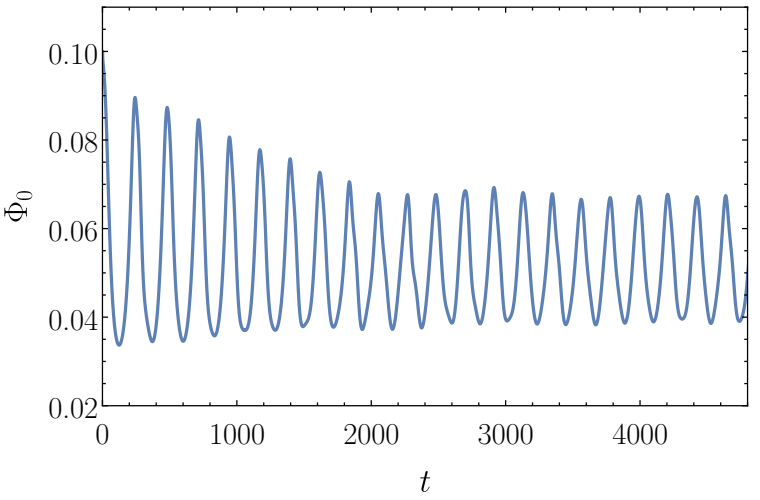

Figure 1.6.: Time evolution of the central value of the scalar field for an unstable boson star with negative binding energy.

Now, we are going to truly perturb this solution. To introduce perturbations, we augment the initial scalar field by 2% using a multiplication factor of 1.02 after solving the Einstein-Klein-Gordon system, and check that this perturbation does not alter the sign of the binding energy E_B. The metric variables a and α are not recomputed. The perturbation results in a slight violation of the constraints. However, given the relatively small magnitude of the perturbation (though larger than the discretization error), the overall solution remains largely unchanged.

To identify the emergence of black holes during the evolution, we determine the black hole mass by evaluating the area A, of the apparent horizon and employing the formula $M_{BH} = \sqrt{A/16\pi}$. Figure 1.7 displays the temporal progression of both, the boson star mass (M_{BS}) and the black hole mass (M_{BH}).

The boson star mass has been calculated using the Komar expression for the mass as shown in [49].

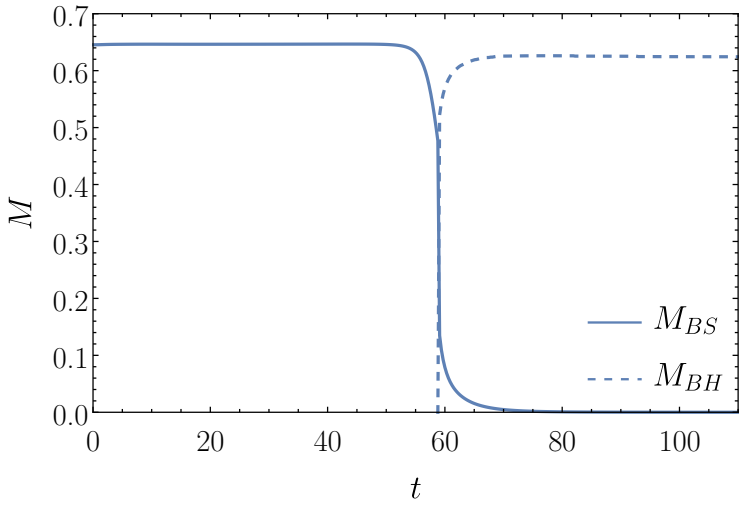

Figure 1.7.: Monitoring the mass of a collapsing boson star (M_{BS}) and the mass of the resulting black hole (M_{BH}).

In contrast to the migrating scenario, introducing a 2% perturbation in the initial data triggers the gravitational collapse, resulting in the eventual formation of an apparent horizon. This transition is evident from the sudden change observed in the boson star's mass evolution, accompanied by a rapid increase in the black hole mass from zero. We are able to observe that the mass of the final black hole is slightly smaller than the mass of the original boson star. This discrepancy arises as a consequence of some of the scalar field being released after the collapse. This indicates that, during the collapse into a black hole, a remnant of the initial scalar field lingers in the form of a spherical shell or cloud encircling the black hole [49]. Comparing the cloud of scalar field with the known behavior of scalar fields around black holes, studied in [50], we arrive to the conclusion that it forms a long-lived quasi-bound state. Moreover, the oscillating frequency of the quasi-bound state is different from that of the initial boson star.

Lastly, we are going to compute the time evolution of a model whose initial conditions are:

$\Phi_0(t=0)$	ω	M	E_B
0.18	0.76904	0.50671	0.01353

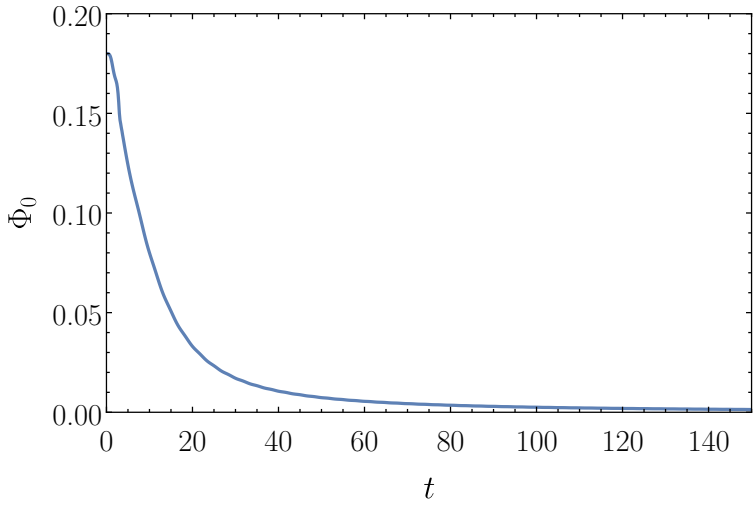

Figure 1.8.: Time evolution of the central value of the scalar field for an unstable boson star with positive binding energy.

This is a unstable boson star with a positive binding energy. In Figure 1.8 we plot the output of the evolution of this model for the central value of the scalar field. As one may see in the plot, the central value of the scalar field exhibits a rapid decline over time, leading to a significant radial expansion of the boson star, ultimately resulting in its dispersion. The occurrence of this unstable scenario is associated with a positive binding energy, which results in an excess of energy causing the star to lose its bounded nature.

1.5. Further aspects of boson stars

In the present chapter, we have explored the construction of spherically symmetric boson stars and investigated their dynamical evolution. However, numerous aspects of boson stars have been extensively studied in the literature. In this section, we briefly discuss some of these aspects that are relevant to our work.

Self-Interacting Boson Stars: A prominent variant of boson stars is the self-interacting boson stars [12]. In this case, the scalar field potential includes a self-interaction term given by

$$V(\Phi) = \mu^2|\Phi|^2 + \frac{\lambda}{2}|\Phi|^4 \quad . \tag{1.80}$$

Previously, we utilized a free-field potential, as discussed in Section 1.2. When assigning constituent boson masses based on known bosonic particles, it results in boson stars with relatively low masses. However, the introduction of the self-interaction term allows larger masses to be obtained. Moreover, self-interacting boson stars can also exhibit solitonic behavior, forming localized and stable configurations.

Spinning boson stars: Spinning boson stars possess notable features that distinguish them from their non-rotating counterparts [51, 52]. Similar to the magnetic or azimuthal quantum number in atomic systems, the angular momentum in spinning boson stars is expected to be quantized, shaping them into a toroidal form [53]. The rotation of boson stars induces frame dragging effects, causing spacetime to become twisted. However, it is crucial to acknowledge that spinning boson stars are susceptible to various instabilities, which can lead to the loss of angular momentum or gravitational collapse. Furthermore, numerical calculations involving spinning boson stars are highly complex requiring three-dimensional fully non-linear numerical simulations [54]. The investigation of these objects' stability remains an active area of research.

Proca Stars: Vector boson stars, also known as Proca stars, possess distinct characteristics compared to boson stars due due to the different nature of the

fields involved. They are composed of spin-1 complex vector fields, while (scalar) boson stars consist of spin-0 complex scalar fields. The matter Lagrangian for Proca stars is described by the Proca Lagrangian [17],

$$\mathcal{L}_{\mathcal{M}} = -\frac{1}{4}F_{ab}\bar{F}^{ab} - \frac{1}{2}\mu^2 A_a \bar{A}^a \quad . \tag{1.81}$$

Despite their spin-1 nature, Proca stars share several features with boson stars, including carrying a conserved Noether charge, exhibiting harmonic time dependence, existing within a certain range of frequencies, and having masses of the same order of magnitude. Remarkably, Proca stars have been observed to be more stable than spin-0 boson stars when angular momentum is introduced [55]. The study of Proca boson stars provides further insight into the behavior and stability of compact objects beyond the scalar field paradigm.

Boson Star Binaries: Systems consisting of two boson stars have received significant attention in the literature, providing insights into various aspects of this complex scenario [54, 56, 57]. The coalescence of boson star binaries serves as a major source of gravitational waves, making their study valuable due to potential observational counterparts. Boson star binaries solely interact gravitationally, resulting in an intriguing phenomenon that highlights their solitonic nature. In head-on collisions with high initial velocities, the boson stars pass through each other, creating an interference pattern during the interaction while approximately retaining their original shapes afterward [58]. Alternatively, for sufficiently low initial velocities, the boson stars can merge and form a new boson star [56]. Depending on the initial energy of the system, this merged state may undergo gravitational collapse and form a black hole.

Boson Star Formation: The scenario of boson star formation has been investigated through numerical simulations of diluted clouds of scalar field [59, 60]. Initially, the cloud represents an unbound state with a higher amount of kinetic energy compared to potential energy. During the process of gravitational cooling, the cloud gradually expels the excess scalar field, reducing its kinetic energy and allowing the system to become bound. As a result, the scalar field cloud collapses under its own self-gravity, shedding excess kinetic energy in

the process. This mechanism provides insights into the formation of boson stars and their dynamical evolution from initially unbound states to bound, self-gravitating structures.

To delve deeper into the subject and gain a broader perspective regarding boson stars, we direct the reader to widely recognized reviews [27, 61].

Chapter 2.

Modified gravity

2.1. Introduction

Gravity, the universal force that governs the interactions between objects with mass, holds the key to comprehend the fundamental mechanics underlying the motion, structure, and dynamics of our physical world. As we survey the current landscape of gravitational research, it becomes undeniable that *General Relativity* stands as the preeminent theory, elegantly explaining the complexities of gravity and shaping our understanding of the fundamental workings of the universe.

Emerging in 1915 [62], General Relativity has been extensively validated through a range of experimental tests across different scenarios [63]. It has provided successful explanations and predictions for various phenomena, including the observed precession of Mercury's orbit and the gravitational deflection of light by massive objects [64]. Notably, General Relativity revolutionized our understanding of gravity by portraying it as a profound geometric effect rather than a conventional force. In this framework, gravity is interpreted as the dynamics of spacetime geometry, where matter fields evolve. This viewpoint conventionally represents the gravitational field using the metric of a pseudo-Riemannian manifold and its associated curvature tensor [25, 65].

An empirical milestone in the validation of General Relativity occurred in September 2015 [66] with the direct detection of gravitational waves, confirming a prediction derived from the theory. This groundbreaking achievement provided direct evidence of the existence of these ripples in spacetime, strengthening the validity of General Relativity. Since then, 90 gravitational wave events have been confirmed.

Furthermore, General Relativity has played a fundamental role in the development of modern cosmology. Independently pioneered by Friedmann [67] and Lemaître [68], and subsequently expanded upon by Robertson and Walker [69, 70], it paved the way for the formulation of the Friedmann-Lemaître-Robertson-Walker (FLRW) metric. This metric provides a descriptive framework for comprehending the large-scale structure and evolution of the universe. However, tensions arise when comparing the predictions of the theory with observational data. To reconcile these discrepancies, the prevailing framework in modern cosmology is the ΛCDM (Λ Cold Dark Matter) model [71]. This model incorporates the influence of dark energy, an unknown form of energy that affects the universe on large scales, and dark matter, an unobserved type of matter that interacts solely through gravity. In particular, various experiments yield conflicting results regarding the value of the Hubble parameter [72], in other words, the rate at which astrophysical bodies move away from us.

In addition to these cosmological implications, General Relativity also predicts the existence of certain singularities, regions in spacetime that are ill-defined and can be reached by observers in a finite proper time. Within this theory, two types of singularities arise. First, the Big Bang singularity corresponds to an early-time singularity associated with the origin of the universe. Second, black holes, astronomical objects of extreme density predicted by General Relativity, accommodate a singularity at their centers. The presence of singularities challenges the viability of General Relativity as a fundamental theory describing gravitational interactions.

While General Relativity has been successful in explaining phenomena in a wide range of scales, it encounters limitations when trying to understand

gravity at extremely small distances. At atomic scales, the classical framework of General Relativity is no longer applicable, and quantum effects become important. General Relativity does not incorporate the principles of quantum mechanics that govern the behavior of particles and fields in these situations. As a result, the reconciliation of these two theories remains unresolved.

Moreover, the theory of General Relativity was formulated based on the principles of mathematical elegance and the fulfillment of the equivalence principle. However, it has not undergone direct experimental verification to validate its fundamental structure. Although its viability has been confirmed across a broad range of scales, from the millimeter scale to the astronomical scale, we cannot definitively assert that this theory is the ultimate description of gravity applicable to all scales. Deviations between the predictions of General Relativity at higher energy regimes and experimental observations are plausible, revealing the potential limitations of the theory.

The tension arising from observational data and theoretical issues within the fundamental framework of General Relativity has led to the exploration of extensions to the theory. Various efforts have been made in this direction, driven either by phenomenological motivations or by theoretical considerations [73]. To better understand these extensions, let us first describe the framework of General Relativity. Differential geometry serves as the mathematical foundation, where spacetime is represented as a manifold equipped with a metric tensor, which measures the distance between events. This leads to the notion of a connection, which describes how vectors are transported along curves in spacetime and gives rise to the concept of the covariant derivative. The gravitational aspect of the theory is encoded in the gravity Lagrangian, which, together with the matter Lagrangian, $\mathcal{L}_{\mathcal{M}}$, forms the action of General Relativity, known as the Einstein-Hilbert action

$$\mathcal{S} = \int d^4x\sqrt{-g}\left(\frac{R}{2\kappa} + \mathcal{L}_{\mathcal{M}}\right) \quad . \tag{2.1}$$

Where, $\kappa = 8\pi$ is the Einstein gravitational constant in natural units, g is the determinant of the metric tensor $g_{\mu\nu}$ and R is the Ricci curvature scalar.

With the aforementioned elements, we establish a framework in which spacetime is described in geometric terms, where matter resides and has the ability to shape the structure of spacetime. Simultaneously, the dynamics of matter are influenced by the properties of spacetime, creating a mutual interplay between the two. At the same time observers evolve in this spacetime respecting the causality of the events observed putting a constraint to the speed of light and the speed at which information is transported. The main ways of going beyond General Relativity are modifying the basic elements of the differential geometry and the description of the gravity Lagrangian.

The connection $\Gamma^{\lambda}_{\mu\nu}$ plays a crucial role in accounting for the effects of gravity on the transport of vectors along curves. In General Relativity, the connection is defined as the Levi-Civita connection, which is compatible with the metric, preserving it ($\nabla_\lambda g_{\mu\nu} = 0$), and torsion-free ($\Gamma^{\lambda}_{\mu\nu} = \Gamma^{\lambda}_{\nu\mu}$).

One approach to extending Einstein's gravity is by considering non-trivial connections, relaxing the assumption of metric preservation and allowing for torsion. This is known as the metric-affine formalism [74, 75]. By introducing this extension, the geometric structure of spacetime changes, and the manifold becomes post-Riemannian. This formulation introduces the non-metricity tensor $Q_{\lambda\mu\nu} \equiv \nabla_\lambda g_{\mu\nu}$ and the torsion tensor $T^{\lambda}_{\nu\mu} \equiv \Gamma^{\lambda}_{\mu\nu} - \Gamma^{\lambda}_{\nu\mu}$. As a result, the general connection $\mathring{\Gamma}^{\lambda}_{\nu\mu}$ is no longer the Levi-Civita connection but includes additional terms related to non-metricity and torsion, given by $L^{\lambda}_{\nu\mu}$ and $K^{\lambda}_{\nu\mu}$, respectively [76]:

$$\mathring{\Gamma}^{\lambda}_{\nu\mu} \equiv \Gamma^{\lambda}_{\nu\mu} + L^{\lambda}_{\nu\mu} + K^{\lambda}_{\nu\mu} \quad . \tag{2.2}$$

The presence of non-metricity and torsion leads to the definition of a general Riemann tensor. Furthermore, symmetric teleparallel gravity and teleparallel gravity [76–78] are extensions of General Relativity in which the traditional curvature tensor, associated with the Levi-Civita connection, is set to be null. Instead, the curvature effects are accounted for by an invariant associated with non-metricity in the case of symmetric teleparallel gravity, or by the the invariant associated with torsion in the case of teleparallel gravity.

Another avenue for extending General Relativity involves modifications to the gravity Lagrangian. Scalar-tensor theories, for example, introduce a scalar field ϕ alongside the Ricci curvature scalar and the metric tensor to mediate gravitational interactions [79]

$$\mathcal{S} = \int d^4x\sqrt{-g}\left(\frac{\phi R}{16\pi} + \mathcal{L}_\phi + \mathcal{L}_\mathcal{M}\right) \quad . \tag{2.3}$$

When field equations involve higher-order derivatives, they can result in a Hamiltonian that is unbounded from below, implying that the system has infinitely many degrees of freedom with negative kinetic energy. This may lead to instabilities in the system which are commonly referred to as Ostrogradski ghost instabilities [80]. In order to avoid them, it is necessary to impose conditions on the Lagrangian $\mathcal{L}_\phi$, such as the absence of higher than second-order derivatives of the field as seen in Brans-Dicke theories [81]. One can further generalize the interaction between the scalar field ϕ and the metric tensor by replacing ϕ with $f(\phi)$. This leads to the most general theory involving the metric tensor and a scalar field, free of ghost instabilities, known as Horndeski theory [82]. It is also possible to substitute the scalar field ϕ with a vector or tensor field, leading to so-called tensor-vector-scalar gravity [79].

We should be briefly mention the ongoing efforts to unify the gravitational interaction with the other known interactions in physics. Various approaches have been explored in this regard, aiming to extend the existing understanding of the field. We can mention some examples, such as Loop Quantum Gravity, string theories and brane theories [83, 84].

Among the various approaches to explore gravity beyond General Relativity, we will focus on $f(R)$ gravity [85]. These models offer significant simplicity and flexibility, providing valuable insights into the behavior of the universe beyond the scales governed by General Relativity. In this theory the Ricci scalar R from the Einstein-Hilbert action is substituted by a more general $f(R)$ function

$$\mathcal{S} = \int d^4x\sqrt{-g}\left(\frac{f(R)}{2\kappa} + \mathcal{L}_\mathcal{M}\right) \quad . \tag{2.4}$$

By examining $f(R)$ models, we can potentially explain both the cosmological expansion of the early universe and its present-day expansion, obviating the need to introduce concepts such as dark energy [86]. This is because the cosmological expansion is an intrinsic effect arising from the gravitational description itself. As a result, $f(R)$ theories have received extensive research attention as the simplest modification to Einstein's gravity. However, it is of significance that these theories are not without their challenges. In the metric formalism, which assumes the connection is determined by the metric, the nonlinearities associated with the $f(R)$ Lagrangian introduce a dynamic degree of freedom in the gravitational sector [87].

On the other hand, if we take an approach to the theory through the Palatini formalism [88], where the metric and connection are treated as two independent and equally fundamental entities, we observe that the additional degree of freedom in the theory is non-dynamic. Thus, the nonlinearities of the Palatini $f(\mathcal{R})$ Lagrangian induce nonlinearities in the matter sector, as we will explore in the upcoming sections. Consequently, the field equations of Palatini $f(\mathcal{R})$ in vacuum are equivalent to those of General Relativity with a cosmological constant, and only in the presence of matter will disparities arise. This stands in stark contrast to metric $f(R)$ theories, where even in vacuum, the space is curved, potentially giving rise to long-range effects within the Newtonian regime. As the reader may have noticed, when referring to the Palatini formalism, the Ricci scalar is denoted as $\mathcal{R}$ since it is the curvature scalar that follows from the independent connection, i.e., $\mathcal{R} \equiv g^{\mu\nu}\mathcal{R}_{\mu\nu}(\Gamma)$, and should not be confused with $R \equiv g^{\mu\nu}\mathcal{R}_{\mu\nu}(g)$, which follows from the Levi-Civita connection.

The Palatini formalism is a metric-affine approach employed in theories where the Lagrangian exclusively incorporates the Riemann curvature tensor and its associated invariants, such as the Ricci tensor and the Ricci scalar. Henceforth, we will interchangeably utilize the terms metric-affine or Palatini formalism to denote the independence of the connection from the metric. The

action for Palatini $f(\mathcal{R})$ can be expressed as follows

$$\mathcal{S} = \int d^4x\sqrt{-g}\left(\frac{f(\mathcal{R})}{2\kappa} + \mathcal{L}_{\mathcal{M}}\right) \quad . \tag{2.5}$$

Palatini $f(\mathcal{R})$ belongs to a broader class of theories known as Ricci-Based Gravity. These theories, as the name implies, are formulated based on the Ricci tensor of the connection and its contractions. From a computational perspective, these theories are particularly interesting. In the Palatini framework, it is possible to transform the problem of a modified gravity theory minimally coupled to a scalar field or other matter source into a standard problem in General Relativity minimally coupled to a modified scalar Lagrangian or other matter Lagrangian [89–93]. This property has recently been utilized to generate new analytical solutions for static, spherically symmetric scalar compact objects in Palatini $f(\mathcal{R})$ and other theories [94].

Remarkably, by starting with a known solution of General Relativity involving a spherically symmetric, static, massless real scalar field, which represents a naked singularity, it has been possible to obtain new exotic compact objects such as wormholes and other configurations with peculiar causal properties within the high-density region. These solutions exhibit nearly identical behavior to the standard General Relativity solution in their exterior regions, where the energy density rapidly drops to zero, and the dynamics approach that of General Relativity. Moreover, this approach has facilitated the construction of new exact rotating solutions [95,96] and even multicenter solutions [97] (without defined symmetry). Such advancements have expanded our understanding of the possibilities offered by Palatini $f(\mathcal{R})$ and related theories.

In this chapter of the present work, we delve into the realm of modified gravity, focusing on the essential aspects of General Relativity as a starting point. We aim to provide a comprehensive review that not only familiarizes the reader with the fundamentals of General Relativity but also explores the motivations behind the quest to extend its mathematical framework. In addition, our objective is to highlight the significance of Palatini $f(\mathcal{R})$ gravity. We emphasize

its correspondence with the space of solutions of General Relativity, which presents a valuable advantage in terms of computational tools for numerical simulations.

2.2. General Relativity essentials

After formulating the theory of special relativity, Einstein aimed to generalize his results to scenarios involving the presence of matter. Einstein based his approach on two fundamental principles. The first was the Principle of Relativity (or covariance), which stated that the laws of physics should be the same for all reference frames. The second principle was the Principle of Equivalence, which asserted that no local experiment could distinguish between an observer in free fall and an inertial observer. In Einstein's own words [98]:

> "For an observer falling freely from the roof of a house, there exists —at least in his immediate surroundings— no gravitational field."

This insight paved the way for the development of General Relativity. However, in order to reconcile these fundamental principles, Einstein recognized the need for a new mathematical framework. It was through the guidance of mathematician Marcel Grossmann that Einstein was introduced to the powerful tools of differential geometry. As Einstein himself remarked [99]:

> "If all systems are equivalent, then Euclidean geometry cannot hold in all of them. To throw out geometry and keep laws is equivalent to describing thoughts without words. We must search for words before we can express thoughts. What must we search for at this point? This problem remained insoluble to me until 1912, when I suddenly realized that Gauss's theory of surfaces holds the key for unlocking this mystery. I realized that Gauss's surface coordinates had a profound significance. However, I did not know at that time that Riemann had studied the foundations of geometry in an even more profound way. I suddenly remembered that Gauss's theory

> was contained in the geometry course given by Geiser when I was a student... I realized that the foundations of geometry have physical significance. My dear friend the mathematician Grossmann was there when I returned from Prague to Zurich. From him I learned for the first time about Ricci and later about Riemann. So I asked my friend whether my problem could be solved by Riemann's theory, namely, whether the invariants of the line element could completely determine the quantities I had been looking for."

Let us introduce the main objects used in differential geometry [25, 65]:

Manifold: A manifold $\mathcal{M}$ is a topological n-dimensional space where each point has a neighbourhood that is homeomorphic to the Euclidean space of dimension n. If it has a globally defined differential structure (each point has a neighbourhood that is diffeomorphic to the Euclidean space) it is a differential manifold.

Tangent space: The vectorial sum of two points in an Euclidean space yields a third point in the same space. This is not the case for a curved space, in which the vector space structure is lost. Nevertheless vector space structure can be recovered in the limit of infinitesimal displacements (tangent vectors) over a point. Furthermore, these tangent vectors must only rely on the intrinsic structure of the manifold and not to its possible embedding in a higher-dimensional space.

The tangent space $T_p\mathcal{M}$, of $\mathcal{M}$ at the point p is defined as the set of all tangent vectors at p. It has the same dimension as the manifold. The disjoint union of all the tangent spaces of $\mathcal{M}$ is called tangent bundle, $T\mathcal{M}$.

Tensors: In the realm of differential geometry, every vector space has an associated dual space. In the context of the tangent space at a point p on a manifold, denoted as $T_p\mathcal{M}$, its dual space is represented as $T_p\mathcal{M}^*$ and consists of elements called 1-forms. If we consider the basis of the tangent space as $\{\partial_\mu\}$, then the corresponding coordinate basis of the dual space, $T_p\mathcal{M}^*$, is given by $\{dx^\mu\}$. Vector fields can be expressed as $v = v^\mu \partial_{x^\mu}$, where v^μ are the

components of the vector field with respect to the chosen coordinate basis. On the other hand, 1-forms are written as $w = w_\mu dx^\mu$, where w_μ represents the components of the 1-form in the coordinate basis.

By combining the tangent space $T_p\mathcal{M}$ and its dual space $T_p\mathcal{M}^*$, we can define tensors, which are multilinear relationships between vectors and covectors. In this context, a covector can be understood as the dual counterpart of a vector, analogous to how a vector field corresponds to a vector. In other words, a covector is in relation to a 1-form what a vector is to a vector field. The defining characteristic of tensors is their transformation properties under coordinate transformations. A tensor of rank (or order) n possesses n indices, and its components exhibit specific transformation laws when changing between different coordinate systems.

$$T^{i'_1\ldots i'_p}_{\quad j'_1\ldots j'_q}(\bar{x}^1,...,\bar{x}^n) = \frac{\partial \bar{x}^{i'_1}}{\partial x^{i_1}}\ldots\frac{\partial \bar{x}^{i'_p}}{\partial x^{i_p}}\frac{\partial x^{j_1}}{\partial \bar{x}^{j'_1}}\ldots\frac{\partial x^{j_q}}{\partial \bar{x}^{j'_q}}T^{i_1\ldots i_p}_{\quad j_1\ldots j_q}(x^1,...,x^n) \tag{2.6}$$

These transformation laws ensure that the tensor remains invariant under coordinate transformations, allowing it to describe physical quantities independent of the chosen coordinate system.

Metric tensor: In differential geometry, the metric tensor is a fundamental concept that characterizes the geometry of a manifold. It is defined as an inner product on the tangent space $T_p\mathcal{M}$ at each point p of a smooth, differentiable manifold $\mathcal{M}$. The metric tensor $g_{\mu\nu}$ assigns a scalar to pairs of tangent vectors and varies smoothly from point to point. It measures distances, angles, and defines the notion of length and inner product in the manifold. The line element, which represents the infinitesimal distance between two points, is given by $ds^2 = g_{\mu\nu}dx^\mu dx^\nu$. The metric tensor is required to be symmetric to ensure that the distance between point A and point B is the same as the distance between point B and point A. In an Euclidean 4-dimensional space, the metric tensor has a signature of $(++++)$, while in a pseudo-Riemannian space, the signature is $(-+++)$ or $(+---)$ depending on the convention used.

Affine connection: The affine connection Γ on a smooth manifold $\mathcal{M}$ is defined as a rule that associates, for each point $p \in \mathcal{M}$, a linear map called the connection map or covariant derivative, denoted by ∇, which takes pairs consisting of a vector field X and a differential function Y defined in a neighborhood of p, and produces another vector field $\nabla_X Y$ defined in the same neighborhood.

The covariant derivative allows us to compare vectors in different tangent spaces from the same manifold using what is called parallel transport. If we have a vector v in a point $p \in M$ we can parallelly transport it along the curve $c(t)$ passing through p if $\nabla_{\dot{c}(t)} v = 0$. Parallelly transporting the vector v to a point $q \in M$ where is defined another vector w allows us to compare them.

Curvature. In flat space, the parallel transport of a vector along a smooth curve results in the vector remaining unchanged. However, in curved space, parallel transport leads to changes in the vector, providing us with information about the curvature of the space. To quantify this curvature, we define the Riemann curvature tensor $R^{\alpha}{}_{\beta\mu\nu}$, and the torsion tensor $S^{\alpha}{}_{\mu\nu}$.

$$R^{\alpha}{}_{\beta\mu\nu} \equiv \partial_\mu \Gamma^{\alpha}_{\nu\beta} - \partial_\nu \Gamma^{\alpha}_{\mu\beta} + \Gamma^{\alpha}_{\mu\lambda}\Gamma^{\lambda}_{\nu\beta} - \Gamma^{\alpha}_{\nu\lambda}\Gamma^{\lambda}_{\mu\beta} \quad , \tag{2.7}$$

$$S^{\alpha}{}_{\mu\nu} \equiv \Gamma^{\alpha}_{\mu\nu} - \Gamma^{\alpha}_{\nu\mu} \quad . \tag{2.8}$$

The Riemman curvature tensor is defined at every point on the manifold, providing a measure of how different neighboring points are from those in Euclidean space. The Riemann curvature tensor exhibits antisymmetry with respect to its last two indices $R^{\alpha}{}_{\beta\mu\nu} = -R^{\alpha}{}_{\beta\nu\mu}$.

The torsion tensor, on the other hand, reveals the twisting of space around a curve. In the absence of torsion, the affine connection is symmetric.

Additionally, by contracting the Riemann curvature tensor, we obtain the Ricci curvature tensor, $R_{\mu\nu} \equiv R^{\alpha}{}_{\mu\alpha\nu}$.

Metric-connection relation: Although the metric tensor and the affine connection are independent objects in differential geometry, there is a way to relate them by imposing that the scalar product of any two vectors, parallel transported along any curve, remains covariantly constant

$$0 = \nabla_\mu g_{\alpha\beta} = \partial g_{\alpha\beta} - \Gamma^\lambda_{\mu\alpha} g_{\lambda\beta} - \Gamma^\lambda_{\mu\beta} g_{\alpha\lambda} \quad , \tag{2.9}$$

In cases where the torsion tensor vanishes, the connection becomes symmetric and is known as the Levi-Civita connection, represented by the Christoffel symbols

$$\Gamma^\lambda_{\mu\nu} = \frac{1}{2} g^{\lambda\rho} [\partial_\mu g_{\rho\nu} + \partial_\nu g_{\rho\mu} - \partial_\rho g_{\mu\nu}] \quad . \tag{2.10}$$

In those cases we say that the associated geometry is Riemannian. The Ricci curvature scalar can be defined by contracting the Ricci curvature tensor with the metric

$$R \equiv g^{\mu\nu} R_{\mu\nu} \quad . \tag{2.11}$$

Then, when metric compatibility is imposed the spacetime geometry is fully described by the metric tensor, which not only characterizes distances and angles but also defines parallel transport through the construction of the Levi-Civita connection.

In this geometric context, Einstein's axioms were reformulated as follows. At each point in spacetime, which is described by a manifold, it is possible to establish a tangent space characterized by a Minkowskian metric as shown

artistically in Figure 2.1. It was also reasoned that the laws of nature should be expressed in tensorial form to adhere to the principle of relativity.

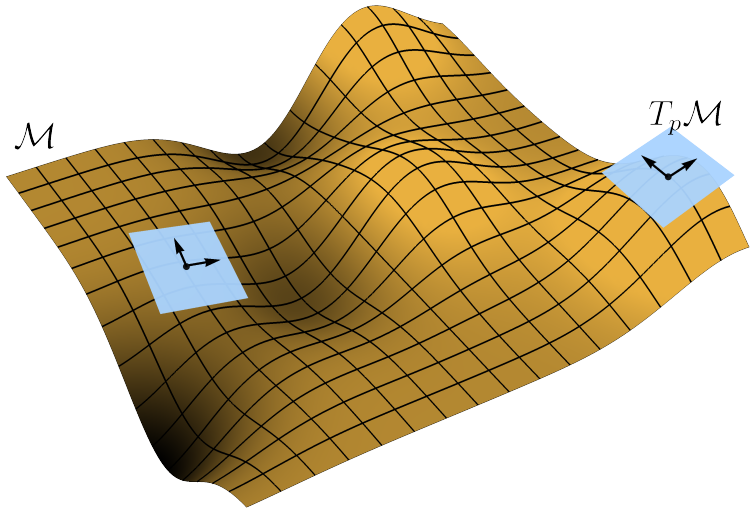

Figure 2.1.: Diagram of the tangent bundle

2.2.1. Einstein's field equations

There are two distinct paths to derive the Einstein field equations, which serve as the fundamental cornerstone of General Relativity. These equations assume the principle of equivalence, the principle of relativity, and must reduce to Newton's laws in the appropriate limit.

Einstein's quest was to establish a connection between the curvature of spacetime and the presence of matter. Since matter can be described by a rank-2 tensor denoted as $T_{\mu\nu}$, the corresponding equations describing curvature should also involve a rank-2 tensor. This leads us to the relationship:

$$G_{\mu\nu} = T_{\mu\nu}. \tag{2.12}$$

However, determining the exact form of the Einstein tensor $G_{\mu\nu}$ in relation to curvature tensors was not initially clear. The conservation of the energy-momentum tensor $\nabla_\lambda T_{\mu\nu} = 0$ implies the same for the Einstein tensor, but its explicit expression remained elusive. Equating the Einstein tensor with the Ricci tensor seemed like a straightforward approach, but it would result in $\nabla_\lambda R_{\mu\nu} = 0$, indicating a constant curvature throughout spacetime, a physically unacceptable scenario leading to a trivial geometry.

Consequently, the search was on for a curvature tensor $G_{\mu\nu}$ of rank 2, characterized by a vanishing divergence. The Riemann tensor was considered, and specific symmetries were imposed to aid in finding a suitable expression for $G_{\mu\nu}$. By imposing the condition $\nabla_\lambda g_{\mu\nu} = 0$, the Bianchi identities emerged, providing valuable insights. Using these identities, Einstein discovered a curvature tensor that meet the requirements

$$G_{\mu\nu} \equiv R_{\mu\nu} - \frac{1}{2} g_{\mu\nu} R = \kappa T_{\mu\nu}, \tag{2.13}$$

where κ is a constant determined through the Newtonian limit of these equations.

On the other hand, we have the formulation by Hilbert, which he developed almost concurrently with Einstein, leading to the same set of equations. This formulation originates from the variational principle, which states that if we can construct an action for a theory, we can derive the equations of motion for that theory by requiring the action's functional to be stationary. Consequently, the crucial task lies in identifying the appropriate functional to represent the action. We seek a scalar quantity that can be integrated over the entire spacetime and incorporates terms related to both matter and curvature. The simplest scalar associated with curvature is the Ricci scalar R. Thus, we propose the Einstein-Hilbert action as follows

$$\mathcal{S} = \int d^4x \sqrt{-g} \left[\frac{1}{2\kappa} R + \mathcal{L}_\mathcal{M} \right] \quad . \tag{2.14}$$

Here, we assume $\nabla_\lambda g_{\mu\nu} = 0$, and the connection does not include any torsion terms, $\Gamma^\gamma_{\alpha\beta} \equiv \Gamma^\gamma_{\beta\alpha}$. Recall that the Ricci scalar R, is also computed with

those assumptions. Therefore, the connection is uniquely determined as the Levi-Civita connection for this particular spacetime. Accordingly, the metric becomes the fundamental object in this theory, and it is with respect to the metric that we variate the action

$$\delta\mathcal{S} = \int d^4x \left[\frac{\delta\left(\sqrt{-g}R\right)}{2\kappa} + \delta\left(\sqrt{-g}\mathcal{L}_{\mathcal{M}}\right)\right] = 0 \quad . \tag{2.15}$$

By employing the identities

$$\delta\sqrt{-g} = -\frac{1}{2}\sqrt{-g}g_{\mu\nu}\delta g^{\mu\nu} \quad , \tag{2.16}$$

$$\delta R = R_{\mu\nu}\delta g^{\mu\nu} + \nabla_\alpha\left(g^{\mu\nu}\delta\Gamma^\alpha_{\mu\nu} - g^{\mu\alpha}\delta\Gamma^\nu_{\mu\nu}\right) \quad , \tag{2.17}$$

and the definition of the energy-momentum tensor

$$T_{\mu\nu} = -\frac{2}{\sqrt{-g}}\frac{\delta\left(\sqrt{-g}\mathcal{L}_{\mathcal{M}}\right)}{\delta g^{\mu\nu}} \quad , \tag{2.18}$$

we can derive the Einstein field equations in the same way as they are represented in Eq. (2.13). Notice that the second term in Eq. (2.17) represents a boundary term, and according to the Stokes theorem, it does not contribute to the resulting Einstein field equations.

2.2.2. General Relativity à la Palatini

As observed, the compatibility of the metric has been postulated based solely on a criterion of simplicity. However, what implications would arise if we were to deviate from this criterion? In 1925, Einstein proposed an approach [100] aimed at extending and generalizing the principles of General Relativity. This alternative formulation sought to explore the consequences of relaxing the assumption of metric compatibility. By considering such a departure, Einstein aimed to investigate potential modifications and broaden our understanding

of the gravitational interaction. This approach is known as the metric-affine formalism, also referred to as the Palatini formalism when the theory only involves the Riemann curvature tensor and its invariants. It is necessary to clarify that the formalism, despite its misattribution to Attilio Palatini, was actually introduced by Einstein himself, as previously mentioned.

To gain physical insight into the concepts of torsion and non-metricity, let us analyze the behavior of an infinitesimal parallelogram formed by parallel transporting two vectors along each other. It is not guaranteed a priori that this process will result in a closed parallelogram. The presence of torsion precisely characterizes the failure of the infinitesimal parallelogram to close properly.

Furthermore, to comprehend the impact of non-metricity on the manifold, let us consider a null vector denoted as u^μ, satisfying the condition $g_{\mu\nu}u^\mu u^\nu = 0$. If the covariant derivative of the metric tensor does not vanish, the parallel transport of this vector may alter its null character. Consequently, the invariant nature of the light cone structure under parallel transport would no longer be preserved. The non-metricity measures the change of lengths and angles along a curve.

Starting from the Einstein-Hilbert action, we consider the Ricci scalar derived from the contraction of the metric with the Ricci tensor, which depends solely on the connection

$$\mathcal{S} = \int d^4x\sqrt{-g}\left[\frac{1}{2\kappa}\mathcal{R} + \mathcal{L}_{\mathcal{M}}(\psi, g_{\mu\nu})\right] \quad , \tag{2.19}$$

where $\mathcal{R} \equiv g^{\mu\nu}\mathcal{R}_{\mu\nu}(\Gamma)$ denotes the Ricci scalar derived from the connection, distinguishing it from the metric Ricci scalar $R \equiv g^{\mu\nu}R_{\mu\nu}(g)$, which is derived from the Levi-Civita connection. The matter lagrangian is determined by the matter field ψ and its coupling to the metric.

Applying the variational principle to the action, considering both the metric and the connection as independent and equally fundamental objects, we calculate the variation with respect to each of them. Varying with respect to the metric,

we have

$$\delta_g S = \int d^4x \left[\delta_g \left(\sqrt{-g} \frac{\mathcal{R}}{2\kappa} \right) + \delta_g \left(\sqrt{-g} \mathcal{L}_{\mathcal{M}} \right) \right] = 0 \quad . \tag{2.20}$$

The second term yields the energy-momentum tensor, while the first term can be expressed as

$$\begin{aligned} \delta_g \left(\sqrt{-g} \mathcal{R} \right) =& \mathcal{R} \delta(\sqrt{-g}) + \sqrt{-g} \mathcal{R}_{\mu\nu} \delta g^{\mu\nu} \\ =& -\frac{1}{2} \sqrt{-g} g_{\mu\nu} \mathcal{R} \delta g^{\mu\nu} + \sqrt{-g} \mathcal{R}_{\mu\nu} \delta g^{\mu\nu} \quad . \end{aligned} \tag{2.21}$$

Consequently

$$\delta_g S = \int d^4x \sqrt{-g} \left[\frac{1}{2\kappa} \left(-\frac{1}{2} g_{\mu\nu} \mathcal{R} \delta g^{\mu\nu} + \mathcal{R}_{\mu\nu} \delta g^{\mu\nu} \right) - \frac{1}{2} T_{\mu\nu} \delta g^{\mu\nu} \right] = 0 \quad . \tag{2.22}$$

Next, considering the variation with respect to the connection

$$\begin{aligned} \delta_\Gamma \mathcal{S} &= \int d^4x \sqrt{-g} \frac{\delta_\Gamma \mathcal{R}}{2\kappa} \\ &= \int d^4x \sqrt{-g} g^{\mu\nu} \frac{\delta_\Gamma \mathcal{R}_{\mu\nu}}{2\kappa} \\ &= \int d^4x \sqrt{-g} g^{\mu\nu} \frac{1}{2\kappa} \left(\nabla_\alpha \delta\Gamma^\alpha_{\mu\nu} - \nabla_\nu \delta\Gamma^\alpha_{\mu\alpha} \right) \\ &= \int \frac{d^4x}{2\kappa} \left[\delta^\nu_\alpha \nabla_\beta \left(\sqrt{-g} g^{\mu\beta} \right) - \nabla_\alpha \left(\sqrt{-g} g^{\mu\nu} \right) \right] \delta\Gamma^\alpha_{\mu\nu} = 0 \, . \end{aligned} \tag{2.23}$$

Here, δ^ν_α represents the Kronecker delta used to manipulate the indices of $\delta\Gamma^\alpha_{\mu\nu}$. This equation implies that

$$\frac{1}{2} \delta^\nu_\alpha \nabla_\beta \left(\sqrt{-g} g^{\mu\beta} \right) + \frac{1}{2} \delta^\mu_\alpha \nabla_\beta \left(\sqrt{-g} g^{\nu\beta} \right) - \nabla_\alpha \left(\sqrt{-g} g^{\mu\nu} \right) = 0 \, . \tag{2.24}$$

After some algebraic manipulation [74, 88, 101], it can be shown that if this equation holds for any arbitrary connection, then

$$\nabla_\alpha g^{\mu\nu} = 0 \quad . \tag{2.25}$$

Consequently, the equations of motion indicate that the connection must be the Levi-Civita connection. By inserting this result into Eq. (2.22), we recover the usual Einstein field equations.

Thus, it can be concluded that both the metric formalism and the metric-affine formalism result in identical equations of motion, the equations of General Relativity, thereby establishing their equivalence.

2.3. Metric $f(R)$ gravity

Practically from the very moment the General Theory of Relativity was formulated and established, models emerged that aimed to extend and refine its framework. As we have seen, Hilbert chose the Ricci scalar as the gravitational Lagrangian term, as it is the simplest scalar quantity that captures the curvature of spacetime. However, it soon became apparent that the gravitational Lagrangian in General Relativity is incomplete and may not fully account for certain phenomena.

To overcome these limitations and explore possible modifications to the theory, alternative approaches have been proposed. One such approach is the $f(R)$ gravity models [85, 102], where the gravitational Lagrangian term is replaced with a more general function of the Ricci scalar, denoted as $f(R)$. This modification allows for a broader description of gravity, accommodating additional terms and dynamics beyond what is captured by the Einstein-Hilbert action.

Furthermore, $f(R)$ gravity models also have implications for the cosmic acceleration and the nature of dark energy [103]. In particular, certain choices

of the $f(R)$ function can lead to modified gravitational equations that produce accelerated expansion of the universe without the need for an exotic energy component such as dark energy.

We will now derive the equations of motion for the aforementioned $f(R)$ gravity theory. The action of $f(R)$ gravity is given by

$$\mathcal{S} = \int d^4x\sqrt{-g}\left[\frac{1}{2\kappa}f(R) + \mathcal{L}_{\mathcal{M}}\right] \quad , \tag{2.26}$$

where κ is a constant, $f(R)$ is a function of the Ricci scalar R, and $\mathcal{L}_{\mathcal{M}}$ represents the Lagrangian of matter fields.

In this metric approach, we consider the metric as the sole independent object of the theory, and the connection is determined by the metric and assumed to be the Levi-Civita connection. Let us now vary the action with respect to the metric. It is important to note that unlike the derivation performed in Section 2.2.1, the term proportional to $\delta R_{\mu\nu}$ now contains an additional scalar factor $f(R)$. As a result, we cannot employ the same steps outlined in Section 2.2.1 that relied on the application of Stoke's theorem.

The equation of motion derived from this theory is given by [104, 105]

$$f_R R_{\mu\nu} - \frac{1}{2}f(R)g_{\mu\nu} - (\nabla_\mu\nabla_\nu - g_{\mu\nu}\Box)\, f_R = \kappa T_{\mu\nu} \quad , \tag{2.27}$$

where $f_R \equiv df(R)/dR$ represents the derivative of the function $f(R)$ with respect to the Ricci scalar R. In addition, we have introduced the D'Alembert operator $\Box \equiv \nabla^\alpha\nabla_\alpha$. As can be seen, the present equation of motion contains second order derivatives of f_R. This is a potential source of instabilities. However, recent works have shown that this specific theory is safe under some restrictions [106].

Up to this point, we have not specified the exact form that the function $f(R)$ should take in the context of $f(R)$ theories of gravity. In order for such theories to be viable, they must satisfy several criteria. Firstly, they should be capable of adequately explaining cosmic expansion and the inflationary

process [85]. Additionally, they should seamlessly recover the predictions of General Relativity in the low-energy regime [87, 104, 105]. Another important criterion is the absence of instabilities or pathologies within the theory.

Regarding the condition of stability, $f(R)$ theories introduce an additional dynamical degree of freedom associated with a scalar field. This can be more clearly observed when employing the scalar-tensor representation of the theory.

2.3.1. Scalar-Tensor gravity

There are various models that fall under the category of scalar-tensor theories, including $f(R)$ theories. These theories introduce an additional scalar field coupled to the metric, thereby adding a new degree of freedom. This modification can be understood as the scalar field acting as a source of gravity coupling with κ, causing the gravitational constant to be no longer constant but dependent on the presence of matter through an auxiliary scalar field [107]. The action for these theories takes the form

$$\mathcal{S} = \int d^4x\sqrt{-g}\left[\frac{1}{2\kappa}\left(\phi R - \frac{\omega(\phi)}{\phi}\nabla_\mu\phi\nabla^\mu\phi - V(\phi)\right) + \mathcal{L}_{\mathcal{M}}(\psi, g_{\mu\nu})\right] \ , \quad (2.28)$$

where $\omega(\phi)$ is an arbitrary function and $V(\phi)$ is a generalization of the cosmological constant.

By varying the action Eq. (2.28) with respect to the metric, we obtain the equations of motion

$$\phi G_{\mu\nu} + \left[\Box\phi + \frac{\omega(\phi)}{2\phi}(\nabla\phi)^2 + \frac{V(\phi)}{2}\right] g_{\mu\nu} - \nabla_\mu\nabla_\nu\phi - \frac{\omega(\phi)}{\phi}\nabla_\mu\phi\nabla_\nu\phi = \kappa T_{\mu\nu} \ , \quad (2.29)$$

and with respect to the scalar field ϕ

$$(2\omega + 3)\Box\phi + \frac{d\omega(\phi)}{d\phi}(\nabla\phi)^2 + 2V(\phi) - \phi\frac{dV(\phi)}{\phi} = \kappa T \quad . \quad (2.30)$$

Scalar-tensor theories can be related to General Relativity via a conformal transformation. Through the transformation $\phi g_{\mu\nu} \to q_{\mu\nu}$, it is possible to arrive at a representation that leads to the Einstein field equations, but with a modified energy-momentum tensor that includes effects from the scalar field ϕ. This scalar field generates curvature even in the absence of matter.

To illustrate this, let us consider the Brans-Dicke model with a vanishing potential, where ω is a constant

$$\mathcal{S} = \int d^4x\sqrt{-g}\left[\frac{1}{2\kappa}\left(\phi R - \frac{\omega}{\phi}\nabla_\mu\phi\nabla^\mu\phi\right) + \mathcal{L}_{\mathcal{M}}(\psi, g_{\mu\nu})\right] . \tag{2.31}$$

By applying the conformal transformation along with the following redefinition of the scalar field

$$\tilde{\phi} = \int \frac{(2\omega+3)^{1/2}}{\phi} d\phi = (2\omega+3)^{1/2}\ln\phi \quad , \tag{2.32}$$

we obtain

$$\mathcal{S} = \int d^4x\sqrt{-q}\left[\frac{1}{2\kappa}\left(\tilde{R} - \nabla_\mu\tilde{\phi}\nabla^\mu\tilde{\phi}\right) + \tilde{\mathcal{L}}_{\mathcal{M}}(\psi, q_{\mu\nu})\right] , \tag{2.33}$$

where $\tilde{R} = \phi R$.

These two actions are dynamically equivalent. However, the representation in accordance with Eq. (2.31), is referred to as the Jordan frame, while representation with Eq. (2.33) is known as the Einstein frame.

2.3.2. Scalar-Tensor representation of metric $f(R)$ gravity

To extract the scalar-tensor representation of metric $f(R)$ gravity, the introduction of an auxiliary field α is required in the action

$$\mathcal{S} = \int d^4x\sqrt{-g}\left[\frac{1}{2\kappa}\left(f(\alpha) + f_\alpha\left(R-\alpha\right)\right) + \mathcal{L}_\mathcal{M}\right] \quad . \tag{2.34}$$

Here, the subscript denotes the derivative with respect to the variable, $f_\alpha \equiv df(\alpha)/d\alpha$.

Consequently, the action presented in Eq. (2.26) becomes dependent on two variables, the metric $g_{\mu\nu}$ and the auxiliary field α. By applying the principle of least action to each of these variables, we find

$$f_{\alpha\alpha}(R-\alpha) = 0 \quad . \tag{2.35}$$

Therefore, if the second derivative $f_{\alpha\alpha}$ is non-zero, it implies $\alpha = R$, thus recovering Eq. (2.26).

Introducing the scalar field $\phi \equiv f_R$ and the associated potential $V(\phi) \equiv \alpha\phi - f(\alpha)$ allows us to rewrite the action as follows

$$\mathcal{S} = \int d^4x\sqrt{-g}\left[\frac{1}{2\kappa}\left(\phi R - V(\phi)\right) + \mathcal{L}_\mathcal{M}\right] \quad . \tag{2.36}$$

This formulation establishes a scalar-tensor representation of metric $f(R)$ gravity. It should be noted that this representation is valid only if $f_{\alpha\alpha} \neq 0$. Therefore, the theory can be considered equivalent to Brans-Dicke theory with $\omega = 0$, $\phi \equiv f_R$, and $V \equiv f_R R - f(R)$.

Consequently, we derive the following equations of motion

$$\phi R_{\mu\nu} - \frac{1}{2}g_{\mu\nu}\left(\phi R - V\right) - \left(\nabla_\mu\nabla_\nu - g_{\mu\nu}\Box\right)\phi = \kappa T_{\mu\nu} \quad , \tag{2.37}$$

$$\Box\phi + \frac{1}{3}\left[2V - \phi\frac{dV}{d\phi}\right] = \frac{1}{3}\kappa T \quad . \tag{2.38}$$

Thus, two equations of motion arise, one representing a modification of the Einstein equations, and the other describing the dynamics of the scalar field ϕ. The latter equation reveals that permutations of the field ϕ can be viewed as possessing an effective mass

$$m_\phi^2 = \frac{1}{3}\left[\phi\frac{d^2V}{d\phi^2} - \frac{dV}{d\phi}\right] \quad . \tag{2.39}$$

Consequently, to avoid the presence of tachyons in the theory, this mass must remain positive. Such a condition imposes further constraints on the permissible forms of the function $f(R)$.

Therefore, due to the induced dynamical scalar degree of freedom, metric $f(R)$ gravity is not generally a viable theory. Instead, the specific form of the function $f(R)$ needs to be appropriately specified in order for it to be viable, satisfying all the conditions mentioned earlier and being in agreement with observational data.

2.4. Palatini $f(\mathcal{R})$ gravity

In analogy to the approach taken in General Relativity with the Einstein-Hilbert action, we now turn our attention to the metric-affine formalism, which allows for the consideration of an arbitrary connection rather than being limited to the Levi-Civita connection. While the metric and Palatini formalisms yield identical field equations for the Einstein-Hilbert action, the same cannot be said for more general Lagrangians, as we will see in this section.

For the Palatini $f(\mathcal{R})$ gravity theories, the action is given by [88, 108]

$$\mathcal{S} = \int d^4x\sqrt{-g}\left[\frac{1}{2\kappa}f(\mathcal{R}) + \mathcal{L}_{\mathcal{M}}(\psi, g_{\mu\nu}, \Gamma)\right] \quad , \tag{2.40}$$

where $\mathcal{R}$ represents the contraction of the Ricci tensor, determined using the connection, with the metric given by $\mathcal{R} \equiv g^{\mu\nu}\mathcal{R}_{\mu\nu}(\Gamma)$.

To provide clarity, let us first derive the field equations in the case when the matter Lagrangian $\mathcal{L}_{\mathcal{M}}$ vanishes. By varying the action with respect to the metric, we obtain

$$\delta_g S = \int d^4x\sqrt{-g}\frac{1}{2\kappa}\left(\frac{1}{2}g_{\mu\nu}f(\mathcal{R}) - f_{\mathcal{R}}\mathcal{R}_{\mu\nu}\right)\delta g^{\mu\nu} = 0 \quad . \tag{2.41}$$

Taking the trace of this expression, we arrive at the algebraic relation

$$f_{\mathcal{R}}\mathcal{R} - 2f(\mathcal{R}) = 0 \quad . \tag{2.42}$$

This equation allows us to determine the value of $\mathcal{R}$ when a specific form of $f(\mathcal{R})$ is chosen. We can face three different scenarios that are: it has some solutions, it has no real solution or it is satisfied for every $\mathcal{R}$. We will not consider the last two situations because it leads to some inconsistencies in the field equations. Hence, we find that

$$f(\mathcal{R}) = \frac{c_i}{2}f_{\mathcal{R}} \quad , \tag{2.43}$$

where c_i is a constant. Substituting this expression into the field equations Eq. (2.41), we obtain

$$\mathcal{R}_{\mu\nu} - \frac{c_i}{4}g_{\mu\nu} = 0 \quad . \tag{2.44}$$

This will lead us to the Einstein field equations with a cosmological constant. Needless to say that here we do not have just one value for the cosmological constant, like in General Relativity, but a set of values corresponding to different solutions. Actions like the one we have used here bring us to consistent field equations in the vacuum.

On the other hand, the variation of the action with respect to the connection leads us to the following expression

$$\begin{aligned}\delta_\Gamma \mathcal{S} &= \int d^4x\sqrt{-g}\frac{\delta_\Gamma f(\mathcal{R})}{2\kappa} \\ &= \int d^4x\sqrt{-g}g^{\mu\nu}f_\mathcal{R}\frac{\delta_\Gamma \mathcal{R}_{\mu\nu}}{2\kappa} \\ &= \int d^4x\sqrt{-g}g^{\mu\nu}\frac{f_\mathcal{R}}{2\kappa}\left(\nabla_\alpha \delta\Gamma^\alpha_{\mu\nu} - \nabla_\nu \delta\Gamma^\alpha_{\mu\alpha}\right) \\ &= \int \frac{d^4x}{2\kappa}\left[\delta^\nu_\alpha \nabla_\beta\left(f_\mathcal{R}\sqrt{-g}g^{\mu\beta}\right) - \nabla_\alpha\left(f_\mathcal{R}\sqrt{-g}g^{\mu\nu}\right)\right]\delta\Gamma^\alpha_{\mu\nu} = 0\,.\end{aligned} \tag{2.45}$$

Similarly to our earlier calculation in Eq. (2.23), we find that [88]

$$\nabla_\lambda\left(f_\mathcal{R}\sqrt{-g}g^{\mu\nu}\right) = 0 \quad . \tag{2.46}$$

Unlike in metric $f(R)$ gravity, there are no high order derivative terms in the field equations derived for Palatini $f(\mathcal{R})$ gravity.

Now that we have established that these theories can reproduce the results of General Relativity in vacuum, let us proceed to include the matter Lagrangian in the most general form possible. The matter Lagrangian depends on both the matter fields and the metric and connection, denoted as $\mathcal{L}_\mathcal{M}(\psi, g\mu\nu, \Gamma)$. By calculating the variation of the matter action with respect to the metric and the connection, we obtain the definitions of the energy-momentum tensor and the hypermomentum tensor, respectively

$$T_{\mu\nu} \equiv -\frac{2}{\sqrt{-g}}\frac{\delta(\sqrt{-g}\mathcal{L}_\mathcal{M})}{\delta g^{\mu\nu}} \quad , \tag{2.47}$$

$$\Delta^{\mu\nu}_\lambda \equiv -\frac{2}{\sqrt{-g}}\frac{\delta(\sqrt{-g}\mathcal{L}_\mathcal{M})}{\delta\Gamma^\lambda_{\mu\nu}} \quad . \tag{2.48}$$

Consequently, the field equations in the presence of matter can be expressed as

$$f_{\mathcal{R}}\mathcal{R}_{(\mu\nu)} - \frac{1}{2}f(\mathcal{R})g_{\mu\nu} = \kappa T_{\mu\nu} \quad , \tag{2.49}$$

$$\begin{aligned}\nabla_\sigma\left(\sqrt{-g}f_{\mathcal{R}}g^{\mu\sigma}\right)\delta^\nu_\lambda - \nabla_\lambda\left(\sqrt{-g}f_{\mathcal{R}}g^{\mu\nu}\right) \\ + 2\sqrt{-g}f_{\mathcal{R}}\left(g^{\mu\nu}S^\sigma_{\lambda\sigma} - g^{\mu\rho}S^\sigma_{\rho\sigma}\delta^\nu_\lambda + g^{\mu\sigma}S^\nu_{\sigma\lambda}\right) = \kappa\Delta^{\mu\nu}_\lambda \quad .\end{aligned} \tag{2.50}$$

Where, $S^\lambda_{\mu\nu} \equiv \Gamma^\lambda_{\mu\nu} - \Gamma^\lambda_{\nu\mu}$ is the torsion tensor.

It is obvious that if we impose a torsionless condition for the connection it will result in $\nabla_\lambda\left(f_{\mathcal{R}}\sqrt{-g}g^{\mu\nu}\right) = 0$, as it was for the vacuum case. However, this condition can be met without imposing the torsion-less condition. By taking the trace over indices ν and λ in Eq. (2.50), we obtain the equation

$$3\nabla_\rho(\sqrt{-g}f_{\mathcal{R}}g^{\mu\rho}) = 4\sqrt{-g}f_{\mathcal{R}}g^{\mu\rho}S^\sigma_{\sigma\rho} \quad . \tag{2.51}$$

Substituting this relation into Eq. (2.50), we derive the following expression

$$-\nabla_\lambda(\sqrt{-g}f_{\mathcal{R}}g^{\mu\nu}) + 2\sqrt{-g}f_{\mathcal{R}}\left(g^{\mu\nu}S^\sigma_{\sigma\lambda} - \frac{\delta^\nu_\lambda}{3}g^{\mu\rho}S^\sigma_{\sigma\rho} + g^{\mu\sigma}S^\nu_{\lambda\sigma}\right) = 0 \quad . \tag{2.52}$$

The connection can be expressed in terms of its symmetric and antisymmetric parts as $\Gamma^\lambda_{\mu\nu} \equiv C^\lambda_{\mu\nu} + S^\lambda_{\mu\nu}$. Similarly, the covariant derivative can be split into these two components

$$\nabla_\lambda v_\mu = \partial_\lambda v_\mu - C^\sigma_{\lambda\mu}v_\sigma - S^\sigma_{\lambda\mu}v_\sigma = \nabla^C_\lambda v_\mu - S^\sigma_{\lambda\mu}v_\sigma \quad . \tag{2.53}$$

Here, ∇^C_λ denotes the covariant derivative with respect to the symmetric part of the connection. Using this notation, we can express the derivative of $\sqrt{-g}f_{\mathcal{R}}g^{\mu\nu}$

as follows

$$\begin{aligned}\nabla_\lambda(\sqrt{-g}f_{\mathcal{R}}g^{\mu\nu}) =&\nabla^C_\lambda(\sqrt{-g}f_{\mathcal{R}}g^{\mu\nu}) \\ &+\sqrt{-g}f_{\mathcal{R}}\left(g^{\mu\sigma}S^\nu_{\lambda\sigma}-g^{\nu\sigma}S^\mu_{\lambda\sigma}+g^{\mu\nu}S^\sigma_{\sigma\lambda}\right) .\end{aligned} \tag{2.54}$$

By substituting this expression into Eq. (2.52), we obtain

$$\nabla^C_\lambda(\sqrt{-g}f_{\mathcal{R}}g^{\mu\nu}) = \sqrt{-g}f_{\mathcal{R}}\left(g^{\mu\sigma}S^\nu_{\lambda\sigma}-g^{\nu\sigma}S^\mu_{\lambda\sigma}+g^{\mu\nu}S^\sigma_{\sigma\lambda}-\frac{2}{3}\delta^\nu{}_\mu g^{\mu\rho}S^\sigma_{\sigma\rho}\right) \quad . \tag{2.55}$$

Considering that the metric tensor is symmetric in its two indices, i.e., $\nabla^C_\lambda(\sqrt{-g}f_{\mathcal{R}}g^{\mu\nu}) = \nabla^C_\lambda(\sqrt{-g}f_{\mathcal{R}}g^{(\mu\nu)})$ i $0 = \nabla^C_\lambda(\sqrt{-g}f_{\mathcal{R}}g^{[\mu\nu]})$, we can express the previous relation as

$$\nabla^C_\lambda(\sqrt{-g}f_{\mathcal{R}}g^{\mu\nu}) = \sqrt{-g}f_{\mathcal{R}}\left[g^{\mu\nu}S^\sigma_{\sigma\lambda}-\frac{1}{3}\left(\delta^\nu_\lambda g^{\mu\rho}+\delta^\mu_\lambda g^{\nu\rho}\right)S^\sigma_{\sigma\rho}\right] \quad , \tag{2.56}$$

and

$$g^{\mu\sigma}S^\nu_{\lambda\sigma}-g^{\nu\sigma}S^\mu_{\lambda\sigma} = \frac{1}{3}\left(\delta^\nu_\lambda g^{\mu\rho}-\delta^\mu_\lambda g^{\nu\rho}\right)S^\sigma_{\sigma\rho} \quad . \tag{2.57}$$

Let us now make use of the projective invariance of the curvature scalar $\mathcal{R}$, which means that under projective transformations, that may include translations, rotations, scaling and shearing, the curvature scalar remains unchanged. This invariance extends the concept of affine transformations. Consequently, the Ricci curvature scalar remains invariant under transformations of the form $\Gamma^\lambda_{\mu\nu} \to \Gamma^\lambda_{\mu\nu} + \delta^\lambda_\mu\xi_\nu$ transformations, where ξ_ν represents an arbitrary vector. Based on the preceding equations Eq. (2.56) and Eq. (2.57), it becomes apparent that the symmetric part of the connection is linked to the antisymmetric part through the contraction $S^\sigma_{\sigma\rho}$. In consideration of this, we introduce the following new variables

$$\tilde{\Gamma}^\lambda_{\mu\nu} = \Gamma^\lambda_{\mu\nu}+\frac{2}{3}\delta^\lambda_\nu S^\sigma_{\sigma\mu} \quad , \tag{2.58}$$

$$\tilde{C}^{\lambda}_{\mu\nu} = C^{\lambda}_{\mu\nu} + \frac{1}{3}\delta^{\lambda}_{\nu}S^{\sigma}_{\sigma\mu} \quad , \tag{2.59}$$

$$\tilde{S}^{\lambda}_{\mu\nu} = S^{\lambda}_{\mu\nu} + \frac{1}{3}\delta^{\lambda}_{\nu}S^{\sigma}_{\sigma\mu} \quad . \tag{2.60}$$

By employing this transformation, the equations derived from Eq. (2.56) and Eq. (2.57) can be expressed as follows

$$\nabla^{\tilde{C}}_{\lambda}(\sqrt{-g}f_{\mathcal{R}}g^{\mu\nu}) = 0 \quad , \tag{2.61}$$

and

$$g^{\mu\sigma}\tilde{S}^{\nu}_{\lambda\sigma} - g^{\nu\sigma}\tilde{S}^{\mu}_{\lambda\sigma} = 0 \quad . \tag{2.62}$$

The second equation, Eq. (2.62), combined with the antisymmetry property of torsion with respect to the last two indices, implies $\tilde{S}^{\lambda}_{\mu\nu} = 0$. Consequently, the relation $\nabla_{\lambda}\left(f_{\mathcal{R}}\sqrt{-g}g^{\mu\nu}\right) = 0$ can be recovered without imposing the torsionless condition.

Furthermore, Eq. (2.62) reveals that torsion arises solely from a vector $A_{\mu} \equiv S^{\sigma}_{\sigma\mu}$. As a result, we can express the connection as

$$\Gamma^{\lambda}_{\mu\nu} = \tilde{C}^{\lambda}_{\mu\nu} - \frac{2}{3}A_{\mu}\delta^{\lambda}_{\nu} \quad . \tag{2.63}$$

The invariance of the Ricci scalar under projective transformations implies that torsion does not have any influence on $\mathcal{R}$. As observed, the connection $\Gamma^{\lambda}_{\mu\nu}$ consists of a symmetric component $\tilde{C}^{\lambda}_{\mu\nu}$ along with a vector-like contribution $-2/3\delta^{\lambda}_{\nu}A_{\mu}$. This vector accounts for the existence of torsion; however, it does not impact the metric field equations. To achieve the complete elimination of torsion, it is only necessary to impose four conditions: $A_{\mu} = 0$.

2.4.1. Scalar-Tensor representation of Palatini $f(\mathcal{R})$ gravity

Palatini $f(\mathcal{R})$ gravity also possesses a scalar-tensor representation. Considering the action Eq. (2.28) and assuming that $\omega(\phi)$ is a constant, as found in Brans-Dicke theories, we use the following relationships to adapt the Palatini $f(\mathcal{R})$ action to the scalar-tensor representation

$$\phi \equiv f_{\mathcal{R}} \quad , \quad V(\phi) \equiv \mathcal{R} f_{\mathcal{R}} - f(\mathcal{R}) \quad . \tag{2.64}$$

The equations of motion derived from this action are described in Eq. (2.29). By comparing them with Eq. (2.49), we can determine the value of the parameter $\omega = -3/2$. Consequently, the equation of motion governing the dynamics of the scalar field ϕ takes the form

$$2V(\phi) - \phi \frac{dV(\phi)}{d\phi} = \kappa T \quad . \tag{2.65}$$

A notable distinction arises between the metric and Palatini approaches in $f(R)$ theories. Not only are their equations of motion inequivalent, but unlike metric $f(R)$ gravity, Palatini $f(\mathcal{R})$ gravity does not propagate any additional degree of freedom [104, 105]. This is evident from the absence of terms involving $\Box\phi$. It is important to emphasize that this behavior is not a consequence of special circumstances or fine-tuning to evade instabilities. Rather, the theory inherently lacks such issues. Hence, we can deduce from Eq. (2.49) (equivalent to Eq. (2.64)) that, unlike in General Relativity where matter fields exhibit a linear relationship with curvature, in Palatini $f(\mathcal{R})$ gravity, this relationship is not necessarily linear, and higher-order terms may be present. The effect of the Palatini $f(\mathcal{R})$ Lagrangian is to induce non-linearities in the matter sector. As a result, the vacuum field equations of Palatini $f(\mathcal{R})$ theories exactly recover those of General Relativity with an effective cosmological constant regardless of the $f(\mathcal{R})$ function chosen. This sharply contrasts with the metric formulation, in which the space-time is generically curved even in the absence of sources,

which can lead to long-range effects in the Newtonian/post-Newtonian regimes (depending on model parameters) and induces an extra polarization mode in the spectrum of gravitational waves. The Palatini formulation, instead, predicts only two polarizations which propagate at the speed of light in vacuum, making them consistent with current constraints coming from neutron stars mergers [109–115].

2.5. Mapping modified gravity into General Relativity

Palatini $f(\mathcal{R})$ gravity is a member of the broader family of theories known as Ricci-based gravity [91]. This family is composed of theories whose Lagrangians are constructed from the trace of powers of the object $M^{\mu}_{\ \nu} \equiv g^{\mu\alpha}\mathcal{R}_{(\alpha\nu)}(\Gamma)$. These models are treated within the Palatini approach, where the metric and connection are independent and equally fundamental. Notable examples within the class of Ricci-based theories include the previously mentioned $f(\mathcal{R})$, $f(\mathcal{R}_{(\mu\nu)}\mathcal{R}^{(\mu\nu)})$, as well as the Eddington-Inspired Born-Infeld models [116–119].

It can be shown that there is a correspondence between the solution space of Ricci-based gravity and that of General Relativity [92, 120]. This implies that Ricci-based gravity theories can be represented in the Einstein frame. In other words, it is possible to perform a transformation on the original action in such a way that ends up in the Einstein-Hilbert action, but with a modified matter Lagrangian.

The action of these theories can be expressed as follows

$$\mathcal{S} = \int d^4x\sqrt{-g}\left[\mathcal{L}_G(g_{\mu\nu}, \mathcal{R}_{(\mu\nu)}) + \mathcal{L}_{\mathcal{M}}(\phi, g_{\mu\nu})\right] \quad , \tag{2.66}$$

where $\mathcal{L}_G$ represents the gravitational Lagrangian specific to the theory under consideration, depending on the metric and the connection through the object

$\mathcal{R}_{(\mu\nu)}$. The matter Lagrangian $\mathcal{L}_{\mathcal{M}}$, on the other hand, solely depends on the matter fields ϕ and their coupling to the metric $g_{\mu\nu}$.

Applying the principle of least action with respect to the connection, akin to the procedure leading to Eq. (2.45), yields

$$\nabla_\lambda \left[\sqrt{-g} \frac{\partial \mathcal{L}_G}{\partial \mathcal{R}_{(\mu\nu)}} \right] = 0 \quad . \tag{2.67}$$

By introducing an auxiliary metric defined as

$$q^{\mu\nu}\sqrt{-q} \equiv 2\kappa \sqrt{-g} \frac{\partial \mathcal{L}_G}{\partial \mathcal{R}_{(\mu\nu)}} \quad , \tag{2.68}$$

we establish a Levi-Civita connection since

$$\nabla_\lambda \left[\sqrt{-q} q^{\mu\nu} \right] = 0 \quad , \tag{2.69}$$

$$\Gamma^\lambda_{\mu\nu} = \frac{1}{2} q^{\lambda\rho} [\partial_\mu q_{\rho\nu} + \partial_\nu q_{\rho\mu} - \partial_\rho q_{\mu\nu}] \qquad . \tag{2.70}$$

Consequently, it is possible to represent the action of Ricci-based gravity in terms of an Einstein frame, by means of which the equations of motion can be reformulated in a manner reminiscent of Einstein's theory. To demonstrate this, a Legendre transformation of the action is performed, so it can be equivalently written as

$$\mathcal{S} = \int d^4x \sqrt{-g} \left[\mathcal{L}_G \left(g_{\mu\nu}, \Sigma_{\mu\nu} \right) + \frac{\partial \mathcal{L}_G}{\partial \Sigma_{\mu\nu}} (\mathcal{R}_{(\mu\nu)} - \Sigma_{\mu\nu}) + \mathcal{L}_{\mathcal{M}}(\psi, g_{\mu\nu}) \right] \quad , \tag{2.71}$$

where $\Sigma_{\alpha\beta}$ is an auxiliary field. This Lagrangian exhibits linearity in $\mathcal{R}_{(\alpha\nu)}$. Subsequently, we derive the equations of motion with respect to the connection

Γ:

$$\nabla_\lambda \left[\sqrt{-g} \frac{\partial \mathcal{L}_G}{\partial \Sigma_{\mu\nu}} \right] = 0 \quad , \tag{2.72}$$

with respect to the metric $g_{\mu\nu}$

$$\begin{aligned} &\frac{\partial \mathcal{L}_G}{\partial g^{\mu\nu}} + \frac{\partial^2 \mathcal{L}_G}{\partial g^{\mu\nu} \partial \Sigma_{\alpha\beta}} \left(\mathcal{R}_{(\alpha\beta)} - \Sigma_{\alpha\beta} \right) \\ &\quad - \frac{1}{2} g_{\mu\nu} \left[\mathcal{L}_G + \frac{\partial \mathcal{L}_G}{\partial \Sigma_{\alpha\beta}} \left(\mathcal{R}_{(\alpha\beta)} - \Sigma_{\alpha\beta} \right) \right] = \frac{1}{2} T_{\mu\nu} \quad , \end{aligned} \tag{2.73}$$

and with respect to the auxiliary field $\Sigma_{\alpha\beta}$

$$\frac{\partial^2 \mathcal{L}_G}{\partial \Sigma_{\mu\nu} \partial \Sigma_{\alpha\beta}} (\mathcal{R}_{(\mu\nu)} - \Sigma_{\mu\nu}) = 0 \quad . \tag{2.74}$$

The last condition reveals that whenever the Lagrangian is nonlinear with respect to the auxiliary field, we have $\Sigma_{\mu\nu} = \mathcal{R}_{(\mu\nu)}$, thereby recovering Eq. (2.66). By introducing the auxiliary metric in a manner similar to the previous derivation

$$q^{\alpha\beta} \sqrt{-q} \equiv 2\kappa \sqrt{-g} \frac{\partial \mathcal{L}_G}{\partial \Sigma_{(\alpha\beta)}} \quad , \tag{2.75}$$

we can rewrite the action as follows

$$\mathcal{S} = \int d^4x \left[\sqrt{-q} q^{\mu\nu} \frac{\mathcal{R}_{(\mu\nu)}}{2\kappa} - \sqrt{-g} V(g_{\mu\nu}, q_{\mu\nu}) + \mathcal{L}_{\mathcal{M}}(\psi, g_{\mu\nu}) \right] \quad , \tag{2.76}$$

where

$$V(g_{\mu\nu}, q_{\mu\nu}) = \frac{\partial \mathcal{L}_G}{\partial \Sigma_{\mu\nu}} \Sigma_{\mu\nu} - \mathcal{L}_G \quad . \tag{2.77}$$

Eq. (2.73) provides an algebraic relationship, enabling us to express $g_{\mu\nu}$ in terms of $q_{\mu\nu}$. Consequently, we can express Eq. (2.66) as the Einstein-Hilbert

action (with $\Sigma_{\mu\nu} = \mathcal{R}_{(\mu\nu)}$ due to the Lagrangian's nonlinearity, as previously mentioned)

$$\mathcal{S} = \int d^4x\sqrt{-q}\left[\frac{R}{2\kappa} + \tilde{\mathcal{L}}_{\mathcal{M}}\right] \quad . \tag{2.78}$$

where R is determined by the Levi-Civita connection compatible with $q_{\mu\nu}$.

However, the right-hand side of the Einstein equations will now contain a modified energy-momentum tensor

$$R_{\mu\nu} - \frac{1}{2}g_{\mu\nu}R = \kappa\tilde{T}_{\mu\nu} \quad . \tag{2.79}$$

Since the Lagrangian of the theory is constructed from $M^{\mu}{}_{\nu} \equiv g^{\mu\alpha}\Sigma_{(\alpha\nu)}$, we have

$$g^{\mu\alpha}\frac{\partial\mathcal{L}_G}{\partial g^{\alpha\nu}} = \frac{\partial\mathcal{L}_G}{\partial\Sigma_{(\mu\alpha)}}\Sigma_{(\alpha\nu)} \quad . \tag{2.80}$$

Applying this relation to Eq. (2.73), along with Eq. (2.74) and utilizing the definition of the auxiliary metric $q_{\mu\nu}$, we can calculate the Ricci tensor and the Ricci scalar, leading to

$$\tilde{T}^{\mu}{}_{\nu} = \frac{1}{|\hat{\Omega}|^{1/2}}\left[T^{\mu}{}_{\nu} - \delta^{\mu}{}_{\nu}\left(\frac{T}{2} + \mathcal{L}_G\right)\right] \quad . \tag{2.81}$$

Here, we have employed the square root of the deformation matrix determinant. The deformation matrix is a nonlinear function of the matter distribution and defines the relationship established between the metrics

$$q_{\mu\nu} = g_{\mu\alpha}\Omega^{\alpha}{}_{\nu} \quad . \tag{2.82}$$

As demonstrated, it is possible to represent Ricci-based gravity theories in the Einstein frame, where the gravitational Lagrangian takes the form of the Einstein-Hilbert action coupled with a modified matter Lagrangian. Thus, the

nonlinearities in the gravitational sector can be translated into nonlinearities in the matter sector.

2.5.1. Mapping a scalar field matter Lagrangian

Our objective is to derive the modified matter Lagrangian that arises from the mapping between a Ricci-based gravity theory coupled to a scalar field matter Lagrangian and General Relativity. Starting with the action [89]

$$\mathcal{S} = \int d^4x\sqrt{-g}\left[\mathcal{L}_G(g_{\mu\nu}, \mathcal{R}_{(\mu\nu)}) - \frac{1}{2}P(X,\phi)\right] \quad . \tag{2.83}$$

where $X^{\mu}_{\ \nu} \equiv g^{\mu\alpha}\partial_\alpha\phi\partial_\nu\phi$, its trace is represented by X, and $P(X,\phi)$ is an arbitrary function of its arguments.

We construct the energy-momentum tensor for this action using its definition Eq. (2.47)

$$T^{\mu}_{\ \nu} = P_X X^{\mu}_{\ \nu} - \frac{P}{2}\delta^{\mu}_{\ \nu} \quad , \tag{2.84}$$

where $P_X \equiv dP/dX$.

Since the deformation matrix $\Omega^{\mu}_{\ \nu}$ depends on the matter distribution, one could use a representation as an infinite power series expansion, though the Cayley-Hamilton theorem reduces the expansion to just four terms

$$\Omega^{\mu}_{\ \nu} = a_0(X,\phi)\delta^{\mu}_{\ \nu} + a_1(X,\phi)T^{\mu}_{\ \nu} + a_2(X,\phi)T^{\mu}_{\ \alpha}T^{\alpha}_{\ \nu} + a_3(X,\phi)T^{\mu}_{\ \alpha}T^{\alpha}_{\ \beta}T^{\beta}_{\ \nu} \ . \tag{2.85}$$

Further simplifications are possible for a scalar field. By considering Eq. (2.84) and the property $(X^{\mu}_{\ \nu})^n = X^{n-1}X^{\mu}_{\ \nu}$, we can express the above relation as

$$\Omega^{\mu}_{\ \nu} = C(X,\phi)\delta^{\mu}_{\ \nu} + D(X,\phi)X^{\mu}_{\ \nu} \quad . \tag{2.86}$$

where $C(X,\phi)$ and $D(X,\phi)$ are model-dependent functions.

Similar to the procedure used for X, we define $Z^{\mu}{}_{\nu} \equiv q^{\mu\alpha}\partial_{\alpha}\phi\partial_{\nu}\phi$. . Using this definition and the relation between the metrics Eq. (2.82) and Eq. (2.85), we obtain

$$X^{\mu}{}_{\nu} = (C + DX)Z^{\mu}{}_{\nu} \quad , \quad Z = \frac{X}{C + DX} \quad . \tag{2.87}$$

Finally, we have established a relation of the form $Z = Z(X,\phi)$, allowing us to express the action in the Einstein frame as

$$\mathcal{S} = \int d^4x\sqrt{-q}\left[\frac{R}{2\kappa} - \frac{1}{2}K(Z,\phi)\right] \quad . \tag{2.88}$$

The corresponding energy-momentum tensor is then derived as

$$\tilde{T}^{\mu}{}_{\nu} = K_Z Z^{\mu}{}_{\nu} - \frac{K(Z,\phi)}{2}\delta^{\mu}{}_{\nu} \quad . \tag{2.89}$$

Comparing this with the previously derived energy-momentum tensor Eq. (2.81),

$$\tilde{T}^{\mu}{}_{\nu} = \frac{1}{|\hat{\Omega}|^{1/2}}\left[P_X X^{\mu}{}_{\nu} - \delta^{\mu}_{\nu}\left(\frac{XP_X - P}{2} + \mathcal{L}_G\right)\right] \quad , \tag{2.90}$$

we obtain the expression for $K(Z,\phi)$

$$K(Z,\phi) = \frac{1}{|\hat{\Omega}|^{1/2}}\left[2\mathcal{L}_G + XP_X - P\right] \quad . \tag{2.91}$$

Hence, we have obtained the expression for the matter Lagrangian in terms of the variables in the Einstein frame.

Another relationship can be derived by comparing the equations of motion in both frames

$$K_\phi = \frac{P_\phi}{|\hat{\Omega}|^{1/2}} \quad . \tag{2.92}$$

Therefore, if it is possible to write $X(Z, \phi)$, we will be able to express $K(Z, \phi)$ through Eq. (2.91). As we have demonstrated, once we determine the matter Lagrangian and the gravitational Lagrangian, it is possible to transform a problem in the context of modified gravity into a problem within the framework of General Relativity. Thus, we have a bi-frame representation of the system where both representations of the action are dynamically equivalent.

This approach offers numerous advantages, particularly from a computational point of view, as the vast majority of techniques and software are developed for working in the context of General Relativity. It is noteworthy that the reverse mapping is also possible, and this mapping works in both directions. Thus, a system initially described in General Relativity can be described in terms of a modified gravity theory. Similarly, we can utilize Numerical Relativity to solve problems within the context of modified gravity. The system initially described in terms of modified gravity can be expressed in the Einstein frame for solving, and once we have the solution, we can return to the original frame.

Even though we have shown in the present chapter the correspondence between Ricci-based gravity coupled to a single scalar field and General Relativity, it has also been demonstrated in Ref. [89] that this correspondence holds when considering multiple scalar fields.

Chapter 3.

Static boson stars in Palatini $f(\mathcal{R})$ gravity

As we have seen in the previous chapters, the tension between theory and observations does not allow us to rule out the possible existence of other compact objects beyond those known so far, namely, white dwarfs, neutron stars, and black holes. Thus, theorizing about the possible existence of boson stars also leads us to be able to observe the behavior of gravity in its strong-field regime. In fact, the absence of a horizon could make the innermost regions of those objects accessible to observation, potentially offering new insights on how to extend Einstein's gravity in the ultraviolet. In this sense, it is of interest to explore how structural properties such as mass and radius of boson stars could be affected by a modification of the gravitational Lagrangian [121, 122]. Given that $f(\mathcal{R})$ theories offer a large amount of freedom while keeping the field equations within reasonable limits of simplicity, we will explore the impact that high-energy modifications of the gravitational interaction of the $f(\mathcal{R})$ type could have on the astrophysical properties of boson stars. Similar studies have already been carried out in other theories of gravity, such as in scalar-tensor theories [123], Horndeski theories [124, 125], and theories with Gauss-Bonnet couplings [126–128], among others.

The approach we will take is as follows. Starting from the action of the problem at hand, namely a boson star in the context of Palatini $f(\mathcal{R})$ gravity

($f(\mathcal{R})$ frame), we will make use of the correspondence between this theory and General Relativity to translate our system into a nonlinear matter Lagrangian coupled to General Relativity (Einstein frame). This will enable us to solve the equations formulated in this context and then undo the transformation to observe the resulting outcome from the perspective of Palatini $f(\mathcal{R})$ gravity. The present chapter is based on the publication [1].

3.1. Field equations and correspondence with General Relativity

For simplicity, and to make contact with the existing literature, we will specify the gravitational Lagrangian by the quadratic function

$$f(\mathcal{R}) = \mathcal{R} + \xi\mathcal{R}^2 \ . \tag{3.1}$$

This is the Palatini version of the so-called Starobinsky model [103], and represents the $\mathcal{R}-$dependent part of the quantum-corrected extension of General Relativity when quantum matter fields are considered in a curved space-time. Within the metric formalism, this model has been exhaustively explored in inflationary cosmological scenarios [79, 85, 129–131], while the Palatini version is known to yield interesting phenomenology involving nonsingular bouncing cosmologies [117, 132], nonsingular black holes [133], wormholes [134], and other exotic compact objects [94].

We will be dealing with a theory of the form

$$S_{f(\mathcal{R})} = \int d^4x\sqrt{-g}\frac{\mathcal{R}+\xi\mathcal{R}^2}{2\kappa} - \frac{1}{2}\int d^4x\sqrt{-g}P(X,\Phi) \quad . \tag{3.2}$$

where gravity is described in terms of a Palatini Starobinsky function and the matter sector is represented by a complex scalar field Φ with Lagrangian $P(X,\Phi) = X - 2V(\Phi)$, where $X = g^{\alpha\beta}\partial_\alpha\Phi^*\partial_\beta\Phi$, $V(\Phi) = -\mu^2\Phi^*\Phi/2$, and μ is the scalar field mass. Here we are defining $\mathcal{R} = g^{\mu\nu}R_{\mu\nu}(\Gamma)$, with $R_{\mu\nu}(\Gamma)$

representing the Ricci tensor of a connection $\Gamma^{\lambda}_{\alpha\beta}$ a priori independent of the metric $g_{\mu\nu}$.

Manipulating the field equations that follow from independent variations of the metric and the connection, one finds that the explicit relation between $\Gamma^{\lambda}_{\alpha\beta}$ and $g_{\mu\nu}$ is given by

$$\Gamma^{\lambda}_{\mu\nu} = \frac{q^{\lambda\rho}}{2}\left[\partial_{\mu}q_{\rho\nu} + \partial_{\nu}q_{\rho\mu} - \partial_{\rho}q_{\mu\nu}\right] \quad , \tag{3.3}$$

where $q_{\mu\nu}$ is introduced as a conformal transformation of the metric tensor $g_{\mu\nu}$ using Eq. (2.68) and Eq. (2.82)

$$q_{\mu\nu} \equiv f_{\mathcal{R}}g_{\mu\nu} \quad , \tag{3.4}$$

with $f_{\mathcal{R}} \equiv \partial f/\partial\mathcal{R}$. Thus, the deformation matrix takes the form $\Omega^{\alpha}{}_{\nu} \equiv f_{\mathcal{R}}\delta^{\alpha}{}_{\nu}$. We note that the conformal factor $f_{\mathcal{R}}$ must be regarded as a function of the metric $g_{\alpha\beta}$ and the matter fields which is specified by the algebraic Eq. (2.42) that yields

$$\mathcal{R} = -\kappa T \quad , \tag{3.5}$$

where T represents the trace of the matter stress-energy tensor, which is defined as in Eq. (2.18)

$$T_{\mu\nu} \equiv -\frac{2}{\sqrt{-q}}\frac{\delta(\sqrt{-q}P(X,\Phi))}{\delta g^{\mu\nu}} \ . \tag{3.6}$$

We will refer to the representation (3.2) of the theory as the $f(\mathcal{R})$ frame. Note that in this frame the scalar field Φ is minimally coupled to the metric $g_{\mu\nu}$.

As we have shown in Section 2.5, there exists a correspondence between the theory (3.2) and the Einstein-Hilbert action of the metric $q_{\mu\nu}$ minimally coupled to a matter Lagrangian $K(Z,\Phi)$ (from now on the Einstein frame),

namely,

$$S_{EH} = \int d^4x\sqrt{-q}\frac{R}{2\kappa} - \frac{1}{2}\int d^4x\sqrt{-q}K(Z,\Phi) \quad , \tag{3.7}$$

where the kinetic term $Z = q^{\alpha\beta}\partial_\alpha\Phi^*\partial_\beta\Phi$ is now contracted with the (inverse) metric $q^{\alpha\beta}$ and R is the Ricci scalar of the metric $q_{\alpha\beta}$, i.e., $R = q^{\alpha\beta}R_{\alpha\beta}(q)$.

Using Eq. (2.91) with the specified $f(\mathcal{R})$ and $P(X,\Phi)$ functions it can be shown that [89]

$$K(Z,\Phi) = \frac{Z - \xi\kappa Z^2}{1 - 8\xi\kappa V} - \frac{2V}{1 - 8\xi\kappa V} \quad . \tag{3.8}$$

As we can see, non-linearities in the gravitational sector of the $f(\mathcal{R})$ frame have been transferred into non-linearities in the matter sector of the Einstein frame. Because of this relation between frames, in order to solve the field equations of $f(\mathcal{R})$ gravity coupled to a scalar field we will solve instead the corresponding problem in General Relativity coupled to the non-linear scalar field matter Lagrangian (3.8). Once the metric $q_{\mu\nu}$ and the scalar field Φ have been found, we automatically have the metric $g_{\mu\nu}$ via the conformal relation (3.4).

To proceed, we will now consider the Einstein-Klein-Gordon system in the Einstein frame. The corresponding stress-energy tensor is given by

$$\begin{aligned}
\tilde{T}_{\mu\nu} &\equiv -\frac{2}{\sqrt{-q}}\frac{\delta(\sqrt{-q}K(Z,\Phi))}{\delta q^{\mu\nu}} \\
&= \frac{1}{2(1+4\xi\kappa\mu^2|\Phi|^2)}\left[\left(\partial_\mu\Phi^*\partial_\nu\Phi + \partial_\nu\Phi^*\partial_\mu\Phi\right)(1-2\xi\kappa Z)\right. \\
&- \left. q_{\mu\nu}\left(\partial^\alpha\Phi^*\partial_\alpha\Phi\,(1-\xi\kappa Z) + \mu^2|\Phi|^2\right)\right] \ ,
\end{aligned} \tag{3.9}$$

which should not be confused with the $T_{\mu\nu}$ defined in (3.6). Following the approach presented in Section 1.2, we will consider spherical stars described by a scalar-field profile of the form $\Phi(x,t) = \phi(x)e^{i\omega t}$, where ω is the oscillation frequency of the field. Since we are describing spherically symmetric config-

urations we will use polar-areal coordinates. Our ansatz for the metric $g_{\mu\nu}$ is

$$ds^2_{f(\mathcal{R})} = -A(r)^2dt^2 + B(r)^2dr^2 + r^2d\theta^2 + r^2\sin^2\theta d\varphi^2 \,. \tag{3.10}$$

Analogously, for the metric $q_{\mu\nu}$ we take

$$ds^2_{\rm GR} = -\mathcal{A}(x)^2dt^2 + \mathcal{B}(x)^2dx^2 + x^2d\theta^2 + x^2\sin^2\theta d\varphi^2 \,. \tag{3.11}$$

Where $A(r)^2$ and $B(r)^2$ are respectively the temporal and radial components of the metric g. They only have dependence on the radial coordinate r. Similarly $\mathcal{A}(x)^2$ and $\mathcal{B}(x)^2$ are respectively the temporal and radial components of the metric q and they depend on the radial coordinate x. These functions are unknown and will be found by solving the Einstein equations for $\mathcal{A}(x)$ and $\mathcal{B}(x)$. Then $A(r)$ and $B(r)$ can be found by using the conformal relation between metrics $q^{\mu\nu} = f_{\mathcal{R}}g^{\mu\nu}$. From the Einstein equations associated with the line element (3.11), the components G_{tt} and G_{xx} lead to

$$\begin{aligned}
\frac{\partial_x\mathcal{B}}{\mathcal{B}} &= \frac{1-\mathcal{B}^2}{2x} + \frac{1}{1+4\xi\kappa\mu^2\phi^2}\frac{\kappa x}{4}\Big\{\mu^2\mathcal{B}^2\phi^2 \\
&+ \left(\omega^2\phi^2\frac{\mathcal{B}^2}{\mathcal{A}^2} + \psi^2\right)\left(1 - 2\kappa\xi\left(-\frac{\omega^2\phi^2}{\mathcal{A}^2} + \frac{\psi^2}{\mathcal{B}^2}\right)\right) \\
&+ 2\kappa\xi\mathcal{B}^2\left(\frac{\omega^2\phi^2}{\mathcal{A}^2} - \frac{\psi^2}{\mathcal{B}^2}\right)^2\Big\}\,, \qquad (3.12)\\
\frac{\partial_x\mathcal{A}}{\mathcal{A}} &= \frac{\mathcal{B}^2-1}{x} + \frac{\partial_x\mathcal{B}}{\mathcal{B}} + \frac{1}{1+4\xi\kappa\mu^2\phi^2}\frac{\kappa x}{4}\Big\{-2\mu^2\mathcal{B}^2\phi^2 \\
&- 2\kappa\xi\mathcal{B}^2\left(\frac{\omega^2\phi^2}{\mathcal{A}^2} - \frac{\psi^2}{\mathcal{B}^2}\right)^2\Big\}\,, \qquad (3.13)
\end{aligned}$$

where the quantity

$$\psi \equiv \partial_x\Phi\,, \tag{3.14}$$

satisfies

$$\begin{aligned}
\partial_x\psi &= \frac{1}{(1+4\xi\kappa\mu^2\phi^2)\left[1-2\xi\kappa\left(-\frac{\omega^2\phi^2}{\mathcal{A}^2}+\frac{3\psi^2}{\mathcal{B}^2}\right)\right]}\Bigg\{ \\
&- \psi\left(\frac{2}{x}+\frac{\partial_x\mathcal{A}}{\mathcal{A}}-\frac{\partial_x\mathcal{B}}{\mathcal{B}}\right)\left(1+4\kappa\xi\mu^2\phi^2\right)\left[1-2\xi\kappa\left(-\frac{\omega^2\phi^2}{\mathcal{A}^2}+\frac{\psi^2}{\mathcal{B}^2}\right)\right] \\
&- \omega^2\phi\frac{\mathcal{B}^2}{\mathcal{A}^2}\left[1+2\xi\kappa\left(\frac{\omega^2\phi^2}{\mathcal{A}^2}+\frac{\psi^2}{\mathcal{B}^2}\right)\right]+\mathcal{B}^2\phi\mu^2\left(1+4\kappa\xi\frac{\psi^2}{\mathcal{B}^2}\right) \\
&+ \kappa\xi\left[\frac{4\omega^2\phi^2\psi}{\mathcal{A}^2}\frac{\partial_x\mathcal{A}}{\mathcal{A}}\left(1+4\kappa\xi\mu^2\phi^2\right)-\frac{4\psi^3}{\mathcal{B}^2}\frac{\partial_x\mathcal{B}}{\mathcal{B}}\left(1+4\kappa\xi\mu^2\phi^2\right)\right] \\
&- 4\kappa^2\xi^2\mu^2\phi\mathcal{B}^2\left(\frac{\omega^4\phi^4}{\mathcal{A}^4}+\frac{3\psi^4}{\mathcal{B}^4}\right)\Bigg\} \ . \qquad (3.15)
\end{aligned}$$

The above four equations Eq. (3.12)-Eq. (3.15) form the Einstein-Klein-Gordon system that we need to solve to build spherically symmetric boson star models in a quadratic $f(\mathcal{R})$ theory. For future reference, it is convenient to write explicitly the form of the conformal factor $f_{\mathcal{R}}$ as follows:

$$\begin{aligned}
f_{\mathcal{R}} &= 1+2\xi R = 1+2\xi\kappa(X-4V) \\
&= 1+2\xi\kappa\left[-\frac{\omega^2\phi^2}{A^2}+\frac{\psi^2}{B^2}+2\mu^2\phi^2\right] \ . \qquad (3.16)
\end{aligned}$$

Note that using the relation $X = f_{\mathcal{R}}Z$ we can also write the conformal factor in terms of the Einstein frame variables

$$\begin{aligned}
f_{\mathcal{R}} &= 1+2\xi\kappa\left[\frac{(1-8\xi\kappa V)\,Z}{1-2\xi\kappa Z}-4V\right] \\
&= \frac{1+4\xi\kappa\mu^2\phi^2}{1-2\xi\kappa\left(-\frac{\omega^2\phi^2}{\mathcal{A}^2}+\frac{\psi^2}{\mathcal{B}^2}\right)} \ . \qquad (3.17)
\end{aligned}$$

3.2. Numerical analysis

3.2.1. Boundary conditions

In order to solve this system of differential equations suitable boundary conditions have to be provided. We will regard the $f(\mathcal{R})$ frame as the frame in which the physical boundary conditions must be specified. Accordingly, we impose asymptotic flatness at infinity and regularity at the origin for the line element (3.10), which translates into

$$\begin{aligned} \phi(\infty) &= 0\ ,\ \psi(\infty)=0\ ,\ B^2(\infty)=1\ ,\ A^2(\infty)=1 \\ \phi(0) &= \phi_0\ ,\ \psi(0)=0\ ,\ \partial_r B^2(0)=0\ ,\ \partial_r A^2(0)=0\ . \end{aligned} \tag{3.18}$$

The asymptotic flatness condition leads us to $f_{\mathcal{R}} \to 1$ when $r \to \infty$. Recalling the conformal relation Eq. (3.4), we can re-express the above conditions in the Einstein frame variables. First, we take a look at the area of the 2-spheres, which are related according to $x^2 = f_{\mathcal{R}} r^2$. If one assumes that $f_{\mathcal{R}} \neq 0$ everywhere then it follows that $x \to 0$ when $r \to 0$, so the boundary conditions read as

$$\phi(\infty) \equiv \phi(x(r))|_{r=\infty} = 0\,, \tag{3.19}$$

$$\psi(\infty) \equiv \psi(x(r))|_{r=\infty} = 0\,, \tag{3.20}$$

$$\mathcal{B}(\infty)^2 \equiv \mathcal{B}(x(r))^2|_{r=\infty} = f_{\mathcal{R}}(\infty)B(\infty)^2 = 1\,, \tag{3.21}$$

$$\mathcal{A}(\infty)^2 \equiv \mathcal{A}(x(r))^2|_{r=\infty} = f_{\mathcal{R}}(\infty)A(\infty)^2 = 1\,, \tag{3.22}$$

$$\phi(0) \equiv \phi(x(r))|_{r=0} = \phi_0\,, \tag{3.23}$$

$$\psi(0) \equiv \psi(x(r))|_{r=0} = 0\,, \tag{3.24}$$

$$\tag{3.25}$$

$$\begin{aligned}\left[\partial_x \mathcal{B}^2\right](0) &\equiv \left[\partial_x \mathcal{B}^2\right](x(r))|_{r=0} = 2\sqrt{f_\mathcal{R}} B \partial_r(\sqrt{f_\mathcal{R}} B)\partial_x r|_{r=0} \\ &= \frac{B^2}{\sqrt{f_\mathcal{R}}}\partial_r f_\mathcal{R}|_{r=0} = 0\,, \qquad (3.26)\\ \left[\partial_x \mathcal{A}^2\right](0) &\equiv \left[\partial_x \mathcal{A}^2\right](x(r))|_{r=0} = 2\sqrt{f_\mathcal{R}} A \partial_r(\sqrt{f_\mathcal{R}} A)\partial_x r|_{r=0} \\ &= \frac{A^2}{\sqrt{f_\mathcal{R}}}\partial_r f_\mathcal{R}|_{r=0} = 0\,. \qquad (3.27)\end{aligned}$$

Substituting Eq. (3.25) and Eq. (3.27) into Eq. (3.12) and Eq. (3.13) respectively leads to $\mathcal{B}(0)^2 = 1$, $\mathcal{A}(0)^2 = \mathcal{A}_0^2$. This puts forward that the assumption of asymptotic flatness and regularity at the origin in the $f(\mathcal{R})$ frame implies the same conditions in the Einstein frame.

3.2.2. Scaling and dimensionless quantities

In order to absorb some parameters to deal with dimensionless expressions, let us perform a re-scaling of the system as $r \to \mu r$, $t \to \omega t$. The factor κ from the Einstein field equations can be absorbed by a redefinition of the matter fields

$$\phi \to \sqrt{\frac{2}{\kappa}}\phi \quad , \quad \psi \to \sqrt{\frac{2}{\kappa}}\psi \quad , \qquad (3.28)$$

which leaves the scaled matter fields dimensionless. Using the symmetry of the equations of motion we can set

$$\mathcal{A} \to \frac{\omega}{\mu}\mathcal{A} \quad . \qquad (3.29)$$

When performing the numerics, we will set the field mass to $\mu = 1$. We now introduce an expression for the Misner-Sharp mass Eq. (1.25) in the bi-frame

way

$$\begin{aligned} M &= \frac{r_{\max}}{2}\left(1-\frac{1}{B^2(r_{\max})}\right) \\ &= \frac{x_{\max}}{2\sqrt{f_{\mathcal{R}}(x_{\max})}}\left(1-\frac{f_{\mathcal{R}}(x_{\max})}{\mathcal{B}(x_{\max})^2}\right) \qquad (3.30) \\ &\approx \frac{x_{\max}}{2}\left(1-\frac{1}{\mathcal{B}(x_{\max})^2}\right) \quad , \qquad (3.31) \end{aligned}$$

which gives us a numerical value for the mass related to the physical one, $M_{\rm phys}$, by

$$M = \frac{\mu M_{\rm phys}}{M_{\rm Pl}}, \qquad (3.32)$$

where $M_{\rm Pl}$ is the Planck mass. Note that the Misner-Sharp mass is the same in both frames. We introduce also an expression for the Noether charge, which arises from the global $U(1)$ symmetry $\Phi \to e^{i\delta}\Phi$, and can be identified as the particle number

$$\begin{aligned} N &= \int_\Sigma dV\sqrt{-q}q^{t\nu}\frac{i}{2}\left(\Phi^*\partial_\nu\Phi - \Phi\partial_\nu\Phi^*\right) \\ &= 4\pi\int_0^\infty dx x^2\omega\frac{\phi^2\mathcal{B}}{\mathcal{A}} \quad , \end{aligned} \qquad (3.33)$$

and its relation with the physical value

$$N_{\rm phys} = \frac{2N}{\kappa\mu^2} \quad . \qquad (3.34)$$

The notion of binding energy arises naturally from the above definitions as we have seen in Section 1.2

$$E_b = M - N\mu \quad , \qquad (3.35)$$

and its sign will determine the fate of the boson star. We have defined the binding energy in the Einstein frame since in this frame is where this expression

has been proven in other scenarios [42, 49]. We will verify that this is also the right choice for our case.

3.2.3. Numerical method

In order to solve numerically the re-scaled analogous Einstein-Klein-Gordon system with the provided boundary conditions we use a fourth-order Runge-Kutta scheme with adaptive stepsize. The conditions at the origin are evaluated at $x = 10^{-6}$ in order to avoid indeterminations. Then an equidistant grid with spatial resolution $\Delta x = 0.0025$ is used and a global tolerance of 1.5×10^{-14}. Furthermore, for a given central value of the scalar field ϕ_0 we have to adjust which frequency ω (integrated in $\mathcal{A}$ after the scaling) matches the desired asymptotic behavior. This is done by using a shooting method that integrates from the origin towards the outer boundary. There exists a set of $\omega^{(n)}$ values that satisfies this condition, and as n increases also does the number of radial nodes of ϕ. Here, we will focus on the nodeless $n = 0$ case, known as the ground state or fundamental family.

From the scalings and redefinitions of parameters that we did in the previous section, the gravitational coupling ξ, with dimensions of length square, is now being measured in units of the inverse length defined by $\mu^2 = 1/l_\mu^2$, such that $\xi\mu^2$ is dimensionless. On physical grounds one expects $\xi\mu^2 \sim l_\xi^2/l_\mu^2 \ll 1$ but since we are mainly interested in a qualitative study of theories with positive and negative ξ, the coupling magnitude has been chosen large enough to easily notice the relevant features of each case. Hence, we choose $\xi\mu^2 = -0.1, -0.05, -0.02, -0.01, 0.01, 0.1$ to explore $f(\mathcal{R})$ theories, and we note that $\xi = 0$ is equivalent to General Relativity. Absolute bounds on ξ in the Palatini approach can be derived from the analysis of the weak-field limit presented in [105], leading to $|\xi| \ll 2 \times 10^{12}$ cm^2. Another bound can be set by considering scenarios in which electric and gravitational (Newtonian) forces become of the same order of magnitude [119, 135], leading to $|\xi| < 6 \times 10^9$ cm^2. By contrast, bounds on ξ in the metric formalism range from $|\xi| < 5 \times 10^{15}$ cm^2 using Gravity

Probe B data to $|\xi| < 1.7 \times 10^{18}$ cm^2 by analysing the precession of binary pulsars, while the Eöt-Wash experiment yields $|\xi| < 10^{-6}$ cm^2 [136].

3.3. Free massive scalar field

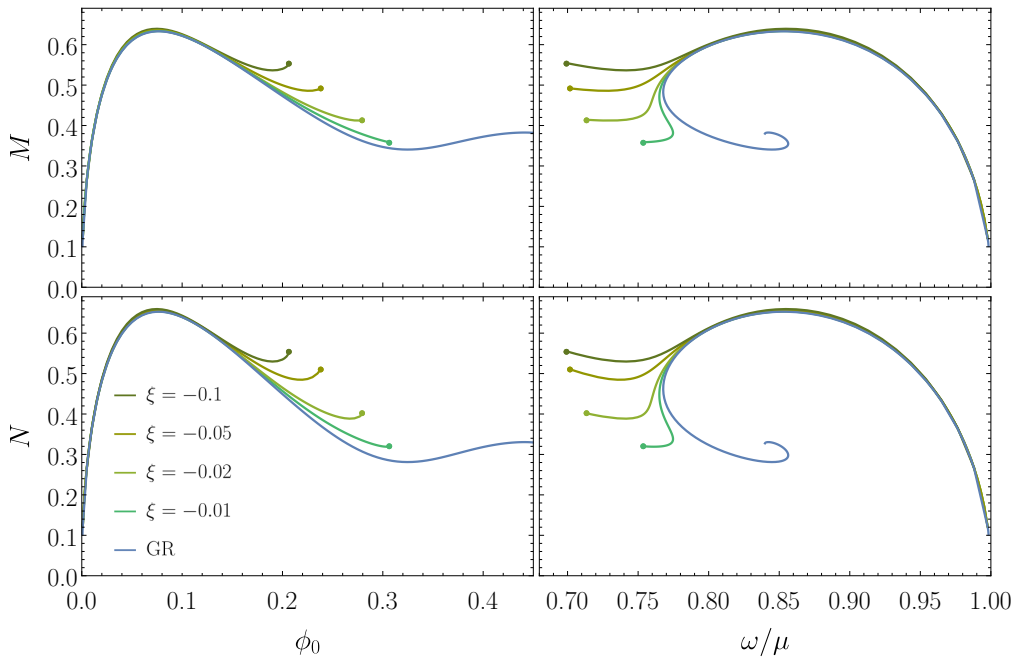

Figure 3.1.: Existence curves of spherically symmetric boson stars in Palatini $f(\mathcal{R})$ gravity, obtained by solving equations Eq. (3.12)-Eq. (3.15). Solutions with $\xi < 0$ are plotted and compared to General Relativity (GR). The left panels display the Misner-Sharp mass and the particle number N against the central value of the scalar field ϕ_0. The same quantities are plotted in the right panels against the frequency of the scalar field ω in units of μ. Circles signal the last solution we could build in $f(\mathcal{R})$. No circle is shown in the General Relativity solutions as further solutions can be built.

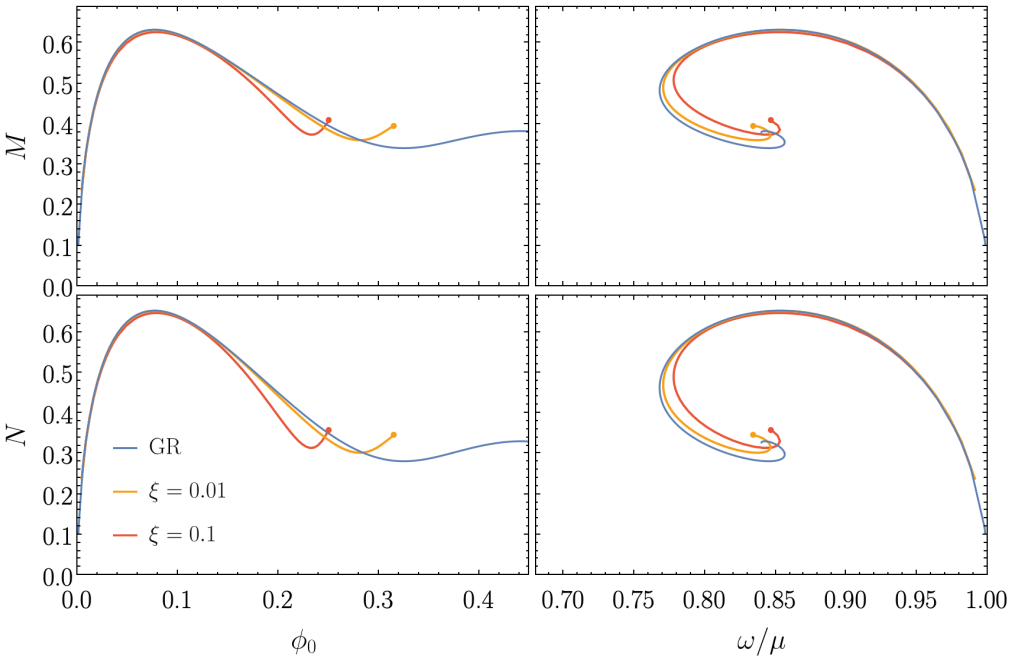

Figure 3.2.: Existence curves of spherically symmetric boson stars in Palatini $f(\mathcal{R})$ gravity, obtained by solving equations Eq. (3.12)-Eq. (3.15). Solutions with $\xi > 0$ are plotted. The left panels display the Misner-Sharp mass and the particle number N against the central value of the scalar field ϕ_0. The same quantities are plotted in the right panels against the frequency of the scalar field ω in units of μ. Circles signal the last solution we could build in $f(\mathcal{R})$. No circle is shown in the General Relativity solutions as further solutions can be built.

Figures 3.1 and 3.2 show existence plots of various boson star solutions in the theories considered i.e. with a potential of the form

$$V(\Phi) = -\frac{1}{2}\mu^2\Phi^*\Phi \quad . \tag{3.36}$$

In 3.1 negative values of the coupling constant ξ have been considered while positive values of ξ have been considered in 3.2. Each solution is characterized by a given central scalar field amplitude ϕ_0 and a frequency ω, for which a mass M and a particle number N is computed. These solutions are consistent with

the imposed boundary conditions, being regular at the origin and asymptotically flat.

As one can see from Figure 3.1 and Figure 3.2, for small values of ϕ_0 the solutions of $f(\mathcal{R})$ theories are almost coincident with those of General Relativity. However, for higher values of ϕ_0 clear differences can be seen. This is due to the fact that the quadratic corrections in the gravitational sector become more relevant for high energy concentrations. The most notorious difference between the boson stars of General Relativity and those of $f(\mathcal{R})$ is in their domain of existence. For General Relativity, the interval shown does not exhibit any upper limit on the ϕ_0 axis while this is not the case in $f(\mathcal{R})$. Similarly to General Relativity, boson stars in $f(\mathcal{R})$ theories exist in a bounded range of frequencies and masses, always with $\omega < \mu$. The case $\omega = \mu$ represents the limit where $M = 0$. We also observe that, as the gravitational coupling grows the maximum mass slightly decreases and the point signalling a vanishing value of the binding energy moves to lower values of the central scalar field amplitude and to larger values of the oscillation frequency.

Let us now focus on the $\xi < 0$ case (Figure 3.1). As the coupling parameter becomes more negative, the solutions depart more clearly from those of General Relativity. The effect of the negative coupling is to generate a repulsive gravitational component when the scalar field density is high enough. This explains why slightly higher values of $M_{\max}$ are allowed in these configurations, because a larger number of particles can be sustained due to the repulsive force.

It is remarkable that at some point below $\xi < -0.01$, the dependence of M with frequency departs from the well-known spiral behavior of General Relativity and becomes a one-valued function. Deviations from the spiral pattern are also observed in other theories of gravity [124, 128, 137], though in those cases solutions can be found over a larger range of frequencies, as well as for different potentials [138]. This behavior is not observed for positive values of ξ, which still produce the same spiral pattern as General Relativity. In addition, between $\xi = -0.02$ and $\xi = -0.05$ the solutions start showing a local minimum for M, which is not observed for positive values of ξ. Table 3.1 provides the values

of ϕ_0 and ω for a sample of our solutions, including those with the largest ϕ_0 achievable, $\phi_0^{\rm last}$, represented by a solid circle in the plots of Figure 3.1. We note that we cannot compute numerically solutions beyond $\phi_0^{\rm last}$, which tends to $\phi_0^2\omega^2/\mathcal{A}_0^2 = -1/(2\xi\kappa)$. Given the boundary condition (3.24), this value of ϕ_0 would make the conformal factor diverge at the origin (see Eq. (3.17)), which precludes finding solutions in this region of the parameter space.

ξ	$M_{\max}$	$\phi_0(M_{\max})$	$\omega(M_{\max})$	$\phi_0(E_b=0)$	$\omega(E_b=0)$
-0.10	0.6393	0.0749	0.855	0.1573	0.772
-0.05	0.6361	0.0756	0.854	0.1639	0.772
-0.02	0.6342	0.0758	0.854	0.1555	0.777
-0.01	0.6336	0.0761	0.854	0.1537	0.780
0.0	0.6330	0.0769	0.853	0.1523	0.779
0.01	0.6323	0.0784	0.853	0.1509	0.781
0.10	0.6270	0.0784	0.851	0.1438	0.786

ξ	$\omega_{\min}$	ϕ_0^{last}	$\mathcal{A}_0^{\text{last}}(\mu/\omega)$	ω^{last}
-0.10	0.697	0.2071	0.4662	0.697
-0.05	0.702	0.2380	0.3876	0.702
-0.02	0.713	0.2795	0.2838	0.713
-0.01	0.772	0.3066	0.2227	0.753
0.0	0.768	-	-	-
0.01	0.769	0.3251	0.0844	0.831
0.10	0.777	0.2567	0.0357	0.835

Table 3.1.: Values of the main physical quantities of our boson star models in Palatini $f(\mathcal{R})$ gravity. The upper Table reports: 1st column: value of the gravitational coupling parameter; 2nd to 4th columns: parameters for maximal-mass solutions; 5th and 6th column: parameters of solutions with null binding energy. The bottom Table reports: 1st column: value of the gravitational coupling parameter; 2nd column: value of minimal frequency in the mass-frequency plot, 3th to 5th column: parameter values for the last solution we are able to compute (circles in Figure 3.1 and Figure 3.2).

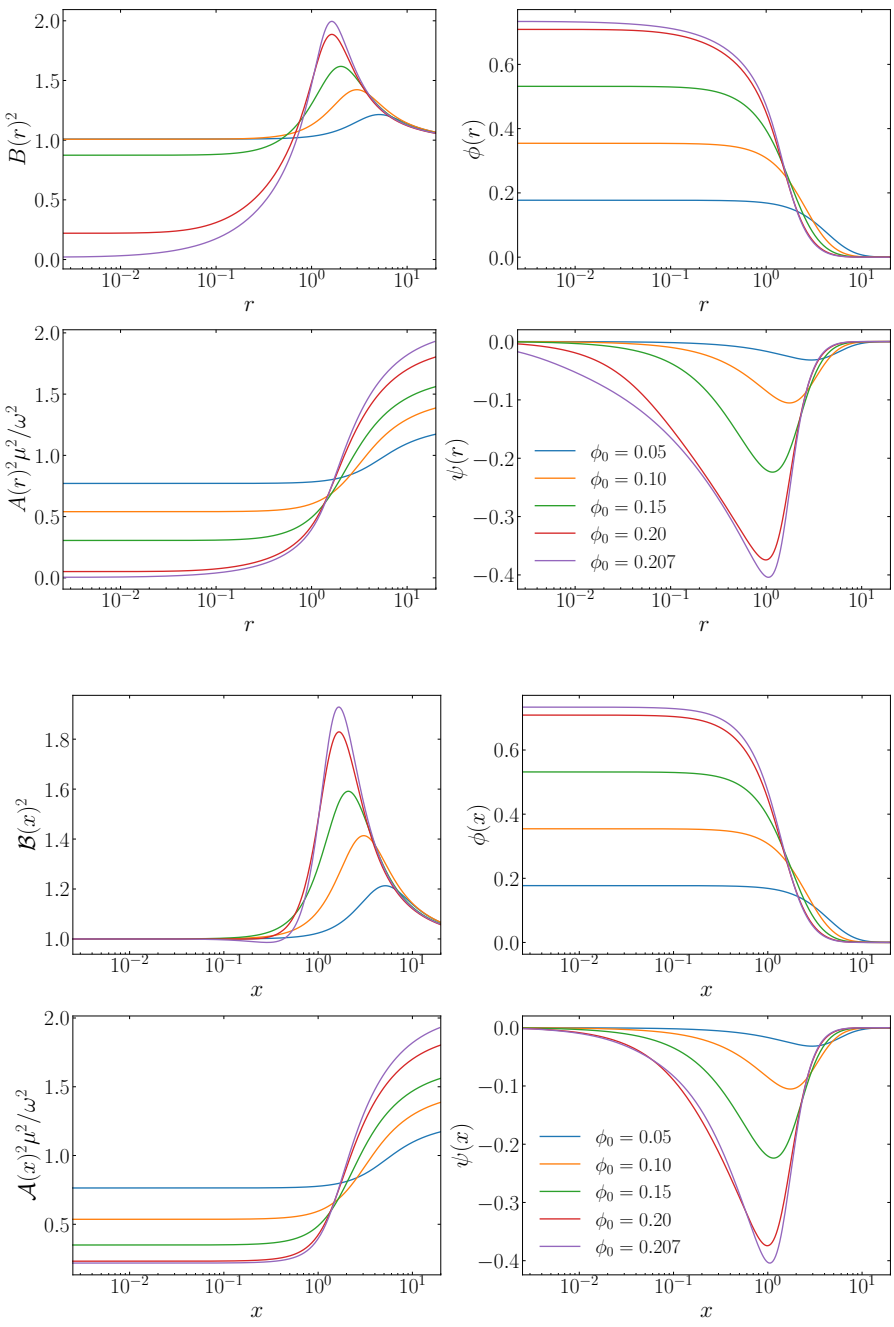

Figure 3.3.: Radial profiles of the metric functions and of the scalar field functions in both frames for $\xi = -0.1$. Five models of boson stars are plotted, as indicated by the value of ϕ_0 shown in the legend. Results for other negative values of ξ are qualitatively similar and, thus, they are not shown.

In Figure 3.3 we show radial plots of the metric components and of the scalar field for different values of ϕ_0 in both frames to facilitate their comparison. From those plots one can see that all the relevant functions are smooth and show no divergences, not even for values close to the critical condition $\phi_0^2\omega^2/\mathcal{A}_0^2 = -1/(2\xi\kappa)$ (see the purple curve in the plots). A close look at the figures in the $f(\mathcal{R})$ frame reveals that the two metric functions $A^2(r)$ and $B^2(r)$ tend to zero at the origin as the critical condition is approached. This is reasonable due to the appearance of the conformal factor $f_{\mathcal{R}}$ in the denominator of those quantities, which has a rapid growth as one approaches the last point in the existence curve, $\phi_0 \to \phi_0^{\text{last}}$, as shown in Figure 3.4. Similarly, in Figure 3.5 we see that the relation between the area of the spherical sectors in the two frames significantly deviates from linearity near the origin as one approaches this critical condition. The observed flattening of $r^2(x)$ is similar to what happens in other Palatini models (coupled to electric fields) in which wormhole solutions arise [133, 134, 139, 140]. Unfortunately, our numerical exploration of the parameter space has not led to any satisfactory wormhole solution, with a minimum in $r(x)$ followed by a bounce, like those found in [94], in which the mapping method was used in combination with the static, massless scalar field

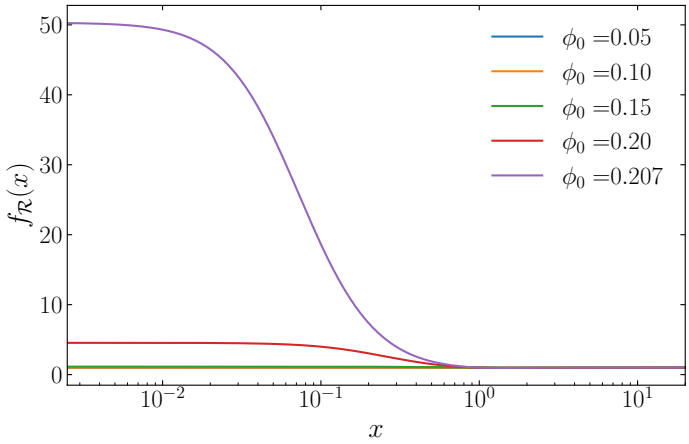

Figure 3.4.: Radial profile of the conformal factor $f_R(x)$, for $\xi = -0.1$ for different boson star configurations. Note that blue, orange, and green curves are overlapped.

solution of General Relativity as seed to generate new exotic compact objects in the same $f(\mathcal{R})$ theory as studied here. We suspect that the impossibility of finding that type of solutions in our analysis is due to the incompatibility of our boundary conditions at the center with those required to produce a bounce in the radial function $r(x)$. This interesting possibility will be further explored elsewhere.

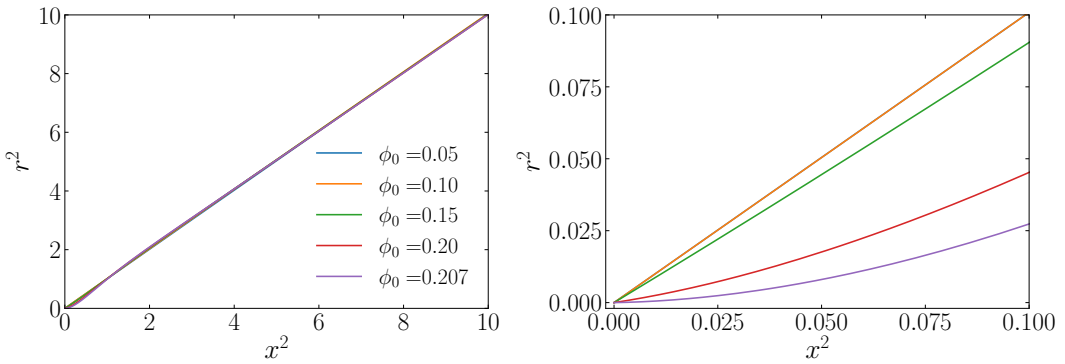

Figure 3.5.: Relation between the area of the 2-spheres in both frames, for $\xi = -0.1$. Notice the linearity between the areas in the two frames for most of the domain. The right panel shows a zoom close to the origin where the linear relation is not satisfied. Note that blue and orange curves overlap.

Let us now focus on the $\xi > 0$ case (Figure 3.2). In this case, as the gravitational coupling increases we see that features such as the local minimum or the spiraling occur earlier than in General Relativity. This can be intuitively justified by the fact that the positive contribution of the quadratic curvature terms in the Lagrangian increase the gravitational attraction as compared to General Relativity. For this reason, for a given central field amplitude ϕ_0, the corresponding solution supports less mass than in General Relativity, which justifies why $M_{\max}$ is slightly lower than in General Relativity. Correspondingly, for the same scalar field density, a higher deformation of spacetime is achieved as compared to General Relativity.

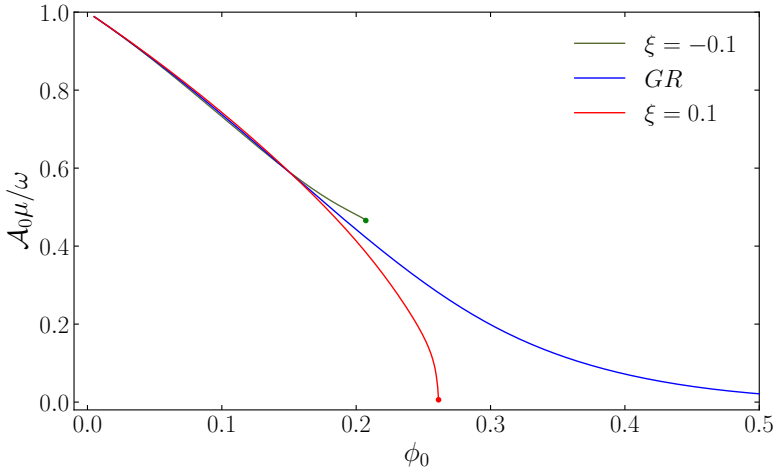

Figure 3.6.: Metric parameter $\mathcal{A}_0$ evaluated at the origin vs ϕ_0 for three different values of ξ.

The characteristic values of the last solutions we can build for the $\xi > 0$ case are also reported on Table 3.1. In this case, we are unable to find further solutions because Eqs. (3.12) and (3.15) diverge at the origin. The reason for the divergence is that $\mathcal{A}_0$ tends to zero, as shown in Figure 3.6. We note that while in General Relativity $\mathcal{A}_0$ tends to zero asymptotically, in $f(\mathcal{R})$ with $\xi > 0$ it tends to zero abruptly. In analogy with the $\xi < 0$ case, in Figure 3.7 we provide plots of the radial profiles of the metric components and of the scalar field for $\xi > 0$. The corresponding figures show how the divergences at the origin in Eqs. (3.12) and (3.15) as $\phi_0 \to \phi_0^{\rm last}$ translate into a diverging $B^2(r)$ function. It is worth noting that even though $\mathcal{A}_0^2$ tends to zero for $\phi_0^{\rm last}$, its conformally related function A_0^2 tends to the finite value 0.204. This confirms that the conformal factor $f_{\mathcal{R}}$ also tends to zero at the origin when $\phi_0 \to \phi_0^{\rm last}$ at the same rate as $\mathcal{A}_0$ (see Figure 3.8). Finally, Figure 3.9 reveals that also in the $\xi > 0$ case the linearity between the area of the 2-spheres in the two frames breaks near the center. However, contrary to the $\xi < 0$ case (cf. Figure 3.5) it is now the curve $x = x(r)$ which flattens. A similar behavior has already been observed in other exotic compact objects and might be related with the

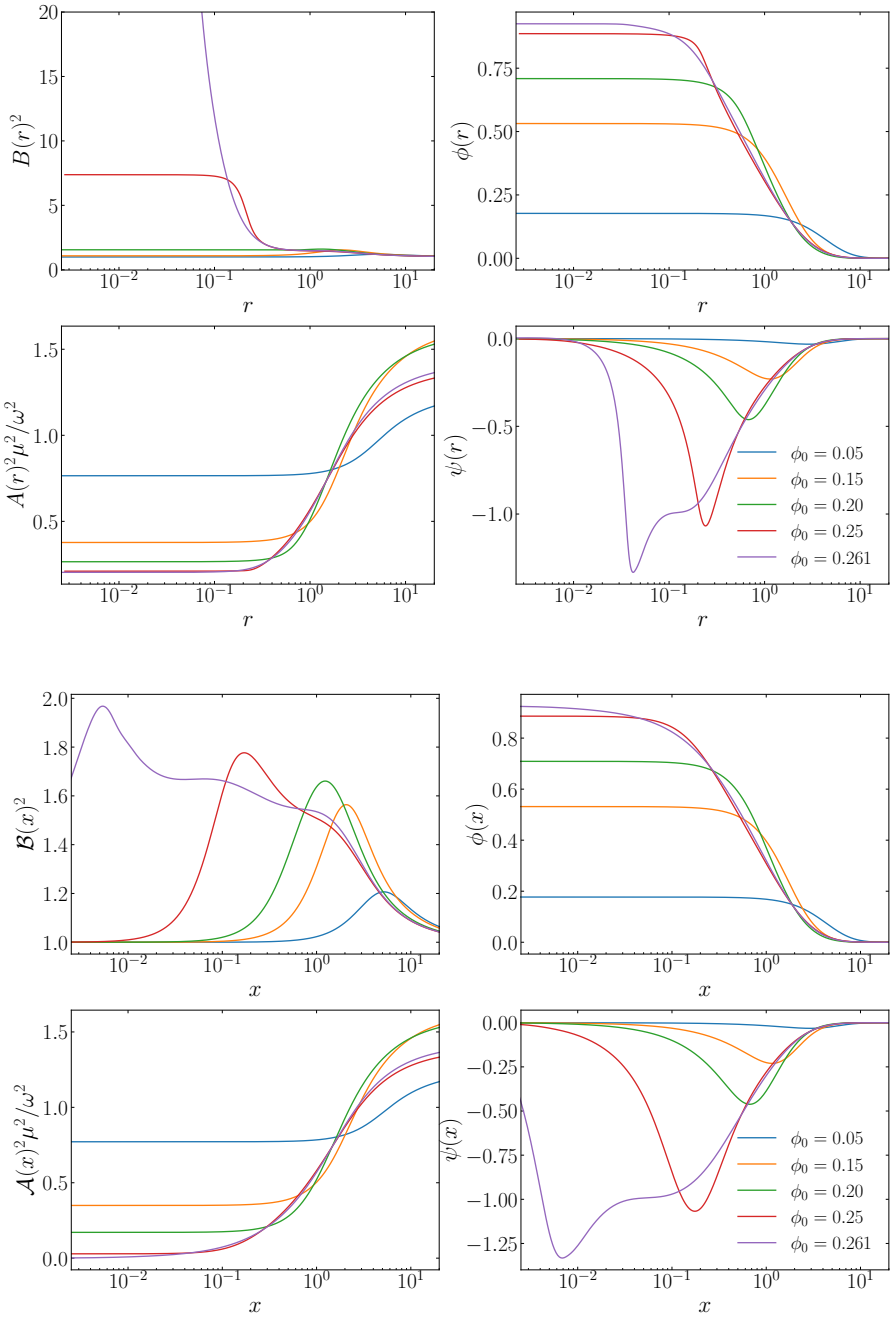

Figure 3.7.: Radial profiles of the metric functions and of the scalar field functions in both frames for $\xi = 0.1$. Five models of boson stars are plotted, as indicated by the value of ϕ_0 shown in the legend.

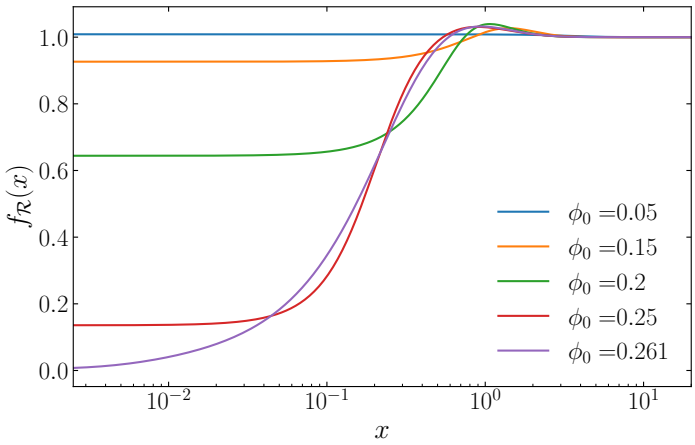

Figure 3.8.: Radial profile of the conformal factor $f_R(x)$, for $\xi = 0.1$ for different boson star configurations.

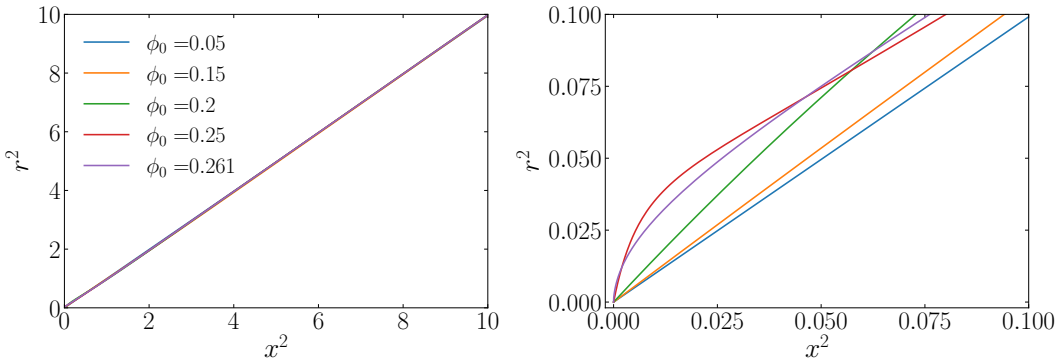

Figure 3.9.: Relation between the area of the 2-spheres in both frames, for $\xi = 0.1$. As in Figure 3.5 the linearity between the areas in the two frames is broken only close to the origin, as shown on the right panel, which is a closer view of the inner region.

existence of wormhole structures in the Einstein frame geometry [94], although in those cases $r^2(x)$ vanishes at a non-zero value of x.

Further useful information regarding the observational features of these solutions can be extracted by looking at their mass-radius relation and compactness. The mass-radius relation is constructed by determining the radius which contains 99% of the mass of the boson star and then plotting that mass versus its corresponding radius. As one can see from Figure 3.10, only for configurations near the maximum of the mass function and small radii do the $f(\mathcal{R})$ models deviate noticeably from the General Relativity result, yielding a larger maximum if $\xi < 0$ and a smaller one if $\xi > 0$. For configurations with radii below the maximum, the $\xi > 0$ branch follows the same trend as General Relativity, presenting a local minimum in the mass which is accompanied by an increase of the radius, whereas in the $\xi < 0$ case the mass function reaches a local minimum (which is much larger than the General Relativity minimum) and then grows again with a continuous reduction of its radius. As a result, see Figure3.11, the compactness of the stars (measured by the ratio M_{99}/R_{99}) becomes a monotonically growing function of the central field amplitude when $\xi < 0$ but reaches a global maximum followed by a minimum in the General Relativity and $\xi > 0$ cases. Thus, $\xi < 0$ allows for more compact objects in its spectrum of solutions, offering a way to observationally discriminate between General Relativity and this branch of the $f(\mathcal{R})$ family.

As has been shown, we have taken advantage of the correspondence that exists between General Relativity and Palatini $f(\mathcal{R})$ gravity to compute solutions for boson stars, such that the original modified gravity theory can be turned into a modified matter theory coupled to standard General Relativity.

From the above discussion, we can assert that the amplitude of the gravitational coupling parameter ξ magnifies the disparity of the boson star solutions in $f(\mathcal{R})$ with respect to General Relativity, keeping the qualitative features of the solutions essentially unchanged for low central densities but showing a trend towards more compact objects and new structures already seen in scenarios with wormholes at higher densities. Furthermore, an important difference with respect to General Relativity is the limited range of scalar field amplitudes allowed at the center of the star, which is much shorter than in General Relativity (see Figure 3.1 and Figure 3.2). For relatively small central field amplitudes ϕ_0,

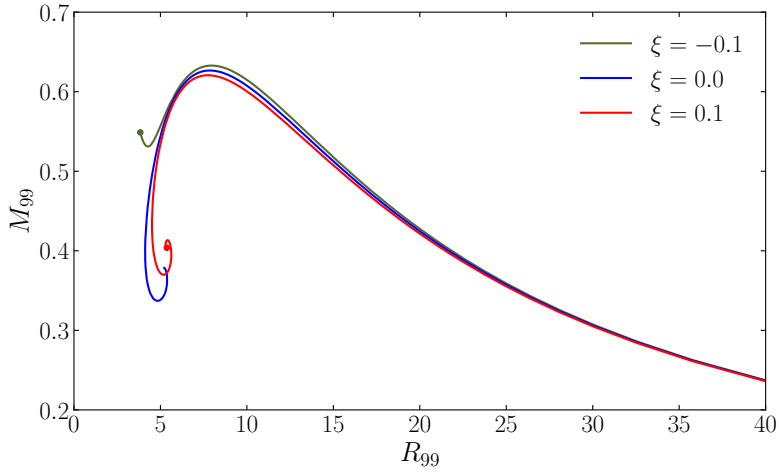

Figure 3.10.: Mass-Radius relation for three different values of ξ.

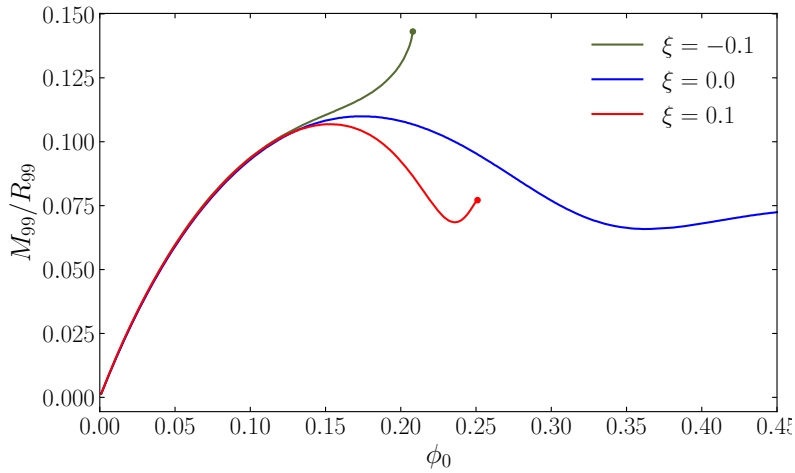

Figure 3.11.: Compactness of boson stars as a function of the central scalar field amplitude ϕ_0 for the same values of ξ shown in Figure3.10.

we found that the solutions do not differ significantly from those of General Relativity, though larger/smaller masses and compactness can be achieved for a given ϕ_0 depending on whether $\xi < 0$ or $\xi > 0$, respectively. It is interesting

to note that the deviations become more important after the maximum mass model, in the unstable branch of solutions. New features arise in the $\xi < 0$ case regarding the dependence of the total mass and particle number of a solution with its oscillation frequency. In General Relativity coupled to canonical matter, these curves exhibit a characteristic spiral pattern which is lost in this case (at least) in the range of parameters explored (see Figure 3.1). Although other theories of gravity may also depart from this spiral pattern [124, 128, 137], the model considered here is peculiar because the range over which solutions are possible is relatively small, which could facilitate its observational discrimination.

Though our focus was on analyzing canonical boson stars coupled to $f(\mathcal{R})$ gravity, the fact is that our computational method forced us to construct boson star solutions in General Relativity coupled to unconventional matter (see Eq. (3.8)). In this regard, we note that the total mass, field amplitudes, and frequencies that we obtained are valid in both theories, namely, in $f(\mathcal{R})$ coupled to the scalar Lagrangian $P(X, \Phi) = X - 2V(\Phi)$ and in General Relativity coupled to the non-canonical scalar Lagrangian $K(Z, \Phi)$. It is also easy to see from Figs. 3.5 and 3.9 that the radius of these stars will also be practically indistinguishable because the conformal factor that relates the radial coordinates r and x is essentially equal to unity at the surface. All this puts forward an interesting degeneracy between the boson stars that arise from coupling General Relativity to a non-lineal matter Lagrangian and the boson stars that arise from coupling $f(\mathcal{R})$ gravity to standard (or canonical) matter Lagrangian.

Moreover, we note that as one approaches the limiting value of the central field amplitude, the conformal factor strongly deviates from unity (either towards infinity if $\xi < 0$ or towards zero if $\xi > 0$) and leads to a deformation of the relation between areas of the $f(\mathcal{R})$ and General Relativity frames (see Figs. 3.5 and 3.9) that reminds of the $r(x)$ relation that appears in scenarios with wormholes such as those described in [94].

3.4. Self-interacting scalar field

The results obtained in the previous section for a free massive scalar field can be extended to the case in which self-interactions are present, as we discuss next. By considering a potential of the form

$$V_{\rm SI}(\Phi) = -\frac{1}{2}\mu^2|\Phi|^2 - \frac{1}{4}\lambda|\Phi|^4 \quad , \tag{3.37}$$

in which the second term is a quartic self-interaction term, the system of differential equations to build the stellar models is modified as follows:

$$\begin{aligned}\frac{\partial_x \mathcal{B}}{\mathcal{B}} = & \frac{1-\mathcal{B}^2}{2x} \\ & + \frac{1}{1+4\xi\kappa\left(\mu^2\phi^2+\frac{\lambda\phi^4}{2}\right)}\frac{\kappa x}{4}\left\{\mathcal{B}^2\left(\mu^2\phi^2+\frac{\lambda\phi^4}{2}\right)\right. \\ & + \left(\omega^2\phi^2\frac{\mathcal{B}^2}{\mathcal{A}^2}+\psi^2\right)\left[1-2\kappa\xi\left(-\frac{\omega^2\phi^2}{\mathcal{A}^2}+\frac{\psi^2}{\mathcal{B}^2}\right)\right] \\ & \left. +2\kappa\xi\mathcal{B}^2\left(\frac{\omega^2\phi^2}{\mathcal{A}^2}-\frac{\psi^2}{\mathcal{B}^2}\right)^2\right\},\end{aligned} \tag{3.38}$$

$$\begin{aligned}\frac{\partial_x \mathcal{A}}{\mathcal{A}} = & \frac{\mathcal{B}^2-1}{x} + \frac{\partial_x \mathcal{B}}{\mathcal{B}} \\ & + \frac{1}{1+4\xi\kappa\left(\mu^2\phi^2+\frac{\lambda\phi^4}{2}\right)}\frac{\kappa x}{4}\left\{-2\mathcal{B}^2\left(\mu^2\phi^2+\frac{\lambda\phi^4}{2}\right)\right. \\ & \left. -2\kappa\xi\mathcal{B}^2\left(\frac{\omega^2\phi^2}{\mathcal{A}^2}-\frac{\psi^2}{\mathcal{B}^2}\right)^2\right\}.\end{aligned} \tag{3.39}$$

$$
\begin{aligned}
\partial_x\psi = & \frac{1}{\left[1+4\xi\kappa\left(\mu^2\phi^2+\frac{\lambda\phi^4}{2}\right)\right]\left[1-2\xi\kappa\left(-\frac{\omega^2\phi^2}{\mathcal{A}^2}+\frac{3\psi^2}{\mathcal{B}^2}\right)\right]}\Bigg\{ \\
& -\psi\left(\frac{2}{x}+\frac{\partial_x\mathcal{A}}{\mathcal{A}}-\frac{\partial_x\mathcal{B}}{\mathcal{B}}\right)\left[1+4\kappa\xi\left(\mu^2\phi^2+\frac{\lambda\phi^4}{2}\right)\right] \\
& \times\left[1-2\xi\kappa\left(-\frac{\omega^2\phi^2}{\mathcal{A}^2}+\frac{\psi^2}{\mathcal{B}^2}\right)\right] \\
& -\omega^2\phi\frac{\mathcal{B}^2}{\mathcal{A}^2}\left[1+2\xi\kappa\left(\frac{\omega^2\phi^2}{\mathcal{A}^2}+\frac{\psi^2}{\mathcal{B}^2}\right)\right] \\
& +\mathcal{B}^2\left(\mu^2\phi+\lambda\phi^3\right)\left(1+4\kappa\xi\frac{\psi^2}{\mathcal{B}^2}\right) \\
& +\kappa\xi\left[\frac{4\omega^2\phi^2\psi}{\mathcal{A}^2}\frac{\partial_x\mathcal{A}}{\mathcal{A}}\left(1+4\kappa\xi\left(\mu^2\phi^2+\frac{\lambda\phi^4}{2}\right)\right)\right. \\
& \left.-\frac{4\psi^3}{\mathcal{B}^2}\frac{\partial_x\mathcal{B}}{\mathcal{B}}\left(1+4\kappa\xi\left(\mu^2\phi^2+\frac{\lambda\phi^4}{2}\right)\right)+2\phi^5\omega^2\lambda\frac{\mathcal{B}^2}{\mathcal{A}^2}\right] \\
& +\kappa^2\xi^2\left[-12\left(\mu^2+\lambda\phi^2\right)\phi\frac{\psi^4}{\mathcal{B}^2}-4\mu^2\frac{\mathcal{B}^2\omega^4\phi^5}{\mathcal{A}^4}+4\lambda\frac{\omega^2\psi^2\phi^5}{\mathcal{A}^2}\right]\Bigg\}.
\end{aligned}
\tag{3.40}
$$

For the numerical analysis it is convenient to re-scale the self-interaction parameter as

$$
\Lambda = \frac{2}{\kappa}\lambda \quad . \tag{3.41}
$$

The corresponding boson star solutions are plotted in Figure 3.12. This figure shows the existence curves for different values of the self-interaction parameter Λ in General Relativity and in Palatini $f(\mathcal{R})$ gravity. We only consider $\Lambda \geq 0$ because a negative value would violate energy conditions. Figure 3.12 exhibits that increasing the self-interaction coupling results in more massive boson stars and in a larger maximum mass (see also [49]). Moreover, this figure reveals that the existence curves shorten as the self-interaction parameter Λ increases. For $\xi < 0$, $\mathcal{A}_0$ decreases faster as Λ increases producing the observed shortening (compare the location of the green circles in the figure with those of the red and blue circles). Paying attention to the green curves in Figure 3.12, corresponding

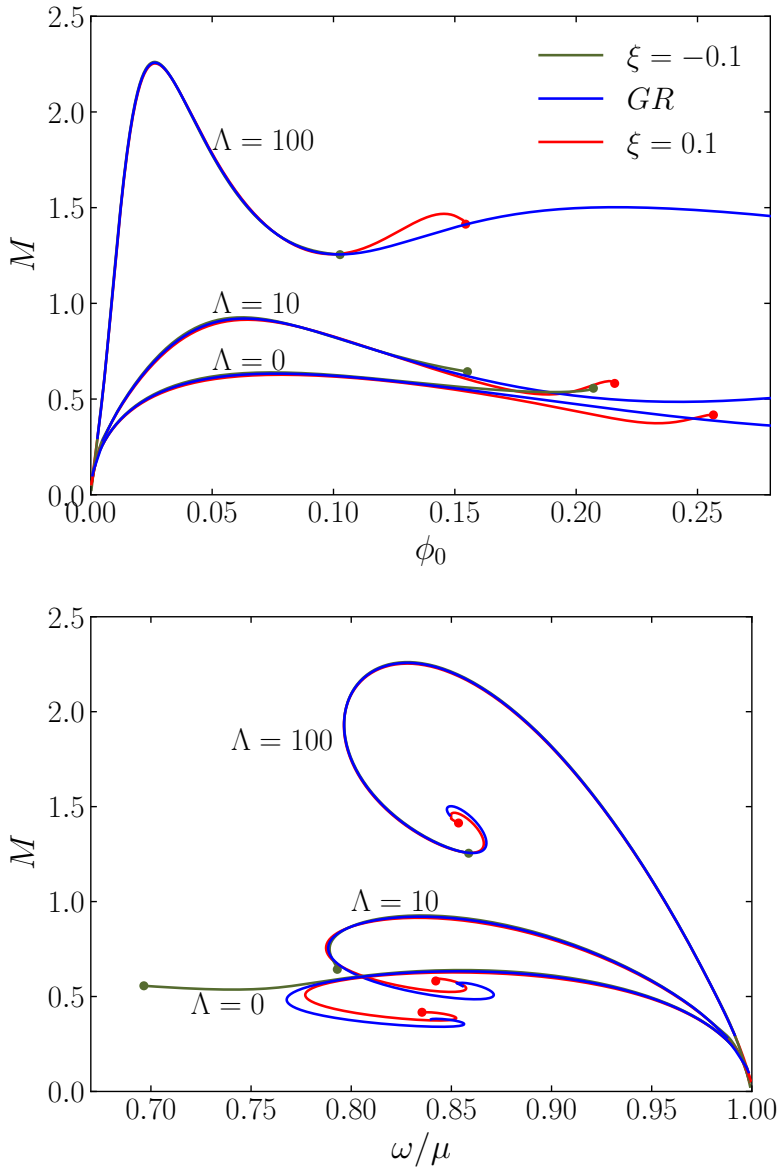

Figure 3.12.: Equilibrium configurations of boson stars in Palatini $f(\mathcal{R})$ gravity for three different values of the coupling parameter ξ and of the self-interaction parameter Λ. Top panel: total mass as a function of the central value of the scalar field. Bottom panel: total mass as a function of the frequency.

to $\xi = -0.1$, one can see that for $\Lambda = 10$ the disparity with General Relativity is hardly noticeable and for $\Lambda = 100$ the existence curve lays over the General Relativity curve making its length the only remarkable difference. Meanwhile for $\xi = 0.1$ (red curves) the curves are shorter by the fact that the conformal factor now goes as

$$f_{\mathcal{R}} = \frac{1 + 4\xi\kappa\mu^2\phi^2 + 2\xi\kappa\lambda\phi^4}{1 - 2\xi\kappa\left(-\frac{\omega^2\phi^2}{\mathcal{A}^2} + \frac{\psi^2}{\mathcal{B}^2}\right)}, \tag{3.42}$$

making the condition $f_{\mathcal{R}} = 0$ easier to achieve.

As can be seen in Figure 3.12, the incorporation of self-interactions in the scalar field potential does not contribute to change qualitatively the behavior of the solutions found in Section 3.3. Furthermore, it contributes to aggravate the degeneracy that exists between the boson stars that arise from coupling General Relativity to a non-lineal matter Lagrangian and the boson stars that arise from coupling $f(\mathcal{R})$ gravity to standard (or canonical) matter Lagrangian.

Chapter 4.

Dynamical boson stars in Palatini $f(\mathcal{R})$ gravity

In the previous chapter, we successfully obtained solutions for boson stars in Palatini $f(\mathcal{R})$ gravity. Achieving these solutions motivate us to compute numerical temporal evolutions, as described in Section 1.4. Specifically, we will use the static configurations as initial data and employ Numerical Relativity methodology to ascertain the system's future endstate.

In the present chapter, written following Ref. [4], we aim to investigate the time evolution of boson stars in Palatini $f(\mathcal{R})$ gravity using state-of-the-art numerical techniques. We will utilize recent improvements in numerical codes to compute various aspects of boson stars. By studying these objects in Palatini $f(\mathcal{R})$ gravity, we seek to understand the effects of modified gravity on the properties and dynamics of these compact objects. Our findings may shed light on the fundamental nature of gravity in the strong gravitational regime and contribute to our understanding of the astrophysical implications of modified gravity theories.

4.1. Framework

We have established the correspondence between a boson star in the Starobinski model à la Palatini and General Relativity coupled to a non-linear matter Lagrangian. In particular, there is an equivalence between the space of solutions of Eq. (3.2) and Eq. (3.7). Where the matter Lagrangians keep the relation described in Eq. (3.8).

Based on this equivalence, our approach is as follows: we formulate the system in the context of $f(\mathcal{R})$ gravity and then translate it into a problem of General Relativity. In the Einstein frame, we employ numerical techniques from Numerical Relativity to compute the temporal evolution of the system. Once this computation is completed, we return to the $f(\mathcal{R})$ frame to validate the obtained results within that specific context.

In order to study the time evolution of boson stars we will use the 3+1 Baumgarte-Shapiro-Shibata-Nakamura (BSSN) formalism of Einstein's equations in the Einstein frame [39, 40], as introduced in Section 1.3.2 . In this formalism the space-time is foliated by a family of spatial hypersufaces Σ_t labeled by its time coordinate t. We denote the (future-oriented) unit normal timelike vector of each hypersurface by $n^\alpha = (1/\alpha, -\beta^i/\alpha)$, and its dual by $n_\alpha = (-\alpha, 0, 0, 0)$. Since the system we study has spherical symmetry, the metric in the Einstein frame reads

$$\begin{aligned} ds^2_{\mathrm{EF}} = &- (\alpha^2 - \beta^x\beta_x)dt^2 + 2\beta_x dx dt \\ &+ e^{4\chi}\left(a(t,x)dx^2 + x^2 b(t,x)d\Omega^2\right) \quad , \end{aligned} \tag{4.1}$$

where $d\Omega^2 = d\theta^2 + sin^2\theta d\varphi^2$, α is the lapse vector, β^x the shift vector, $a(t,x)$ and $b(x,t)$ are the metric functions and χ is the conformal factor defined by

$$\chi = \frac{1}{12}\ln(\gamma/\hat{\gamma}) \quad . \tag{4.2}$$

Here, γ is the determinant of the spacelike induced metric on every hypersuface Σ_t,

$$\gamma_{\alpha\beta} = q_{\alpha\beta} + n_\alpha n_\beta \quad , \tag{4.3}$$

and $\hat{\gamma}$ is the determinant of the conformal metric. The latter relates to the full 3-metric by

$$\hat{\gamma}_{ij} = e^{-4\chi}\gamma_{ij} \quad . \tag{4.4}$$

Initially, the determinant of the conformal metric fulfills the condition that it equals the determinant of the flat metric in spherical coordinates $\hat{\gamma}(t=0) = x^4 \sin^2\theta$. Moreover, we follow the so called *Lagrangian* condition $\partial_t \hat{\gamma} = 0$.

As shown in equations (1.52) - (1.56), the evolved fields are the conformally related 3-dimensional metric functions a and b, the conformal exponent χ, the trace of the extrinsic curvature K, the independent component of the traceless part of the conformal extrinsic curvature, $A_a \equiv A^x_x$, $A_b \equiv A^\theta_\theta = A^\varphi_\varphi$ and the radial component of the conformal connection functions $\hat{\Delta}^x \equiv \hat{\gamma}^{mn}(\hat{\Gamma}^x_{mn} - \hat{\Gamma}^x_{mn}(t=0))$ [45,49]. For the specific case under investigation and considering the symmetries specified, the aforementioned evolution equations can be expressed as:

$$\partial_t a = \beta^x \partial_x a + 2a\partial_x \beta^x - \frac{2}{3} a \hat{\nabla}_x \beta^x - 2\alpha a A_a \quad , \tag{4.5}$$

$$\partial_t b = \beta^x \partial_x b + 2b\frac{\beta^x}{x} - \frac{2}{3} b \hat{\nabla}_x \beta^x - 2\alpha b A_b \quad , \tag{4.6}$$

$$\partial_t \chi = \beta^x \partial_x \chi + \frac{1}{6}\left(\alpha K - \hat{\nabla}_x \beta^x\right) \quad , \tag{4.7}$$

$$\begin{aligned}\partial_t K =&\beta^x \partial_x K - \nabla^2 \alpha + \alpha(A_a^2 + 2A_b^2 + \frac{1}{3}K^2) \\ &+ 4\pi\alpha\left(\rho + S_a + 2S_b\right) \quad ,\end{aligned} \tag{4.8}$$

$$\begin{aligned}\partial_t A_a =&\beta^x \partial_x A_a - \left(\nabla^x \nabla_x \alpha - \frac{1}{3}\nabla^2\alpha\right) + \alpha\left(R^x_x - \frac{1}{3}R\right) \\ &+ aKA_a - 16\pi\alpha(S_a - S_b) \quad ,\end{aligned} \tag{4.9}$$

$$\begin{aligned}\partial_t \hat{\Delta}^x =&\beta^x \partial_x \hat{\Delta}^x - \hat{\Delta}^x \partial_x \beta^x + \frac{1}{a}\partial_x^2 \beta^x + \frac{2}{b}\partial_x\left(\frac{\beta^x}{x}\right) \\ &+ \frac{1}{3}\left(\frac{1}{a}\partial_x(\hat{\nabla}_x \beta^x) + 2\hat{\Delta}^x \hat{\nabla}_x \beta^x\right) \\ &- \frac{2}{a}\left(A_a \partial_x \alpha + \alpha \partial_x A_z\right) \\ &+ 2\alpha\left(A_a \hat{\Delta}^x - \frac{2}{xb}(A_a - A_b)\right) \\ &+ \frac{\xi\alpha}{a}\left[\partial_x A_a - \frac{2}{3}\partial_x K + 6A_a \partial_x \chi\right. \\ &\left.+(A_a - A_b)\left(\frac{2}{x} + \frac{\partial_x b}{b}\right) - 8\pi j_x\right] \quad .\end{aligned} \tag{4.10}$$

Where we denote with $\hat{\nabla}$ the covariant derivative with respect to the conformal metric $\hat{\gamma}$ while using ∇ to denote the covariant derivative with respect to the physical metric.

When performing the time evolution of the above functions we have to specify a stress-energy tensor and its 3+1 projection. The case we are concerned with is a boson star in Palatini $f(\mathcal{R}) = \mathcal{R} + \xi\mathcal{R}^2$ gravity. Its expression in the Einstein frame has been written in Eq. (3.9).

The projections are performed using the unit normal vector n^α and the induced metric $\gamma^{\alpha\beta}$. The matter source terms appearing in the BSSN evolution

equations are:

$$\begin{aligned}\rho =&n^{\mu}n^{\nu}\tilde{T}_{\mu\nu}\\ =&\frac{1}{2(1+4\kappa\xi\mu^2\Phi^2)}\left[\Pi^2+\frac{\Psi^2}{ae^{4\chi}}+\mu^2\Phi^2\right.\\ &\left.-\kappa\xi\left(\frac{\Psi^2}{ae^{4\chi}}\right)^2+3\kappa\xi\Pi^4-2\kappa\xi\frac{\Psi^2}{ae^{4\chi}}\Pi^2\right] \quad ,\end{aligned} \tag{4.11}$$

$$\begin{aligned}S_a =&\gamma^{x\mu}\tilde{T}_{x\mu}\\ =&\frac{1}{2(1+4\kappa\xi\mu^2\Phi^2)}\left[\Pi^2+\frac{\Psi^2}{ae^{4\chi}}-\mu^2\Phi^2\right.\\ &\left.-3\kappa\xi\left(\frac{\Psi^2}{ae^{4\chi}}\right)^2+\kappa\xi\Pi^4+2\kappa\xi\frac{\Psi^2}{ae^{4\chi}}\Pi^2\right] \quad ,\end{aligned} \tag{4.12}$$

$$\begin{aligned}S_b =&\gamma^{\theta\mu}\tilde{T}_{\theta\mu}\\ =&\frac{1}{2(1+4\kappa\xi\mu^2\Phi^2)}\left[\Pi^2-\frac{\Psi^2}{ae^{4\chi}}-\mu^2\Phi^2\right.\\ &\left.+\kappa\xi\left(\frac{\Psi^2}{ae^{4\chi}}\right)^2+\kappa\xi\Pi^4-2\kappa\xi\frac{\Psi^2}{ae^{4\chi}}\Pi^2\right] \quad ,\end{aligned} \tag{4.13}$$

$$\begin{aligned}j_x =&-\gamma^{\mu}_{x}n^{\nu}\tilde{T}_{\mu\nu}\\ =&\frac{1}{2(1+4\kappa\xi\mu^2\Phi^2)}\left[\frac{1}{ae^{4\chi}}\left(\Pi\Psi^*+\Pi^*\Psi\right)\right.\\ &\left.+\frac{2\kappa\xi\Psi^2}{a^2e^{8\chi}}\left(\Pi\Psi^*+\Pi^*\Psi\right)-\frac{2\kappa\xi\Pi^2}{ae^{4\chi}}\left(\Pi\Psi^*+\Pi^*\Psi\right)\right] \quad .\end{aligned} \tag{4.14}$$

Correspondingly, the equations of motion for the scalar field are obtained by reformulating the Klein-Gordon equation in terms of the following two

first-order variables

$$\begin{aligned} \Psi &:= \partial_r \Phi \quad , \\ \Pi &:= n^\alpha \partial_\alpha \Phi = \frac{1}{\alpha}\left(\partial_t \Phi - \beta^r \Psi\right) \quad . \end{aligned} \tag{4.15}$$

In this way the equations of motion for the scalar field read

$$\partial_t \Phi = \beta^x \partial_x \Phi + \alpha \Pi \quad , \tag{4.16}$$

$$\partial_t \Psi = \beta^x \partial_x \Psi + \Psi \partial_x \beta^x + \partial_x \left(\alpha \Pi\right) \quad , \tag{4.17}$$

$$\partial_t \Pi = \frac{1 - 2\kappa\xi Z + \kappa\xi|\Pi|^2}{1 - 2\kappa\xi Z + 2\kappa\xi|\Pi|^2}\left\{\Xi - \frac{\kappa\xi\Pi^2}{1 - 2\kappa\xi Z + \kappa\xi|\Pi|^2}\bar{\Xi}\right\} \quad , \tag{4.18}$$

where we have introduced the new variable Ξ in order to simplify the notation, defined as

$$\begin{aligned}
\Xi :=&\beta^x\partial_x\Pi + \frac{\Psi}{ae^{4\chi}}\partial_x\alpha + \frac{\alpha}{ae^{4\chi}}\left[\partial_x\Psi + \Psi\left(\frac{2}{x} - \frac{\partial_x a}{2a} + \frac{\partial_r b}{b} + 2\partial_x\chi\right)\right] \\
&+\alpha K\Pi - \frac{\alpha\mu^2\Phi}{1-2\kappa\xi Z} + \frac{\alpha\left(Z - \kappa\xi Z^2 + \mu^2|\Phi|^2\right)4\xi\kappa\Phi\mu^2}{\left(1+4\kappa\xi\mu^2|\Phi|^2\right)\left(1-2\kappa\xi Z\right)} \\
&-\frac{4\kappa\xi\mu^2\alpha}{1+4\kappa\xi\mu^2|\Phi|^2}\left[-\frac{\Pi}{\alpha}\left(\partial_t\Phi^*\Phi + \Phi^*\partial_t\Phi\right)\right. \\
&\left.+\left(\frac{\Psi}{e^{4\chi}a} + \frac{\Pi\beta^x}{\alpha}\right)\left(\partial_x\Phi^*\Phi + \Phi^*\partial_x\Phi\right)\right] \\
&+\frac{\alpha\kappa\xi}{1-2\kappa\xi Z}\left[\frac{\left(\partial_t\Psi^*\Psi + \Psi^*\partial_t\Psi\right)e^{4\chi}a - |\Psi|^2\left(4e^{4\chi}a\partial_t\chi + e^{4\chi}\partial_t a\right)}{e^{8\chi}a^2}\frac{\Pi}{\alpha}\right. \\
&+\left(\frac{\Psi}{e^{4\chi}a} + \frac{\Pi\beta^x}{\alpha}\right)\left(\partial_x\Pi^*\Pi + \Pi^*\partial_x\Pi + \right. \\
&\left.\left.+\frac{\left(\partial_x\Psi^*\Psi + \Psi^*\partial_x\Psi\right)e^{4\chi}a - |\Psi|^2\left(4e^{4\chi}a\partial_x\chi + e^{4\chi}\partial_x a\right)}{e^{8\chi}a^2}\right)\right] \quad ,
\end{aligned} \tag{4.19}$$

and

$$Z \equiv q^{\mu\nu}\partial_\mu\Phi^*\partial_\nu\Phi = \frac{|\Psi|^2}{e^{4\chi}a} - |\Pi|^2 \qquad . \tag{4.20}$$

Within the BSSN formalism we have gauge freedom to choose the *kinematical variables*, i.e. the lapse function and the shift vector (see Section 1.3.3). As customary in Numerical Relativity, we choose the so-called *non-advective 1+log* condition for the lapse function [141], and a variation of the *Gamma-driver* condition for the shift vector [142, 143],

$$\begin{aligned}
\partial_t\alpha &= \beta^x\partial_x\alpha - 2\alpha K \quad , \\
\partial_t B^x &= \beta^x\partial_x B^x + \frac{3}{4}\partial_t\hat{\Delta}^x - \frac{3}{4}\beta^x\partial_x\hat{\Delta}^x \quad , \\
\partial_t\beta^x &= \beta^x\partial_x\beta^x + B^x \ .
\end{aligned} \tag{4.21}$$

We also provide the explicit form of the conformal factor $f_{\mathcal{R}}$. From the Einstein field equations of the Palatini quadratic $f(\mathcal{R})$ model it can be shown that $\mathcal{R} = -\kappa T$. Therefore,

$$f_{\mathcal{R}} = 1 + 2\xi\kappa\mathcal{R} = \frac{1 - 8\kappa\xi V}{1 - 2\kappa\xi Z} \ . \tag{4.22}$$

In addition to the evolution equations, the Einstein-Klein-Gordon system also contains the Hamiltonian and momentum constraint equations. These equations read

$$\mathcal{H} \equiv R - (A_a^2 + 2A_b^2) + \frac{2}{3}K^2 - 2\kappa\rho = 0 \quad , \tag{4.23}$$

$$\begin{aligned} \mathcal{M}_x \equiv & \partial_x A_a - \frac{2}{3}\partial_x K + 6A_a\partial_x\chi \\ & + (A_a - A_b)\left(\frac{2}{x} + \frac{\partial_x b}{b}\right) - \kappa j_x = 0 \quad . \end{aligned} \tag{4.24}$$

The problem in question is set in the $f(\mathcal{R})$ frame, the time evolution of boson stars in Palatini $f(\mathcal{R})$ gravity. We used the conformal relation Eq. (3.4) to translate it to the Einstein frame, as can be seen in the energy-momentum tensor modifications Eq. (3.9). In the Einstein frame we are able to use the BSSN formalism to solve the evolution equations and then translate it to the $f(\mathcal{R})$ frame again. The metric of this frame is

$$ds^2_{f(\mathcal{R})} = -g_{tt}dt^2 + 2g_{rt}drdt + g_{rr}dr^2 + \tilde{R}^2(t,r)d\Omega^2 \quad , \tag{4.25}$$

where the radial coordinate is expressed with an r in order to distinguish it from the radial coordinate of the Einstein frame and it has been use $\tilde{R}$ with a tilde for the spherical sector in order to distinguish it from the metric Ricci curvature scalar.

It is important to note that selecting $\xi = 0$ corresponds to the case where $f(\mathcal{R}) = \mathcal{R}$, which corresponds to the theory of General Relativity. Consequently,

all the equations presented earlier transform into those discussed in Chapter 1 for a boson star within the framework of General Relativity.

4.2. Initial data

The initial data obtained in Chapter 3 is expressed in polar-areal coordinates, where the line element is given by the expression Eq. (3.11), rewriting it here

$$ds^2_{\rm pa} = -\mathcal{A}^2(x)dt^2 + \mathcal{B}^2(x)dx^2 + x^2 d\Omega^2 \quad , \tag{4.26}$$

To solve for the static configurations of boson stars, it is assumed that the scalar field can be expressed as $\Phi(x,t) = \phi(x)e^{i\omega t}$, where $\phi(x)$ is the radial distribution of the scalar field and ω is the frequency. The Einstein-Klein-Gordon system is then derived. The integration is done providing proper boundary conditions and using a fourth-order Runge-Kutta scheme with adaptive stepsize and a shooting method, which leaves $\Phi_0 \equiv \phi(x=0)$ as a free parameter. By solving this system, the metric functions $\mathcal{A}^2$ and $\mathcal{B}^2$, as well as the frequency ω and the radial distribution of scalar field $\phi(x)$, can be obtained. This results in a collection of static configurations of boson stars, each described by a different value of Φ_0. They are plotted in Figure 3.1 and Figure 3.2. We show mass profiles as function of the central scalar field, Φ_0, for five different values of the gravitational coupling ξ, two of them are positive, two negative and the zero value which is equivalent to General Relativity.

The grid used to compute the initial data is a equidistant grid with spatial resolution $\Delta x^{\rm pa} = 0.0025$. The mass of the distributions is computed using the Misner-Sharp expression Eq. (3.30). Notably, we find that the computed mass remains consistent in both frames. This is because the Misner-Sharp expression captures the mass that a distant observer would perceive, and when observations are made far away from the matter sources, the frames are effectively indistinguishable in terms of the computed mass.

The binding energy E_B, which is a crucial parameter in determining the fate of the boson star, can be calculated using the mass and number of particles in the Einstein frame, as this is the frame where the evolution of the system will be performed. Specifically, the binding energy is given by $E_B = M - \mu N$, where M is the Misner-Sharp mass.

Another crucial factor in determining its ultimate fate is its mass. Boson star configurations with a central field value Φ_0 lower than $\Phi_0(M_{\max})$ are expected to be stable over time, where $M_{\max}$ represents the maximum mass of the family of boson stars configurations with the same gravitational coupling ξ, that is each curve displayed in Figures 3.1 and 3.2. On the other hand, configurations with a central field value Φ_0 higher than $\Phi_0(M_{\max})$ are expected to be unstable. For the latter case, the fate of unstable boson stars depends on its binding energy. Specifically, the binding energy will determine whether the unstable configuration migrates to a stable one ($E_B < 0$) or if it disperses ($E_B > 0$). The interplay between the maximum mass and binding energy is critical in understanding the long-term stability and dynamical behavior of boson stars.

Nine different configurations have been studied, and their initial parameters are presented in Table 4.1. Each model's name is composed of two letters, where the capital letter indicates the boson star parameters used. Models with names starting with 'A' are expected to be stable, while those starting with 'B' and 'C' are considered unstable. The lowercase letter in each model's name represents one of the three different gravitational scenarios, $\xi = \{-0.1, 0 \equiv \text{General Relativity}, 0.1\}$, denoted by 'n', 'z', and 'p', respectively. We could have chosen other magnitude for ξ however qualitatively its dynamic evolution will not experience any difference. We have chosen as magnitude for the gravitational coupling parameter $|\xi| = 0.1$ since it is high enough to make visible any difference with respect to General Relativity while being one order of magnitude suppressed. Configurations with any other value for $|\xi|$ would have experienced different behavior quantitatively but not qualitatively.

Model	ξ	$\Phi(x=0)$	ω	M	$E_B = M - \mu N$
An	-0.1	0.02	0.95392	0.47925	-0.00692
Az	0.0 (GR)	0.02	0.95419	0.47514	-0.00679
Ap	0.1	0.02	0.95445	0.47108	-0.00665
Bn	-0.1	0.1	0.82241	0.62571	-0.01758
Bz	0.0 (GR)	0.1	0.82296	0.62180	-0.01775
Bp	0.1	0.1	0.82350	0.61787	-0.01790
Cn	-0.1	0.18	0.75311	0.53922	0.00576
Cz	0.0 (GR)	0.18	0.76904	0.50671	0.01353
Cp	0.1	0.18	0.77840	0.48574	0.01780

Table 4.1.: Parameters for nine initial boson star configurations. In each column respectively we show the model name, its gravitational coupling factor, the value of the scalar field at $x = t = 0$, its frequency, the Misner-Sharp mass associated to this configuration and the binding energy in both frames. Mind that if $\xi = 0$ the gravitational framework is General Relativity.

4.3. Numerical method

Since the initial boson star configurations are obtained in polar-areal coordinates while the time evolution is carried out using the numerical code `NADA1D` which employs isotropic coordinates [144], a change of coordinates is necessary. By comparing equations Eq. (4.1) and Eq. (4.26), we can deduce that

$$\mathcal{B}^2(x_{\rm pa})dx^2_{\rm pa} = e^{4\chi(t,x)}a(t,x)dx^2 \quad , \tag{4.27}$$

$$x^2_{\rm pa} = e^{4\chi(t,x)}b(t,x_{\rm pa})x^2_{\rm pa} \quad . \tag{4.28}$$

Here, $x_{\rm pa}$ and x represent the radial coordinates in polar-areal coordinates and isotropic coordinates, respectively. Since the change of coordinates is performed before the time evolution begins, i.e., at $t = 0$, the metric functions can be set

as $a(0,x) = b(0,x) = 1$. Combining the two previous equations, we obtain

$$\frac{dx}{dx_{\rm pa}} = \mathcal{B}(x_{\rm pa})\frac{x}{x_{\rm pa}} \quad . \tag{4.29}$$

From the fact that the spacetime resembles the Schwarzschild spacetime far away from the object, we can deduce that

$$x^{\rm max} = \left[\left(\frac{1+\sqrt{\mathcal{B}(x_{\rm pa}^{\rm max})}}{2}\right)^2 \frac{x_{\rm pa}^{\rm max}}{\mathcal{B}(x_{\rm pa}^{\rm max})}\right] \quad , \tag{4.30}$$

which will be used as the initial value to solve Eq. (4.29). For further details about this calculation, we refer the reader to Appendix D of [54]. Upon establishing the change of coordinates, we can then proceed to calculate the initial conformal factor $e^{4\chi}$ in isotropic coordinates, which is given by the expression

$$e^{4\chi(0,x)} = \left(\frac{x_{\rm pa}}{x}\right)^2 \quad . \tag{4.31}$$

This allows us to establish the relationship between the conformal factor and the radial coordinates in the initial state of the system.

Once the coordinate transform has been carried out, we can determine the initial values of the scalar field quantities in isotropic coordinates. Specifically, we obtain the values of $\Phi(t=0,x)$, $\Psi(t=0,x)$, and $\Pi(t=0,x)$.

After transforming the polar-areal grid into an isotropic grid we interpolate with a cubic-spline over the radial coordinate in order to have the initial configuration on a two patch composed grid. A geometrical progression in the interior part up to a given radius and a hyperbolic cosine outside. Details about the computational grid can be found in [145]. For the logarithmic grid the minimum resolution used is $\Delta x = 0.025$. With this choice the inner boundary is then set to $x_{\rm min} = 0.0125$ and the outer boundary is placed at $x_{\rm max} = 8000$.

The time step is given by $\Delta t = 0.3\Delta x$ in order to obtain long-term stable simulations.

The BSSN equations are solved numerically using a second-order Partially Implicit Runge-Kutta (PIRK) scheme [43, 44]. This scheme can handle in a satisfactory way the singular terms that appear in the evolution equations due to our choice of curvilinear coordinates. It is implemented in the `NADA1D` code described in [144]. Further details about the numerical method can be found in [49].

In Appendix A a convergence analysis of the simulations performed here is reported.

4.4. Stable models

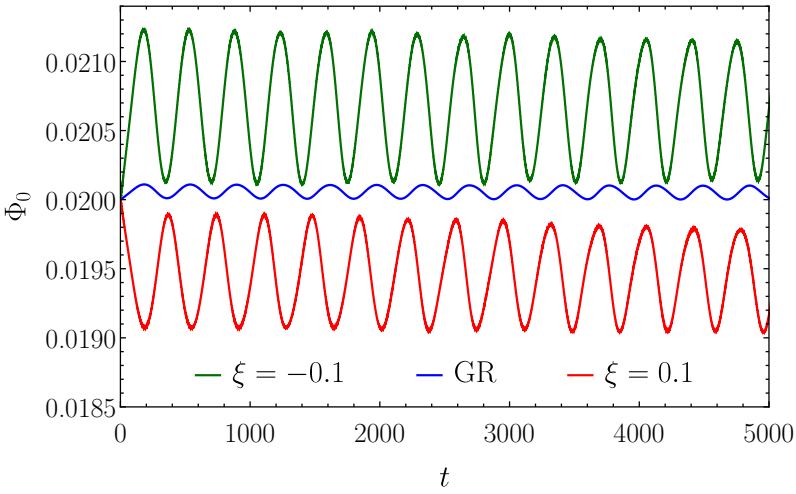

Figure 4.1.: Time evolution of the central value of the scalar field for An, Az and Ap models.

The fate of a boson star is determined by the maximum mass of its static configurations, as previously discussed. Specifically, initial configurations with

a central value of the scalar field lower than $\Phi_0(M_{\max})$ are expected to exhibit stable evolution.

The time evolution results for models An, Az, and Ap are depicted in Figure 4.1. The plot illustrates the temporal behavior of the central value of the scalar field, denoted as $\Phi_0(t) \equiv \sqrt{\mathrm{Re}[\Phi(x=0,t)]^2 + \mathrm{Im}[\Phi(x=0,t)]^2}$. Remarkably, considering that $f_{\mathcal{R}}(x=0) \neq 0$ and based on the conformal relation between metrics given by Eq. (3.4), it follows that $\Phi_0 \equiv \Phi(x=0) = \Phi(r=0)$. Despite all three configurations having the same initial value for the scalar field at the center, $\Phi_0(t=0) = 0.02$, the frequencies of the scalar field differ due to the distinct gravitational theories in which they are described, as shown in Table 4.1.

In the context of General Relativity, i.e. in the evolution of the model Az, it is expected that a stable boson star would be observed, with the central value of the scalar field remaining constant. However, due to discretization errors associated with the numerical grid used in the time evolution, physical quantities, including the central value of the scalar field Φ_0, instead exhibit oscillations around an equilibrium value. In our particular simulation with the used resolution, the amplitude of these oscillations is found to be $\Delta\Phi = 5 \times 10^{-5}$.

Qualitatively, the same kind of oscillatory behaviour is found in $f(\mathcal{R})$ gravity. However, interestingly, the amplitudes of the oscillations are significantly larger in $f(\mathcal{R})$ gravity (see green and red curves in Fig. 4.1). For the models An and Ap, the amplitudes are measured to be $\Delta\Phi = 6.2 \times 10^{-4}$ and $\Delta\Phi = 4.7 \times 10^{-4}$, respectively. Notably, the amplitude of the oscillations is found to be proportional to the gravitational coupling parameter ξ, indicating a dependence on the specific gravity model being considered. Furthermore, there is a phase shift observed in the Ap model compared to the other two models, causing the oscillations to shift downwards.

To study the impact of the polar-areal grid resolution on the amplitude of the oscillations, we also performed numerical simulations by systematically varying the resolution of the grid used for computing the initial data. The results are displayed in Figure 4.2, which is similar to Figure 4.1, but shows data

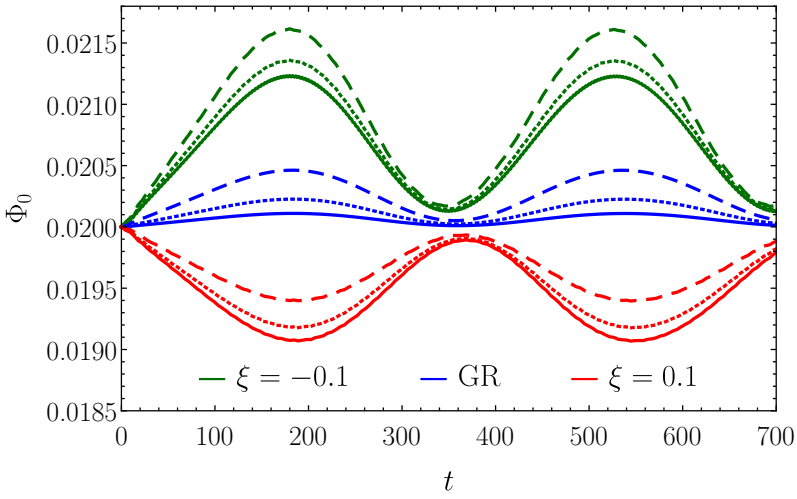

Figure 4.2.: Comparison of the time evolution of the scalar field central value for An (green lines), Az (blue lines) and Ap (red lines) models with three different grid resolutions for the initial data. Solid line $\Delta x_{\rm pa} = 0.0025$, dotted line $\Delta x_{\rm pa} = 0.005$ and dashed line $\Delta x_{\rm pa} = 0.01$.

for three different grid resolutions and in a shorter time span. We observe that the amplitude of the oscillations strongly depends on the resolution. From our convergence analysis, for models An and Ap the oscillation seems to tend to a finite value as the resolution becomes finer rather than disappearing. This is in contrast to General Relativity models, for which the oscillation decreases with resolution as expected. The reason behind this effect is that, when non-linear terms in the matter Lagrangian are present the change of coordinates and subsequent interpolation introduce a larger source of numerical error that we cannot get rid of at these resolutions, which contributes to the amplitude of the mentioned oscillations. However, the qualitative output of the simulation remains unaffected, as the amplitude of the oscillations is only up to 3% of the total scalar field amplitude for a polar-areal grid resolution $\Delta x_{\rm pa} = 0.0025$.

By performing several evolution with different resolutions, we are able to infer the convergence order of the code with respect to the polar areal grid, which is of first order. This loss of convergence is due to the change of coordinates from

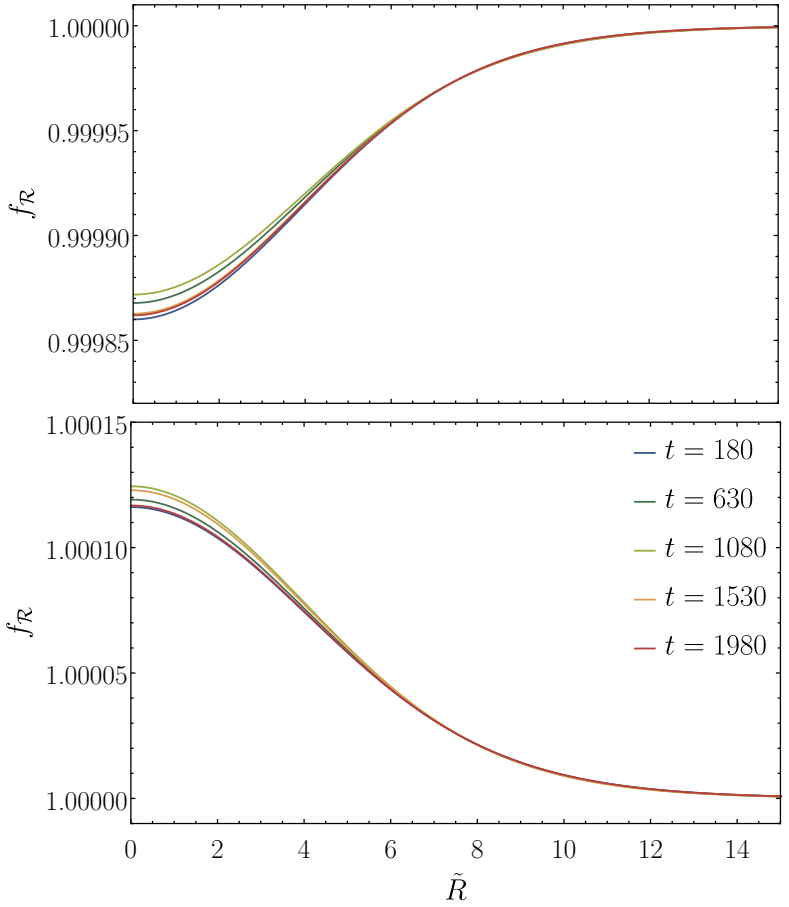

Figure 4.3.: Radial profiles of the conformal factor for models An (upper panel) and Ap (bottom panel) at selected evolution times.

polar-areal to isotropic, also observed in [49] (see also the related discussion in [2]). Moreover, since we do not further change Δx_{pa} in the simulations, increasing the isotropic grid resolution for the computation of the initial data does not lead to an improved convergence. We refer the reader to Appendix A for details on the convergence analysis of the evolution code.

Regarding the behavior of the space-time variables in different theories, we depict in Figure 4.3 radial profiles of the conformal factor $f_{\mathcal{R}}$ for models An

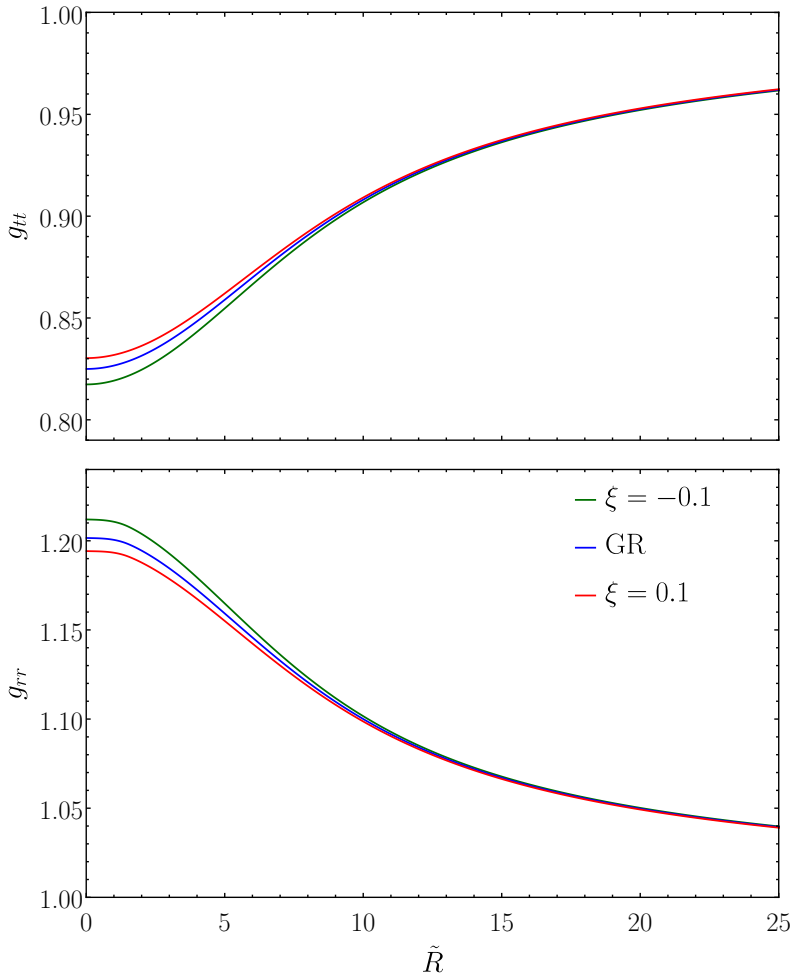

Figure 4.4.: Radial profile of the g_{tt} and g_{rr} metric functions for the models An and Ap at $t = 1575$.

and Ap at selected evolution times. To express the radial position in terms of variables within the $f(\mathcal{R})$ frame, we employ the area of the two-spheres $\tilde{R}^2$ as a pseudo-coordinate due to the absence of an explicit expression for r. As one can observe deviations from unity are only noticeable for points close to the boson star center, where the maximum of the energy density is located, and even in this case it is a minute difference. This suggests that the disparity

between the metrics of both frames will be minimal. It can also be noticed that the conformal factor exhibits oscillations of a similar nature as those previously discussed for the maximum of the scalar field Φ_0. The amplitude of these oscillations is about 10^{-5}. Furthermore, the opposite signs of the coupling parameter ξ affect the radial profile of $f_{\mathcal{R}}$ in opposite ways for both models. Specifically, the negative sign of ξ (top panel in the figure) tends to enlarge the conformal factor close to the boson star's center, while the opposite effect is observed for $\xi = 0.1$.

Next, in Figure 4.4 we show the radial profiles of the metric functions at $t = 1575$ for models An and Ap. Those exhibit a behavior reminiscent to the boson star profiles in the case of General Relativity. For both models, the metric function g_{tt} starts from a finite positive value below 1, gradually increasing with radial distance and asymptotically approaching 1. As for the function g_{rr}, a similar behavior is observed, but with an initial value at the center of the star that is finite and greater than 1 and tending asymptotically toward 1. The discrepancy between the two models becomes visible only close to the center of the boson star. Though not shown here, these two functions are subject to the aforementioned oscillations as well.

4.5. Unstable models

Let us now discuss the temporal evolution of the Bn, Bz, and Bp models, which are located in the unstable branch and exhibit a negative binding energy. When the only perturbation to the initial data is the discretization error, we observe a migration of these unstable configurations towards the corresponding boson star with the same mass but located in the stable branch, as depicted in Figure 4.5. The initial data for all three models is set to have $\Phi_0 = 0.1$, and it evolves over time until reaching a configuration with $\Phi_0 \approx 0.055$, which corresponds to stars with approximately the same mass but situated in the stable branch.

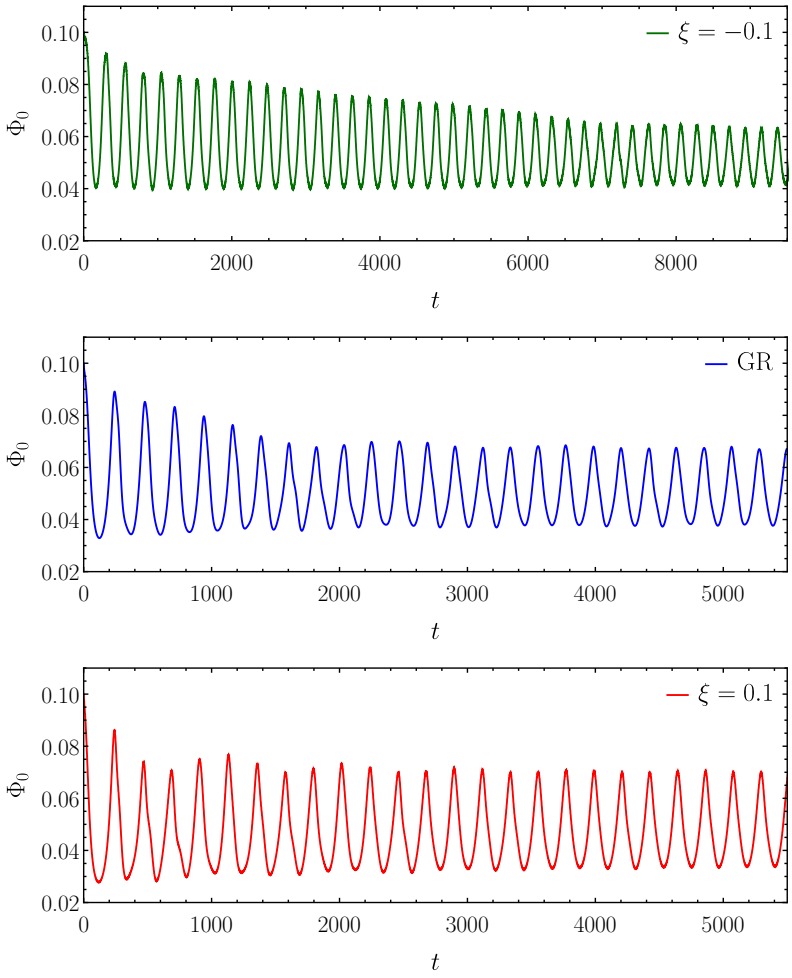

Figure 4.5.: Time evolution of the scalar field central value Bn, Bz and Bp models displayed at the top, middle and bottom panel respectively.

In Figure 4.6 we plot radial profiles of the conformal factor $f_{\mathcal{R}}$ at both the initial time and selected times during the evolution. This figure shows that the initial configuration of the conformal factor exhibits a significant deviation from unity, which gradually diminishes over time. Specifically, for model Bn (top panel), the value of the conformal factor at the center of the boson star initially exceeds unity but decreases below 1 as the system approaches a stable

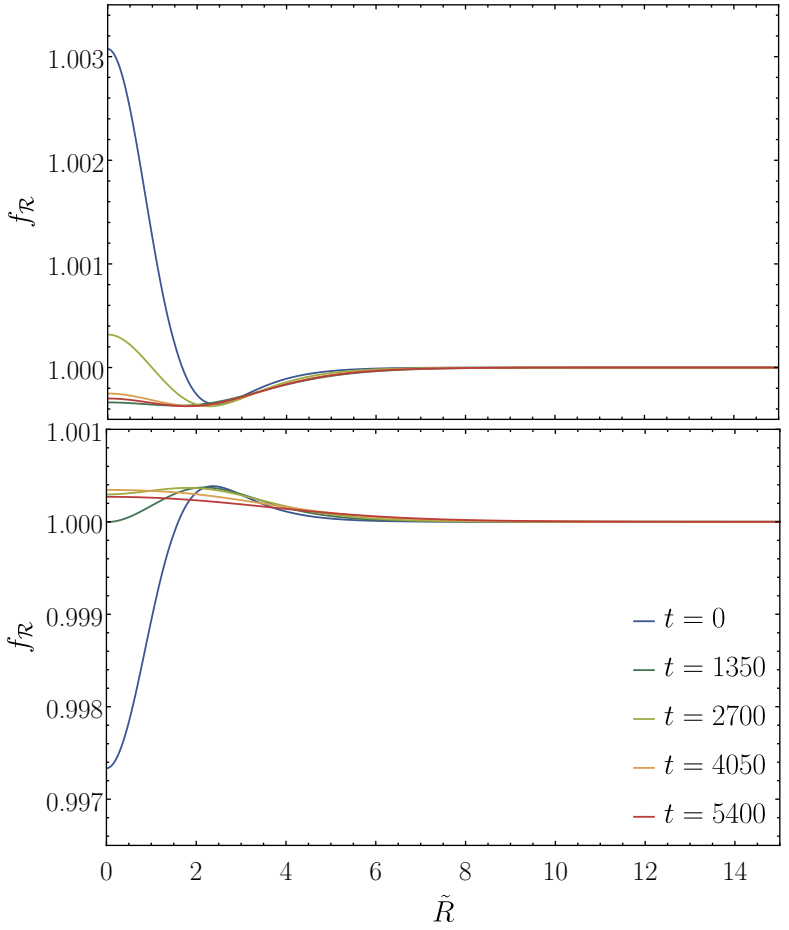

Figure 4.6.: Evolution of the radial profiles of the conformal factor for models Bn (upper panel) and Bp (bottom panel).

configuration. Conversely, in the case of model Bp (bottom panel) the conformal factor follows the opposite trend. However, it is important to note that the conformal factor consistently approaches one asymptotically, either increasing for the Bn model or decreasing for the Bp model. Additionally, we show in Figure 4.7 the radial profiles of metric functions g_{tt} and g_{rr}. The central values of both metric functions transition towards one during the evolution. We also note that both the conformal factor and the metric functions exhibit oscillations,

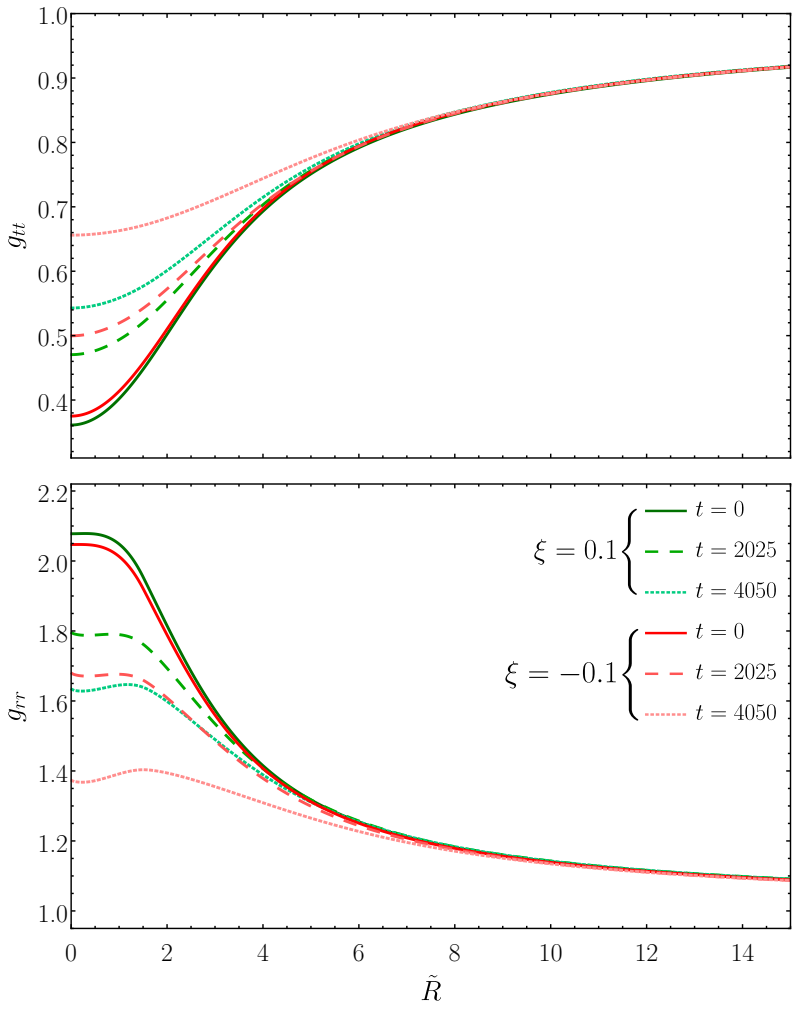

Figure 4.7.: Radial profile of the g_{tt} and g_{rr} metric functions for the models Bn and Bp.

which become more apparent when observing the central values over time, as shown in Figure 4.5.

Turning our attention towards the time evolution of C models, characterized by initial data $\Phi_0 > \Phi_0(M_{\max})$ and a positive binding energy $E_B > 0$. These models, denoted as Cn, Cz, and Cp, respectively, are representative of different

gravitational theories and are also summarized in Table 4.1. The evolution of the central value of the scalar field, Φ_0, is depicted in Figure 4.8. It is observed that Φ_0 rapidly decreases with time, leading to a drastic radial expansion of the boson star, which ultimately disperses away. Similar behavior is observed for all three models, although slight quantitative differences exist in the evolution of the central value of the scalar field.

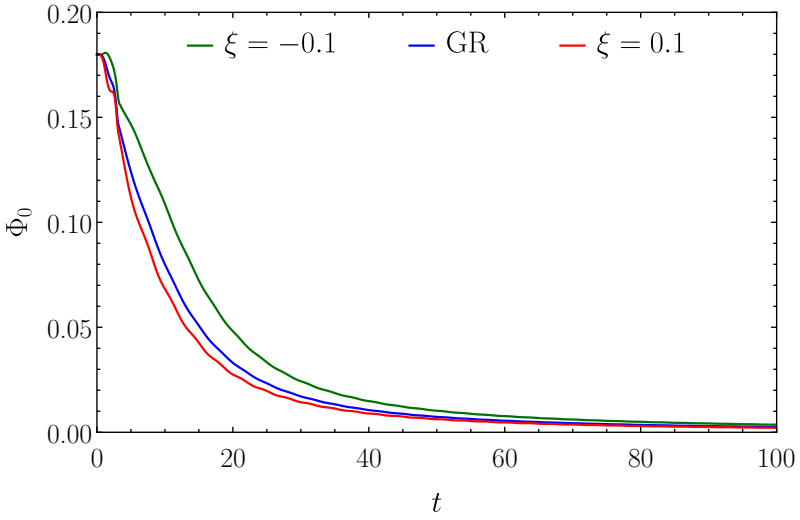

Figure 4.8.: Time evolution of the scalar field central value Cn, Cz and Cp models.

Let us now come back on the B models. However, if we do not rely on discretization error but truly perturb the initial data for the Bn, Bz, and Bp models, the resulting dynamics can be markedly different. In particular, we can trigger the gravitational collapse of the boson stars, as first shown in [2]. To do so, once we have solved the Einstein-Klein-Gordon system, which provides the initial data for the evolution, we multiply the radial profile of the scalar field by 1.02, i.e., we add a 2% perturbation to this profile (3% for the Bp model). This results in a slight violation of the constraints in polar-areal coordinates. After adding the perturbation we do not recompute the spacetime variables $\mathcal{A}$ and $\mathcal{B}$. This decision is based on the observation that it only leads to a 3% increase in the magnitude of the Hamiltonian constraint violation in regions near the

center, when compared to the unperturbed case. We note that the introduced perturbation is larger than the one associated with the discretization error, but small enough not to substantially alter our original solution. Once the perturbed scalar field has been obtained, we re-compute the remaining scalar field quantities for the BSSN evolution.

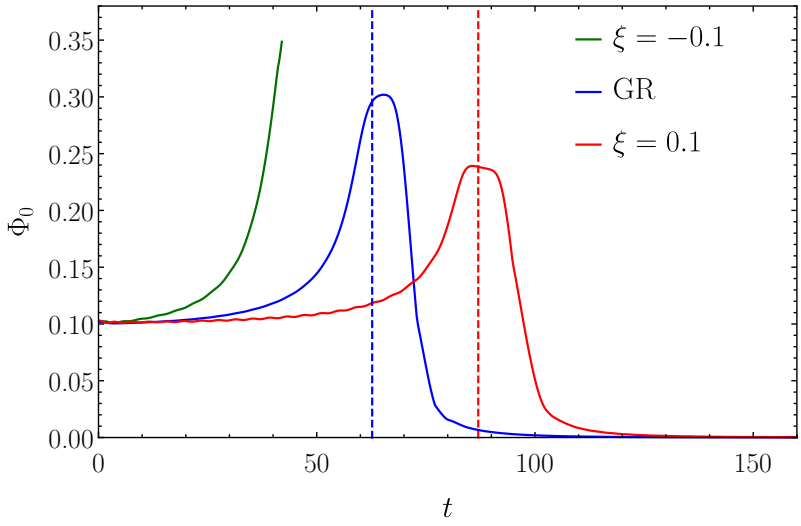

Figure 4.9.: Time evolution of the scalar field central value Bn, Bz and Bp models with a perturbation. In dashed lines we point out the moment in which an apparent horizon is formed for each model.

Figure 4.9 shows the evolution of the central value of the scalar field for all three perturbed B models. When evolving these configurations with a perturbation in General Relativity (blue curve), the outcome is the gravitational collapse of the boson star and the formation of a black hole [49]. The central scalar field is seen to grow up to a maximum value to then decay when an apparent horizon appears, which is signaled with a vertical blue dashed line in Fig. 4.9. It is computed using the apparent horizon finder described in [146]. The mass of the resulting black hole is slightly smaller than the mass of the initial boson star, since some amount of the scalar field is not swallowed by the black hole. This results in a long-lived cloud of scalar field around the black hole (see [49] for further details).

Upon analyzing the gravitational collapse of the Bn model, we observe that after a few time steps, the code stops. If we examine the conformal factor during this evolution, we can observe that it grows rapidly and eventually leads to a divergence. This is due to the fact that the condition $1-2\kappa\xi Z=0$ is being met. Similarly, we find that the equations governing the scalar field evolution also diverge. If we examine Eq. (4.18), we can see that $1-2\kappa\xi Z$ appears as a denominator. The divergence of Π would also induce divergences in Φ and Ψ. Thus, we are unable to accurately predict the outcome of the gravitational collapse for $\xi=-0.1$ using the formalism presented here.

For the Bp model, the gravitational collapse results in the formation of a black hole surrounded by a cloud of scalar field, similar to the Bz case. However, the innermost region of the collapsing object exhibits the formation of a finite-size, exponentially-expanding baby universe connected with the outer universe via a throat. This cosmic bounce scenario is always hidden under a horizon. Given the implications and significant importance of this case, we will delve into a more detailed analysis of the gravitational collapse of the Bp model in the following chapter.

As we have seen, studying the time evolution of boson stars in Palatini $f(\mathcal{R})$ gravity reveals notable differences compared to General Relativity models. These differences emphasize the profound influence of the gravitational theory on the behavior and ultimate fate of boson stars both for stable and unstable boson stars. Further, additional research is needed to obtain the initial data in an isotropic grid in order to get rid of the coordinates transformation and consequently minimizing the sources of numerical error.

Chapter 5.

Birth of baby universes

The formation of singularities under reasonable initial conditions in General Relativity [147–149] has been the driving force of multiple efforts to understand the nature and implications of these pathologies and also of possible mechanisms that could avoid them. Quantum approaches and phenomenological descriptions [150–154] suggest that our expanding universe could come from a previously contracting phase and that geodesic completeness in black hole geometries could be restored, among other possibilities [155], via a bounce in the radial sector, leading generically to the existence of minimal nonzero bounds to the area/volume in which matter fields can be concentrated. In this sense, the classical collapse model of Oppenheimer and Snyder [156] offers a glimpse on how a nonsingular collapse process could proceed. The innermost region of the collapsing object could be modeled as a contracting cosmology which would bounce at a certain critical density, preventing total collapse. The evolution of the bouncing material should depend crucially on the formation or not of a horizon, because the causal structures in both cases are radically different. Without a horizon, the collapsing material should be ejected back to where it came from, though the energy scales expected in such a quantum gravity process have never been observed. If a horizon forms, the bounce should proceed much more quietly for an external observer, as the interior would be causally disconnected from it. What may happen inside is still a matter of speculation.

In this chapter, based on the publication [2], we consider the gravitational collapse of boson stars in Palatini quadratic $f(\mathcal{R})$ gravity, that is known to provide bouncing cosmological solutions [132]. This theory is also intimately related to effective descriptions of nonsingular models of quantum gravity [157, 158].

5.1. Initial data and methodology

To perform the numerical simulation, we employed the methodology outlined in Chapter 4. The stellar model studied is the Bp model, as outlined in Table 4.1. This particular model is characterized by its instability, with a positive gravitational coupling parameter $\xi = 0.1$.

While the General Relativity case (Bz model) and the $\xi = -0.1$ case (Bn model) required a perturbation of only 2% to initiate gravitational collapse, our investigation revealed that the Bp model discussed in this study exhibited a greater threshold for perturbation. In order to trigger collapse in the Bp model, a 3% perturbation was needed. The Bp model displays enhanced robustness against perturbations, capable of withstanding and accommodating higher levels of disturbance.

The mentioned perturbation leads to a slight violation of the Hamiltonian constraint, only 3% higher than the unperturbed case. The resolution of the polar-areal grid has been increased with respect to the other scenarios considered in the previous Chapter in order to improve the output ($\Delta x_{\rm pa} = 0.0025$). In the same sense, to properly capture the highly non-linear, strong-field dynamics of the system close to the center of the star (see below) a fairly small minimum resolution is required for the isotropic logarithmic grid, namely $\Delta x = 1.25 \times 10^{-3}$. With this choice, the inner boundary is placed at $x_{\rm min} = 6.25 \times 10^{-4}$ and the outer boundary at $x_{\rm max} = 1500$, using a grid with 2×10^4 zones. A time step that satisfies the Courant-Friedrichs-Lewy condition is chosen to obtain long-term stable simulations, $\Delta t = 0.3 \Delta x$.

We have reported in Appendix A a convergence analysis of the numerical simulations performed here.

5.2. Outcome

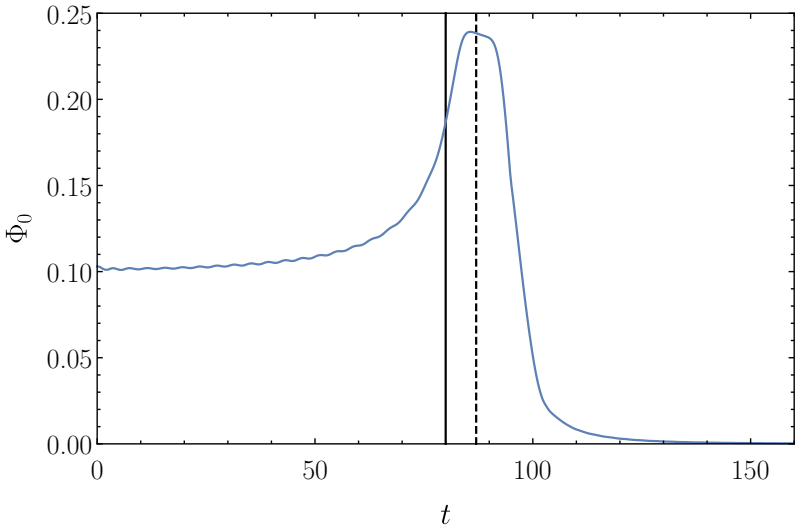

Figure 5.1.: Time evolution of the central value of the scalar field. The black solid line indicates the instant at which the event horizon forms ($t \approx 80$) while the black dashed line is the time at which the apparent horizon is found ($t \approx 87$).

We start analyzing the dynamics of the collapse in the Einstein frame (i.e. the General Relativity problem Eq. (3.7)). Figure 5.1 shows the evolution of the central value of the scalar field Φ_0. This quantity grows up to a maximum to then decay when an apparent horizon appears. The figure also depicts the instant at which the event horizon forms. The apparent horizon, defined as the outermost closed surface on which all outgoing photons normal to it have zero expansion, is a local notion and can be monitored on each time step. On the contrary, the event horizon is computed *a posteriori* tracing backwards the last trapped null geodesic [159]. The apparent horizon is first found at time $t \approx 87$

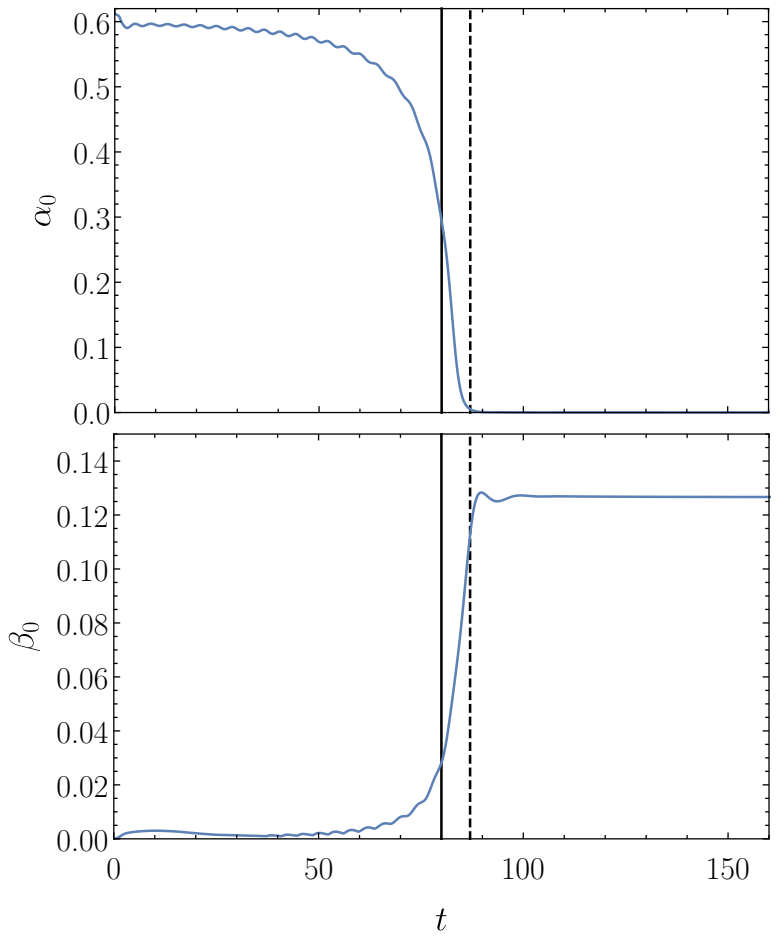

Figure 5.2.: Time evolution of the central values of the lapse function (upper panel) and of the shift vector (bottom panel). The black solid line indicates the instant at which the event horizon forms ($t \approx 80$) while the black dashed line is the time at which the apparent horizon is found ($t \approx 87$).

and its mass, in units of $M_{\rm Pl}/\mu$, is $M_{\rm AH} = 0.61831$, slightly lower than the Misner-Sharp mass of the initial boson star, $M = 0.61918$. Figure 5.2 displays the time evolution of the central value of the lapse function, α_0, showing the distinctive collapse-of-the-lapse once the horizon forms. In addition, the shift vector at the origin β_0 attains non-zero values. The behavior of both α_0 and

β_0 reflect the singularity-avoiding slicing employed in the simulation and the presence of a singularity at the origin. The small-amplitude oscillations of Φ_0,

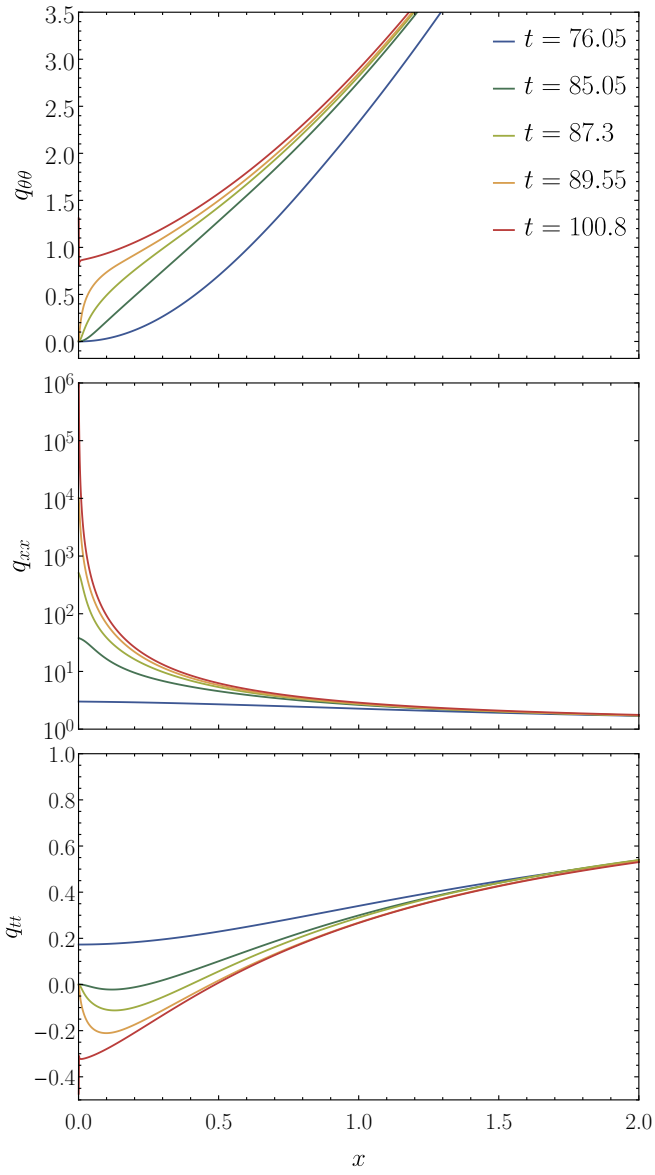

Figure 5.3.: Five snapshots at different times of the metric functions $q_{\theta\theta}$, q_{xx} and q_{tt}.

α_0 and β_0 during the collapse are induced by the non-linearities of the $f(\mathcal{R})$ matter Lagrangian.

In 5.3 we show that the slicing condition chosen also affect the $q_{\theta\theta}$ function, which finds a limit value after the apparent horizon has been formed. The metric function q_{xx} grows rapidly near the center when the collapse starts, reaching values that are several orders of magnitude higher than the initial one. On the other hand, q_{tt}, that initially is everywhere positive, decreases changing sign and approaching zero from below at the center. Therefore, all metric functions mark the presence of a black hole. In the matter sector, almost all of the scalar field is swallowed by the black hole by the end of the simulation. However, a remnant of scalar field is left outside the apparent horizon in the form of a quasi-stationary long-lived cloud [49,160], as it is shown in Figure 5.4. This explains the small mass disparity between $M_{\rm AH}$ and M. We note that this evolution is qualitatively identical to that of a collapsing boson star in General

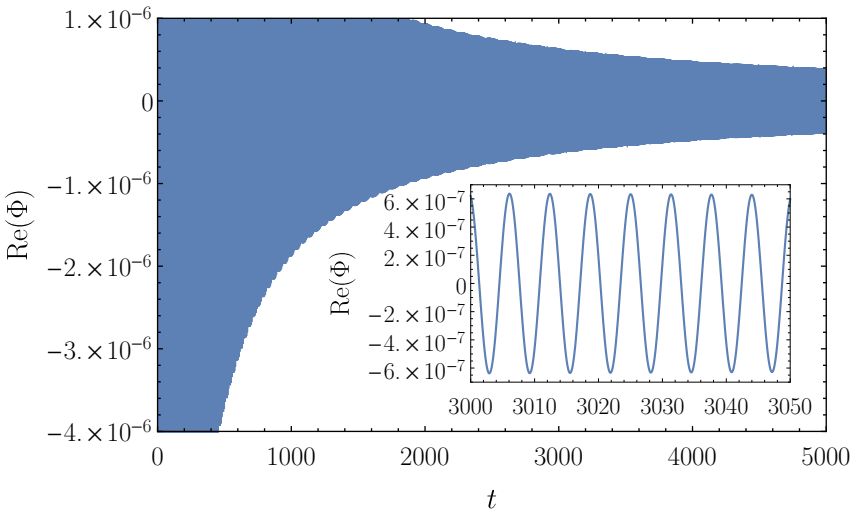

Figure 5.4.: Time evolution of the real part of the central value of the scalar field for the perturbed boson star model Bp. The insets show a magnified view of $t \in [3000, 3050]$ in the evolution to highlight the oscillatory behavior of the scalar field that lingers outside of the black hole.

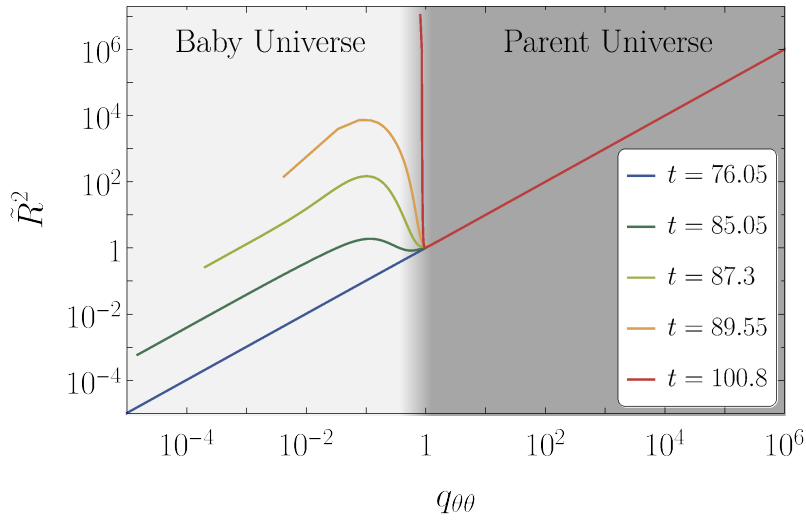

Figure 5.5.: Relationship between the area of the two-spheres in both frames at five selected times. The background indicates the regions referred to as *baby universe* and *parent universe*.

Relativity (without the $\xi\mathcal{R}^2$ term in the $f(\mathcal{R})$ functional). The outcome is also a black hole whose parameters are determined by the progenitor boson star model.

To analyze the evolution in the $f(\mathcal{R})$ frame, we need to pay special attention to the conformal factor $f_{\mathcal{R}}$ that relates the metrics in both frames via Eq. (3.4). As shown in Figure 5.5, at the onset and until $t \approx 80$, the area of the two-spheres of the $f(\mathcal{R})$ frame, $A \sim \tilde{R}^2$, decreases monotonically as the center[1] of the boson star is approached (blue curve). As the collapse proceeds and the energy density grows at the center, $f_{\mathcal{R}}$ evolves towards zero at a certain distance close to the center of the boson star. As a result, a local minimum arises in $\tilde{R}^2$ which is soon followed by a local maximum, whose height grows exponentially fast in time. The presence of a minimal two-sphere in $\tilde{R}^2$ can be interpreted as a cosmic bounce, i.e. as the hypersurface that connects the contracting two-spheres (from the apparent horizon inwards) with the expanding two-spheres

[1] In the Einstein frame, the center is where $q_{\theta\theta} = 0$.

of the newborn universe. This baby universe is thus growing out of the patch comprised between the minimal two-sphere and the boson star center. We will refer to the outer universe as *parent universe* while the term *baby universe* will be used for the inner expanding patch. Their corresponding areas are displayed in Figure 5.5. Following [161] the late-time phase of the collapse can thus be interpreted as generating a quasi-permanent inter-universe wormhole, with the bounce representing a kind of umbilical cord connecting the parent universe and the baby universe.

One can verify that radial null geodesics between the minimal and maximal spheres follow divergent trajectories, which refocus as they go from the maximal sphere towards the center. Due to numerical limitations associated with the singularity-avoiding slicing conditions used in the Einstein frame, we can not confirm if they converge at the center. In particular, the region between the center and the maximal sphere becomes unreachable beyond $t = 91.8$. In the time interval $t \in [84.6, 91.8]$ the expansion of the baby universe is exponential and superluminal, always preserving the original $\mathbb{R}^4$ topology.

Figure 5.6 displays embedding diagrams illustrating the late-time spacetime geometry through three representative snapshots. These diagrams were generated using the methodology outlined in [162, 163]. The procedure involves taking the line element Eq. (4.25) and setting t to a constant value and θ to $\pi/2$. The resulting metric induced on this specific hypersurface is

$$\begin{aligned} ds^2_\Sigma =& g_{rr}(r)dr^2 + \tilde{R}^2(r)d\varphi^2 \\ =& dl^2 + \tilde{R}^2(l)d\varphi^2 \quad . \end{aligned} \tag{5.1}$$

Through a coordinate transformation, given by $dl^2 = g_{rr}(r)dr^2$, the integration of which yields

$$l(r) = \int_0^r \sqrt{g_{rr}(r')}dr' \quad . \tag{5.2}$$

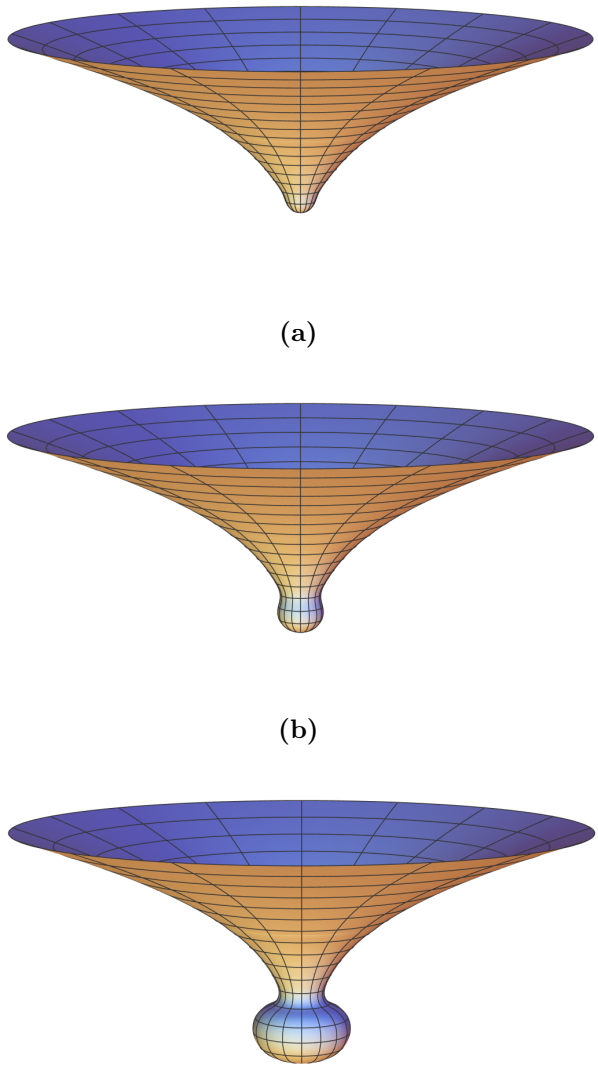

(a)

(b)

(c)

Figure 5.6.: Embedding diagrams of the late-time spacetime geometry at (a) $t = 83.7$, (b) $t = 84.6$ and (c) $t = 85.5$.

The metric in the embedding space takes the form

$$ds^2_{\text{emb}} = dz^2 + d\rho^2 + \rho^2 d\varphi^2 \quad . \tag{5.3}$$

By comparing both metrics, it becomes evident that they share the same radial and angular coordinates, denoted as $\rho = \tilde{R}$ and φ respectively. Consequently, we are left with the relationship

$$dl^2 = dz^2 + d\rho^2 \quad . \tag{5.4}$$

Rearranging the above equation leads to

$$z(l) = \int_0^l \sqrt{1 - \left(\frac{d\tilde{R}(l')}{dl'}\right)^2}\, dl' \quad . \tag{5.5}$$

Finally, the function $\tilde{R}(z)$ is obtained, as depicted in Figure 5.6.

The diagrams display an infinite parent universe connected to a finite baby universe through a throat. The bubble observed at the bottom part of the diagrams corresponds to the baby universe and its size grows exponentially with time. The time evolution of the position of the throat, apparent horizon, and event horizon in the $f(\mathcal{R})$ frame is displayed in Figure 5.7. The event horizon appears at $t \approx 80$, the throat at $t \approx 84.6$, with a nonzero finite area, and the apparent horizon at $t \approx 87$. Note that the position of the throat initially grows and then decreases towards an asymptotic value of $\tilde{R}^2 \approx 0.89$. This is a consequence of the slicing employed in the simulation since $\tilde{R}^2$, which is equivalent to $g_{\theta\theta}$, is calculated in terms of $q_{\theta\theta}$ and, as mentioned before, the area of the two-sphere does not cover the whole domain. In practice, $\tilde{R}^2$ approaches the smallest value of $q_{\theta\theta}$ available in the simulation. Since the area of the minimal two-sphere depends directly on the energy density of the scalar field, the slow absorption of the external scalar cloud indicates that it will eventually shrink to zero, closing the umbilical chord connecting the two universes. The evolution reveals that the throat is always hidden inside the event horizon, preventing light rays emitted at the baby universe from escaping to the exterior of the parent universe. Accordingly, distant external observers will not be able to tell if the outcome of the collapse is an ordinary black hole or a black hole with an inner expanding universe through electromagnetic observations.

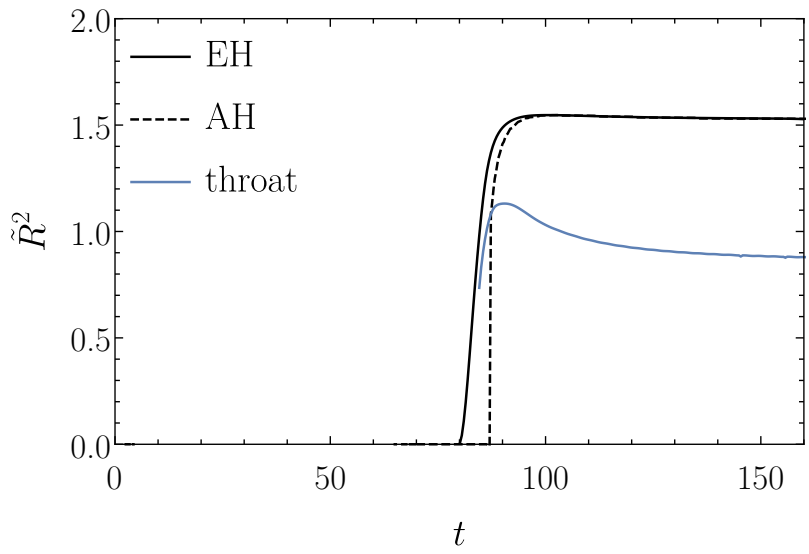

Figure 5.7.: Time evolution of the location of the throat, apparent horizon, and event horizon in the $f(\mathcal{R})$ frame using $\tilde{R}^2$ as pseudocoordinate.

Let us now proceed to discuss the temporal evolution of the metric functions, g_{rr} and g_{tt} of the $f(\mathcal{R})$ frame, as depicted in Figure 5.8. To express the radial position in terms of variables within the $f(\mathcal{R})$ frame, we employ the area of the two-spheres $\tilde{R}^2$ as a pseudocoordinate due to the absence of an explicit expression for r.

Before the formation of the throat and the subsequent wormhole structure, the metric functions approach the Schwarzschild solution at infinity and finite values at the center. It is observed that g_{tt} remains positive across its entire domain, as it is expected (blue line). Within the parent universe, the opening of the throat is coincides with a rapid increase in the value of g_{rr} near the throat, while g_{tt} experiences a decrease and even undergoes a sign change in close proximity to the same region.

Within the baby universe, g_{rr} initially has a finite value at the throat and exhibits nearly linear growth until reaching the point of maximum $\tilde{R}^2$ (middle panels). Subsequently, it remains relatively constant within the inner portion

of the baby universe (left panels). The exponential growth of g_{rr} in conjunction with the exponential expansion of spacetime establishes a linear relationship between g_{rr} and $\tilde{R}^2$. Similarly, a corresponding behavior is observed for g_{tt} with negative values. However, at the inner part of the baby universe g_{tt} tends toward zero.

Finally, it is worth noting that the line corresponding to $t = 100.8$ exhibits non-smooth behavior, primarily due to the finite resolution of the computational grid, resulting in numerical flaws. Additionally, due to the chosen slicing technique, the line corresponding to $t = 100.8$ is not visible within the inner part of the baby universe, and the others do not appear complete. It should also be mentioned that the blue line does not appear depicted in the baby universe because it is still not formed at that time.

Summing up, our analysis of the gravitational collapse of boson stars in a metric-affine modified gravity scenario indicates that new dynamics able to trigger dramatic deformations of the space-time structure may be excited at very high energy densities. We have seen that a small patch of space can inflate giving rise to an exponentially growing baby universe. This universe expands at superluminal speed and the minimal surface is sustained by the energy density of the scalar field, which leaks in from a quasistationary cloud that remains bounded around the black hole. This exterior solution is consistent with previous results in the literature of General Relativity [50, 164] and the numerical evolution suggests that the minimal area will decay to zero when the scalar cloud is completely absorbed by the black hole. In our model, this occurs in parallel with the development of an apparent horizon, making the internal process analogous to a cosmic bounce and preventing its observation by external observers. During the stationary phase, the spacetime is qualitatively in agreement with results from the loop quantization of black holes [165], heuristic *black bounce* models [166, 167], and other static solutions [168, 169], though always preserving an Euclidean topology.

These new features persist for all values of the gravitational coupling parameter ξ and for other scalar field central amplitudes Φ_0 as long as they are in the

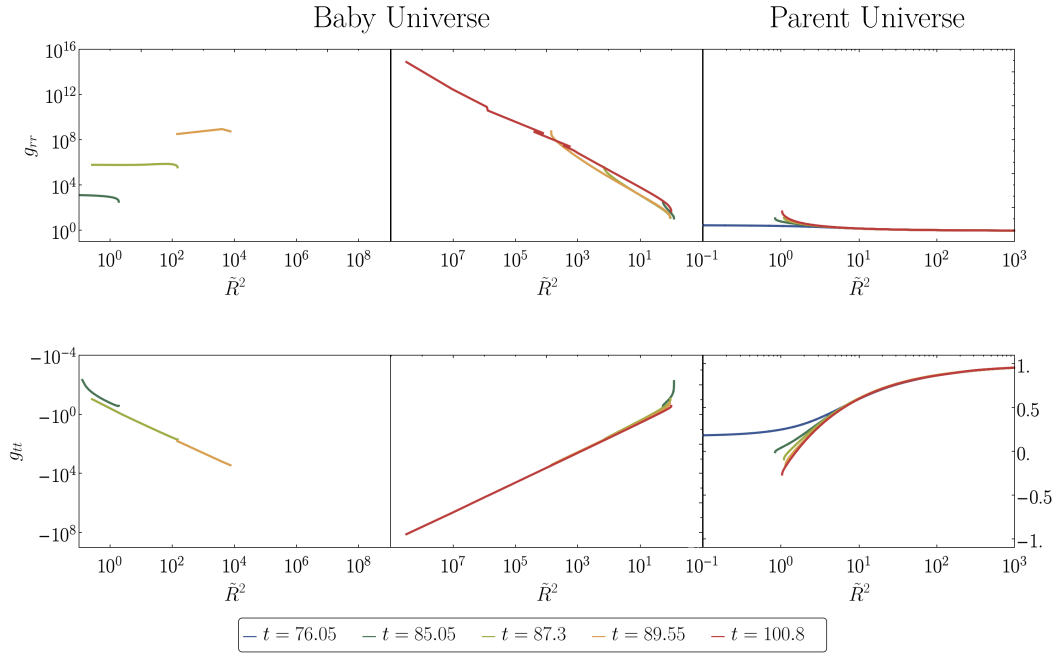

Figure 5.8.: Five snapshots at different times of the metric functions g_{tt} and g_{rr}. The left panel illustrates the inner section of the baby universe, spanning from the central point to the local maximum of the 2-sphere area. The central panel showcases the outer part of the baby universe, extending from the local maximum of the 2-sphere area to the throat. Finally, the right panel pertains to the parent universe, encompassing the region from the wormhole throat to asymptotic infinity.

unstable branch and the perturbation is high enough to excite the gravitational collapse. The fact that metric-affine theories lead to cosmic bounces quite generically suggests that other forms of matter, such as unstable neutron stars, and other gravity theories could lead to outcomes similar to those presented in the current chapter[2]. In this sense, we note that the density-dependent modified dynamics of Palatini theories is also present in some instances of scalar-tensor

[2]Cosmic bounces may also occur in theories in which the relation between the metrics $g_{\mu\nu}$ and $q_{\mu\nu}$ is not conformal [117, 119], which lie beyond the $f(\mathcal{R})$ family. Moreover, the torsion in Einstein-Cartan theories can also induce cosmic bounces [170].

theories of the Horndeski type (compare [171] and [172]). This suggests that the phenomenology that we find here in the Palatini $f(\mathcal{R})$ framework could also be present in other relevant gravity theories, which deserves further independent analysis.

We have seen that the throat area shrinks as the external quasi-stationary scalar cloud is absorbed, suggesting that it will eventually close. However, numerical limitations do not allow to establish a direct correlation between the throat area and the density of the scalar field across it at late times.

Part II.

Wormholes

Chapter 6.

Historical approach to wormholes

The emergence of wormhole-like structures in the context of gravitational collapse in Palatini $f(\mathcal{R})$ gravity, shown in Chapter 5 has captured our interest in these intriguing phenomena. Our aim is to expand our understanding of wormhole structures and their features in various astrophysical scenarios.

Wormholes [161, 173, 174], extensively portrayed in science fiction, are topological structures that allow the connection of distant points in space and time. Acting as shortcuts through the fabric of spacetime, they enable effectively superluminal travel between remote locations, although the speed of light is not surpassed locally.

The study of wormholes lies at the interface between General Relativity and Quantum Physics, where speculation finds fertile ground and the interplay of quantum and astrophysical effects takes center stage. As we are pointing out, due to their elusive nature, the existence of these structures remains a topic of speculation. Numerous completely valid arguments can be held against their existence, leading to legitimate skepticism. Nevertheless, investigating wormholes offers an avenue to explore the foundational aspects of the currently accepted theories and expand our understanding of the underlying reality while pushing the boundaries of our current models. Despite their speculative nature, they are grounded in the firmly established frameworks of Quantum Physics and General Relativity. Though the final implications might seem unconventional,

speculative, controversial, or purely theoretical, researching wormholes deserves attention due to the valuable insights they can offer into the boundaries and limitations of the underlying theoretical frameworks.

Moreover, the enormous implications of the existence of wormholes requires a rigorous analysis of their consistency as theoretical solutions and a careful consideration of their empirical implications. One of our tasks as theoretical physicists is thus to understand the conditions under which objects of this type could be experimentally accessible. Engaging in speculations of scenarios that lie beyond experimental reach is in clear contradiction with the principles of the scientific method, and this is clearly not our purpose. In fact, the study of wormholes and their observational features is as rigorous a study as the properties of black holes and of other compact objects, such as neutron stars or white dwarfs. This is so because in all such scenarios, one is facing strong gravity effects, with peculiar signatures that characterize each specific object.

Lastly, it is pertinent to mention that in the conventional approach to solving the equations of a given gravitational system, one typically begins with a reasonable description of the matter sources and then employs the Einstein field equations to derive the corresponding spacetime geometry. However, when dealing with wormhole configurations, the process has been traditionally implemented the other way around, namely, a geometry with some desired properties is proposed and then the Einstein field equations are used to derive the corresponding matter distribution. A popular argument in favor of this approach is that an absurdly advanced civilization should be able to find the energy sources needed to produce that geometry, transferring the problem to the engineering side.

In this chapter, our main goal is to thoroughly explore the concept of wormholes and how it has evolved over time, starting from its introduction by Einstein and Rosen to its current interpretation in modern physics. We'll delve into the fundamental theories and important milestones that have contributed to our understanding of these fascinating topological structures.

6.1. Einstein-Rosen bridge

After Schwarzschild's publication of his solution to Einstein's equations in 1916 [175, 176], Flamm initiated the study of these solutions in the same year and presented an analysis [177]. In this work, he provided the initial insights into what is now recognized as a wormhole, although he did not actively consider this possibility and did not extend his study in this direction [178]. The pivotal breakthrough occurred in 1935 when Einstein and Rosen began to work with the concept now known as *wormhole*, which they introduced as a *bridge* [179]. Their primary objective was to develop a framework capable of describing the nature of particles while avoiding the presence of singularities, since classical particles conventionally involve an abstraction where their mass is confined to a single point, leading to geodesic singularities. In their manuscript, Einstein and Rosen considered charged and also neutral particles. The former is built using the Reissner-Nordström solution while the latter follows from the Schwarzschild one.

In order to construct the (neutral) Einstein-Rosen bridge, we start from the Schwarzschild solution in vacuum

$$ds^2 = -\left(1 - \frac{2M}{r}\right) dt^2 + \frac{1}{1 - 2M/r} dr^2 + r^2 d\Omega^2 \quad . \tag{6.1}$$

By introducing the coordinate transformation $u^2 = r - 2M$, the line element transforms as

$$ds^2 = -\frac{u^2}{u^2 + 2M} dt^2 + 4\left(u^2 + 2M\right) du^2 + (u^2 + 2M)^2 d\Omega^2 \quad . \tag{6.2}$$

This choice of coordinates excludes the interior of the Schwarzschild domain $r \in [0, 2M)$ while covering the asymptotic region twice $r \in [2M, \infty)$. Then, the new coordinates span from $u \in (-\infty, \infty)$ and encompass the exterior of the Schwarzschild region twice. For a sphere at a fixed and unchanging time t =constant, the area of the sphere is governed by the spherical sector of the metric $A(u) = 4\pi(u^2 + 2M)^2$. Consequently, we note that the area of the two-

spheres defined in the Einstein-Rosen metric, as opposed to the Schwarzschild scenario, does not approach zero as $u \to 0$. Instead, as illustrated in Figure 6.1, at $u = 0$, the area possesses a non-zero minimum value. The location of this minimal area defines what is now called the *throat* of the wormhole.

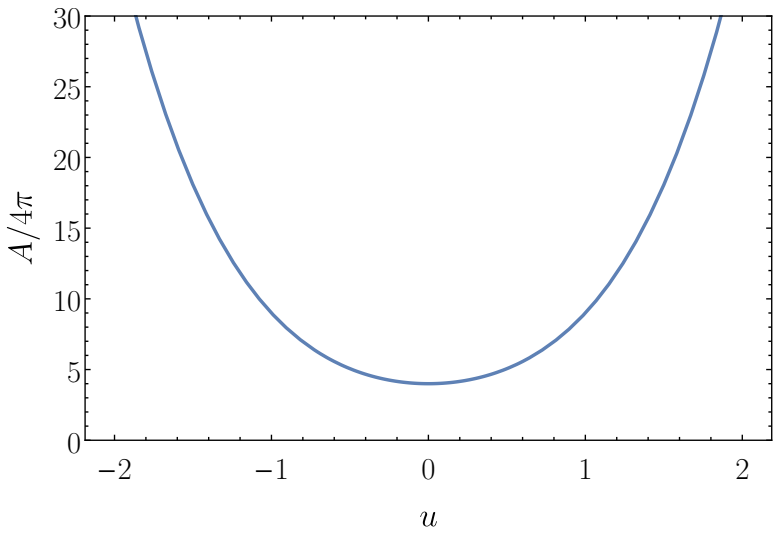

Figure 6.1.: Representation of the area of spheres within the Einstein-Rosen spacetime at a fixed time. A notable feature is the existence of a non-zero minimum area at $u = 0$, which is now commonly referred to as the throat of the wormhole.

In order to model charged particles, Einstein and Rosen implemented a similar change of coordinates using the Reissner-Nordström solution, which describes a black hole with electric charge.Though the motivation behind this construction was to establish a model for singularity-free particles, this Einstein-Rosen bridge can be rescaled using the mass M to any magnitude, allowing to reach astrophysical sizes if desired.

The neutral and charged bridges can be extended to encompass more general scenarios, as we will show next. Given that the construction of an Einstein-Rosen bridge fundamentally relies on a geometry with horizons, one can generically investigate spacetimes that include an event horizon at r_h. The corresponding

line element can be formulated as

$$ds^2 = -e^{-\varphi(r)}\left(1 - \frac{b(r)}{r}\right)dt^2 + \frac{1}{1 - b(r)/r}dr^2 + r^2 d\Omega \quad . \tag{6.3}$$

The function $b(r)$, referred to as the wormhole shape parameter, satisfies $b(r_h) = r_h$, and the function $\varphi(r)$ is named the redshift function for obvious reasons. Now, we introduce a coordinate transformation in a manner similar to what we did for Schwarzschild, $u^2 = r - r_h$

$$ds^2 = -e^{-\varphi(x)}\left(1 - \frac{b(x)}{x}\right)dt^2 + \frac{1}{1 - b(x)/x}dx^2 + x^2 d\Omega \quad . \tag{6.4}$$

For clarity in notation we have defined $x = u^2 + r_h$. Here, the radial coordinate x behaves non-monotonically, decreasing from infinity to a minimum at r_h, which corresponds to the throat of the wormhole.

The Einstein-Rosen bridge can be understood as an artifact of the coordinate choice. The chosen coordinates naturally cover the Schwarzschild exterior twice. This corresponds with a specific space-like hypersurface of the maximally extended Schwarzschild spacetime. Through the utilization of Kruskal-Szekeres coordinates [180, 181], we can effectively depict both the outer and inner regions of the Schwarzschild solution, as illustrated in Figure 6.2. By means of the Kruskal-Szekeres coordinates, we achieve a comprehensive description of both the exterior and interior sectors of Schwarzschild, delivering a maximal extension of this spacetime. This extension shows us that the singularity at the horizon manifests itself as a coordinate singularity, while the central singularity stands as a physical one. Moreover we can split the maximal extended Schwarzschild spacetime in four distinct regions: regions I and III correspond to two identical Schwarzschild exteriors ($r > 2GM$), whereas regions II and IV represent the Schwarzschild interior ($r < 2GM$), incorporating the physical singularity—analogous to black and white holes, respectively. The central point, where the regions converge, is the location of the Einstein-Rosen bridge. In this visualization, light rays follow null paths at 45^{o}. The blue hyperbolic lines denote surfaces of constant radius which increase outwards in

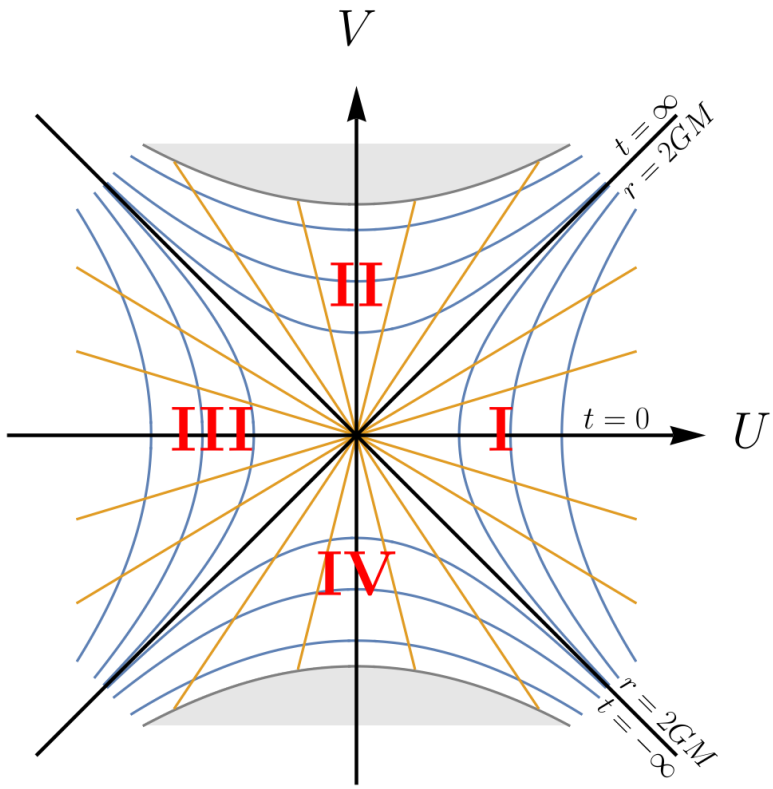

Figure 6.2.: Diagram depicting the maximally extended Schwarzschild spacetime using Kruskal-Szekeres coordinates. Regions I and III denote two distinct yet identical Schwarzschild exteriors where $r > 2GM$. While, regions II and IV are also identical, but time-reversed, housing the physical singularities (shaded area). Constant r coordinates are depicted with blue hyperbolic lines, while constant t coordinates are indicated by straight orange lines.

regions I and III, while the radius diminishes outwards in regions II and IV. The orange radial lines represent surfaces of constant time.

Usually, when one thinks of Schwarzschild spacetime, it is perceived as static. However, this geometry is only invariant under translations $t \to t + \Delta t$ in regions I and III, corresponding to the exterior regions of the maximally extended Schwarzschild spacetime. Yet, this same translation in regions II

and IV represents a spacelike motion. Thus, a spatial surface such as the one defined by the Einstein-Rosen bridge, spanning from $(U, V) = (-\infty, 0)$ to $(U, V) = (\infty, 0)$ passing through $(U, V) = (0, 0)$, will exhibit this spacelike evolution, pushing it into region II. Consequently, the wormhole throat only forms briefly. It will subsequently close at a velocity high enough to prevent anything from traversing it. The outcome is the division of spacetime into two disconnected entities, both of them containing singularities. It is also easy to deduce from the diagram, considering that light rays travel along lines drawn at 45^{o} angles, that there is no way for an object initially located in region I to reach region III without exceeding the speed of light. Therefore, any observer attempting to cross the Einstein-Rosen bridge will inevitably fall into a black hole, as that is essentially what it is.

6.2. Wheeler wormhole

After the work of Einstein and Rosen, the field remained quiet for twenty years until 1955 when Wheeler revived it introducing a new concept, namely, the notion of *Geon* [6]. We briefly introduced these objects as precursors to boson stars in Section 1.1, but now we will delve into them in greater detail.

Wheeler, like Einstein and Rosen, aimed to create a self-gravitating entity free from divergences, capable of fulfilling the role that particles traditionally play. To recap what we discussed in the first chapter, these objects are characterized by a smooth, classical electromagnetic field coupled to gravity, which adopts a closed circular toroidal form with a high concentration of energy. The gravitational attraction associated with the field energy sustains this system, resulting in what Wheeler termed "mass without mass." Wheeler's exploration also led to the introduction of the *tunnel* concept, known as wormhole today. This notion was developed based on Gauss's theorem and the concept of charge as a flux integral. Gauss's theorem explains that the measurement of electric charge on an object corresponds to the number of field lines traversing a closed surface enclosing the object, a geon for the case we are interested in. Wheeler

noticed that setting up a Riemannian manifold does not necessarily require spacetime to be topologically simple. Rather, he suggested considering a metric where two far-apart regions are linked by a *tunnel*, as illustrated schematically in Figure 6.3. Consequently, the count of field lines penetrating the surface of the closed sphere encircling one end of the tunnel equals the number passing through the sphere enclosing the other end. As a result, we measure the same charge but with opposite signs on both sides of the tunnel. This approach effectively quantified a charge without an actual enclosed charge. Thus, adding Wheeler's concept of "mass without mass" the concept of "charge without charge."

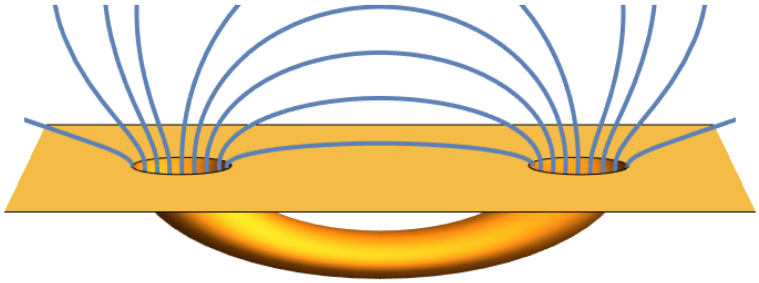

Figure 6.3.: Schematic depiction of the wormhole concept introduced by Wheeler. Closed blue lines represent electric field lines.

From this point, Wheeler expanded his research in two different directions. On one hand, he delved into studying quantum gravity processes that could explain the nature of geons. This path led him to conceptualize what we now refer to as *spacetime foam* [182]. In his analysis, he emphasized the crucial role of the Planck length, near which spacetime ceases to have the smooth and continuous nature depicted in classical physics. Instead, it becomes a turbulent and fluctuating medium due to quantum mechanical effects. This foam-like structure of spacetime introduces fluctuations and uncertainty into the fabric of the universe's geometry. Wheeler suggested that at the spacetime

foam level (the Planck scale), wormholes (or geons) might sporadically emerge and disappear, giving rise to a dynamic interplay of interconnected spacetime regions.

On the other hand, Wheeler's research pursued the analysis of classical dynamics associated with these configurations. Together with Misner, this path led to the establishment of the concept "Physics is Geometry" [183]. It is in this article [183] that the term "wormhole" first appears. Their objective was to utilize an appropriate non-trivial topology alongside sourceless Maxwell's equations coupled to Einstein's gravity to construct models of electric charges and particles from classical physics.

It is now known that these geon solutions display instability, driving the energy distributions to form black holes via gravitational collapse. This outcome inevitably hides any associated topological effects behind event horizons. In previous chapters of this thesis we have already seen effects of this type in the case of scalar matter.

6.3. Traversable wormholes

After the contributions of Wheeler and Misner, the field remained relatively quiet again for about 30 years. During this time, research was conducted on the spacetime foam and the geons, seeking to deepen the understanding of these objects. There were also isolated contributions that presented new geometries, such as the Ellis wormhole, a special case of the Ellis drainhole [184, 185]. Interestingly, Morris and Thorne later rediscovered this concept, without being aware of Ellis' prior work.

The field was reinvigorated in 1988 when Morris and Thorne published their work [186]. In their study, they presented a new approach to constructing wormholes that avoid the issues encountered in the Einstein-Rosen bridge or the geon. As we have seen, the Einstein-Rosen bridge was a coordinate artifact, so any attempt to traverse it would result in the subject being absorbed by a black

hole. Even if the geometry described by Einstein and Rosen could remain static, the tidal forces would be extremely high, tearing apart anyone attempting to cross it into countless pieces. Furthermore, an observer located far from the bridge would never see their adventurous companion cross the bridge, nor could they receive any news from the other side. On the other hand, geons turn out to be unstable, and the range of sizes in which they could exist, on the order of the Planck length, eliminates any possibility of a human traversing them.

Morris and Thorne introduced wormhole configurations that were traversable, in the sense that a human being could hypothetically cross them within an acceptable lapse of time and without perishing during the journey. To meet these criteria, the wormholes they proposed had to be free from horizons and naked singularities.

The procedure for constructing these wormholes goes in the opposite direction from the conventional way in which solutions to Einstein's equations have typically been found. Instead of starting with a plausible matter distribution and subsequently solving Einstein's equations to determine the spacetime geometry, their method involved imposing an interesting geometry and solving Einstein's equations in order to find the matter distribution responsible for producing such a geometry.

Let us start by writing the metric that characterizes this particular class of wormholes

$$ds^2 = -e^{2\Phi(l)}dt^2 + dl^2 + r(l)^2 d\Omega^2 \quad . \tag{6.5}$$

Here, the coordinate l spans from negative infinity to positive infinity. The function r takes is non-monotonic, starting from infinity at the asymptotically region, decreasing to a minimum value of $r(0) = r_0$ at the throat of the wormhole, and then growing back to infinity as it tends to the other asymptotically region. This value r_0 serves as a measure for the size of the wormhole's throat. To illustrate the behavior of the function $r(l)$, refer to Figure 6.4. This value r_0 also indicates the size of the wormhole throat.

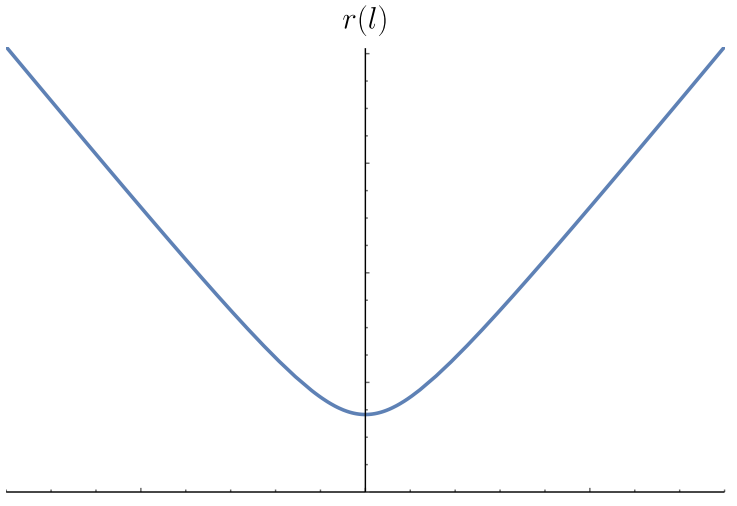

Figure 6.4.: Representation of the behavior of the radius $r(l)$ of the spheres surrounding the throat of the Morris-Thorne wormhole with respect to proper distance. The throat of the wormhole is located at $l = 0$.

To simplify our analysis, let's transform the previous line element into Schwarzschild-like coordinates

$$ds^2 = -e^{2\Phi(r)}dt^2 + \frac{1}{1 - b(r)/r}dr^2 + r^2 d\Omega^2 \quad . \tag{6.6}$$

Where $\Phi(r)$ is referred to as the redshift function. To satisfy our condition of avoiding horizons, $\Phi(r)$ must remain finite across its entire range. Additionally, we label $b(r)$ as the shape function, which satisfies $b(r_0) = r_0$ at the throat. It's worth noting that the metric exhibits asymptotic flatness.As it is evident, g_{rr} is a function that exhibits divergence at the wormhole throat. Nevertheless, the radial proper distance is well-defined

$$l(r) = \pm \int_{r_0}^{r} \left(1 - \frac{b(r)}{r}\right)^{1/2} dr \quad , \tag{6.7}$$

with a null value at the throat, $l(r_0) = 0$.

As previously mentioned, once we have selected the metric, we can proceed to calculate the curvature tensors. Utilizing Einstein's field equations, we can then deduce the components of the energy-momentum tensor. The spherical symmetry imposed on the system leads to a diagonal energy-momentum tensor, represented as

$$T_{\mu\nu} = \begin{pmatrix} -\rho(r) & 0 & 0 & 0 \\ 0 & p_r(r) & 0 & 0 \\ 0 & 0 & p_t(r) & 0 \\ 0 & 0 & 0 & p_t(r) \end{pmatrix} \quad . \tag{6.8}$$

The energy-momentum tensor components and the metric functions relate as follows

$$\rho(r) = \frac{1}{\kappa}\frac{b'}{r^2} \quad , \tag{6.9}$$

$$p_r(r) = \frac{1}{\kappa}\left[2\left(1-\frac{b}{r}\right)\frac{\Phi'}{r} - \frac{b}{r^3}\right] \quad , \tag{6.10}$$

$$p_t(r) = \frac{1}{\kappa}\left(1-\frac{b}{r}\right)\left[\Phi'' + \left(\Phi' - \frac{b'r-b}{2r^2\left(1-b/r\right)}\right)\left(\Phi' + \frac{1}{r}\right)\right] \quad . \tag{6.11}$$

Here, $\kappa = 8\pi G$. Rearranging these equations, we obtain

$$b' = \kappa\rho r^2 \quad , \tag{6.12}$$

$$\Phi' = \frac{b-\kappa\tau r^3}{2r^2\left(1-b/r\right)} \quad , \tag{6.13}$$

$$p_r(r)' = 2\frac{p_t - p_r}{r} - \left(\rho + p_r\right)\Phi' \quad . \tag{6.14}$$

The last equation Eq. (6.14) results from differentiating equation Eq. (6.10) with respect to r, while substituting the expressions for b' and Φ''. Alternatively, this equation can be derived from the conservation of the energy-momentum tensor, $\nabla_\nu T^{\mu\nu} = 0$.

The system we are dealing with is composed of three equations and five unknowns—b, Φ, p_r, p_t, and ρ. Different approaches can be used to solve it, either by imposing equations of state, defining the expression for the shape in advance, or defining the redshift function in advance, too.

By integrating equation Eq. (6.12), we obtain

$$b(r) = b(r_0) + \kappa \int_{r_0}^{r} \rho(r) r^2 dr \quad , \tag{6.15}$$

and considering the mass definition

$$m(r) = \frac{4\pi r_0}{\kappa} + 4\pi \int_{r_0}^{r} \rho(r) r^2 dr \quad , \tag{6.16}$$

we find that $b(r) = m(r)\kappa/4\pi$. Thus, the mass distribution depends on the shape function.

6.3.1. Traveling time, acceleration and tidal forces

As mentioned earlier, for a wormhole to be traversable by a human (or an extraterrestrial being), it should allow the traveler to cross within a reasonable lapse of time without perishing to the effects of accelerations or tidal forces during the journey.

Let us consider a scenario where a traveler initiates the journey from a station situated at $l = -l_1$ and aims to conclude the trip at a station on the opposite side of the wormhole throat at $l = l_2$ [186]. The traveler's velocity as measured by a stationary observer at distance r is denoted as $v(r)$, and it can

be expressed as

$$v = e^{-\Phi}\frac{dl}{dt} = \mp\frac{e^{-\Phi}}{(1-b/r)^{1/2}}\frac{dr}{dt} \quad . \tag{6.17}$$

While the proper velocity of the traveler is given by

$$v\gamma \equiv \frac{v}{(1-v^2/c^2)^{1/2}} = \frac{dl}{d\tau} = \mp\frac{1}{(1-b/r)^{1/2}}\frac{dr}{d\tau} \quad . \tag{6.18}$$

The stations must be positioned far enough from the wormhole throat to ensure that spacetime in that region remains nearly flat ($b/r \ll 1$). Moreover, the gravitational redshift experienced by signals transmitted from the stations to infinity, denoted as $\Delta\lambda/\lambda = e^{-\Phi} - 1 \cong -\Phi$, must be sufficiently small ($|\Phi| \ll 1$). The gravitational acceleration measured at the stations should be comparable to or less than Earth's gravitational acceleration ($|\Phi'| \leq g_{\oplus}$).

Hence, the amount of time measured by both observers at the stations and the traveler will be, respectively,

$$\Delta t = \int_{-l_1}^{l_2}\frac{dl}{ve^{\Phi}} \quad , \tag{6.19}$$

$$\Delta\tau = \int_{-l_1}^{l_2}\frac{dl}{v\gamma} \quad . \tag{6.20}$$

As an example, Morris and Thorne require that these quantities do not exceed a year, $\Delta t \leq 1$ year, $\Delta\tau \leq 1$ year.

To determine the acceleration, we establish an orthonormal basis for the traveler's proper frame denoted as $\{\mathbf{e}_{\hat{0}'}, \mathbf{e}_{\hat{1}'}, \mathbf{e}_{\hat{2}'}, \mathbf{e}_{\hat{3}'}\}$, and express it in terms of the orthonormal basis of static observers, represented by $\{\mathbf{e}_{\hat{t}}, \mathbf{e}_{\hat{r}}, \mathbf{e}_{\hat{\theta}}, \mathbf{e}_{\hat{\varphi}}\}$

$$\mathbf{e}_{\hat{0}'} = \gamma\mathbf{e}_{\hat{t}} \mp \gamma v\mathbf{e}_{\hat{r}} \ , \quad \mathbf{e}_{\hat{1}'} = \mp\gamma\mathbf{e}_{\hat{r}} + \gamma v\mathbf{e}_{\hat{t}} \ , \quad \mathbf{e}_{\hat{2}'} = \mathbf{e}_{\hat{\theta}} \ , \quad \mathbf{e}_{\hat{3}'} = \mathbf{e}_{\hat{\varphi}}. \tag{6.21}$$

Consequently, the acceleration experienced by the traveler, as expressed in their proper reference frame, is determined by

$$|\mathbf{R}| = \left| \left(1 - \frac{b}{r}\right)^{1/2} e^{-\Phi} \left(\gamma e^{\Phi}\right)' \right| \leq g_{\oplus} \quad , \tag{6.22}$$

which we have required to be weaker than Earth's surface acceleration.

Finally, we must ensure that tidal forces remain within a sufficiently tolerable range, preventing the traveler from being ripped apart during their passage through the wormhole's throat. These tidal forces, experienced by the traveler, are determined by the equation

$$\Delta a^{\hat{\mu}'} = -R^{\hat{\mu}'}{}_{\hat{\nu}'\hat{\alpha}'\hat{\beta}'} U^{\hat{\nu}'} \eta^{\hat{\alpha}'} U^{\hat{\beta}'} \quad , \tag{6.23}$$

where $U^{\hat{\mu}'} = \delta^{\hat{\mu}'}_{\hat{0}'}$ represents the traveler's four-velocity in their reference frame, and $\eta^{\hat{\alpha}'}$ signifies the separation between two arbitrary parts of their body. In the traveler's reference frame, this separation is purely spatial, $U^{\hat{\mu}'}\eta_{\hat{\mu}'} = 0$, with $\eta^{\hat{0}'} = 0$. Consequently, the acceleration also has a purely spatial nature, as denoted by the components

$$\Delta a^{\hat{1}'} = -R_{\hat{1}'\hat{0}'\hat{1}'\hat{0}'}\eta^{\hat{1}'} \ , \quad \Delta a^{\hat{2}'} = -R_{\hat{2}'\hat{0}'\hat{2}'\hat{0}'}\eta^{\hat{2}'} \ , \quad \Delta a^{\hat{3}'} = -R_{\hat{3}'\hat{0}'\hat{3}'\hat{0}'}\eta^{\hat{3}'} \quad . \tag{6.24}$$

We need to restrict tidal forces to values experienced on Earth. Expressing explicitly the Riemann tensor, we have

$$\left| \left(1 - \frac{b}{r}\right) \left[\Phi'' + (\Phi')^2 - \frac{b'r - b}{2r(r-b)}\Phi'\right] \right| \left|\eta^{\hat{1}'}\right| \leq g_{\oplus} \quad , \tag{6.25}$$

$$\left| \frac{\gamma^2}{2r^2} \left[v^2 \left(b' - \frac{b}{r}\right) + 2\left(r - b\right)\Phi'\right] \right| \left|\eta^{|\eta^{\hat{2}'}|}\right| \leq g_{\oplus} \quad . \tag{6.26}$$

Hence, when constructing a wormhole using the method proposed by Morris and Thorne, the three constraints of time, acceleration, and tidal forces presented here must all be taken into account.

6.3.2. Energy conditions

The Null Energy Condition (NEC) emerges from the Raychaudhuri equation, which describes the evolution of geodesic congruences. The NEC asserts that the sum of energy density and radial pressure associated with any form of matter or energy within a spacetime should remain non-negative for any observer following a null trajectory. In other words, for any future-directed null vector k^μ, the principle states that the inequality $T_{\mu\nu}k^\mu k^\nu \geq 0$ must be satisfied [187, 188]. In our present analysis, this condition translates into the requirement that

$$\rho + p_r \geq 0 \quad \text{and} \quad \rho + p_t \geq 0 \quad . \tag{6.27}$$

By combining the aforementioned equations, namely Eq. (6.9) and Eq. (6.10), we arrive at

$$\rho + p_r = \frac{1}{\kappa}\left[\frac{b'}{r^2} + 2\left(1 - \frac{b}{r}\right)\frac{\Phi'}{r} - \frac{b}{r^3}\right] \quad . \tag{6.28}$$

Evaluating this expression at the throat and considering the finite value of the redshift function, we have

$$\rho + p_r|_{r_0} = \frac{1}{\kappa}\left[\frac{b'}{r_0^2} - \frac{b}{r_0^3}\right] \quad . \tag{6.29}$$

Moving forward, we invoke the flaring-out condition, a concept which asserts that $r(l)$ reaches its minimum at the throat and progressively increases as it moves away. Consequently,

$$\frac{d^2r}{dl^2} > 0 \quad . \tag{6.30}$$

Equating the line elements provided earlier, Eq. (6.5) and Eq. (6.6), yields

$$\frac{dr}{dl} = \sqrt{1 - \frac{b(r)}{r}} \quad , \tag{6.31}$$

and differentiating this with respect to l,

$$\frac{d^2r}{dl^2} = \frac{1}{2}\left(\frac{b}{r^2} - \frac{b'}{r}\right) \quad . \tag{6.32}$$

Hence, the flaring-out condition implies that

$$\left(\frac{b}{r^2} - \frac{b'}{r}\right) > 0 \quad . \tag{6.33}$$

Revisiting Eq. (6.29), we reach the conclusion that at the throat,

$$\rho + p_r\Big|_{r_0} < 0 \quad . \tag{6.34}$$

Then, we observe that the flaring-out condition triggers the violation of the NEC near the throat. Furthermore, it signals the violation of all pointwise energy conditions [161], including the weak, dominant, and strong energy conditions. Thus, it can be seen that the throat of the wormhole will be supported by what is termed *exotic matter*, a label used for matter that violates the NEC.

It's important to clarify that violating the energy conditions does not automatically eliminate the potential existence of Morris-Thorne wormholes. Firstly, such violations do not directly imply a negative energy density. The sign of the energy density ρ depends directly on the radial derivative of the shape function b', which is not necessarily negative. In that case, it is the radial pressure that would exhibit a negative sign to sustain the wormhole. Secondly, the energy conditions are grounded in the realm of classical physics. However, there are examples, both theoretical and experimental, where quantum fields exhibit violations of the energy conditions, such as the Casimir effect—although

it's important to note that the Casimir effect's violation of the energy conditions are typically on the order of $\hbar$.

The violation of the pointwise energy conditions prompted the formulation of the averaged energy conditions along timelike or null geodesics. These allow for occasional energy condition violations, as long as the integral sum along the curve respects them. Unfortunately, traversable Morris-Thorne wormholes also breach these averaged energy conditions, particularly when possessing spherical symmetry. However, it remains an open question whether quantum field theory permits violations of the averaged energy conditions. Therefore, if experimental confirmation of the averaged energy conditions were possible, the wormholes described in this section would struggle to survive. Nevertheless, designs for wormholes that might bypass these challenges still remain viable.

Moreover, if we consider theories of modified gravity, the Raychaudhuri equation— from which the NEC is derived—provides us with a generalized NEC of the form $T^{\text{eff}}_{\mu\nu}k^\mu k^\nu \geq 0$. Here, $T^{\text{eff}}_{\mu\nu}$ is an effective energy-momentum tensor that includes the usual energy-momentum tensor, as shown in, for instance, Eq. (3.9). Consequently, there can be matter distributions that violate the generalized NEC, in order to support the wormhole, while satisfying the usual NEC, resulting in wormholes supported by non-exotic matter [189–193].

6.4. Thin-Shell Wormholes

Morris and Thorne considered non-localized matter distributions, spherical symmetry, and temporal independence when establishing their formalism. Nevertheless, these assumptions can be relaxed to yield remarkably valuable insights. An interesting strategy to mitigate the violation of the NEC involves confining exotic matter solely within an infinitesimally thin layer situated at the wormhole's throat. This approach is facilitated by the *thin-shell formalism* and the *cut-and-paste procedure* [161, 174, 194–196]. By considering two smooth manifolds one may *cut* them so that each one becomes bounded by a time-like surface.

After that, one may *paste* them together at their boundary time-like surfaces, producing a single manifold with a thin hypersurface that connects two regions. In fact, across the thin hypersurface several discontinuities on geometric and matter quantities may exist [197], then one needs to use a suitable framework to describe these structures (one may use tensorial distributions instead of tensorial functions). In essence, the geometric and matter quantities must satisfy at the junction thin hypersurface the so-called *junction conditions* [198, 199].

Now, let us provide a generalized overview of this procedure to describe spherically symmetric wormholes. We start with two distinct manifolds, denoted as $\mathcal{M}_+$ and $\mathcal{M}_-$, each associated with its own metric—namely, $g^+_{\mu\nu}$ and $g^-_{\mu\nu}$, respectively. By joining these two manifolds along their respective boundaries Σ_+ and Σ_-— making the identification $\Sigma = \Sigma_+ = \Sigma_- = \mathcal{M}_+ \cap \mathcal{M}_-$—we obtain the unified manifold denoted as $\mathcal{M} = \mathcal{M}_+ \cup \mathcal{M}_-$. An illustrative representation is depicted in Figure 6.5.

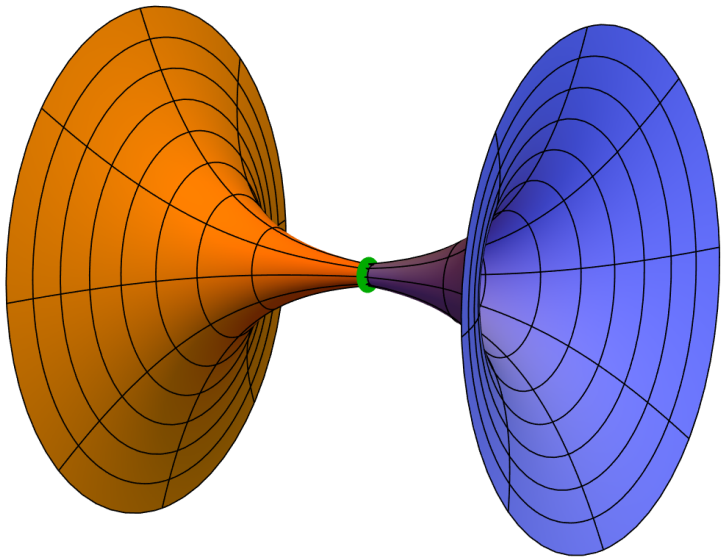

Figure 6.5.: Schematic representation of the embedding diagram for a thin-shell wormhole. In orange we have depicted the $\mathcal{M}_-$ universe while using blue for the $\mathcal{M}_+$ universe. The green line represents the location of the thin-shell.

Considering that both manifolds are spherically symmetric their associated line elements are

$$ds^2 = -e^{2\Phi_\pm(r_\pm)}\left[1-\frac{b_\pm(r_\pm)}{r_\pm}\right]dt_\pm^2 + \left[1-\frac{b_\pm(r_\pm)}{r_\pm}\right]^{-1}dr_\pm^2 + r_\pm^2\, d\Omega_\pm^2 \quad . \tag{6.35}$$

Where the plus sign corresponds to the $\mathcal{M}_+$ manifold and the minus sign corresponds to the $\mathcal{M}_-$ manifold. In order to analyse the glued spacetimes, we move to a consistent mathematical framework to study geometric and matter fields, i.e, we start to consider tensorial distributions instead of tensorial functions. In this approach, the metric distribution can be written as

$$\underline{g}_{\mu\nu} = g^+_{\mu\nu}\underline{\Theta} + g^-_{\mu\nu}(\underline{1}-\underline{\Theta}) \quad , \tag{6.36}$$

where underlined quantities denote distributions and $\underline{\Theta}$ is the Heaviside step function, which takes the value 1 in $\mathcal{M}_+$, 0 in $\mathcal{M}_-$ and any reference value on the junction hypersurface. We also ask the metric to be continuous across the shell, that is $[g_{\mu\nu}] = 0$, where we have defined the notation $[X] = X^+|_\Sigma - X^-|_\Sigma$.

Having established the metric, we can now follow a similar approach as employed for the Morris-Thorne wormhole. By solving the Einstein field equations, we establish a connection between the components of the stress-energy tensor and the metric functions. Given the spherical symmetry of the system, the stress-energy tensor adopts a diagonal form like in Eq. (6.8), and its components are related with the metric functions in the following way

$$\rho_\pm(r_\pm) = \frac{1}{\kappa}\frac{b'_\pm}{r_\pm^2} \quad , \tag{6.37}$$

$$p_{r\pm}(r_\pm) = \frac{1}{\kappa}\left[2\left(1-\frac{b_\pm}{r_\pm}\right)\frac{\Phi'_\pm}{r_\pm} - \frac{b'_\pm}{r_\pm^2}\right] \quad , \tag{6.38}$$

$$p_{t\pm}(r_\pm) = -\frac{1}{2\kappa r_\pm^2}\left[\left(-b_\pm + 3r_\pm b'_\pm - 2r_\pm\right)\Phi'_\pm \right. \\ \left. +2r_\pm\left(b_\pm - r_\pm\right)\left((\Phi'_\pm)^2 + \Phi''_\pm\right) + b''_\pm r_\pm\right] \quad . \tag{6.39}$$

The energy-momentum distribution is

$$\underline{T}_{\mu\nu} = T^+_{\mu\nu}\underline{\Theta} + T^-_{\mu\nu}(\underline{1} - \underline{\Theta}) + S_{\mu\nu}\underline{\delta}^\Sigma \quad . \tag{6.40}$$

Here, $T^\pm_{\mu\nu}$ are the energy-momentum tensors on each side of the hypersurface, respectively $\mathcal{M}_\pm$; $\underline{\delta}^\Sigma$ is a Dirac's delta-type distribution with support on the hypersurface, defined by $<\underline{\delta}^\Sigma, X> \equiv \int_\Sigma X$, for any function X and $S_{\mu\nu}$ is the singular part of the energy-momentum tensor on the hypersurface. Similarly the distributional form of the trace of the stress-energy tensor reads

$$\underline{T} = T^+\underline{\Theta} + T^-(\underline{1} - \underline{\Theta}) + S\underline{\delta}^\Sigma \quad . \tag{6.41}$$

We have joined together two manifolds, $\mathcal{M}_+$ and $\mathcal{M}_-$, along their respective boundaries Σ_+ and Σ_-, effectively identifying the hypersurface where these two spacetimes meet as $\Sigma = \Sigma_+ = \Sigma_- = \mathcal{M}_+ \cap \mathcal{M}_-$. On this common hypersurface, we have induced the metrics $g^+_{ij}(\xi)$ and $g^-_{ij}(\xi)$, and these metrics are in fact isometric, meaning that $g^+ij(\xi) = g^-ij(\xi) = g_{ij}(\xi)$. Now, consider three tangent vectors of the holonomic basis, denoted as $\mathbf{e}_{(i)} = \partial/\partial\xi^i$, defined on Σ. The components of these vectors are given by $e^\mu_{(i)}|_\pm = \partial x^\mu_\pm/\partial\xi^i$. By utilizing these tangent vectors, we can compute the induced metric on the junction hypersurface, which takes the form $g_{ij} = \mathbf{e}(i)\cdot\mathbf{e}(j)$. This calculation leads us to the expression

$$ds^2_\Sigma = -d\tau^2 + R^2(\tau)\left(d\theta^2 + \sin^2\theta d\varphi^2\right) \quad . \tag{6.42}$$

Here, τ corresponds to the proper time of an observer moving along with the junction surface. The specific location of the junction surface is parameterized as $x^\mu(\tau,\theta,\varphi) = (t(\tau), R(\tau), \theta, \varphi)$ and it defines the constraint $f(r,\tau) = r - R(\tau) = 0$. Consequently, the unit 4-vector n^μ, which is perpendicular to the surface Σ,

is defined as

$$n_\mu = \pm \left| g^{\alpha\beta} \frac{\partial f}{\partial x^\alpha} \frac{\partial f}{\partial x^\beta} \right|^{-1/2} \frac{\partial f}{\partial x^\mu} \quad . \tag{6.43}$$

Thus,

$$n^\mu_\pm = \pm \left(\frac{e^{-\Phi}}{1 - b_\pm(R)/R} \dot{R}, \sqrt{1 - \frac{b_\pm(R)}{R} + \dot{R}}, 0, 0 \right) \quad . \tag{6.44}$$

Where the overdot denotes a derivative with respect to τ. We have chosen both normals to point from $\mathcal{M}_-$ to $\mathcal{M}_+$. It's important to note that $n^\mu n_\mu = +1$, indicating that the unit vector is spacelike, as the junction surface Σ is a timelike hypersurface.

By definition, the extrinsic curvature, also referred to as the second fundamental form, is expressed as $K_{ij} = \nabla_\nu n_\mu e^\mu_{(i)} e^\nu_{(j)}$. This formulation will lead us to derive expressions for the non-trivial terms.

$$K^{\theta\ \pm}_{\theta} = \pm \frac{1}{R} \sqrt{1 - \frac{b_\pm(R)}{R} + \dot{R}} \quad , \tag{6.45}$$

$$K^{\tau\ \pm}_{\tau} = \pm \left[\frac{\ddot{R} + \frac{b_\pm(R) - b'_\pm(R) R}{2R^2}}{\sqrt{1 - b_\pm(R)/R + \dot{R}^2}} + \Phi'_\pm(R) \sqrt{1 - \frac{b_\pm(R)}{R} + \dot{R}^2} \right] \quad . \tag{6.46}$$

The distributional form of the Einstein tensor is

$$\underline{G}_{\mu\nu} = G^+_{\mu\nu} \underline{\Theta} + G^-_{\mu\nu} (\underline{1} - \underline{\Theta}) + \mathcal{G}_{\mu\nu} \underline{\delta}^\Sigma \quad , \tag{6.47}$$

where $\mathcal{G}_{\mu\nu}$ represents the singular part of the Einstein tensor on Σ. Considering the projector tensor on Σ

$$h_{\mu\nu} \equiv g_{\mu\nu} - n_\mu n_\nu \quad , \tag{6.48}$$

we can express the Einstein tensor as

$$\mathcal{G}_{\mu\nu} = -[K_{\mu\nu}] + h_{\mu\nu}[K^{\rho}{}_{\rho}] \quad . \tag{6.49}$$

Therefore, the Einstein field equations associated with the junction thin hypersurface can be expressed as follows

$$S_{\mu\nu} = \frac{1}{\kappa}\left(-[K_{\mu\nu}] + h_{\mu\nu}[K^{\rho}{}_{\rho}]\right) \quad . \tag{6.50}$$

Because of the inherent spherical symmetry within the system, it follows that

$$[K^{i}{}_{j}] = \begin{pmatrix} [K^{\tau}{}_{\tau}] & 0 & 0 \\ 0 & [K^{\theta}{}_{\theta}] & 0 \\ 0 & 0 & [K^{\theta}{}_{\theta}] \end{pmatrix} \quad , \tag{6.51}$$

and

$$S^{i}{}_{j} = \begin{pmatrix} -\sigma & 0 & 0 \\ 0 & \mathscr{P} & 0 \\ 0 & 0 & \mathscr{P} \end{pmatrix} \quad . \tag{6.52}$$

Consequently, the Einstein equations on the junction surface yield

$$\sigma = -\frac{2}{\kappa}[K^{\theta}{}_{\theta}] \quad , \tag{6.53}$$

$$\mathscr{P} = \frac{1}{\kappa}\left([K^{\tau}{}_{\tau}] + [K^{\theta}{}_{\theta}]\right) \quad . \tag{6.54}$$

Finally, we can use the previously obtained equations Eq. (6.45) and Eq. (6.46) to reach the following expressions

$$\sigma = -\frac{2}{\kappa R}\left[\sqrt{1-\frac{b_+(R)}{R}+\dot{R}^2}+\sqrt{1-\frac{b_-(R)}{R}+\dot{R}^2}\right] \quad , \tag{6.55}$$

$$\begin{aligned}\mathscr{P} =& \frac{1}{\kappa R}\left[\frac{1+\dot{R}^2+R\ddot{R}-\left(b_+(R)+Rb'_+(R)\right)/2R}{\sqrt{1-b_+(R)/R+\dot{R}^2}}\right. \\ & +R\Phi'_+(R)\sqrt{1-\frac{b_+(R)}{R}+\dot{R}^2} \\ & \frac{1+\dot{R}^2+R\ddot{R}-\left(b_-(R)+Rb'_-(R)\right)/2R}{\sqrt{1-b_-(R)/R+\dot{R}^2}} \\ & \left.+R\Phi'_-(R)\sqrt{1-\frac{b_-(R)}{R}+\dot{R}^2}\right] \quad .\end{aligned} \tag{6.56}$$

As the reader may notice, the energy density σ will always be negative, consequently violating the energy conditions.

Next, we will examine the constraints arising from the conservation of the energy-momentum tensor

$$\nabla_\nu \underline{T}^{\mu\nu} = n_\nu \left[T^{\mu\nu}\right] \underline{\delta}^\Sigma + \nabla_\nu S^{\mu\nu}\underline{\delta}^\Sigma + S^{\mu\nu}n_\nu \underline{\delta'}^\Sigma = 0 \quad . \tag{6.57}$$

On one hand, we find that

$$S^{\mu\nu}n_\nu = 0 \quad , \tag{6.58}$$

since the surface on which $S^{\mu\nu}$ is defined is perpendicular to n^ν. On the other hand, we have the following conservation equation

$$\nabla_\nu S^{\mu\nu} = -n_\nu \left[T^{\mu\nu}\right] \quad . \tag{6.59}$$

Interestingly, we could have derived the same equation through the second Gauss-Codazzi equation in conjunction with equation Eq. (6.50). Moreover, the contracted first Gauss-Codazzi equation, when combined with the Einstein equations, also leads to a conservation equation that culminates in a system constraint [174]

$$\left(K^{+}_{\rho\sigma} + K^{-}_{\rho\sigma}\right) S^{\rho\sigma} = 2n^{\rho}n^{\sigma}\left[T_{\rho\sigma}\right] \quad . \tag{6.60}$$

Finally we can rewrite these conservation equations as constraints for the components of the stress-energy tensor in terms of the metric functions

$$\begin{aligned}\frac{d\sigma}{dR} =& -\frac{2}{R}\left(\sigma + \mathscr{P}\right) \\ &+ \frac{2}{\kappa R}\left[\Phi'_{+}(R)\sqrt{1 - \frac{b_{+}(R)}{R} + \dot{R}^{2}} + \Phi'_{-}(R)\sqrt{1 - \frac{b_{-}(R)}{R} + \dot{R}^{2}}\right] \quad ,\end{aligned} \tag{6.61}$$

obtaining then an equation for the evolution of the density for the thin-shell.

In the preceding discussion, we have presented the expression for the energy density of the thin shell in terms of the metric functions, as shown in equation Eq. (6.55). By rearranging this expression, we can formulate it in the following manner

$$\frac{1}{2}\dot{R} + V(R) = 0 \quad , \tag{6.62}$$

where the potential takes on the specific form

$$V(R) = \frac{1}{2}\left[1 - \frac{b_{+} + b_{-}}{2R} - \left(\frac{\kappa R\sigma}{4}\right)^{2} - \left(\frac{b_{+} - b_{-}}{R^{2}\kappa\sigma}\right)\right] \quad . \tag{6.63}$$

Therefore, we can proceed to conduct a stability analysis using a Taylor expansion centered around an equilibrium point R_0 of the potential

$$V(R) \approx \frac{1}{2}V''(R_0)(R-R_0)^2 + O[(R-R_0)^3] \quad . \tag{6.64}$$

Consequently, the thin-shell stability is assured if $V''(R_0) > 0$.

To summarize, we have introduced the *cut-and-paste* formalism, a method that enables the construction of traversable thin-shell wormholes. The primary aim of these structures is to minimize the violation of the energy conditions, limiting such violations exclusively to the thin-shell junction surface. This thin-shell is subject to the junction conditions outlined in equations Eq. (6.50), Eq. (6.59), and Eq. (6.60). These conditions govern the discontinuities that manifest across the shell and lead us to derive an equation of state for the matter within the thin-shell. Additionally, ensuring the stability of this wormhole requires the stability analysis we've presented, which imposes further conditions on the parameters.

Due to the robustness and versatility displayed by the construction of thin-shell wormholes, this procedure has been widely employed in the literature, with numerous studies focusing on different types of thin-shell wormholes and their stability [196, 200–203].

It is worth noting that the gravitational framework we have employed for this *cut-and-paste* procedure is rooted in General Relativity. However, there is room for alternative gravitational models that can yield stable thin-shell wormholes without necessitating exotic matter, negative densities, or violation of the energy conditions [191].

6.4.1. Junction conditions in Palatini $f(\mathcal{R})$ gravity

We can replicate the aforementioned procedure within the gravitational context of Palatini $f(\mathcal{R})$ gravity to derive the constraints that the shell must satisfy for a stable wormhole solution [90].

As previously discussed in Section 2.4, in order to extract the field equations of Palatini $f(\mathcal{R})$ gravity, we must vary the action Eq. (2.40) with respect to both the metric $g_{\mu\nu}$ and the connection Γ, as they are two equally fundamental and independent entities. By solving the connection equation, the resulting equations for the metric can be formulated as [88, 204]

$$\begin{aligned} f_{\mathcal{R}} G_{\mu\nu}(g) + \frac{\mathcal{R} f_{\mathcal{R}} - f}{2} g_{\mu\nu} - \left[\nabla_\mu \nabla_\nu f_{\mathcal{R}} - g_{\mu\nu} \Box f_{\mathcal{R}}\right] \\ + \frac{3}{2 f_{\mathcal{R}}} \left[\nabla_\mu f_{\mathcal{R}} \nabla_\nu f_{\mathcal{R}} - \frac{1}{2} g_{\mu\nu} \left(\partial f_{\mathcal{R}}\right)^2\right] = \kappa T_{\mu\nu} \quad . \end{aligned} \tag{6.65}$$

Tracing the metric field equation Eq. (2.49) leads to

$$f_{\mathcal{R}} \mathcal{R} - 2f = \kappa T \quad , \tag{6.66}$$

which gives rise to

$$\mathcal{R}_T \equiv dR/dT = \kappa/(R f_{\mathcal{R}\mathcal{R}} - f_{\mathcal{R}}) \quad . \tag{6.67}$$

Expressing the field equations Eq. (6.65) in their distributional form may arise some challenges. Consider the term

$$\nabla_\mu f_{\mathcal{R}} \nabla_\nu f_{\mathcal{R}} = f_{\mathcal{R}\mathcal{R}}^2 \mathcal{R}_T^2 \nabla_\mu T \nabla_\nu T \quad , \tag{6.68}$$

where we have employed the aforementioned expression for $\mathcal{R}_T$. However, the distributional form of the covariant derivative of the stress-energy tensor trace reads

$$\nabla_\mu \underline{T} = \nabla_\mu \underline{T}^+ \underline{\Theta} + \nabla_\mu \underline{T}^- \left(\underline{1} - \underline{\Theta}\right) + n_\mu \left[T\right] \underline{\delta}^\Sigma + \nabla_\mu \left(S \underline{\delta}^\Sigma\right) \quad . \tag{6.69}$$

As the term $\nabla_\mu T \nabla_\nu T$ in Eq. (6.68) involves products like $\underline{\Theta}, \underline{\delta}$ and $\underline{\delta}, \underline{\delta}$, which lack clear definitions in distributional theory, we must require both the continuity of the stress-energy tensor trace across the shell and the absence of a singular

part in the stress-energy tensor

$$[T] = 0 \quad \text{and} \quad S = 0 \quad . \tag{6.70}$$

Furthermore, an expression for terms involving $\nabla_\mu \nabla_\nu \underline{T}$ is required to compute the distributional form of the field equations

$$\nabla_\mu \nabla_\nu \underline{T} = \nabla_\mu \nabla_\nu \underline{T}^+ \underline{\Theta} + \nabla_\mu \nabla_\nu \underline{T}^- \left(\underline{1} - \underline{\Theta}\right) + n_\mu n_\nu n^\alpha \left[\nabla_\alpha T\right] \underline{\delta}^\Sigma \quad . \tag{6.71}$$

Then, the singular part of the field equations yields the following constraint equation

$$\frac{S_{\mu\nu}}{f_R|_\Sigma} = \frac{1}{\kappa}\left(- \left[K_{\mu\nu}\right] + \frac{1}{3} h_{\mu\nu} \left[K^\rho{}_\rho\right] \right) \quad , \tag{6.72}$$

which differs from the corresponding equation in General Relativity Eq. (6.50).

Within the context of Palatini $f(\mathcal{R})$ gravity, the two Bianchi identities lead to two constraint equations that also deviate from those of General Relativity:

$$h^\rho{}_\alpha \nabla^\alpha S_{\rho\nu} = -n^\rho h^\sigma_\nu [T_{\rho\sigma}] \quad , \tag{6.73}$$

and

$$\left(K^+_{\rho\sigma} + K^-_{\rho\sigma}\right) S^{\rho\sigma} = 2 n^\rho n^\sigma [T_{\rho\sigma}] - \frac{3\mathcal{R}_T^2 f^2_{\mathcal{R}\mathcal{R}}}{f_\mathcal{R}} [b^2] \quad . \tag{6.74}$$

For a detailed derivation of these equations we refer the interested reader to Ref. [90].

Chapter 7.

Asymmetric wormholes in Palatini $f(\mathcal{R})$ gravity

We have followed the chronological evolution of various descriptions of wormholes, leading us to the concept of thin-shell wormholes. Nowadays, the exploration of wormholes is still ongoing, with dedicated efforts focused on understanding and simulating their distinctive features [161, 205–207], and also to characterise their observational signatures [208–211]. This field of research has become more prominent due to the launch of gravitational wave observatories and the detection of gravitational waves originated from the merger of compact objects.

This has led the scientific community to question whether some detections, traditionally attributed to black holes, might actually arise from other entities known as *black hole mimickers*, due to their black hole-like behavior. The wide spectrum of black hole mimickers includes various types of wormholes and other ultra-compact objects [94, 139, 212–220], as they can share similarities with Schwarzschild/Kerr-like objects [221, 222]. However, despite these resemblances, the crucial factor lies in the potential signatures that these mimickers can leave on certain observables, revealing their true nature. These signatures may manifest as *shadows* [223–226], gravitational wave ringdown *echoes* [227–231], and the propagation of waves and quantum fields in these regions.

In connection with this, extensive study has been conducted on particle and field absorption and scattering, both concerning black holes [232–244] and ultra-compact objects [245] in an effort to improve our understanding of the spectroscopy of compact objects [246]. In particular, fields existing in the vicinity of compact objects can give rise to phenomena such as the emergence of *quasi-bound states* [245, 247, 248]. Wormholes, too, fall within this category, possibly hosting quasi-bound states and thus creating resonances in their absorption spectra. As a consequence, this may create resonances in their absorption spectra [249, 250], and also change their ringdown profile [229, 251].

As observed in the previous chapter, stable thin-shell wormholes in four-dimensional General Relativity typically demand exotic matter. It is always desirable to find stable solutions that do not necessarily require negative energies. It has been recently shown that this is indeed the case in $f(\mathcal{R})$ extensions in the Palatini formulation [90, 189]. In this framework, stable wormhole solutions can be found with both positive and negative energy densities. The choice of the Palatini $f(\mathcal{R})$ formulation is advantageous, as it avoids the strong model dependence inherent in the metric $f(R)$ case, where thin-shell dynamics depend on the selected $f(R)$ function [252]. Nevertheless, it is important to acknowledge that the cut-and-paste procedure can also yield thin-shell wormholes supported by positive energy matter in other modified gravity theories [190–192], and in General Relativity in higher dimensions [193].

In this chapter, based on Ref. [3], we will focus on analyzing the propagation of a massless scalar field in a background constructed by gluing together two Reissner-Nordström (RN) solutions—a charged black hole configuration. The junction conditions for these configurations correspond to those of Palatini $f(\mathcal{R})$ theories. We can deal with symmetric and asymmetric wormholes that represent electrovacuum spacetimes, which can have the same or different charge and mass on each side. The asymmetric configurations will be referred to as RN-AWH, which stands for Reissner-Nordström asymmetric wormhole.

7.1. Spacetime surgery

Here we will consider the family of $f(\mathcal{R})$ gravity theories constructed *à la* Palatini, i.e, with the spacetime metric and the affine connection being independent gravity fields (Section 2.4). Similarly to Eq. (2.40), the action of the $f(\mathcal{R})$ model is

$$\mathcal{S} = \frac{1}{2\kappa}\int d^4x\sqrt{-g}f(\mathcal{R}) + \int d^4x\sqrt{-g}\mathcal{L}_m(g_{\mu\nu},\psi_m) \quad , \tag{7.1}$$

where κ is the gravitational constant in suitable units, g is the metric determinant and $\mathcal{L}_m$ is the matter Lagrangian, which depends on the metric and matter fields.

In the same way as Section 6.4, where we introduced the cut-and-paste procedure, by considering two smooth manifolds, say $\mathcal{M}_\pm$ (with associated metrics $g^\pm_{\mu\nu}$), one may *cut* them so that each one becomes bounded by a time-like surface $\Sigma_\pm$. After that, one may *paste* them together at their boundary time-like surfaces, producing a single manifold $\mathcal{M} = \mathcal{M}_- \cup \mathcal{M}_+$ with a thin hypersurface $\Sigma = \Sigma_\pm = \mathcal{M}_- \cap \mathcal{M}_+$ that connects two regions with geometries governed by $g^-_{\mu\nu}$ and $g^+_{\mu\nu}$.

As mentioned in the previous chapter, although the metric is required to be continuous (but not necessarily differentiable) across the hypersurface, other curvature and matter distributions are not. In order to identify the *allowed* discontinuities of these quantities across the hypersurface, one has to make use of the junction conditions, which introduces constrains in the discontinuities of curvature and matter quantities in both sides of the hypersurface. These junction conditions are highly influenced by the considered gravitational framework, and in alternative theories of gravity these conditions may change significantly from General Relativity. Considering the Palatini $f(\mathcal{R})$ framework, the junction

conditions derived in Section 6.4.1 following Ref. [90] are

$$[g_{\mu\nu}] = 0 \text{ and } [h_{\mu\nu}] = 0 \quad , \tag{7.2}$$

$$[T] = 0 \text{ and } S = 0 \quad , \tag{7.3}$$

$$\frac{1}{3} h_{\mu\nu}[K^{\rho}_{\rho}] - [K_{\mu\nu}] = \kappa^2 \frac{S_{\mu\nu}}{f_{\mathcal{R}|_\Sigma}} \quad , \tag{7.4}$$

$$D^{\rho} S_{\rho\nu} = -n^{\rho} h^{\sigma}_{\nu} [T_{\rho\sigma}] \quad , \tag{7.5}$$

$$\left(K^{+}_{\rho\sigma} + K^{-}_{\rho\sigma}\right) S^{\rho\sigma} = 2 n^{\rho} n^{\sigma} [T_{\rho\sigma}] - \frac{3\mathcal{R}_T^2 f^2_{\mathcal{R}\mathcal{R}}}{f_{\mathcal{R}}} [b^2] \quad . \tag{7.6}$$

where we introduced the notation $D^{\rho} \equiv h^{\rho}{}_{\alpha} \nabla^{\alpha}$.

As already mentioned (and demonstrated) in Section2.2.2, in General Relativity, both the metric and Palatini formalisms result in the same set of field equations. However, by considering a $f(R)$ Lagrangian, the metric and Palatini approaches lead to completely different sets of equations of motion. Consequently, the junction conditions of Palatini $f(\mathcal{R})$ largely depart from the corresponding expressions in General Relativity (showed in Eqs. (6.50), (6.59) and (6.60)) and in the metric version of $f(R)$. A remarkable aspect of the Palatini $f(\mathcal{R})$ junction conditions is the vanishing of brane tension, S. In the framework of General Relativity, one has $h_{\mu\nu}[K^{\rho}_{\rho}] - [K_{\mu\nu}] = \kappa^2 S_{\mu\nu}$ instead of Eq. (7.4), and the brane tension in general is non-vanishing, $\kappa^2 S = 2[K^{\rho}_{\rho}]$. In the framework of Palatini $f(\mathcal{R})$ it does happen regardless of the behavior of $[K^{\rho}_{\rho}]$.

7.2. Asymmetric RN-RN wormholes

Since the matter content of the thin shell (the singular part of the energy-momentum tensor) can be modelled as a perfect fluid distribution (Eq. (6.52)), one finds that due to Eq. (7.3) the pressure density $\mathscr{P} = \sigma/2$ is fully determined by the energy density σ (particularly inheriting its sign), hence in Palatini $f(\mathcal{R})$ no equation of state $\mathscr{P} = \mathscr{P}(\sigma)$ is required to close the system, which contrasts

with General Relativity and metric $f(\mathcal{R})$ [189], and the number of effective degrees of freedom is reduced to just one.

With the junction condition Eq. (7.4), one moves the problem to determine the energy density of the system to compute the difference between the discontinuities of the extrinsic curvature components, i.e,

$$[K^{\tau}{}_{\tau}] - [K^{\theta}{}_{\theta}] = \frac{3\kappa^2}{2f_{\mathcal{R}|\Sigma}}\sigma \quad . \tag{7.7}$$

Finally, we look for the energy conservation relation Eq. (7.5), which in the spherically symmetric case reduces to

$$-D^{\rho}S_{\rho\nu} = \left[\dot{\sigma} + \frac{2\dot{R}}{R}(\sigma + \mathscr{P})\right]\delta^{\tau}{}_{\nu} = n^{\rho}h^{\sigma}{}_{\nu}[T_{\rho\sigma}] \quad , \tag{7.8}$$

where $\delta^{\tau}{}_{\nu} = (1, 0, 0)$. Using the relation between the pressure and energy densities, one finds that

$$\frac{1}{R^3}\frac{d\,(\sigma R^3)}{d\tau}\delta^{\tau}{}_{\nu} = n^{\rho}h^{\sigma}{}_{\nu}[T_{\rho\sigma}] \quad , \tag{7.9}$$

which leads to simple solutions for σ in the case where its right-hand side vanishes, namely $\sigma = C/R^3$, where C is an integration constant. Fortunately, in the electrovacuum scenario this is true. To see it, we recall that for any electrostatic, spherically symmetric field described by a nonlinear electrodynamics, the energy-momentum tensor associated to it can be written as $T_{\rho}{}^{\sigma} = \mathrm{diag}(-\phi_1(r), -\phi_1(r), \phi_2(r), \phi_2(r))$, where the functions ϕ_i characterize each particular configuration. (In Maxwell electrodynamics, $\phi_i(r) = -q^2/r^4$, with q being the charge per unit mass of the system. In vacuum, $\phi_i = 0$.) By contracting the normal vector to the hypersurface with the energy-momentum tensor, one finds that $n^{\rho}T_{\rho}{}^{\nu} = -\phi_1(r)n^{\nu}$, hence the right-hand side of Eq. (7.9) becomes

$$n^{\rho}h^{\sigma}{}_{\nu}[T_{\rho\sigma}] = n^{\rho}h_{\sigma\nu}[T_{\rho}{}^{\sigma}] = -(\phi_1^{+}(r) - \phi_1^{-}(r))n^{\sigma}h_{\sigma\nu} \quad , \tag{7.10}$$

which is identically zero, since

$$n^{\sigma}h_{\sigma\nu} = n^{\sigma}\left(g_{\sigma\nu} - n_{\sigma}n_{\nu}\right) = n_{\nu} - n_{\nu} \equiv 0 \quad . \tag{7.11}$$

Therefore, any two electrovacuum spacetimes supported by electrostatic and spherically symmetric fields can be glued together at a hypersurface Σ with surface energy density $\sigma = C/R^3$. Here, in particular, we are interested in cutting and pasting two Reissner-Nordström (RN) spacetimes, that have different charges and masses, being described by the following line elements

$$ds^2_{\pm} = -f_{\pm}(r_{\pm})dt^2 + \frac{dr^2_{\pm}}{f_{\pm}(r_{\pm})} + r^2_{\pm}\,d\Omega^2 \quad , \tag{7.12}$$

with $f_{\pm}(r_{\pm}) = 1 - 2M_{\pm}/r_{\pm} + Q^2_{\pm}/r^2_{\pm}$, where $M_{\pm}$ and $Q_{\pm}$ are the mass and charge on each RN spacetime, respectively. We point out that we do not impose the restriction $Q < M$. For $Q > M$, the line element Eq. (7.12) describes an overcharged RN space-time, which is a naked singularity. We emphasize that all wormholes studied here are geodesically complete, since the matching surface is located beyond where the singularity would be.

One can use the field equation on the shell Eq. (7.7) to write [226]

$$\ddot{R} = \frac{\gamma - \frac{3M_{+}R - 2Q^2_{+} - R^2(\dot{R}^2+1)}{\sqrt{f_{+}(R)+\dot{R}^2}} - \frac{3M_{-}R - 2Q^2_{-} - R^2(\dot{R}^2+1)}{\sqrt{f_{-}(R)+\dot{R}^2}}}{R^3\left(\frac{1}{\sqrt{f_{+}(R)+\dot{R}^2}} + \frac{1}{\sqrt{f_{-}(R)+\dot{R}^2}}\right)} \quad , \tag{7.13}$$

where $\gamma = 3\tilde{\kappa}^2 C/2$ is the energy parameter, with $\tilde{\kappa}^2 = \kappa^2/f_{\mathcal{R}|_{\Sigma}}$ being a constant, once $\mathcal{R} = \mathcal{R}(T)$ in any Palatini $f(\mathcal{R})$ theory is determined, and we are considering a trace-free energy-momentum tensor. In order to study the linear stability of these asymmetric wormhole solutions, one assumes that there is an equilibrium configuration, such that $\dot{R} = 0$, and expands Eq. (7.13) in Taylor series around the throat radius of the equilibrium configuration R_0 [226], which

at first order gives

$$\ddot{R} \approx C_1(R_0) + C_2(R_0)(R - R_0) + \mathcal{O}(R - R_0)^2 \quad , \tag{7.14}$$

where C_1 and C_2 are cumbersome functions of R_0, γ, and of the masses and charges of each side. As discussed in Ref. [226], to have an equilibrium configuration, the first term of the expansion must vanish, and the second one must be negative for a stable equilibrium.

Before we discuss the stability condition, it will be convenient to introduce a set of dimensionless variables, in order to simplify the expressions, namely

$$\begin{aligned}
&r_\pm = x_\pm M_-, && R = xM_-, && R_0 = x_0 M_-,\\
&\tau = \tilde{\tau} M_-, && t = \tilde{t} M_-, && Q_-^2 = y M_-^2,\\
&Q_+^2 = \eta\, Q_-^2, && M_+ = \xi M_-, && \gamma = \tilde{\gamma} M_-^2,
\end{aligned}$$

where $x_\pm$ are the dimensionless radial coordinates on each side of the throat, x is the dimensionless radius of the throat, x_0 is the dimensionless radius of the throat of an equilibrium configuration, y is the charge-to-mass ratio in $\mathcal{M}_-$, η gives the relation between the charge content in $\mathcal{M}_+$ and in $\mathcal{M}_-$ (for simplicity, we shall later on refer to η as charge-to-charge ratio), $\tilde{\tau}$ and $\tilde{t}$ are dimensionless time variables, and ξ is the mass-to-mass ratio between the two sides, which due to the continuity of the metric across Σ, must satisfy

$$\xi = 1 - \frac{y}{2x}(1 - \eta) \quad . \tag{7.15}$$

Now we can continue our discussion about the stability of equilibrium solutions. The equilibrium condition ($C_1 = 0$) leads us to

$$\tilde{\gamma} = -x_0 \frac{4(x_0 - 3)x_0 + (\eta + 7)y}{2\sqrt{(x_0 - 2)x_0 + y}} \quad , \tag{7.16}$$

and substituting this expression in Eq. (7.14), one finds an equation of the form

$$\frac{d^2\delta(\tilde{\tau})}{d\tilde{\tau}^2} + \varpi^2\delta(\tilde{\tau}) = 0 \quad , \tag{7.17}$$

where $\delta(\tilde{\tau}) \equiv x(\tilde{\tau}) - x_0$ and ϖ^2 is given by

$$\begin{aligned}\varpi^2 = &-\frac{4x_0y(\eta-(\eta-7)x_0-17)+((\eta-1)^2+16)y^2}{8x_0^4((x_0-2)x_0+y)} \\ &-\frac{8(2x_0^2-8x_0+9)x_0^2}{8x_0^4((x_0-2)x_0+y)} \quad .\end{aligned} \tag{7.18}$$

Therefore, the stability condition ($C_2 < 0$) is obtained by requiring that $\varpi^2 > 0$.

7.3. Parameter space

Equations (7.16) and (7.18) can be used to track the set of parameters $\{x_0, \eta, y\}$ that describes stable ($\varpi^2 > 0$) thin shells wormhole solutions supported by positive ($\tilde{\gamma} > 0$) or negative ($\tilde{\gamma} < 0$) surface energy densities. Let us investigate these two scenarios.

Positive energy stable configurations

By requiring $\varpi^2 > 0$ and $\tilde{\gamma} > 0$, one finds that the dimensionless parameters $\{x_0, \eta, y\}$ are constrained by

$$\frac{2}{15}(10-\sqrt{10}) < x_0 < \frac{2}{15}(10+\sqrt{10}) \quad , \tag{7.19}$$

$$\eta_1^- < \eta < \eta_1^+ \quad , \tag{7.20}$$

$$y_1^- < y < y_1^+ \quad , \tag{7.21}$$

where

$$\eta_1^{\pm} = \frac{-15 + 34x_0 - 12x_0^2}{33 - 28x_0 + 6x_0^2} \tag{7.22}$$

$$\pm 2\frac{\sqrt{-(216 - 504x_0 + 399x_0^2 - 130x_0^3 + 15x_0^4)}}{33 - 28x_0 + 6x_0^2} \quad , \tag{7.23}$$

$$y_1^- = \frac{a - 2\sqrt{b}}{\eta^2 - 2\eta + 17}, \tag{7.24}$$

$$y_1^+ = \frac{4x_0(3 - x_0)}{\eta + 7} \quad , \tag{7.25}$$

with $a = 2x_0(17 - \eta + (\eta - 7)x_0)$ and $b = -x_0^2(17 - 2\eta + 17\eta^2 - 2x_0(17 + 8\eta + 7\eta^2) + x_0^2(19 + 3\eta(\eta + 2)))$. Equations (7.19)-(7.21) determine the possible stable, positive energy (SPE) configurations allowed by gluing two RN spacetimes in Palatini $f(\mathcal{R})$ framework. The banana-shaped blue region in Figure 7.1 represents the parameter space of SPE wormholes.

Negative energy stable configurations

Now, looking for $\varpi^2 > 0$ and $\gamma < 0$, one finds stable, negative energy (SNE) wormhole configurations—that are associated with two different parameter spaces. The first group of solutions lies in the region identified by the constraints:

$$\text{If } \frac{2}{3} < x_0 \leq \frac{2}{15}(10 - \sqrt{10}),\ \eta_2^- < \eta < \eta_2^+ \quad , \tag{7.26}$$

$$\text{if } \frac{2}{15}(10 - \sqrt{10}) < x_0 < 1,\ \eta_2^- < \eta \leq \eta_1^- \text{ or } \eta_1^+ < \eta < \eta_2^+ \quad , \tag{7.27}$$

$$\text{if } 1 \leq x_0 < \frac{2}{15}(10 + \sqrt{10}),\ \eta_2^- < \eta < \eta_1^- \text{ or } \eta_1^+ < \eta < \eta_2^+ \quad , \tag{7.28}$$

$$\text{if } x_0 = \frac{2}{15}(10 + \sqrt{10}),\ \eta_2^- < \eta < \eta_1^- \text{ or } \eta_1^- < \eta < \eta_2^+ \quad , \tag{7.29}$$

$$\text{if } \frac{2}{15}(10 + \sqrt{10}) < x_0 < 2,\ \eta_2^- < \eta < \eta_2^+ \quad , \tag{7.30}$$

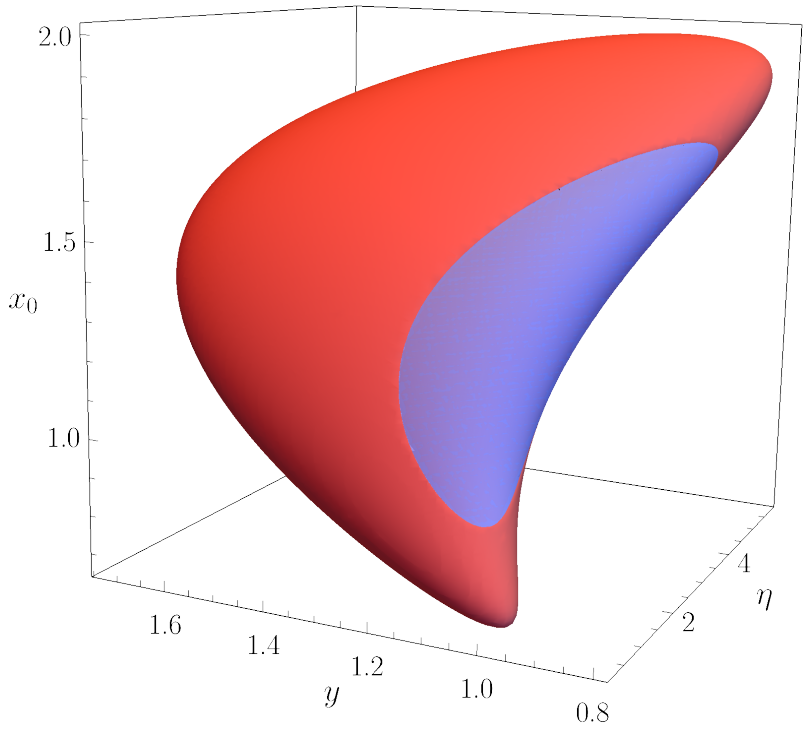

Figure 7.1.: Parameter spaces for positive (blue region) and negative (red region) energy stable asymmetric wormholes.

with dimensionless charge (in $\mathcal{M}_-$) bounded by

$$y_1^- < y < y_2^+ \quad , \tag{7.31}$$

where

$$\begin{aligned} \eta_2^{\pm} &= \frac{1+8x_0-3x_0^2}{x_0(3x_0-14)+17} \\ &\quad \pm \frac{2\sqrt{2}\sqrt{-(6x_0^4-40x_0^3+99x_0^2-104x_0+36)}}{x_0(3x_0-14)+17} \quad , \\ y_2^+ &= \frac{a+2\sqrt{b}}{\eta^2-2\eta+17} \quad . \end{aligned}$$

The second group of solutions lies in the region identified by the constraints:

$$\text{If } \frac{2}{15}(10-\sqrt{10}) < x_0 < 1,\ \eta_1^- < \eta < \eta_1^+ \quad , \tag{7.32}$$

$$\text{if } 1 < x_0 < \frac{2}{15}(10+\sqrt{10}),\ \eta_1^- \leq \eta \leq \eta_1^+ \quad , \tag{7.33}$$

$$\text{if } x_0 = \frac{2}{15}(10+\sqrt{10}), \eta = \eta_1^- \quad , \tag{7.34}$$

with dimensionless charge constrained by

$$y_1^+ < y < y_2^+ \quad . \tag{7.35}$$

The union of the two parameter spaces that identify SNE asymmetric wormholes is plotted in red in Figure 7.1.

As we can see in Figure 7.1 SPE space of parameters is embedded onto the SNE space of parameters. However it has to be pointed out that there is not any intersection between both regions. Then, as one can expect, there is not any configuration for which we can have positive and negative energy at the same time. In Appendix B an orthographic projection of Figure 7.1 is depicted for the sake of showing in a more clear way the features explained above.

Henceforth, we will consider only stable configurations, i.e, for now on we will always locate the throat of the wormhole at x_0.

Event horizon location

Since (two-way) traversable wormholes must have their two sides causally connected, an important point to set up is whether a RN-AWH has an event horizon, and if it does, whether the throat covers it. Using the dimensionless variables, one finds that the event horizon location, on each side, is given by

$$x_{h-} = 1 + \sqrt{1-y}, \tag{7.36}$$

$$x_{h+} = \xi + \sqrt{\xi^2 - \eta y}. \tag{7.37}$$

Then, in order to prevent the two universes to be causally disconnected, x_0 must be put above $x_{h\pm}$ on each side of the wormhole. This requirement leads to the following constraints:

$$\begin{aligned}
&0 < y \leq 1 \text{ and } x_0 > 1 + \sqrt{1-y},\\
&y > 1 \text{ and } 0 < x_0 < \frac{y}{2} \text{ or } x_0 > \frac{y}{2},\\
&0 < \eta \leq 1 + \frac{2x_0(x_0 - 1 - \sqrt{x_0(x_0-2)+y})}{y}.
\end{aligned}$$

In the subsequent sections, we investigate only stable two-way traversable wormholes, that is either a RN black hole glued with a RN naked singularity or two naked singularities glued together. The possibility of having two RN black holes glued together is excluded because it leads to unstable configurations. Nnote that when we mention either the RN black hole or the RN naked singularity, we are specifically referring to their respective spacetimes beyond the event horizon and the singularity itself. Consequently, the asymmetric wormhole spacetime does not possess a horizon or a singularity.

7.4. Absorption and spectral lines

7.4.1. Wave equation

Let us consider a massless scalar field, Φ, lying in a RN-AWH background. The dynamics of this field, on each side of the wormhole, is described by the Klein-Gordon equation

$$\Box_\pm \Phi_\pm = 0, \tag{7.38}$$

where $\Box_\pm$ and $\Phi_\pm$ denote the d'Alembertian operator and the scalar field, respectively, on each side of the throat. Due to spherical symmetry, the solution

of Eq. (7.38) can be written as

$$\Phi_{\pm} = \frac{\psi_{\pm}(x_{\pm})}{x_{\pm}} Y_{\ell m}(\theta, \phi) e^{-i\tilde{\omega}\tilde{t}}, \tag{7.39}$$

where $\tilde{\omega}$ is a dimensionless frequency (defined by $\tilde{\omega} \equiv \omega M_{-}$), and the radial functions $\psi_{\pm}$ satisfy

$$f_{\pm}(x_{\pm}) \frac{d}{dx_{\pm}} \left(f_{\pm}(x_{\pm}) \frac{d\psi_{\pm}}{dx_{\pm}} \right) + \left(\tilde{\omega}^2 - \tilde{V}_{\pm}(x_{\pm}) \right) \psi_{\pm} = 0, \tag{7.40}$$

with $\tilde{V}_{\pm}$ being the dimensionless effective potential on each side of the throat, given by

$$\tilde{V}_{\pm}(x_{\pm}) = \frac{f_{\pm}(x_{\pm})}{x_{\pm}} \frac{df_{\pm}}{dx_{\pm}} + \frac{f_{\pm}(x_{\pm})}{x_{\pm}^2} \ell(\ell+1). \tag{7.41}$$

The metric functions $f_{\pm}(x_{\pm})$ explicitly written in terms of the dimensionless radial coordinates are

$$f_{-}(x_{-}) = 1 - \frac{2}{x_{-}} + \frac{y}{x_{-}^2}, \tag{7.42}$$

$$f_{+}(x_{+}) = 1 - \frac{2\xi}{x_{+}} + \frac{\eta y}{x_{+}^2}. \tag{7.43}$$

One could think that the non-differentiability of the metric would introduce a delta-type contribution at the throat in the effective potential. However, one can argue that, since the metric is continuous across the shell and the d'Alembertian operator contributes only with the first derivative of the metric, $\partial_{\mu} g_{\alpha\beta}$, and the first derivative of the metric determinant, $\partial_{\mu} g = g g^{\alpha\beta} \partial_{\mu} g_{\alpha\beta}$; no delta-type distribution will appear in the effective potential. In the distributional approach, we have [197]

$$\partial_{\mu} \underline{g}_{\alpha\beta} = \partial_{\mu} g^{+}_{\alpha\beta} \, \underline{\Theta} + \partial_{\mu} g^{-}_{\alpha\beta} \, (\underline{1} - \underline{\Theta}) + n_{\mu} [g_{\alpha\beta}] \, \underline{\delta}^{\Sigma}, \tag{7.44}$$

and analogously

$$\partial_\mu \underline{g} = \partial_\mu g^+ \, \underline{\Theta} + \partial_\mu g^- \, (\underline{1} - \underline{\Theta}) + n_\mu[g] \, \underline{\delta}^\Sigma. \tag{7.45}$$

If the metric is continuous across the shell, both $[g_{\alpha\beta}]$ and $[g]$ must vanish, therefore no delta-type distribution appears in the effective potential. However, if the metric is discontinuous across the shell, as in the case of dirty black holes [253], one expects the appearance of a delta-type contribution in the effective potential.

It will be convenient to introduce a global radial coordinate to describe the spacetime, which is implicitly defined by

$$dx_\star = \pm \frac{dx_\pm}{f_\pm(x_\pm)}. \tag{7.46}$$

The main advantage of this new coordinate is that it combines the information of two independent domains, namely $x_- \in [x_0, \infty)$ and $x_+ \in [x_0, \infty)$, in a single domain $x_\star \in (-\infty, \infty)$. Moreover, with a suitable choice of integration constant, the throat location moves to $x_\star(x_0) = 0$. By using the global radial coordinate Eq. (7.46), one may write Eq. (7.40) as a Schrödinger-like equation, namely

$$\frac{d^2\psi}{dx_\star^2} + \left(\tilde{\omega}^2 - \tilde{V}(x_\star)\right)\psi = 0, \tag{7.47}$$

where we dropped the $\pm$ in the subscripts, since the global radial coordinate allows us to express the radial function and the effective potential as functions of $x_\star$, respectively, $\psi(x_\star)$ and $\tilde{V}(x_\star)$.

7.4.2. Effective potential

The effective potential plays a key role in understanding the dynamics of the scalar field. Since the RN-AWH consists of two RN spacetimes glued, it is

convenient to analyze the effective potential of the RN spacetime first. The effective potential of a RN spacetime is [254]

$$V_{\rm RN}(r) = \frac{f(r)}{r}\frac{df}{dr} + \frac{f(r)}{r^2}\ell(\ell+1), \tag{7.48}$$

where $f(r) = 1 - 2M/r + Q^2/r^2$, with M and Q being the mass and charge of the black hole, respectively. Similar to Eq. (7.46), one may define a new radial coordinate, the so-called tortoise coordinate, that moves the event horizon location to $-\infty$, namely $dr_\star = dr/f(r)$, so that the causally connected part of the manifold is described by $r_\star \in (-\infty, \infty)$. From Eq. (7.48) we notice that the effective potential vanishes at the event horizon $r = M + \sqrt{M^2 - Q^2}$ and at the spacial infinity, i.e, $V_{\rm RN} \to 0$, $r_\star \to \pm\infty$. In Figure 7.2 we plot the effective potential, for $Q^2/M^2 = 0.5$ and some angular momentum numbers ℓ, as a function of the tortoise coordinate. As can be seen from Figure 7.2, the effective potential has a peak that varies with ℓ.

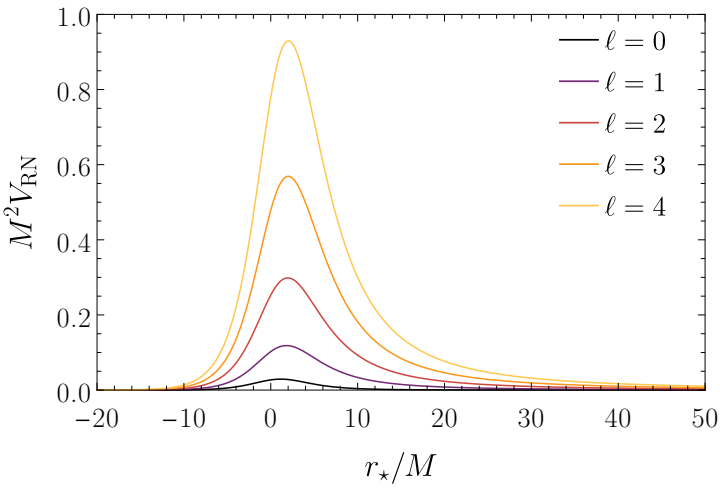

Figure 7.2.: Effective potential of a RN black hole with $Q^2/M^2 = 0.5$.

In the eikonal limit ($\ell \gg 1$) the dominant term of the effective potential is proportional to $f(r)/r^2$, i.e, it has the same dependence on r as the classical scattering potential that appears when studying the motion of null-like particles in the RN background. Consequently, for large values of ℓ, the location of the effective potential peak is at the photon sphere, namely

$$r_\gamma = \frac{3M}{2} + \frac{1}{2}\sqrt{9M^2 - 8Q^2}. \tag{7.49}$$

In the classical scattering process, the peak of the effective potential has the value $V_{\rm RN}(r_\gamma) = f(r_\gamma)/r_\gamma^2 = 1/b_c^2$, where b_c is the so-called critical impact parameter.

Now we can discuss the effective potential of RN-AWHs. Just like in the black hole case, the effective potential of the RN-AWH vanishes far from the throat, i.e, $\tilde{V} \to 0$, $x_\star \to \pm\infty$. As we get closer to the throat, the effective potential increases and it may have a peak on each side of the throat, depending on the shell location. Since the metric function is not differentiable at $x_\star = 0$, the effective potential may have a discontinuity (*jump*) at the throat, that is, $[\tilde{V}] \neq 0$, when gluing different spacetimes. In Figure 7.3 and Figure 7.4 we plot some typical behaviors of the effective potential for RN-AWHs. We notice that the number of peaks varies, depending on the throat location, since it may be located before or after the peak of the effective potential on each side. By gluing a RN black hole with a RN naked singularity at least one peak is present. By gluing two different RN naked singularities a sharp *discontinuous peak* appears apart from the possible smooth peaks; however, it is important to point out that, at this peak, $d\tilde{V}/dx_\star = 0$ is not satisfied. Actually, $\tilde{V}$ is not differentiable at $x_\star = 0$ (one can also find discontinuous effective potentials in Refs. [253, 255, 256]). In Figure 7.5 and Figure 7.6, we exhibit the embedding diagrams of the RN-AWHs considered in Figure 7.3 and Figure 7.4, respectively.

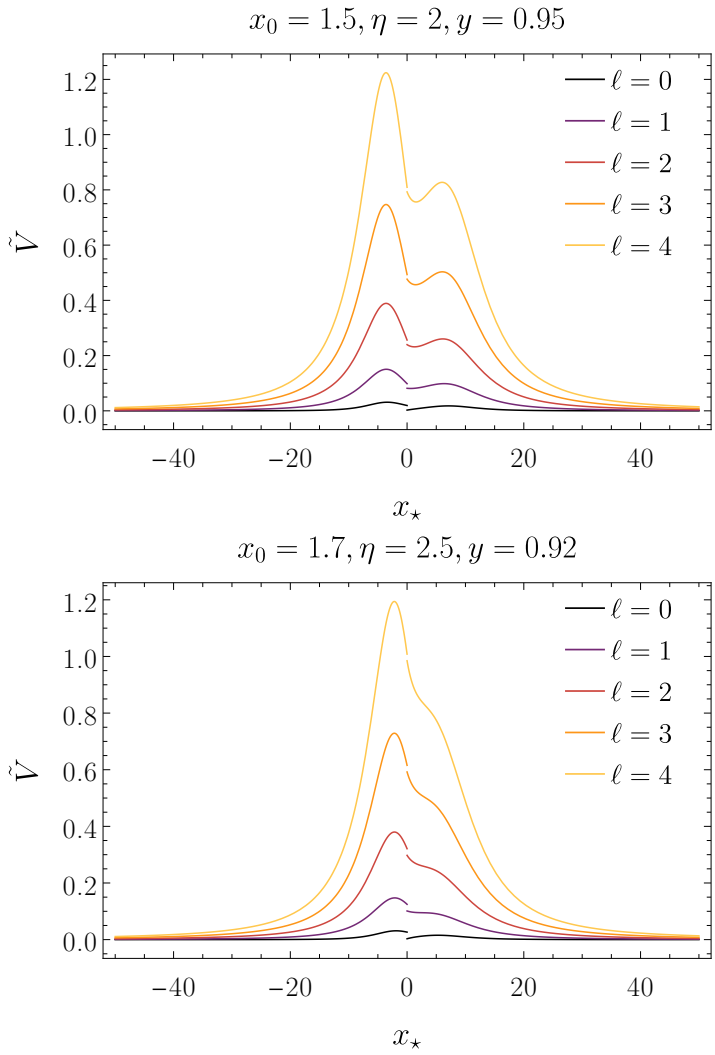

Figure 7.3.: Typical behaviors of the effective potential of RN-AWHs for SPE configurations.

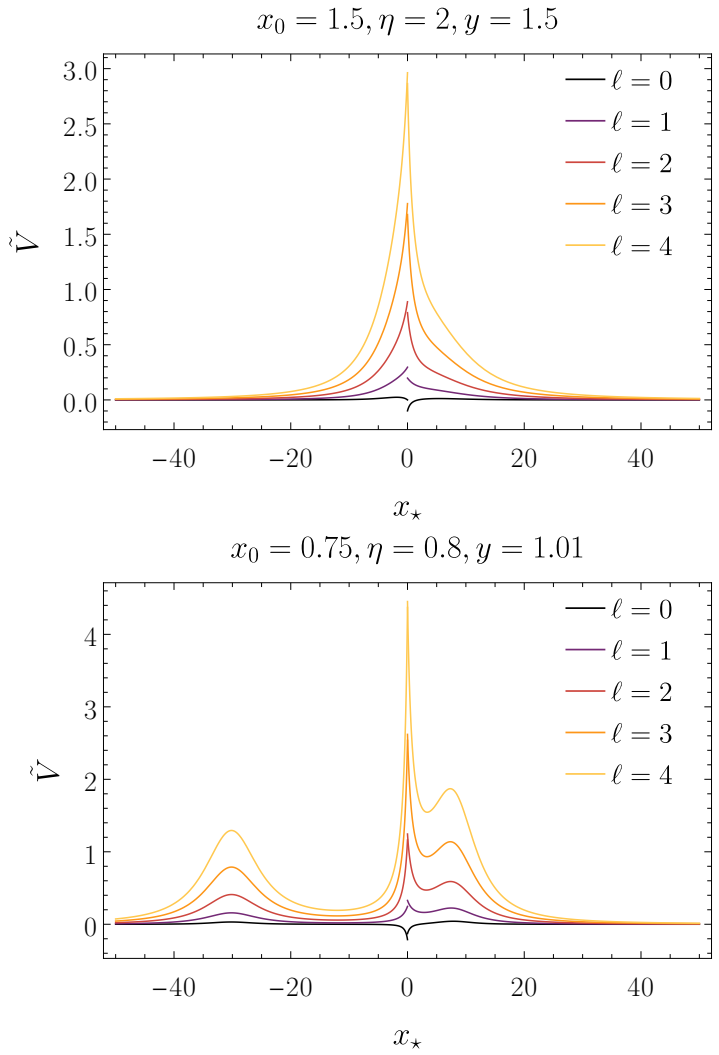

Figure 7.4.: Typical behaviors of the effective potential of RN-AWHs for SNE configurations

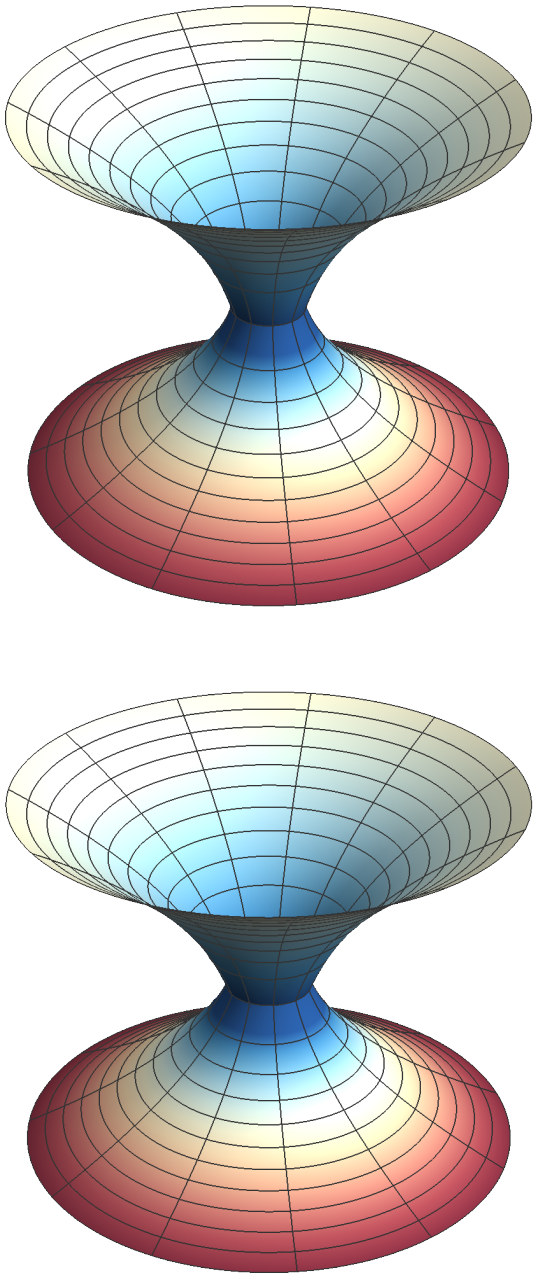

Figure 7.5.: Embedding diagrams of the RN-AWHs considered in Figure 7.3 (the display order is the same as in Figure 7.3).

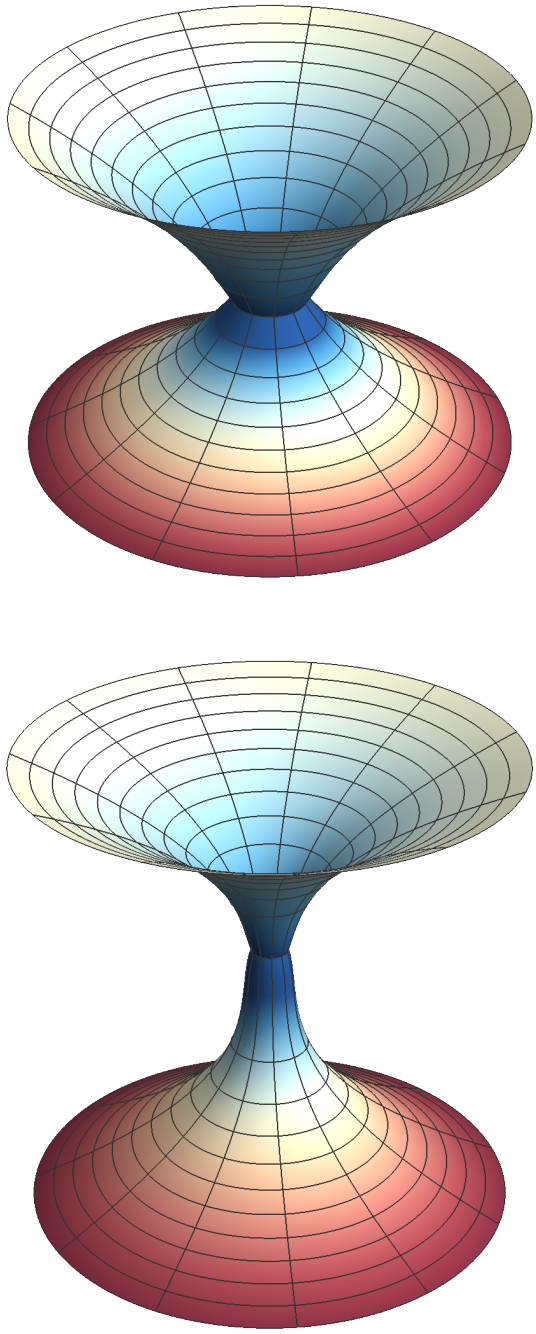

Figure 7.6.: Embedding diagrams of the RN-AWHs considered in Figure 7.4 (the display order is the same as in Figure 7.4).

7.4.3. Boundary conditions

In Figure 7.7, using the Carter-Penrose diagram of RN-AWHs, we illustrate the scattering process. Let us consider a monochromatic plane scalar wave incoming from the past null infinity of $\mathcal{M}_+$, $\mathscr{I}^-_{\mathcal{M}_+}$. This wave will interact with the effective potential; part of it will be reflected to the future null infinity of $\mathcal{M}_+$, $\mathscr{I}^+_{\mathcal{M}_+}$; and part of it will be transmitted to the future null infinity of $\mathcal{M}_-$, $\mathscr{I}^+_{\mathcal{M}_-}$. Therefore, the stationary boundary conditions of this phenomenon consist of a composition of ingoing and outgoing (*distorted*) plane waves far from the object in one side of the wormhole, and purely outgoing waves far from the object on the other side, i.e,

$$\psi(x_\star) \sim \begin{cases} e^{-i\tilde{\omega}x_\star} + \mathcal{R}_{\tilde{\omega}\ell} e^{i\tilde{\omega}x_\star}, & x_\star \to +\infty, \\ \mathcal{T}_{\tilde{\omega}\ell} e^{-i\tilde{\omega}x_\star}, & x_\star \to -\infty, \end{cases} \tag{7.50}$$

where $\mathcal{R}_{\tilde{\omega}\ell}$ and $\mathcal{T}_{\tilde{\omega}\ell}$ are complex coefficients related to the reflection and transmission coefficients, respectively. In order to obtain $\mathcal{R}_{\tilde{\omega}\ell}$ and $\mathcal{T}_{\tilde{\omega}\ell}$, one performs an integration from one asymptotic region to the other.

We have also to specify the behavior of the field at the throat. Just like the metric, we assume that the field is continuous across the throat, i.e, $[\Phi] = 0$ (hence $[\psi] = 0$), and since no delta-type distribution appears in the effective potential, we can assume that the field is also differentiable at the shell, that is, $[d\psi/dx_\star] = 0$ (see Refs. [227, 229] for some works in the literature considering the differentiability of the field, despite the non differentiability of the metric function).

7.4.4. Scalar absorption

By using the partial wave expansion together with the boundary conditions Eq. (7.50), one can write the (dimensionless) total scalar absorption cross section of RN

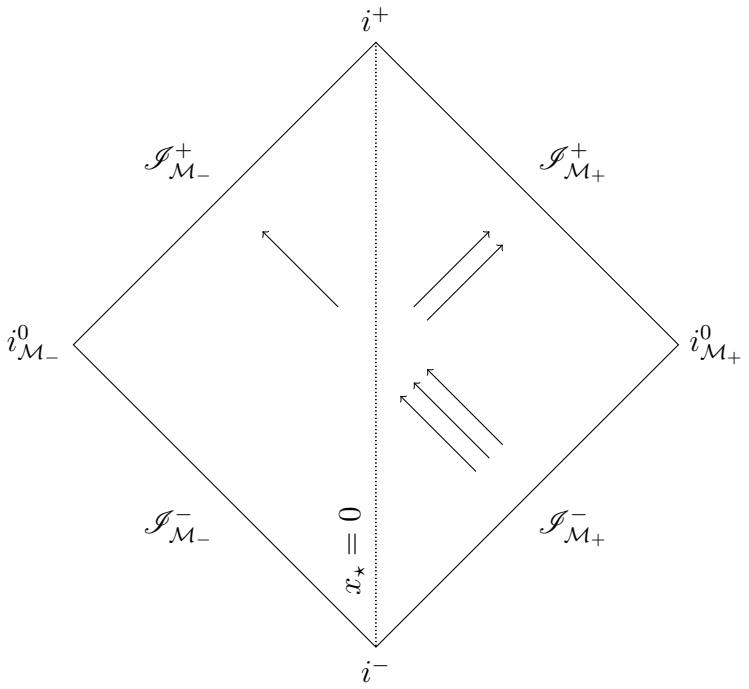

Figure 7.7.: Carter-Penrose diagram of a RN-AWH. Each triangle represents an asymptotically flat spacetime, connected by a wormhole throat, represented by the vertical dotted line. The arrows illustrate the scattering process. Here, $\mathscr{I}^+$ and $\mathscr{I}^-$ represent, respectively, the future and past null infinities, i^0 indicates the space-like infinity and i^+ and i^- are, respectively, the future and past time-like infinities. (Labels without subscript represent regions of the two sides of the wormhole that are superposed in the Carter-Penrose diagram.)

and RN-AWHs as [250, 254]

$$\tilde{\sigma}_{\rm abs} = \sum_{\ell=0}^{\infty} \tilde{\sigma}_\ell, \tag{7.51}$$

where $\tilde{\sigma}_\ell \equiv \pi(2\ell+1)\Gamma_{\tilde{\omega}\ell}/\tilde{\omega}^2$ are the (dimensionless) partial absorption cross sections, and $\Gamma_{\tilde{\omega}\ell} \equiv 1 - |\mathcal{R}_{\tilde{\omega}\ell}|^2 = |\mathcal{T}_{\tilde{\omega}\ell}|^2$ is the so-called grey-body factor, i.e., the transmission probability of a mode with frequency $\tilde{\omega}$. In black hole scenarios,

the total absorption cross section Eq. (7.51) has two well-known limits for stationary geometries, namely, the low–frequency regime ($\tilde{\omega} \to 0$), where the absorption cross section goes to the area of the black hole [257], and the high-frequency regime ($\tilde{\omega} \to \infty$), where the absorption cross section oscillates around the geometrical absorption cross section [258] (the area of a disk with radius equal to the critical impact parameter). In wormhole scenarios these limits are not so clear. For instance, some previous results in the literature show that, in the zero-frequency regime, the total absorption cross section for wormholes can differ from black hole cases [249, 250].

In Figure 7.8 we plot the total absorption cross section of two SPE wormholes, namely $\{x_0 = 1.7, \eta = 2.5, y = 0.92\}$ and $\{x_0 = 1.5, \eta = 2, y = 0.95\}$, and compare it with the total absorption cross section of a RN black hole with the same charge-to-mass ratio as for the case of $\mathcal{M}_-$, i.e., $y = Q_-^2/M_-^2 = Q^2/M^2$. The effective potential of the two wormhole configurations considered in Figure 7.8 are exhibited in Figure 7.3. We notice that, in the high-frequency regime, the total absorption cross section of RN-AWHs (constructed with a RN black hole in $\mathcal{M}_-$) goes to the RN black hole profile, i.e., it oscillates around the classical absorption cross section. However, at low-frequencies the behavior of the absorption spectra is different from the corresponding black hole case. In the zero-frequency limit, the total absorption cross section of RN-AWHs is much smaller than the corresponding black hole one, in accordance to what has been obtained in other wormhole configurations [249, 250].

In order to investigate how the energy density of the shell that supports the wormhole configuration affects the absorption spectra, let us first analyze SPE and SNE configurations with the same wormhole throat, x_0, and charge-to-charge ratio, η, but with dimensionless charge, y, constrained in different ways. By fixing $x_0 = 1.5$ and $\eta = 2$, the energy parameter of the shell diminishes as one increases the charge-to-mass ratio y (see Eq. (7.16)). For these parameters, one finds that shells with positive-energy density can support stable solutions with dimensionless charge $0.919184 < y < 1$. However, to support stable wormholes with higher values of dimensionless charge, shells with negative energy content are required. With this choice of parameters, a negative-energy

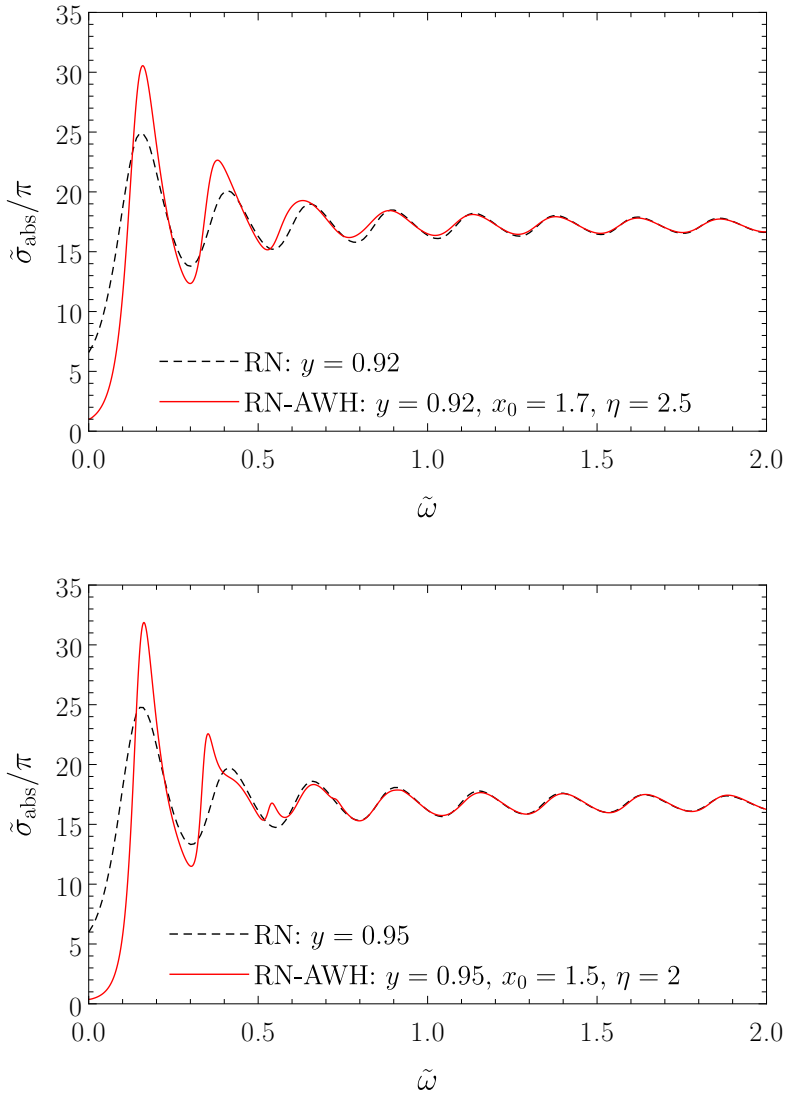

Figure 7.8.: Comparison of the absorption cross section of RN-AWHs and RN black holes with the same charge-to-mass ratio.

shell can support a stable wormhole with dimensionless charge $1 < y < 1.72787$. A glance at Figure 7.4 shows that these two families of configurations have solutions with significant differences in their effective potentials. For instance,

we can have SPE configurations with $x_0 = 1.5$ and $\eta = 2$, presenting two local maxima and a discontinuous valley between them for moderate-to-high values of ℓ, while we can have SNE configurations, with $x_0 = 1.5$ and $\eta = 2$, without a local maximum (where $d\tilde{V}/dx_\star = 0$), but with a sharp peak near the shell for moderate-to-high values of ℓ. One may expect that these differences in the effective potential lead to different behaviors of the absorption profile. This will be explored later in this section.

In Figure 7.9, we exhibit the absorption cross section of some SPE (top panel) and SNE (bottom panel) RN-AWHs configurations. We notice that increasing the dimensionless charge in $\mathcal{M}_-$ diminishes the total absorption cross section for moderate-to-high frequencies for both SPE and SNE wormholes. For SPE configurations, as we decrease y (consequently increasing the energy parameter of the shell $\tilde{\gamma}$) additional peaks arise. These new peaks get higher and are shifted to the left as the positive-energy density of the shell increases. The new peaks are related with quasibound states that can exist around the throat [249, 250], that appear due to the presence of valleys in the effective potential (a discussion about them will follow in Sec. 7.4.5). On the other hand, for SNE configurations, as y increases (hence requiring "more" negative shells) the behavior of the total absorption cross section can differ significantly from previous absorption profiles found in the literature. For this family of parameters, in the zero-frequency limit, as the energy density of the shell becomes more negative, the absorption cross section increases, getting bigger than the ones of standard black holes. This result should be related with the effective potential for $\ell = 0$. Additionally, the oscillatory pattern of the total absorption cross section slowly diminishes and approaches a straight line. This high-frequency behavior is related with the sharp peaks that appear in the effective potential at the throat. In the eikonal limit, the total absorption cross section of spherically symmetric black holes oscillates around their shadow area, with the shadow radius being the critical impact parameter, which is associated with null geodesics trapped in the last photon orbit —the photon sphere. In wormholes scenarios, it is possible to have an effective photon sphere at the throat, and it may cast novel shadows and different gravitational lensing features compared with black holes [225, 259, 260].

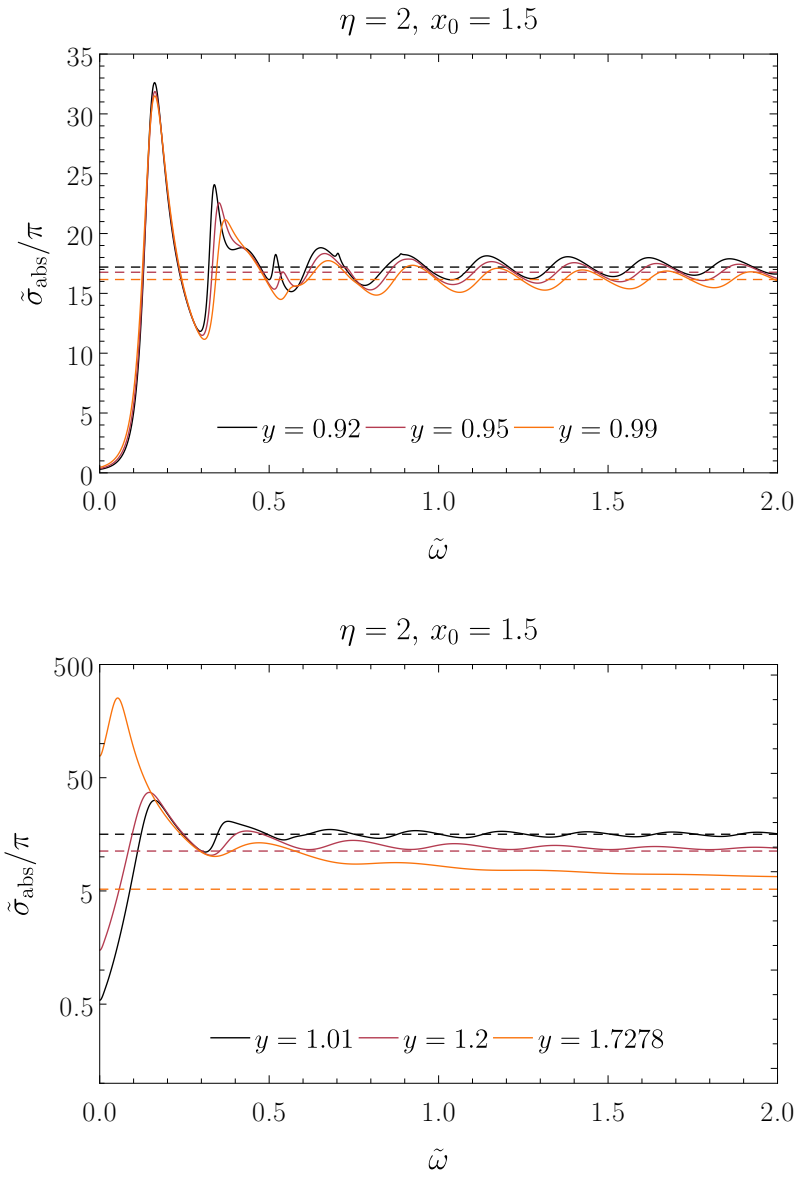

Figure 7.9.: Absorption spectra of RN-AWHs with $x_0 = 1.5$ and $\eta = 2$, supported by SPE- (top panel) and SNE (bottom panel) thin shells. The dashed lines are the shadow areas associated with the highest peak of the effective potential in the eikonal limit ($\ell \gg 1$).

Here we notice that, the throat, where we have the sharp peak of the effective potential, acts like an effective photon sphere, which can be associated with an effective critical impact parameter, $b_{\rm ec} = x_0/\sqrt{f_\pm(x_0)}$, that gets smaller as one increases the dimensionless charge y (i.e. the sharp peak gets higher as y approaches $y \approx 1.72787$). Hence, one expects that in the high-frequency regime, the absorption cross section goes to the area of this novel shadow, $A_{\rm ns} = \pi x_0^2/f_\pm(x_0)$.

Since $0 < y < 1$, the absorption spectra of RN-AHWs goes to the RN one in the eikonal limit, and the effects of the other parameters, namely x_0 and η, are less relevant in the limit that $\tilde{\omega} \gg 1$. However, for low-energy waves the absorption profile has a deep dependence on the shell location, x_0, and on the charge-to-charge ratio between the wormhole sides, η. In order to investigate how the parameters beyond the charge-to-mass ratio influence the absorption process, let us first fix the dimensionless charge and the shell location, namely let us set $y = 0.92$ and $x_0 = 1.5$. For fixed values of x_0 and y, the energy parameter of the shell decreases as we increase the charge-to-charge ratio η. Then, one finds that with this choice of parameters, wormholes are supported by SPE shells if $1.98959 < \eta < 2.78261$ and are supported by SNE shells if $2.78261 < \eta < 3.27128$. In Figure 7.10 we plot SPE (top panel) and SNE (bottom panel) configurations with $x_0 = 1.5$ and $y = 0.92$ for different choices of η. In the high-frequency regime the total absorption cross section oscillates around the classical absorption cross section, as in the RN case, and the role of η is less relevant. However, we notice that the charge-to-charge ratio strongly affects the absorption spectra for $\tilde{\omega} < 1$. From Figure 7.10 we notice that the narrower peaks that arise in the wormhole absorption spectra are shifted to the left as we increase the value of η, and the first peak gets higher for greater values of η, regardless of the sign of the shell's energy-density. The behavior of the other narrower peaks is different depending on the energy content of the shell, namely: (i) if the shell has a positive-energy density, then increasing the charge-to-charge ratio (which corresponds to decrease the energy parameter $\tilde{\gamma}$) diminishes the other narrower peaks; (ii) if the shell has negative-energy density,

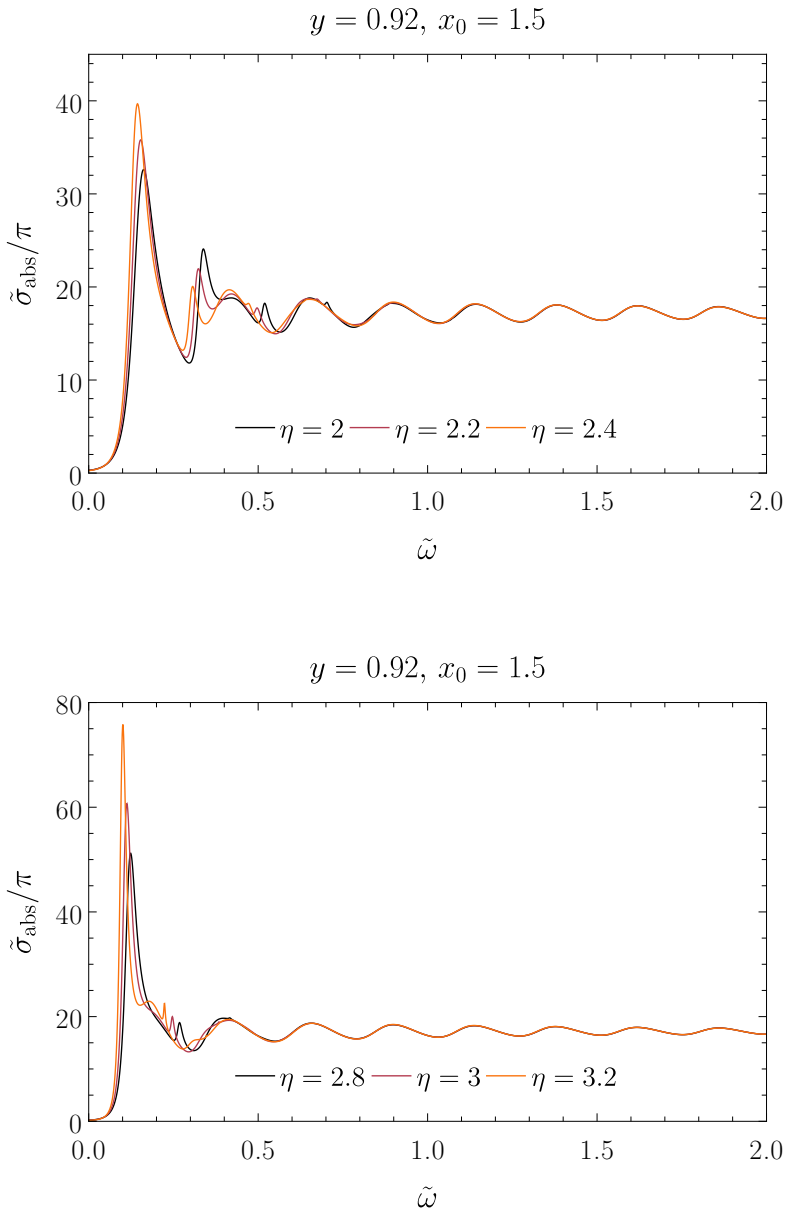

Figure 7.10.: Absorption spectra of RN-AWHs with $x_0 = 1.5$ and $y = 0.92$, supported by SPE (top panel) and SNE (bottom panel) thin shells.

increasing η (consequently going to more negative values of $\tilde{\gamma}$) also increases the other narrower peaks.

In order to investigate how the shell location affects the absorption cross section, let us first consider a configuration with dimensionless charge $y < 1$. In Figure 7.11 we plot the total absorption cross section for some RN-AWHs with $y = 0.92$, $\eta = 2.5$ and different shell locations, x_0. We also compare the absorption spectra of those AWH configurations with the one of a RN black hole with the same value as dimensionless charge. Again, we notice that in the high-frequency regime, the total absorption cross section of these configurations presents the RN profile, oscillating around the classical absorption cross section. However, in the low-frequency regime, the behavior of the absorption spectra is significantly modified by the shell location, since the shape of the effective potential is particularly dependent on the throat location. From Figure 7.11, we notice that configurations with smaller shell radius have bigger absorption

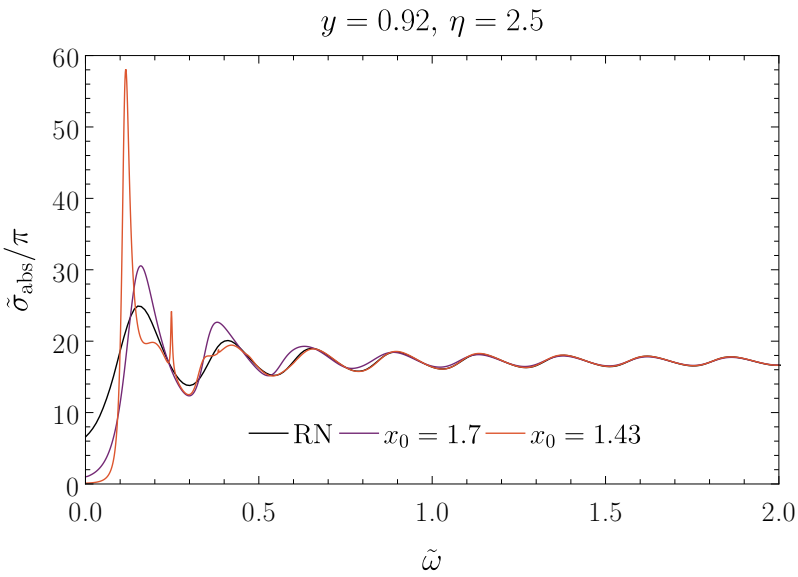

Figure 7.11.: Absorption spectra of RN-AWHs with $y = 0.92$ and $\eta = 2.5$ and some choices of x_0 compared with the absorption of a RN black hole with the same dimensionless charge as $\mathcal{M}_-$.

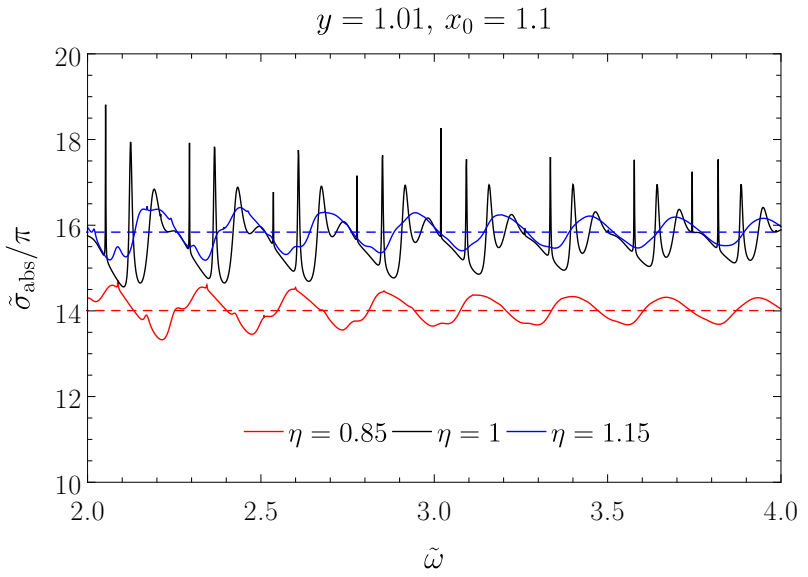

Figure 7.12.: High-frequency absorption spectra of wormholes with $x_0 = 1.1$ and $y = 1.01$ and some choices of η. The dashed lines represent the classical absorption cross sections for each spacetime.

peaks, slightly shifted to the left, in the low-frequency regime, and may exhibit additional sharp peaks as x_0 diminishes.

When considering $y > 1$, both η and x_0 may remarkably affect the absorption spectra. If $\mathcal{M}_-$ is a naked RN spacetime, then the charge-to-charge ratio may be $\eta < 1$, which leads to an effective potential with a higher peak in $\mathcal{M}_+$ instead of $\mathcal{M}_-$, and consequently with a total absorption cross section, in the high-frequency regime, smaller than for $\eta \geq 1$. We show this behavior in Figure 7.12 where we plot the high-frequency regime of the total absorption cross section of a symmetric wormhole ($\eta = 1$) and two asymmetric wormholes ($\eta = 0.85$ and $\eta = 1.15$) with $x_0 = 1.1$ and $y = 1.01$. It is important to point out that in both asymmetric configurations the presence of sharp peaks is attenuated in the high-frequency regime when compared with a symmetric configuration. The role of the symmetry in the presence of the sharp peaks will be discussed in the next section.

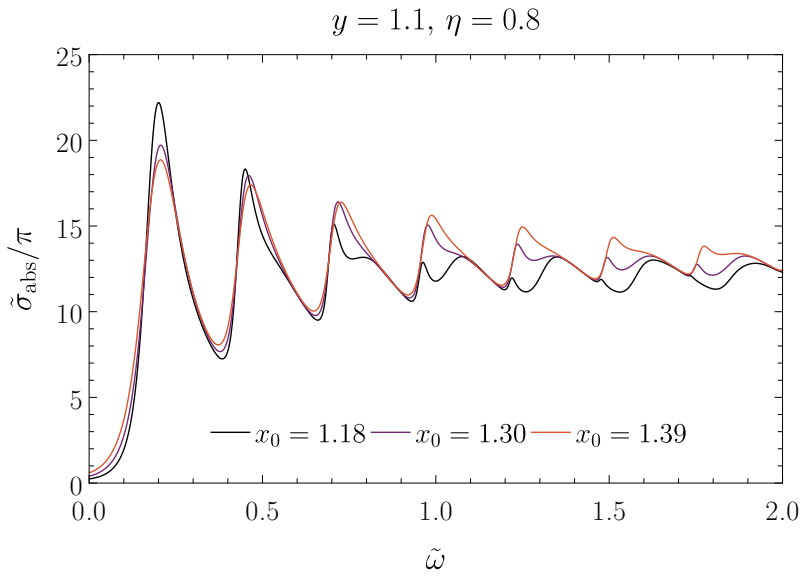

Figure 7.13.: Absorption spectra of RN-AWHs with $y = 1.1$ and $\eta = 0.8$ and some choices of x_0.

The throat location, x_0, may also imply interesting features when $y > 1$. In Figure 7.13 we plot the total absorption cross section for some RN-AWH with $y = 1.1$, $\eta = 0.8$ and different values of the shell radius, x_0. We notice that, differently from the $y < 1$ case, the shell radius plays a non-negligible role in the moderate-to-high frequency regime. We see that smaller values of x_0 present bigger absorption peaks in the low-frequency regime. However, for moderate-to-high frequencies the absorption peaks of those configurations are smaller if compared with the ones of bigger shell radius. Additionally, wormholes with smaller shell radius may present new absorption peaks in the high frequency regime, differently from the $y < 1$ case, where the new peaks appear usually in the low-frequency region.

7.4.5. Quasibound states

A remarkable feature that appears in wormhole scenarios is the existence of sharp peaks in the absorption spectra. These peaks are associated with the shape of the effective potential. If the effective potential has a valley, quasibound states can exist around the wormhole throat, producing resonant amplifications in the absorption cross section. These modes are similar to the trapped modes found in ultracompact objects [245], which in the eikonal limit may be associated with a stable light ring [248].

The quasibound states are characterized by complex frequencies with small imaginary part. In order to find the trapped modes one considers the boundary conditions

$$\psi(x_\star) \sim \begin{cases} e^{i\tilde{\omega}x_\star}, & x_\star \to +\infty, \\ e^{-i\tilde{\omega}x_\star}, & x_\star \to -\infty. \end{cases} \tag{7.52}$$

These boundary conditions generate an eigenvalue problem to $\tilde{\omega}$, and one may apply standard methods to determine those frequencies. From an approximation based on the Breit-Wigner expression for nuclear scattering [261, 262], one can relate the grey-body factor with the trapped modes, namely [245]

$$|\mathcal{T}_{\tilde{\omega}\ell}|^2\Big|_{\tilde{\omega}\approx\tilde{\omega}_r} \propto \frac{1}{(\tilde{\omega}-\tilde{\omega}_r)^2+\tilde{\omega}_i^2}. \tag{7.53}$$

Hence, one notices that the position of the resonant peaks in the transmission coefficients is determined by the real part of the mode, $\tilde{\omega}_r$, while the imaginary part, $\tilde{\omega}_i$, determines the sharp shape and height of the peaks.

Due to the freedom that we have to construct wormholes in Palatini $f(\mathcal{R})$ gravity, the effective potential of those configurations may present different *asymmetries* (cf. Figure 7.3 and Figure 7.4), which, as we saw in the previous section, may lead to more or less additional peaks in the absorption spectra. In Figure 7.14 we plot the effective potential (top row), the total absorption cross section (middle row) and the transmission coefficients (bottom row) of

a symmetric ($\eta = 1$) wormhole supported by SNE shells. The same thing regarding an asymmetric ($\eta = 1.3$) wormhole is plotted in Figure 7.15. We notice that both configurations present sharp peaks for $\tilde{\omega} < 1$. By using the direct integration method, and a standard root-finder method, one can find the frequencies that solve the eigenvalue problem and characterize the trapped modes. In Table 7.1 we present some trapped modes for the asymmetric wormhole considered in Figure 7.15.

$x_0 = 1.1$, $y = 1.01$, $\eta = 1.3$		
ℓ	$\tilde{\omega}_r$	$\tilde{\omega}_i$
0	0.0919	-2.4781×10^{-3}
	0.1707	-8.7901×10^{-3}
	0.2535	-9.2636×10^{-3}
	0.3404	-9.3142×10^{-3}
	0.4401	-9.8017×10^{-3}
	0.5155	-9.9624×10^{-3}
1	0.1985	-1.5661×10^{-5}
	0.2809	-6.4116×10^{-4}
	0.3500	-6.1025×10^{-3}
	0.4176	-6.3230×10^{-3}
	0.5753	-6.6483×10^{-3}
	0.6614	-6.7927×10^{-3}
2	0.3024	-4.6635×10^{-8}
	0.3907	-4.6659×10^{-6}
	0.4695	-1.5562×10^{-4}
	0.5383	-2.1412×10^{-3}
	0.6023	-1.7040×10^{-2}
	0.6722	-1.7339×10^{-2}

Table 7.1.: Trapped modes frequencies for RN-AWHs.

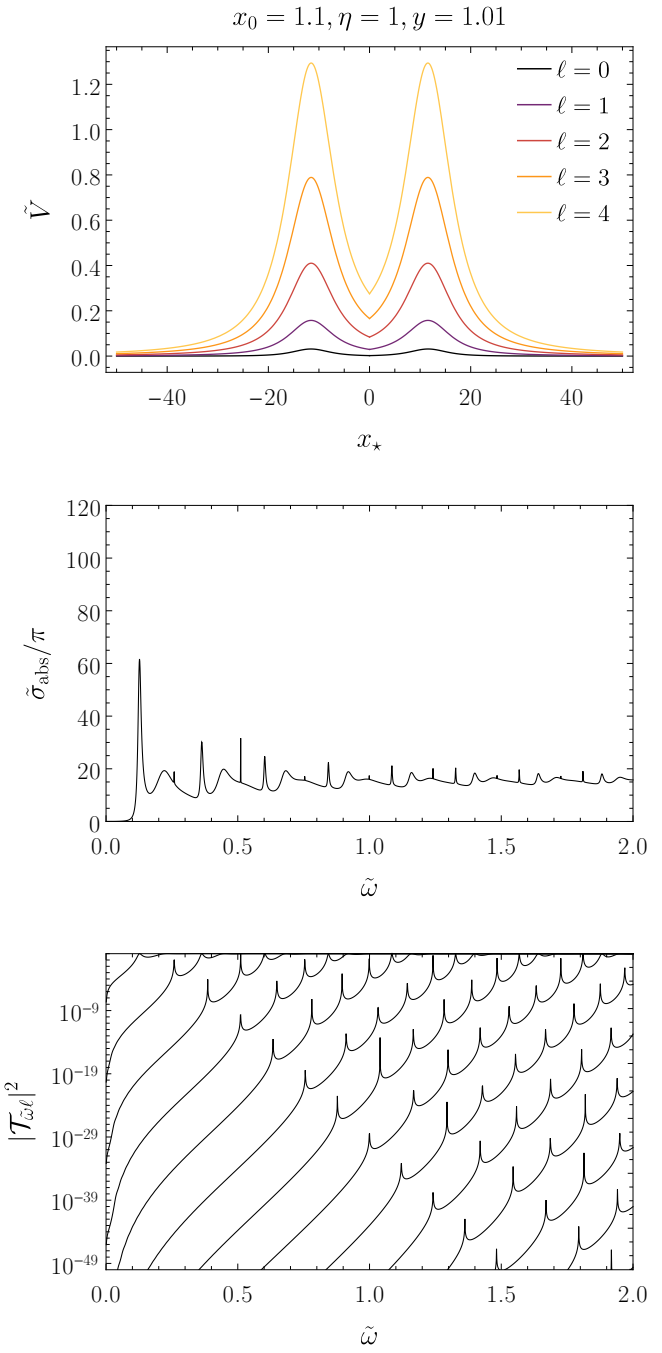

Figure 7.14.: Effective potential (top row), absorption spectra (middle row) and transmission coefficients (bottom row) of a RN symmetric wormhole with $\eta = 1$, $y = 1.01$ and $x_0 = 1.1$.

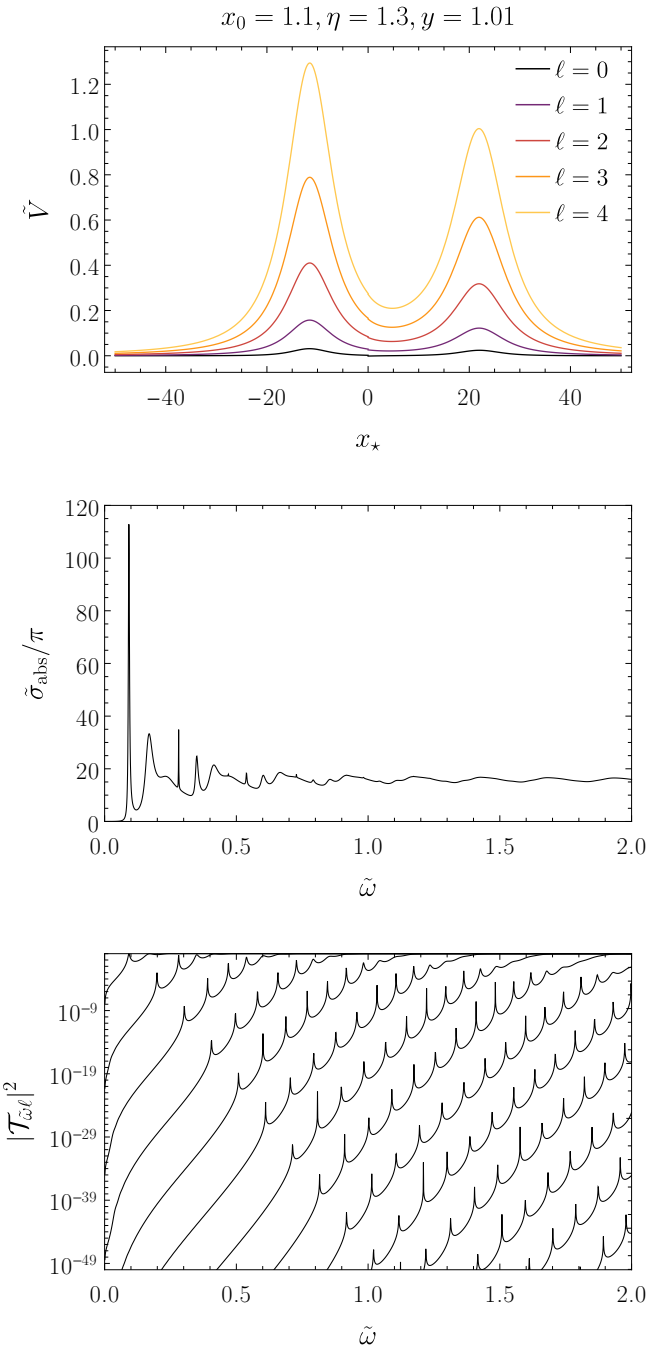

Figure 7.15.: Effective potential (top row), absorption spectra (middle row) and transmission coefficients (bottom row) of a RN-AWH with $\eta = 1.3$, $y = 1.01$ and $x_0 = 1.1$.

For the asymmetric configuration, as the frequency increases we can barely see the additional peaks in the absorption spectra. This can be understood by analyzing the asymmetry in the effective potential as one increases the ℓ number. For lower values of the angular momentum mode, the difference between the heights of the peaks in the effective potential is much smaller when compared with that difference for large values of ℓ. Hence, low-frequency trapped modes lie between two potential peaks with almost the same height, creating the resonances in the absorption spectra for $\tilde{\omega} < 1$. For larger values of ℓ the difference between the heights of the effective potential peaks becomes non-negligible, and since in the high-frequency regime the higher effective potential peak determines the absorption behavior, we almost do not see resonant amplifications in the absorption cross section. However, a glance at the transmission coefficients of the asymmetric configuration shows that we still have trapped modes around the wormhole in the eikonal limit, notwithstanding we can not see the resonant peaks in the absorption profile. Therefore, the presence of spectral lines is more evident as one restores the symmetry of the thin shell wormholes.

7.4.6. Summing up

Let us now summarize the results obtained from the analysis presented in this section. In first place, by analyzing the massless scalar field in the vicinity of stable RN-AWHs (see Figure 7.1), we found basically four effective potential behaviors, namely: (i) two smooth peaks connected by a discontinuous valley (for all values of ℓ); (ii) a single smooth peak in the effective potential for $\ell \geq 1$, and a discontinuous valley for $\ell = 0$; (iii) a discontinuous sharp peak at the throat for $\ell \geq 1$, and a discontinuous well for $\ell = 0$; and (iv) a sharp discontinuous peak at the throat followed by a smooth valley and a smooth peak on each side for $\ell \geq 1$ (for $\ell = 0$ the sharp discontinuous peak is replaced by a discontinuous well). Cases (i) and (ii) occur when one black hole spacetime is used to build the wormhole, while cases (iii) and (iv) occur when both sides are composed by naked singularity spacetimes. Since the shape of the effective

potential varies considerably with the chosen parameters, one expects noticeable changes in the absorption profile of RN-AWHs. In order to investigate how the throat location and the charge values influence the absorption, we analyzed several SPE and SNE configurations.

If the effective potential has a valley (continuous or discontinuous), quasi-bound states emerge around the throat of the wormhole. These quasitrapped modes create resonances in the absorption spectra (sharp peaks appear in the absorption cross section), which make the RN-AWH absorption profiles very different from the ones of RN black holes. These new peaks are highly influenced by the symmetry of the potential well. If the effective potential exhibits a symmetric valley, the resonances are noticeable in the whole range of frequency. On the other hand, the presence of an asymmetry in the effective potential results in the attenuation of the resonant peaks associated with quasibound states for higher ℓ-modes. Thus, the high-frequency regime of the absorption cross section becomes degenerate with the prediction for the standard RN black hole, in contrast to symmetric wormhole configurations. Consequently, even minor deviations from symmetry in wormhole spacetimes can yield significant differences on the observable characteristics associated to quasibound states. If the resonances of the symmetric case persist at very high frequencies, one could expect nontrivial effects even in the geometrical optics approximation. This could lead to unexpected features in gravitational waves spectra and electromagnetic shadows.

By considering an asymmetric configuration with dimensionless charge $y < 1$, the wormhole can mimic the standard RN black hole absorption. This can be understood by the fact that the total absorption cross section depends on the dominant light ring (associated with the highest peak of the effective potential in the eikonal limit [263]). Therefore, by grafting a RN black hole (before its photon sphere) with a RN naked singularity spacetime, the dominant light ring will be the one of the RN black hole and it will dictate the absorption cross section profile in the eikonal limit. By restoring the symmetry ($\eta \to 1$), although the absorption cross section oscillates around the classical value of RN black hole, it can be distinguished by the presence of the spectral lines.

A remarkable absorption behavior appears when we cut and paste two naked singularities, presenting discontinuous sharp peaks at the throat in the effective potential. In these scenarios, the throat acts like an effective photon sphere. Since, at the throat, the effective potential reaches a maximum value, the effective light ring related to it is the dominant light ring; therefore, the total absorption cross section will go to the area of the shadow associated with the effective light ring. Interestingly, the oscillatory pattern of the absorption profile rapidly attenuates and the absorption cross section slowly goes to the shadow area associated with null geodesics trapped on the throat.

Finally, the SPE configurations present a low-frequency limit of the total absorption cross section much smaller than the corresponding black hole ones . On the other hand, although several SNE configurations also present this typical almost zero low-frequency regime, we found configurations supported by negative energy shells such that, as we intensify the charge contents on both sides of the wormhole, the total absorption cross section noticeably increases in the low-frequency regime. This indicates that the low-frequency absorption properties are sensitive to the wormhole model parameters, having no obvious trend, which might be related with the presence of a discontinuous well in the effective potential for $\ell = 0$.

As we have seen, asymmetric wormholes exhibit distinct absorption and quasibound mode spectra in comparison to both black holes and symmetric wormholes. Therefore, it is reasonable to infer that these spacetime asymmetries could give rise to detect additional distinctions in other observables. For instance, they might lead to significant features in the quasi-normal mode spectrum and the possible presence of echoes.

Chapter 8.

Asymmetric Ellis wormhole with finite areal radius

Throughout this part of the thesis, we have delved into various types of wormholes, ranging from the foundational Einstein-Rosen bridge to the Reissner-Nordström thin-shell wormhole. A common feature among these diverse wormholes is that they are all formed by connecting an infinite universe to another (or the same) also infinite universe using different methods such as, bridges or thin shells. Returning to the outcomes detailed in Chapter 5, we see that in the case of the gravitational collapse of a boson star in Palatini $f(\mathcal{R})$ gravity, a dynamically evolving wormhole structure emerges. However, in this case, the wormhole posses a distinctive topology—one side is characterized by an infinite universe, while the other describes a finite universe undergoing expansion. Thus, in this chapter, we aim to revisit this idea and analyze observables for potential signals that could indicate the presence of such structures. Nonetheless, as the reader will notice, the wormholes we represent in this chapter are not exactly the same as those described in Chapter 5—neither is the gravitational framework, which for the present chapter is General Relativity. Rather, they provide an initial insight into the topic and should be regarded as a toy model.

One of the simplest wormhole configurations of General Relativity is represented by the already mentioned Ellis wormhole solution [184], a special case of the Ellis drainhole [184, 185]. Morris and Thorne, unaware of Ellis'

prior work, later rediscovered this configuration [186]. The Ellis wormhole also constitutes a particular solution within the broader category of Morris-Thorne traversable wormholes. It consists in two asymptotically flat spacetime regions, i.e. Minkowski spacetime, connected by a throat. In the current chapter we modify one of the infinite asymptotic region of the Ellis wormhole replacing it by some inner spatial volume endowed with finiteness in one or more directions.

On the other hand, the emission of gravitational waves by the coalescence of compact objects can distinguish between black holes (objects with an event horizon) and wormholes (no event horizon). Wormholes are expected to emit a sequence of echoes [229] absent in objects with horizons, from which nothing escapes(though these echoes are not unique to wormholes, see for instance [230]). Furthermore, the deflection of light trajectories by black holes and wormholes could differ substantially, not only due to the possibility of light escaping from the internal region of wormholes, but also because the number and structure of light rings may manifest distinct behaviors [224, 264].

Given that the effective potential experienced by scalar modes might be influenced by the finiteness of spacetime, we expect that echoes could be generated, bringing the question of how to distinguish, in a phenomenological sense, our geometrical setting with respect to analogous results from different scenarios [230, 251, 265–268].

We will also discuss the geodesic completeness of the proposed spacetime, since it is not a priori guarantee (see [94, 269] for examples of geodesically incomplete wormholes). In order to clarify this delicate issue we analyze to some extent the geodesic motion for radial and non-radial trajectories.

The present chapter is based on Ref. [5].

8.1. The model

One of the simplest (symmetric) traversable wormholes within General Relativity is represented by the Ellis wormhole, whose line element is given by [184]

$$ds^2 = -dt^2 + dx^2 + r(x)^2(d\theta^2 + \sin^2\theta d\varphi^2), \tag{8.1}$$

with radial coordinate $x \in (-\infty, \infty)$ and areal radius $r(x) = \sqrt{x^2 + a^2}$. The areal radius has a regular minimum at $x = 0$, which corresponds to the wormhole throat with radius a. As $|x|$ increases, the areal radius monotonically grows and the line element Eq. (8.1) approaches Minkowski spacetime as $x \to \pm\infty$.

Here we present a toy model of an asymmetric wormhole-like object, characterized by a bounded 2-sphere radius inner region surrounded by an asymptotically flat exterior, formally described by the line element Eq. (8.1), but with the modified radial function

$$r^2(x) = \begin{cases} x^2 + a^2, & x \geq 0, \\ x^2 + a^2 - (x^2 + a^2 - R^2)\tanh^2(c\,x^2), & x < 0, \end{cases} \tag{8.2}$$

where a and R are constants with dimension of length, while c has dimension of length^{-2}. One can check that Eq. (8.2) is endowed with a throat-like structure in $x = 0$, where $r(x)$ exhibits the regular minimum $r^2(0) = a^2$, with a taken to be the throat radius. In the asymptotic internal region, as $x \to -\infty$, the radial function $r^2(x) \to R^2$, that is, the 2-sphere radius is asymptotically bounded. In particular, when $R^2 = 0$, the 2-sphere radius shrinks to zero exponentially. The role of the parameter c is to control how much the radial function $r^2(x)$ departs from a parabola close to the throat, so that the asymptotic value R is reached faster as one increases the value of c. If $c = 0$, the radial function Eq. (8.2) reduces to the one of the Ellis wormhole, that is, $r(x)^2 = x^2 + a^2$.

In this model, the outer universe ($x \geq 0$) is described by the same line element as the Ellis wormhole spacetime. The modified areal radius Eq. (8.2), however, sharply modifies the structure of the inner universe ($x < 0$). In

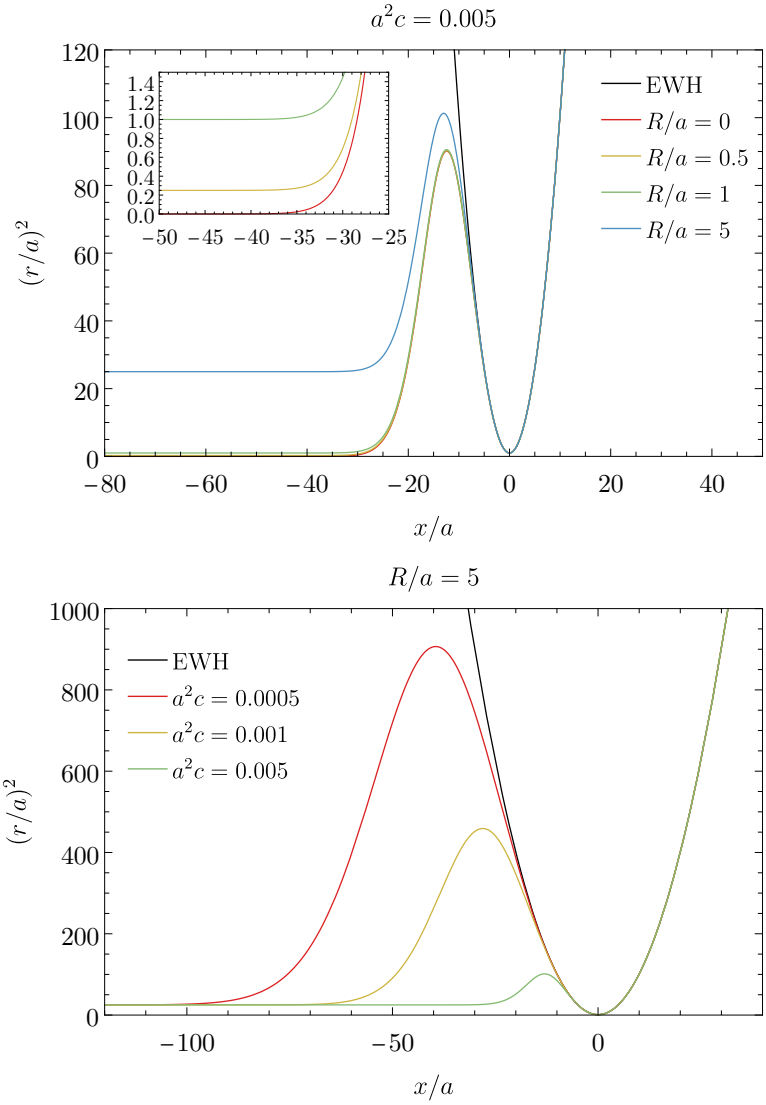

Figure 8.1.: Modified areal radius Eq. (8.2). Top panel: $r(x)^2$ for fixed value of c and different asymptotic 2-sphere radius R. Bottom panel: $r(x)^2$ for fixed R and some choices of c. We normalized the plots with the throat radius a.

Figure 8.1 we exhibit the behavior of the modified areal radius squared in both sides of the throat and compare it with the standard parabolic behavior of Ellis wormhole ($r(x)^2 = x^2 + a^2$). In the top panel we fixed the value of the parameter c and consider some values of the asymptotic 2-sphere radius R. In the bottom panel we fixed the asymptotic radius and consider different values of c. From Figure 8.1 one notices that the areal radius may present a local maximum in the inner region. One can check that maximum location, x_m, must satisfy $M(x_m) = 0$ and $r_{xx}(x_m) < 0$, where

$$M(x) \equiv 1 - 2c(x^2 + a^2 - R^2)\tanh(c\,x^2) \tag{8.3}$$

and r_{xx} stands for the second derivative of $r(x)$ (similarly r_x denotes the first derivative of $r(x)$). Since $M(x)$ is continuous in the interval $(-\infty, 0)$, and $M(x) \to -\infty$ as $x \to -\infty$ and $M(x) \to 1$ as $x \to 0^-$, there is at least one point $x_m \in (-\infty, 0)$ such that $M(x_m) = 0$, and this point is a maximum whether $r_{xx}(x_m) < 0$.

In Figure 8.2 we show the embedding diagrams of four modified Ellis wormholes with bounded 2-sphere radius in the inner region described by Eq. (8.2). In particular, in the top-left panel, we exhibit the embedding diagram of a wormhole-like object whose 2-sphere radius shrinks to zero in the asymptotic region, creating a sort of *bubble* below the throat in the embedding diagram. Additionally, we also show three configurations of finite R, with $R < a$, $R = a$ and $R > a$.

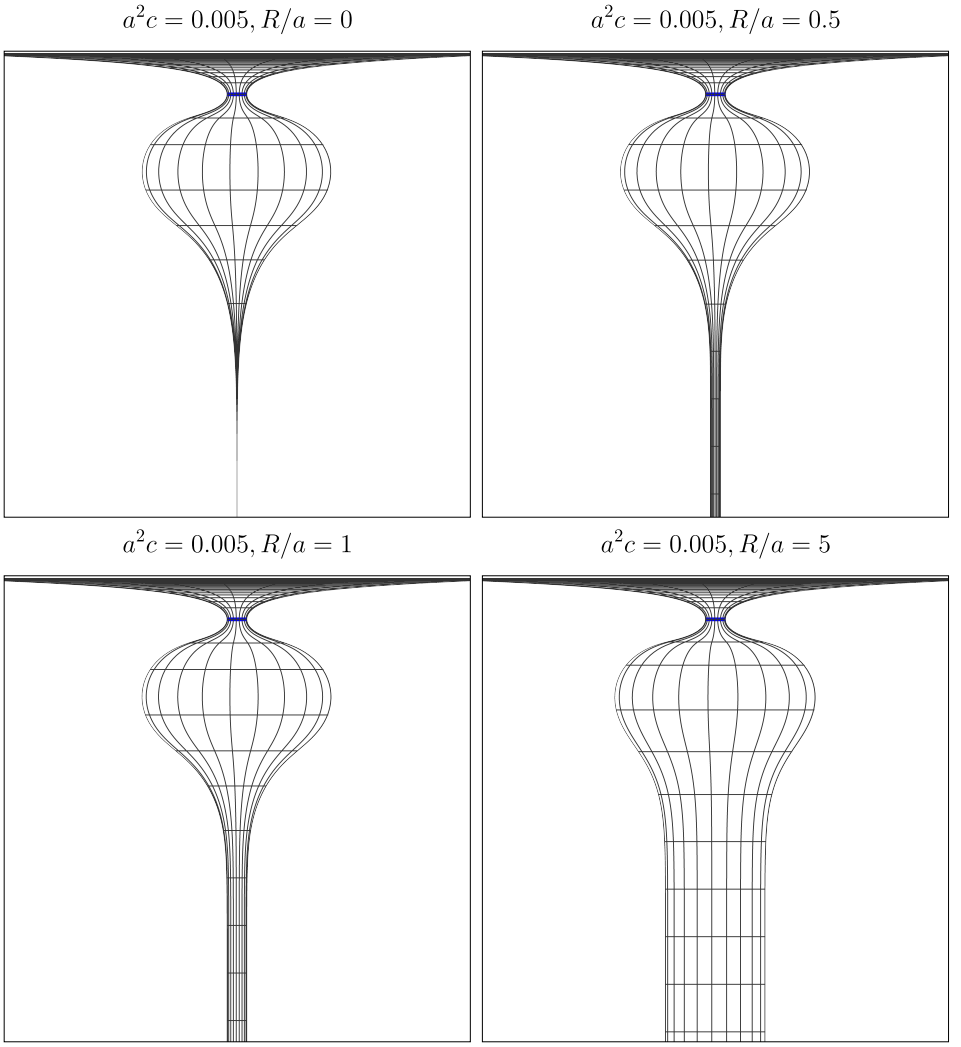

Figure 8.2.: Embedding diagrams of finite 2-sphere radius Ellis wormholes (Eq. (8.2)) with fixed value of c. In the top-left panel we exhibit a wormhole-like object in which the 2-sphere radius shrinks to zero, creating a sort of *bubble* in the internal region. The other panels correspond to asymptotic 2-sphere radius R smaller (top-right), equal (bottom-left) and bigger (bottom-right) than the wormhole throat a (represented by the blue circle).

8.1.1. Curvature, energy density and pressures

To have a better physical view of the solutions modeled by the line element Eq. (8.1) with areal radius Eq. (8.2), one can compute the curvature invariants related with it, which read

$$g_{\mu\nu}R^{\mu\nu} = \frac{2\left(1 - r_x^2 - 2rr_{xx}\right)}{r^2}, \tag{8.4}$$

$$R_{\mu\nu}R^{\mu\nu} = \frac{2\left(\left(r_x^2 - 1\right)^2 + 2r\left(r_x^2 - 1\right)r_{xx} + 3r^2 r_{xx}^2\right)}{r^4} \tag{8.5}$$

$$R_{\alpha\beta\gamma\lambda}R^{\alpha\beta\gamma\lambda} = \frac{4\left(1 - 2r_x^2 + r_x^4 + 2r^2 r_{xx}^2\right)}{r^4}. \tag{8.6}$$

Since the spacetime is asymptotically flat in the exterior region all the curvature scalars vanish very far from the throat. In the internal region, instead, curvature invariants may be bounded or unbounded depending on the asymptotic 2-sphere radius R. As the radial coordinate approaches $x \to -\infty$, one finds that $g_{\mu\nu}R^{\mu\nu} \to 2/R^2$, $R_{\mu\nu}R^{\mu\nu} \to 2/R^4$ and $R_{\alpha\beta\gamma\lambda}R^{\alpha\beta\gamma\lambda} \to 4/R^4$, corresponding to the curvature invariants of a 2-sphere of radius R. If $R = 0$ the curvature scalars are unbounded in the internal region, as they diverge as $x \to -\infty$. However, such a behaviour does not represent actually any pathology in the spacetime, since all the geodesics can be extended forever in this geometry, and no spacetime singularity is present (see discussion in Sec. 8.2).

It is a well established fact that standard Ellis wormholes can be sustained in General Relativity only in the presence of exotic matter fields, resulting in the explicit violation of the different energy conditions [186, 270]. Here,we demonstrate that our modified Ellis wormhole model, considered in the context of General Relativity, does not evade such a restriction, and exotic matter sources are still required. As we have mentioned in the previous chapters, when considering modified theories of gravity wormhole configurations can emerge in the absence of exotic matter sources [3, 139, 217, 271–276]. For the purpose of

analyzing the energy conditions, it is convenient to introduce the orthonormal frame

$$\mathbf{e}_{\hat{t}} = \partial_t,\ \mathbf{e}_{\hat{x}} = \partial_x,\ \mathbf{e}_{\hat{\theta}} = \frac{\partial_\theta}{r(x)},\ \mathbf{e}_{\hat{\phi}} = \frac{\partial_\phi}{r(x)\sin\theta}, \tag{8.7}$$

that satisfy $g_{\mu\nu}e^{\mu}_{\hat{a}}e^{\nu}_{\hat{b}} = \eta_{\hat{a}\hat{b}}$, where $\eta_{\hat{a}\hat{b}} \equiv \mathrm{diag}(-1,1,1,1)$ is the Minkowski metric. In such a frame the Einstein tensor takes the form $G_{\hat{a}\hat{b}} = G_{\mu\nu}e^{\mu}_{\hat{a}}e^{\nu}_{\hat{b}}$, whose components are:

$$G_{\hat{t}\hat{t}} = \frac{1 - r_x^2 - 2r_{xx}}{r^2}, \tag{8.8}$$

$$G_{\hat{x}\hat{x}} = \frac{r_x^2 - 1}{r^2}, \tag{8.9}$$

$$G_{\hat{\theta}\hat{\theta}} = G_{\hat{\phi}\hat{\phi}} = \frac{r_{xx}}{r}. \tag{8.10}$$

Similarly to the procedure detailed in Section 6.3, by assuming for the source of the wormhole a fluid description, in the orthonormal basis we can write the energy momentum tensor in the form $T_{\hat{a}\hat{b}} = \mathrm{diag}(-\rho(x), p_r(x), p_t(x), p_t(x))$, where its components have a well-known physical interpretation in terms of the energy density $\rho(x)$, the radial pressure $p_r(x)$ and the lateral pressure $p_t(x)$. Now, requiring that our model is a solution of General Relativity, i.e. $G_{\hat{a}\hat{b}} = \kappa T_{\hat{a}\hat{b}}$, we obtain the expressions

$$\rho = \frac{1 - r_x^2 - 2rr_{xx}}{\kappa r^2},\ p_r = -\frac{1 - r_x^2}{\kappa r^2},\ p_t = \frac{r_{xx}}{\kappa r}, \tag{8.11}$$

with $\rho = -2p_t - p_r$. Henceforth we will omit the dependence on x in the compontens of the energy momentum tensor.

Let us now write the four General Relativity energy conditions in terms of the energy-momentum tensor components. They are the null energy condition (NEC)

$$\rho + p_r \geq 0 \text{ and } \rho + p_t \geq 0, \tag{8.12}$$

the weak energy condition (WEC)

$$\rho \geq 0,\ \rho + p_r \geq 0 \text{ and } \rho + p_t \geq 0, \tag{8.13}$$

the strong energy condition (SEC)

$$\rho + p_r + 2p_t \geq 0,\ \rho + p_r \geq 0 \text{ and } \rho + p_t \geq 0, \tag{8.14}$$

and the dominant energy condition (DEC)

$$\rho \geq 0,\ p_r \in [-\rho, \rho] \text{ and } p_t \in [-\rho, \rho]. \tag{8.15}$$

As one expects, at the throat all four energy conditions are automatically violated since $r_x(0) = 0$ and $r_{xx}(0) > 0$, i.e.

$$\rho|_{\,x=0} = -\frac{2ar_{xx}(0) + 1}{\kappa a^2} < 0, \tag{8.16}$$

$$(\rho + p_r)|_{\,x=0} = -2p_t|_{\,x=0} = -\frac{2ar_{xx}(0)}{\kappa a^2} < 0. \tag{8.17}$$

Since in the inner region the areal radius goes smoothly to a finite value, its first and second derivatives vanishes asymptotically. Therefore, inside the throat, when $r \to R > 0$, the lateral pressure vanishes in the very inner region of the object, whereas the density and radial pressure are finite and positive in this limit. The finiteness of these quantities were expected since the curvature scalars are bounded in those models. On the other hand, when the areal radius shrinks until it vanishes, all the components of $T_{\hat{a}\hat{b}}$ blow up in the very inner region of the object. This is due to the fact that r goes to zero more rapidly than its derivatives, therefore even the lateral pressure diverges in this limit.

8.2. Geodesic analysis

In this section we examine into some details the geodesic trajectories of free point-like particles in their motion over the two regions of the modified Ellis wormhole.

The geodesic equation is obtained from the Lagrangian $\mathcal{L} = \dot{s}^2/2 = k/2$, where the overdot denotes a derivate with respect to an affine parameter λ and k is the normalization of the four-velocity ($k = -1, 0$ for massive particles and light-rays, respectively). Due to the symmetries of the Lagrangian, two quantities are conserved along the geodesics, namely E and L, respectively related with the time translation symmetry (the Lagrangian is independent of t) and with the rotational symmetry (the Lagrangian is independent of φ). Therefore, in the equatorial plane the geodesic equation reads

$$\dot{x}^2 = E^2 - \left(\frac{L^2}{r(x)^2} - k\right), \tag{8.18}$$

and by conducting a thorough analysis of Eq. (8.18) together with the radial function Eq. (8.2), we can unveil the underlying geodesic structure of the models we propose.

Let us first consider radial geodesics ($L = 0$) moving toward the asymptotic internal region, which, regardless of the asymptotic internal 2-sphere radius R, are given in this case by

$$\dot{x}^2 = E^2 + k, \tag{8.19}$$

$$\dot{r}^2 = r_x^2(E^2 + k). \tag{8.20}$$

Upon integration of Eq. (8.19), one obtains the trajectory for outgoing particles that cross the throat into the inner region $x(\lambda) = -\sqrt{(E^2 + k)}\lambda + x_0$, where x_0 is an integration constant. Therefore, one notices that radial geodesics can extend indefinitely, regardless of the asymptotic 2-sphere radius. This is particularly relevant when then inner 2-sphere radius shrinks to zero, and the curvature scalars, energy density and pressures diverge in the asymptotic limit $x \to -\infty$. Since it takes an infinite affine time λ to reach the asymptotic infinity, the region with ill-defined quantities is actually inaccessible for massive or massless particles in radial motion. From Eq. (8.20), one notices that the areal velocity $\dot{r}$ of particles in radial motion goes to zero when $\lambda \to \infty$ (particles going to $x \to -\infty$).

The analysis for non-radial geodesics is more involved, since we cannot obtain an analytical expression for the geodesics. However, some approximations and numerical analysis lead to some interesting conclusions. First, let us consider that the asymptotic radius R is finite and non-vanishing. When it does happen, as one approaches the asymptotic internal region, $\dot{x}^2$ is approximately

$$\dot{x}^2 \approx E^2 - \left(\frac{L^2}{R^2} - k\right), \tag{8.21}$$

which can also be integrated leading to the conclusion that even non-radial geodesic are complete for both massive and massless particles moving in the internal region of the modified Ellis wormhole with $R \neq 0$.

When $R = 0$ an interesting feature happens. The effective potential $V_{\text{eff}} = 1/r^2(x)$ grows without bound in the internal region, therefore any particle with non-zero angular momentum must suffer a bounce in the internal region being reflected to the outer universe. The only particle capable of propagating indefinitely within this object is one with zero angular momentum, whether it is massive or massless, exhibiting purely radial motion. Hence, even in the vanishing R case, all geodesics are complete.

8.2.1. Photon orbits and photon spheres

To better understand the geodesic structure of the modified Ellis wormhole, one may study the orbits in these geometries. For simplicity let us consider null geodesics ($k = 0$), and rewrite Eq. (8.18) as

$$\frac{1}{r^4}\left(\frac{dx}{d\varphi}\right)^2 = \frac{1}{b^2} - V_{\text{eff}}(x), \tag{8.22}$$

where $b = L/E$ is the impact parameter that a photon has in the exterior region. Since $x = 0$ is a regular minimum of $r^2(x)$, it is also a local maximum of the effective potential. Therefore, the throat radius a plays the role of a critical impact parameter of light-rays, since photons impinging from infinity

with impact parameter greater than the throat radius, $b > a$, do not enter in the inner universe and are scattered back to infinity; while photons with impact parameters smaller than the throat radius, $b < a$, do cross the throat and enter in the inner universe; whereas, photons with impact parameter equal to the throat radius, $b = a$, stay trapped in an unstable orbit. The location of this unstable orbit is at the local maximum of the effective potential, that is, $x = 0$ or $r = a$. This orbit is called photon sphere, and since it is at an unstable point it is called *unstable* photon sphere. If $r(x)$ has a local maximum, the effective potential also exhibits a local minimum in the inner universe. This local minimum corresponds to a *stable* photon sphere, whose existence may support long-lived modes (radiation may be trapped by these compact object). In Section 8.3 we perform a discussion of trapped scalar modes.

The behavior of the effective potential inside the throat deeply departs from the standard profile of the Ellis wormhole. For a non-vanishing asymptotic 2-sphere radius, the potential goes to a barrier of magnitude $1/R^2$ as $x \to -\infty$, while for $R = 0$, the effective potential exponentially grows inside the throat. Any photon able to enter in the inner universe ($b < a$), propagates in a bounded 2-sphere universe, and the behavior of these curves depends on the asymptotic radius R. For $R \geq a$, any photon crossing the throat must propagate toward the asymptotic infinity, since the asymptotic value of the effective potential $1/R^2 \leq 1/a^2$. However for $R < a$, after crossing the throat, depending on the photons' impact parameter, photons may suffer a bounce in the inner universe at x_b and be scattered back to the outer universe, since $1/R^2 > 1/a^2$. For non-radial geodesics ($L \neq 0$), the bounce happens if given an impact parameter b, there is an $x = x_b$ such that $V_{\text{eff}}(x_b) = 1/b^2$ and $V_{\text{eff}} > 1/b^2$ for $x < x_b$. At x_b therefore a bounce happens and the particle is scattered to the outer universe. In Figure 8.3 we show the effective potential of the configurations depicted in Figure 8.2, together with the inverse of the impact parameter squared of some photons able to cross the throat ($1/b^2 > 1/a^2$). The point $x = x_b$ where the vertical lines have the same value of the effective potential is the bounce location, where a photon is reflected in the inner universe and scattered back to the outer one.

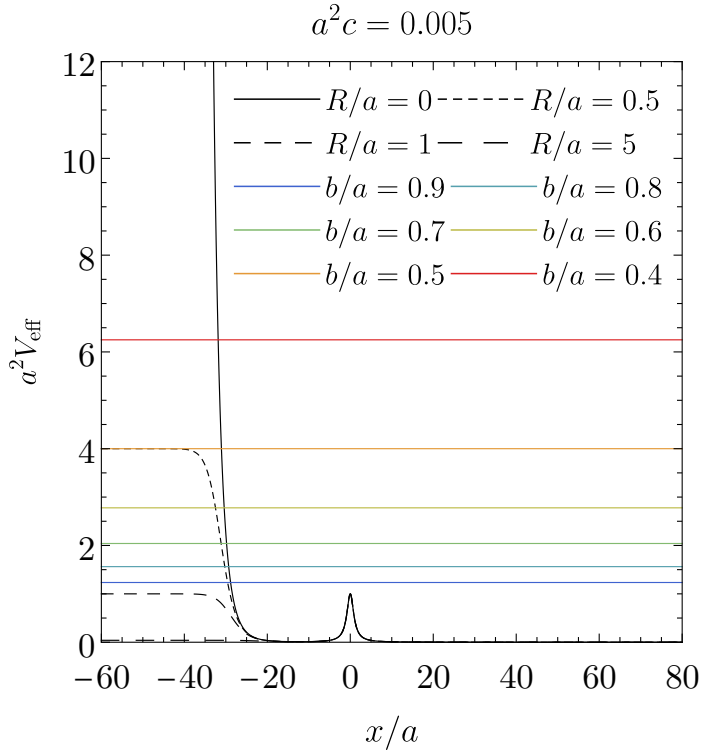

Figure 8.3.: Effective potential of four modified Ellis wormholes with fixed c and four choices of R, namely $R/a = 0, 0.5, 1$ and 5. We also plot the inverse of the impact parameter squared of some photons that enter in the inner region of the modified Ellis wormhole.

In Figure 8.4 we show how the four configurations shown in Figure 8.3 scatter light rays with the same impact parameter in the outer universe. In the top-left panel, the geodesics progapate in a modified Ellis wormhole with vanishing asymptotic 2-sphere radius. As previously discussed, any non-radial geodesic moving through the inner region must suffer a bounce. This behavior is shown in the top-left panel of Figure 8.4. When $R < a$, depending on the impact parameter the geodesic can be scattered to the outer universe or propagate to the asymptotic inernal region. We exhibit this behavior in the top-right panel of Figure 8.4. We can see that, geodesics with impact parameter $b \leq R$ are scattered back to the outer universe, and any other geodesic crossing the

throat must propagate to the asymptotic internal region with bounded 2-sphere. The bottom-left and bottom-right panels, respectively, exhibit geodesics in $R = a$ and $R > a$ modified Ellis wormholes. In these configurations any photon crossing the throat to the inner universe, propagates toward it to the asymptotic internal region with bounded 2-sphere.

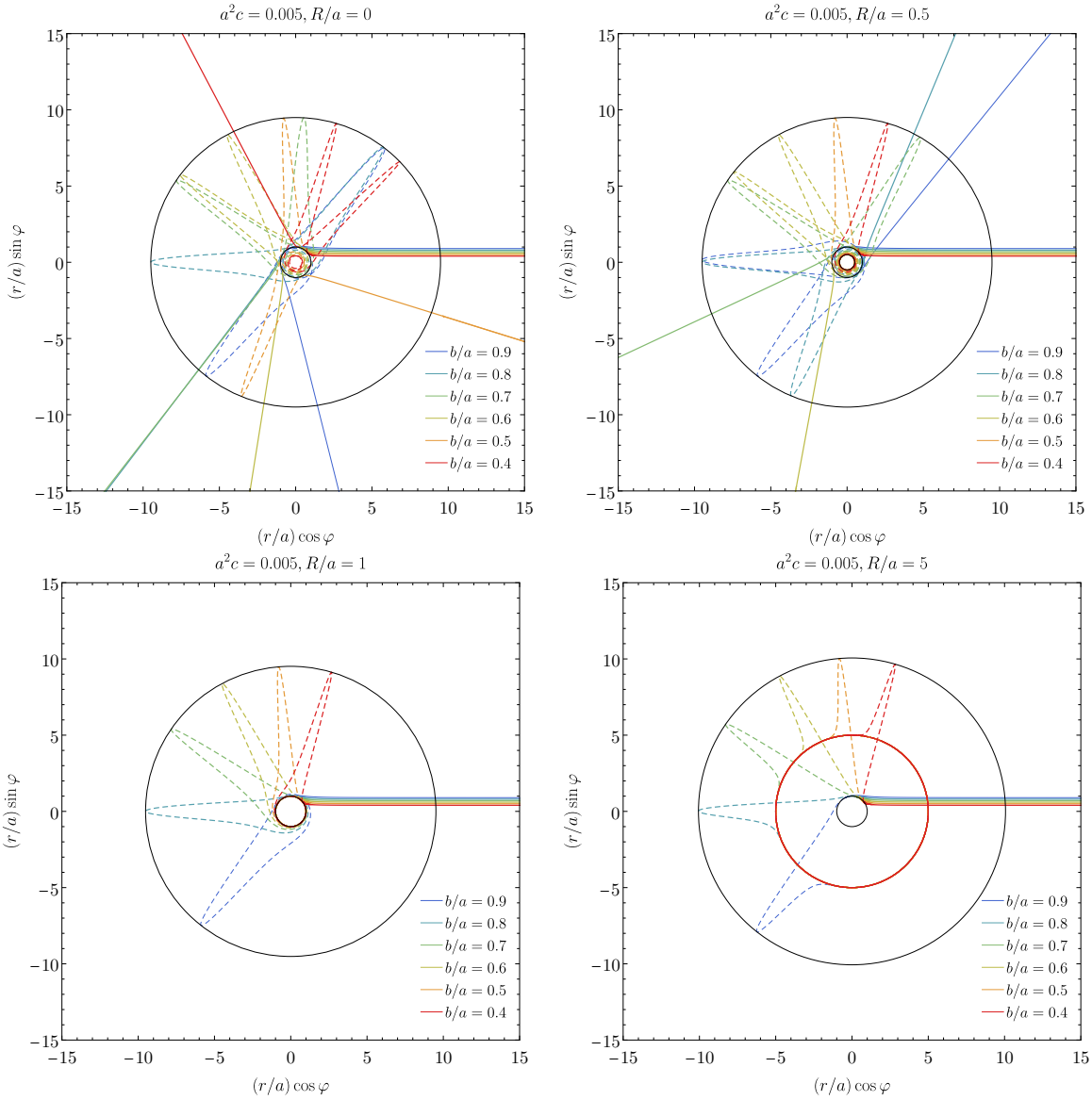

Figure 8.4.: Null geodesics in the modified Ellis wormhole. Solid lines correspond to light rays propagating in the outer universe, while dashed lines represent geodesics in the inner universe. We are considering photons with the same values of impact parameter in the outer universe, and showing how these photons are scattered or absorbed depeding on the modified Ellis wormhole configuration. The circle with radius 1 corresponds to the throat of the wormhole; the outermost circle corresponds to the local maximum of the areal radius $r(x)$ in the inner universe. The other circles are the asymptotic 2-sphere radius of each configuration.

8.3. Scalar field perturbations

In order to extract valuable information about the geometries investigated in this study, we turn our attention to the analysis of scalar perturbations on the background metric $g_{\mu\nu}$. By examining the evolution of these perturbations, we can discern the distinctive effects that these geometries imprint on the time-domain profiles, making them distinguishable from other black hole and wormhole configurations.

For a massless scalar field Ψ localized within the background metric $g_{\mu\nu}$, the dynamics of the field are governed by the Klein-Gordon equation

$$\Box\Psi(t,x,\theta,\varphi)=0. \tag{8.23}$$

Due to the spherical symmetry of the problem, we can decompose the field in the following way

$$\Psi(x^{\mu})=\sum_{\ell=0}^{\infty}\sum_{m=-\ell}^{\ell}\frac{\Phi(x,t)}{r(x)}Y_{\ell m}(\theta,\varphi), \tag{8.24}$$

where $Y_{\ell m}(\theta,\varphi)$ denotes spherical harmonics of degree ℓ and order m. By substituting Eq. (8.24) in Eq. (8.23), one obtains that the radial function

$$\left(\frac{d^2}{dt^2}-\frac{d^2}{dx^2}+V_{\Phi}\right)\Phi=0, \tag{8.25}$$

where the effective potential V_{Φ} is given by

$$V_{\Phi}=\frac{\ell(\ell+1)}{r(x)^2}+\frac{r_{xx}}{r(x)}. \tag{8.26}$$

Now, in order to integrate the wave equation Eq. (8.25) we follow the procedure described in [277]. This involves introducing light-cone coordinates, specifically the advanced time coordinate denoted as $v\equiv t+x$ and the retarded time coordinate denoted as $u\equiv t-x$. Thus, the wave equation can be expressed

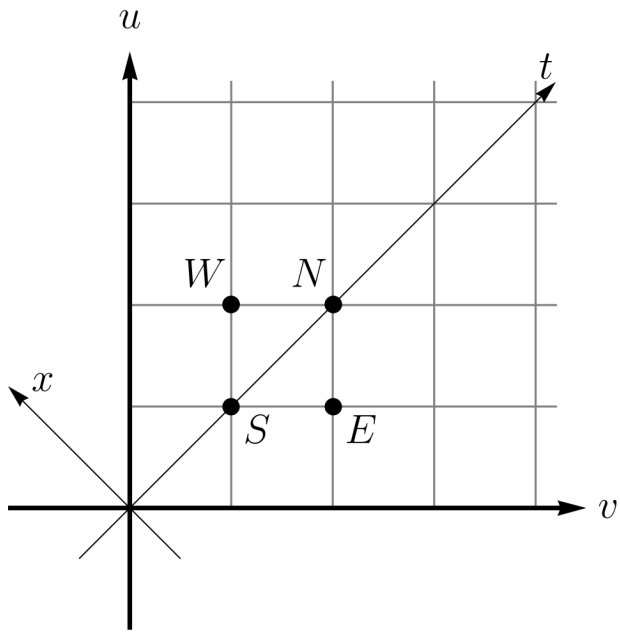

Figure 8.5.: Representation of the numerical grid used for the integration of Eq. (8.27). The evaluation points of Eq. (8.28) are represented with S, W, E and N. The stepsize of the grid can be visualized by the distance between to consecutive points in the same axis $h = u_E - u_S = v_N - v_E$.

as

$$\left(4\frac{d^2}{dudv} + V_\Phi\right)\Phi = 0. \tag{8.27}$$

The integration of this differential equation is done numerically on a null grid which leads to the following expression for the discretized scalar field evolution

$$\Phi_N = \Phi_E + \Phi_W - \Phi_S - \frac{h^2}{8}V_\Phi(S)(\Phi_W + \Phi_E) + O(h^4), \tag{8.28}$$

where h is the stepsize between two neighboring grid points and subscripts indicate the point in the grid where the function is evaluated. Explicitly, $S = (u, v)$, $W = (u + h, v)$, $E = (u, v + h)$ and $N = (u + h, v + h)$, as can be seen more clearly in Fig 8.5.

The initial distribution for the scalar perturbation is set on the null surfaces $u = 0$ and $v = 0$. Then, the grid is computed line by line using the mechanism described in Eq. (8.28), with a stepsize $h = 0.1$ and grid values ranging from $u_{\min} = 0$ to $u_{\max} = 1000$ and $v_{\min} = 0$ to $v_{\max} = 1000$. As initial conditions for the scalar perturbation we use a gaussian distribution on the $u = 0$ surface, together with a constant profile on the $v = 0$ surface, i.e.:

$$\Phi(0, v) = Ae^{-(v-v_c)^2/(2\sigma^2)}, \tag{8.29}$$

with height $A = 1$, width $\sigma^2 = 4.5$ and centered at $v_c = 20$.

The effective potential is then calculated by applying Eq. (8.26) and using the radial function $r(x)$ as presented in Eq. (8.2). Radial profiles of the effective potential with $R/a = 0$ are depicted in Figure 8.6, where, in order to optimize the grid we designed, the throat of the wormhole has been conveniently shifted to $x = -20$. As one can see, the effective potential exhibits a peak like in standard Ellis wormholes, which is associated to the throat of the wormhole, and with their maximum value increasing in proportion to ℓ. Conversely, as x tends to $-\infty$, the potential does not drop to zero, but it shows a rapid and smooth growth, remaining finite for all finite radial values. It is remarkable that the effective potential exhibits a significantly slower growth as x approaches $-\infty$ for the fundamental ℓ-mode as compared to higher ℓ-modes. Moreover, with increasing values of ℓ, it approaches infinity at a faster rate, although the most prominent discrepancy in growth rate is observed between $\ell = 0$ and $\ell = 1$. Such a behavior, combined with the first peak, gives rise to a well, which is expected to lead to echoes in the time-domain spectrum. For the fundamental ℓ-mode, the effective potential assumes negative values within the well near the peak associated with the throat of the wormhole. The radial extent over which negative effective potential occurs diminishes as ℓ increases. Finally, it is worth mentioning that the parameter c exerts an influence on the effective potential, causing the well formed between the throat peak and the asymptotic boundary to narrow as its value increases.

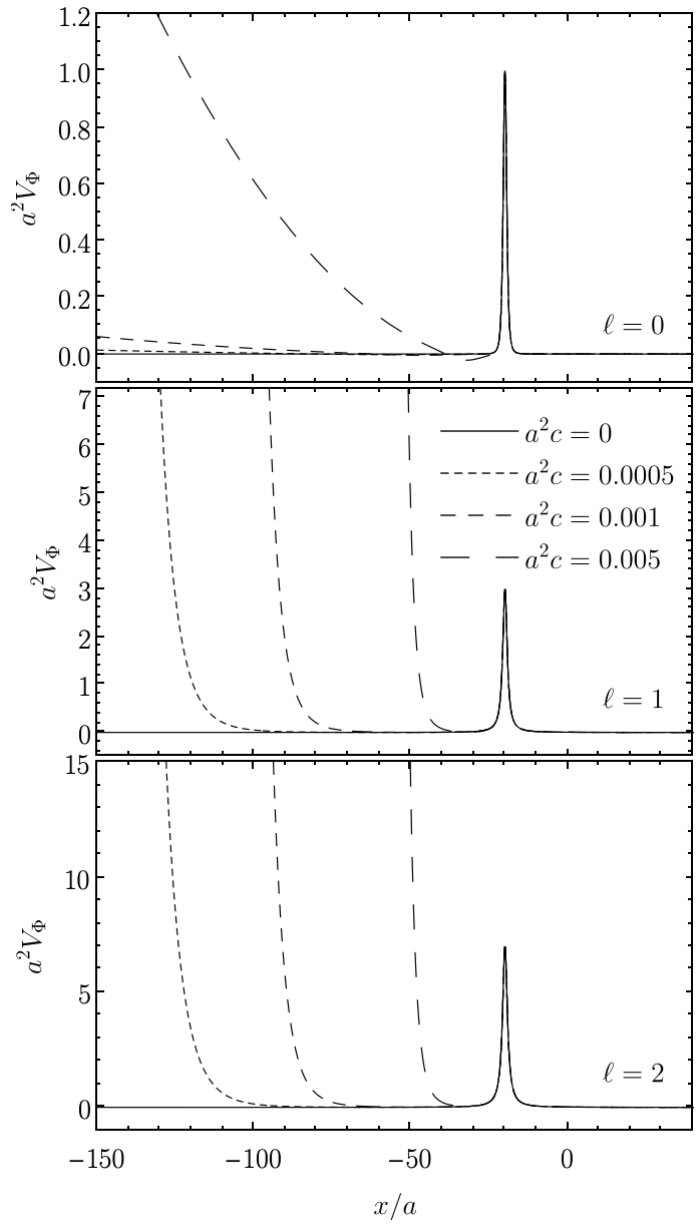

Figure 8.6.: The radial profiles of the effective potential Eq. (8.26) are presented for three ℓ-modes and $R/a = 0$. The top panel displays the case for $\ell = 0$, the central panel shows $\ell = 1$, and the bottom panel shows $\ell = 2$. The solid line represents the radial profile of the effective potential for the standard Ellis wormhole, while dashed lines correspond to three different configurations of modified Ellis wormhole with varying c parameters.

For the non-vanishing R case, one can show that the asymptotic behavior of V_Φ reads

$$\lim_{x\to+\infty} V_\Phi = 0, \tag{8.30}$$

$$\lim_{x\to-\infty} V_\Phi = \begin{cases} 0, & \ell = 0, \\ \dfrac{\ell(\ell+1)}{R^2}, & \ell \neq 0. \end{cases} \tag{8.31}$$

It is worth nothing that in the asymptotic internal region, whenever $\ell \neq 0$ and $R \neq 0$, the effective potential goes to a threshold value. The massless scalar field propagating in this region would behave equivalently to a scalar field with effective mass in a Minkowski background, namely

$$\left(\frac{d^2}{dt^2} - \frac{d^2}{dx^2} + \mu_e^2\right)\Phi = 0, \tag{8.32}$$

where $\mu_e = \sqrt{\ell(\ell+1)}/R$. This kind of effective mass in scalar field dynamics typically arises in non-asymptotically flat spacetimes, such as when scalar waves propagate around a black hole immersed in a magnetic field [278, 279]. For the case $\ell = 0$, the effective potential vanishes asymptotically in both sides of the modified Ellis wormhole, therefore no effective mass term appears.

In Figure 8.7, we depict the radial profiles of the effective potential for $\ell = 1$ and various values of the R parameter. As observed in the geodesic analysis, the presence of a non-zero R leads to the asymptotic finiteness of the potential as $x \to -\infty$. The finite value towards which the potential tends is inversely proportional to the magnitude of R, with the potential becoming approximately two orders of magnitude smaller than the throat peak for $R/a = 5$.

As the 2-sphere approaches its asymptotic value, the effective potential exhibits a sort of effective centrifugal barrier for $R = 0$, playing the role of an effective mirror for the scalar field perturbation. For $R \neq 0$ in this same limit, one can see that the effective potential tends to a plateau which height is proportional to $1/R^2$.

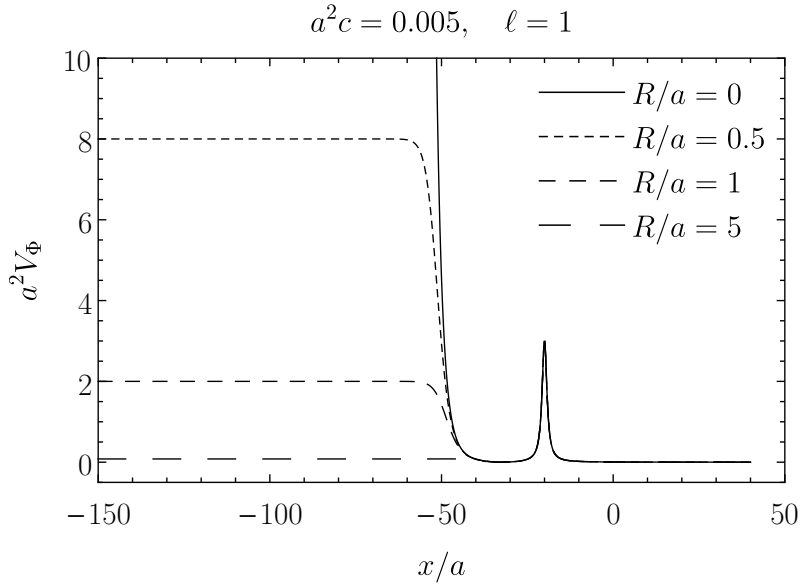

Figure 8.7.: The radial profiles of the effective potential Eq. (8.26) are presented for four configurations with different R parameter and $\ell = 1$.

8.3.1. Time-domain profile

After solving the discretized wave equation, we extract the scalar field values at the observation point $x_{\rm obs} = 0$ using the coordinate transformation $x = (u-v)/2$ and $t = (u+v)/2$. The numerical integration results are displayed in Figure 8.8. In the top panels, the time-domain evolution of the scalar field for an Ellis wormhole is shown as a reference. Even though our model allows arbitrary large values of c, here we are focusing on small deviations of Ellis wormholes in the throat scale, therefore restricting our analysis to $a^2c \leq 0.01$. This makes with the potential peak at the throat to be almost the same as Ellis wormhole (see Figs. 8.6 and 8.7). As the initial wave packet impinges on the modified Ellis wormhole, it encounters the throat peak first, causing a portion of the wave to return to the observation point and exhibiting a characteristic ringdown. Due to the similarities between the throat peaks of modified and standard Ellis

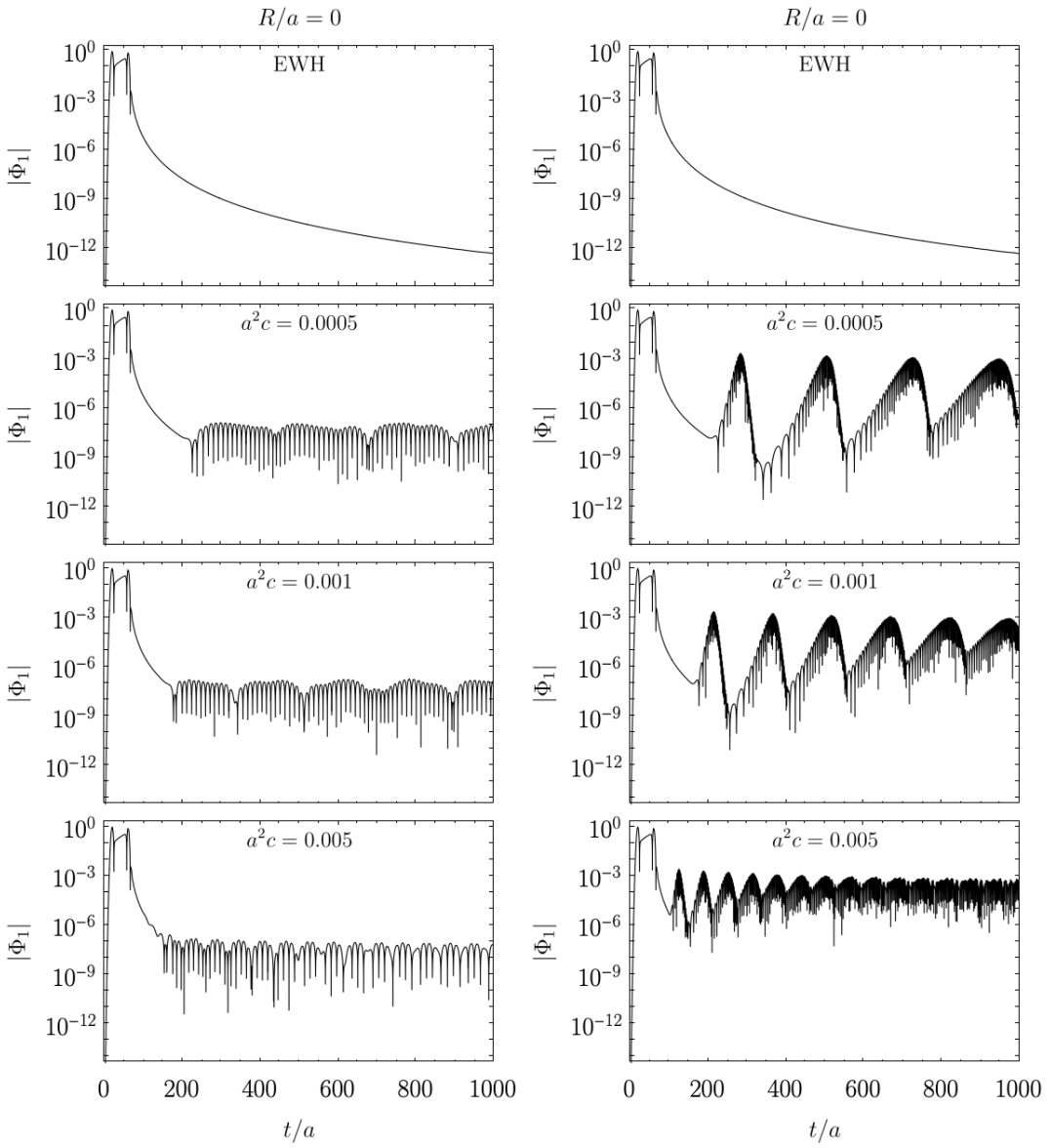

Figure 8.8.: Time-domain profile of the absolute value of the scalar field perturbation for the $\ell = 1$ mode. The top panels depict identical geometries associated with the Ellis wormhole. In the left column, three configurations with varying values of the parameter c and $R/a = 0$ are displayed. In the right column, three configurations with different values of the parameter c are shown, but with $R/a = 5$. The disparity between the Ellis wormhole and the other cases are the so-called echoes.

wormholes, the prompt contribution and initial ringdown signal in the time profile of scalar perturbations are expected to be basically the same in both scenarios.

The portion of the scalar wave packet that is transmitted by the throat peak passes through the well and encounters the potential barrier extending to $x \to -\infty$. It then reflects back towards the observation point. However, in order to reach $x_{\rm obs}$, it must interact with the throat peak once again. A portion of the incident wave is reflected, repeating the same process, while another portion is transmitted. The transmitted portion, after being detected at the observation point, evolves towards $x \to \infty$ and does not pass through the observation point again. Each time a wave is reflected and passes through the observation point, it is recorded as a peak in the time-domain profile of $|\Phi_l|$. As expected based on the description of the effective potential of modified Ellis wormhole, (unstable) photon sphere modes from the scalar perturbation exist and ring in the same way as in standard Ellis wormhole. However, in this case, there is a stable photon sphere in the inner universe, causing the bounded 2-sphere region of the wormhole to act as a cavity, trapping photon sphere modes. This results in a series of echoes in the scalar perturbation time profile, which are illustrated in Figure 8.8. The characteristics of these echoes vary depending on the parameters used to construct the spacetime, since the width and height of the cavity in the effective potential deeply depend on c and R.

Let us now discuss the $R = 0$ spacetimes, corresponding to the left column of Figure 8.8. It can be observed that there is a relationship between the value of the parameter c and the frequency of the echoes. This arises from the fact that c influences the width of the effective potential well. As the well becomes narrower with increasing c, it can be observed that the time interval between two consecutive echoes decreases (or, equivalently the frequency increases), as the waves have to travel a shorter distance.

Another notable feature that can be observed is the gradual decay of peak amplitudes. Each time the scalar wave packet interacts with the throat peak, it is divided into transmitted and reflected parts, resulting in weaker successive

echoes. This effect contrasts with the case of the Ellis wormhole, where the signal exhibits a rapid decay compared to the modified Ellis scenario. The presence of two asymptotic infinities and the absence of a potential well in the Ellis wormhole prevent the emergence of echoes, thereby contributing to the faster signal decay. When the potential well is narrower, the superposition of different echoes becomes more noticeable, leading to deformations in their waveforms. This behavior is particularly evident in the late-time regime, as shown by the bottom plot in the left column of Figure 8.8.

Similar features are noticeable also in the right column of Figure 8.8, corresponding to the $R/a = 5$ configuration. However, the echoes' amplitudes are notably smaller compared to the previous scenario, making it difficult to differentiate distinct echoes due to their reduced amplitude.

The absence of an unbounded growing effective potential results in wave packets interacting with a finite barrier, leading once again to the division of the package into a reflected part and a transmitted part that propagates towards $x \to -\infty$ without bouncing back to the outer universe. The height of the barrier diminishes as R increases, making it evident that the reflected part of the wave also is smaller as one considers bigger values of R, as shown in Figure 8.9. Notably, there is a distinct transition regime depending on the asymptotic value to which the effective potential tends. Specifically, the asymptotic value aligns with the height of the throat peak for $R/a \approx 0.8$ for the considered configurations. When the barrier exceeds the throat peak height ($R/a < 0.8$), the echoes are easily distinguishable. However, when the barrier is smaller ($R/a > 0.8$), a higher proportion of the wave is lost, leading to a reduction in the amplitude of the echoes.

Remarkably, in the asymptotic limit $R \to \infty$, the effective potential V_Φ recovers the usual behaviour of the one of Ellis wormhole in the inner universe, that is, $V_\Phi \to 0$ as $x \to -\infty$. Therefore, the time-domain profile of modified Ellis wormhole with large asymptotic 2-sphere radius, tends towards the expected profile of a standard Ellis wormhole.

Finally, it is noteworthy that while the results presented here are for the $\ell = 1$ mode, the qualitative characteristics are present in the other ℓ-modes as well.

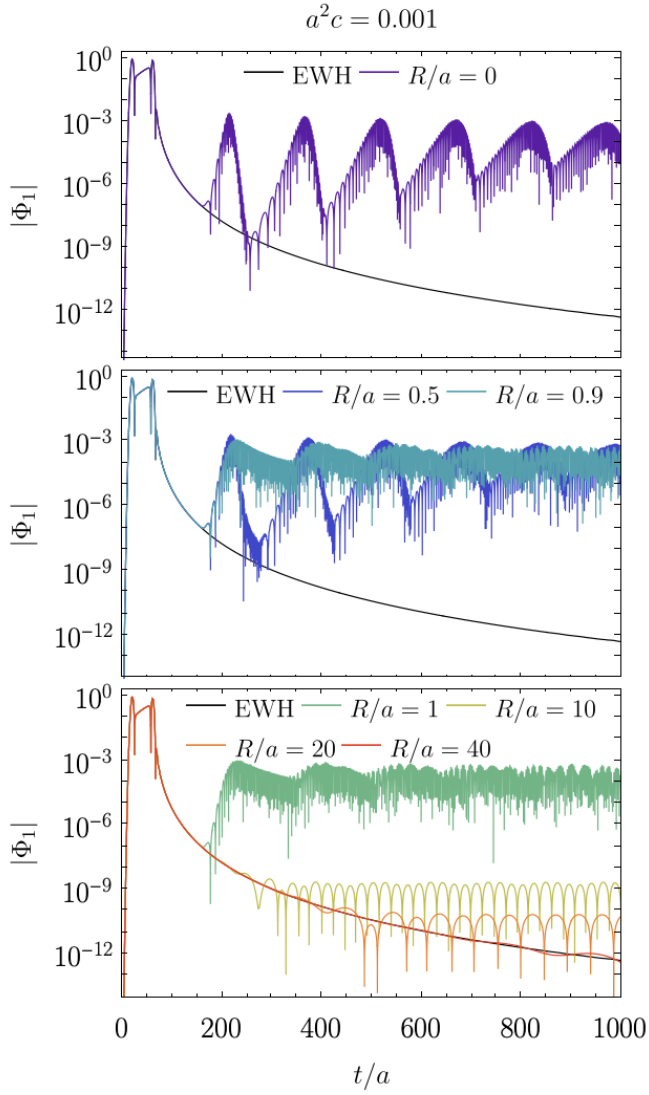

Figure 8.9.: Time-domain profile of the absolute value of the scalar field perturbation for the $\ell = 1$ mode. Seven configurations with the following values $R/a = \{0, 0.5, 0.9, 1, 10, 20, 40\}$ are plotted, along with the Ellis wormhole as a reference.

The results presented in the current chapter suggests that the global structure of wormholes may give rise to remarkable observational aspects, even though they can share a very similar throat-like structure. The study of perturbations can be used for example to extract information about possible compactness of the inner universe, and this could be useful in future spectroscopy experiments trying to identify new compact objects.
It is remarkable that even if the hypothesis of an asymptotic Euclidean geometry for the spherical sector is quite restrictive, the toy model here discussed is solid in seizing the main properties modified Ellis wormholes are expected to be endowed with, when echoes are included in the analysis. Geometry can be then further complicated either by relaxing the Euclidean assumption, e.g. Schwarzschild-like scenarios, or by ulteriorly compactifying the spacetime fabric of the bounded 2-sphere patch, i.e. truncating the range of the possible values spanned by the coordinate x. These configurations are expected to generate a great variety of phenomenological signatures, due to the appearance of additional potential barriers or closed universe effects in geodesic motion.

Appendices

Appendix A.

Convergence analysis

In order to carry out the convergence analysis of the simulations showed in Chapter 4 and Chapter 5 we introduce the following notion for the total mass of the spacetime. It can be calculated by integrating the stress-energy tensor at each spatial hypersurface Σ [280]

$$M = \int_{\Sigma} \left(2T_t^t - T_\mu^\mu\right) \alpha\sqrt{\gamma}\, dr\, d\theta\, d\varphi \ . \tag{A.1}$$

A.1. Stable models

In this analysis we are only considering the numerical error coming from the finite-differencing of the differential equations. This dominates the error if we use resolutions coarser than that used to compute the initial data. However, we note that the change of coordinates from polar-areal to isotropic (see details on the specific transformation in [49]) also introduces an additional source of error.

Setting $\Delta x_{\rm pa} = 0.0025$ (the spatial resolution needed in the polar-areal grid used to compute the initial data) and choosing three resolutions for the isotropic

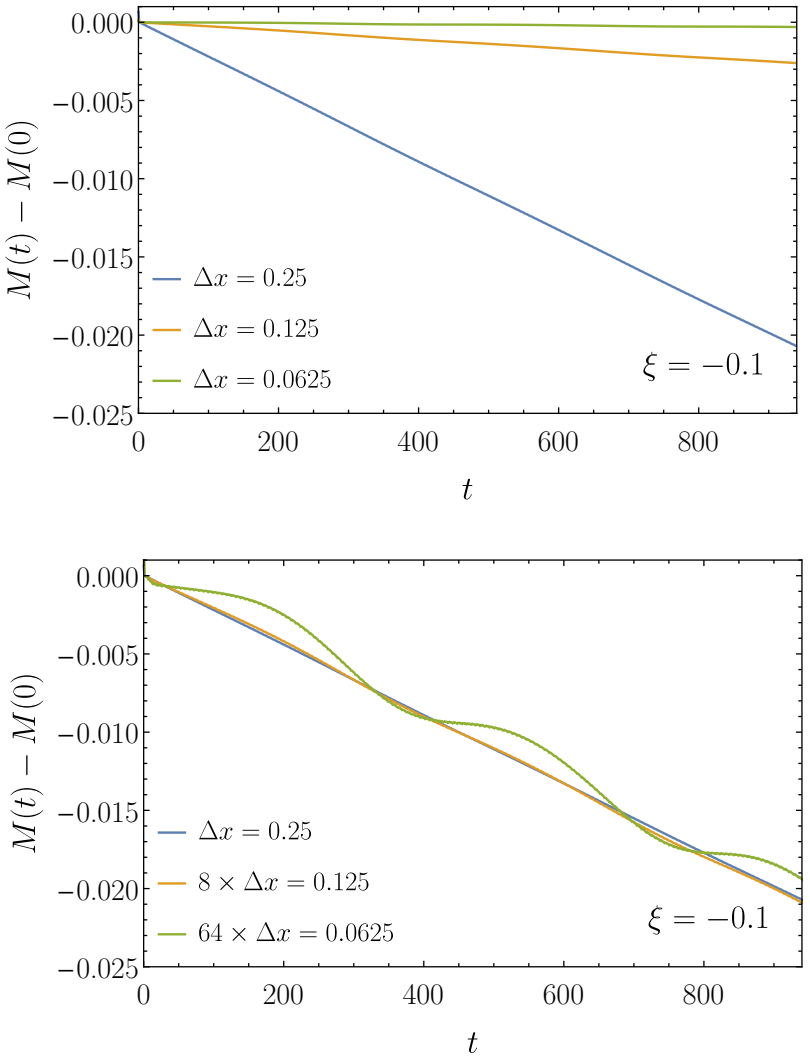

Figure A.1.: Time evolution of the total mass of stable boson stars models An. Top panel: Difference of the instantaneous total mass and its initial value for three different evolution grid resolutions Δx (isotropic grid). Bottom panel: The quantities of the top panel are rescaled to show third-order convergence.

grid, namely $\Delta x = 0.25$, $\Delta x = 0.125$ and $\Delta x = 0.0625$, we find third-order convergence.

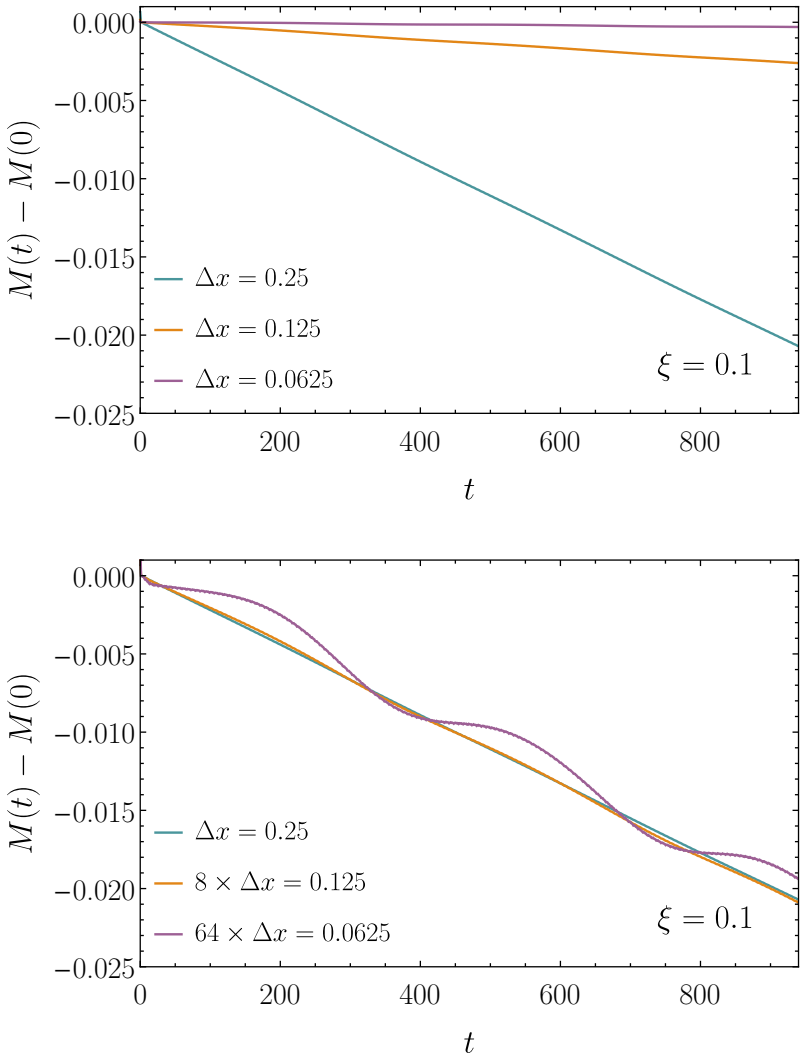

Figure A.2.: Time evolution of the total mass of stable boson stars models Ap. Top panel: Difference of the instantaneous total mass and its initial value for three different evolution grid resolutions Δx (isotropic grid). Bottom panel: The quantities of the top panel are rescaled to show third-order convergence.

The results are plotted in Figure A.1 and Figure A.2. For the Ap model, numerical errors from finite-differencing dominate the evolution and the total

mass decreases with a drift that depends on resolution (see top panel of Fig. A.2). The rate of convergence of the total mass for this stable model is third order, as shown in the bottom panel of Fig. A.2. Similar results are showed for model An (Figure A.2).

A.2. Gravitational Collapse

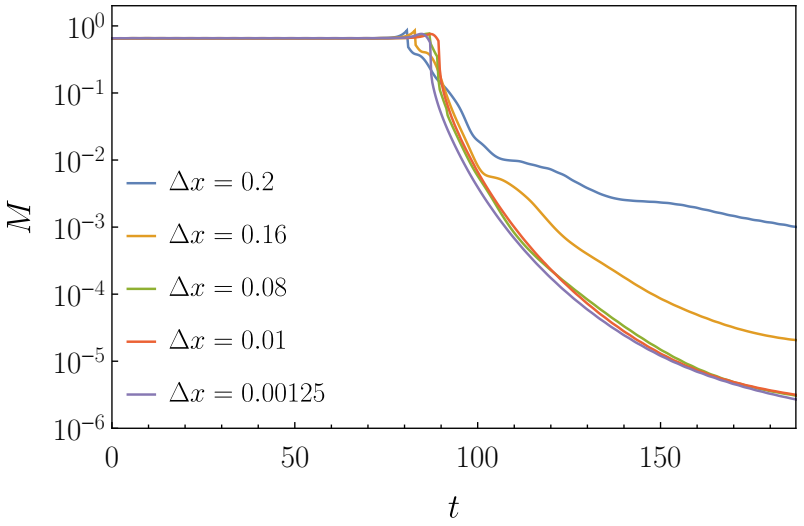

Figure A.3.: Time evolution of the total mass of the perturbed Bp model for different isotropic grid resolutions with fixed polar-areal grid resolution $\Delta x_{\mathrm{pa}} = 0.0025$. The finest isotropic grid (purple curve) is the one used in the simulations discussed in Chapter 5.

Figure A.3 shows the time evolution of the total mass for several isotropic grid resolutions. In order to check the convergence of the results, masses calculated from different grid resolutions are compared according to

$$M_{u-v} = |M(\Delta x = u) - M(\Delta x = v)| \quad . \tag{A.2}$$

Setting $\Delta x_{\rm pa} = 0.0025$ (the spatial resolution needed in the polar-areal grid used to compute the initial data) and choosing several resolutions for the isotropic grid, namely from $\Delta x = 0.2$ to $\Delta x = 0.04$, we find second-order convergence during the early contraction phase and third-order convergence during the collapse and black hole formation phase. This can be inferred by the multiplicative factors employed in the first three curves in the legend of the top panel of Figure A.4. However, increasing the resolution of the isotropic grid from $\Delta x = 0.04$ to $\Delta x = 0.02$, the convergence order drops to ~ 1.8 in the early phase. In addition, for even higher resolutions of the isotropic grid, the accuracy of the evolution does not improve (see bottom panel of Figure A.4).

As previously mentioned, when employing resolutions that are coarser than those used for computing the initial data, the dominant source of error stems from the finite-difference method. Nonetheless, it is important to acknowledge that the transformation of coordinates from polar-areal to isotropic, as described in [49], introduces an additional source of error. This error is evident in the observed loss of convergence, as illustrated in the bottom panel of Fig. A.4. Thus, while the primary focus of our discussion has centered on the numerical error arising from finite differences, it is crucial to recognize that the coordinate transformation itself contributes to the overall error in our analysis. In addition, since we do not further change $\Delta x_{\rm pa}$ in this analysis, increasing the isotropic grid resolution does not lead to an improved convergence for the higher resolution cases discussed here.

Despite the lack of convergence for an isotropic grid with $\Delta x = 0.00125$, our simulations needed to use such high resolution in order to populate the vicinity of the origin with a sufficiently large number of cells (even though the accuracy of the result does not increase at the expected rate). A remedy to this shortcoming, which we believe does not affect the validity of the findings reported in this work, would be to compute the initial data directly in isotropic coordinates and thus avoid the coordinate transformation for the evolution.

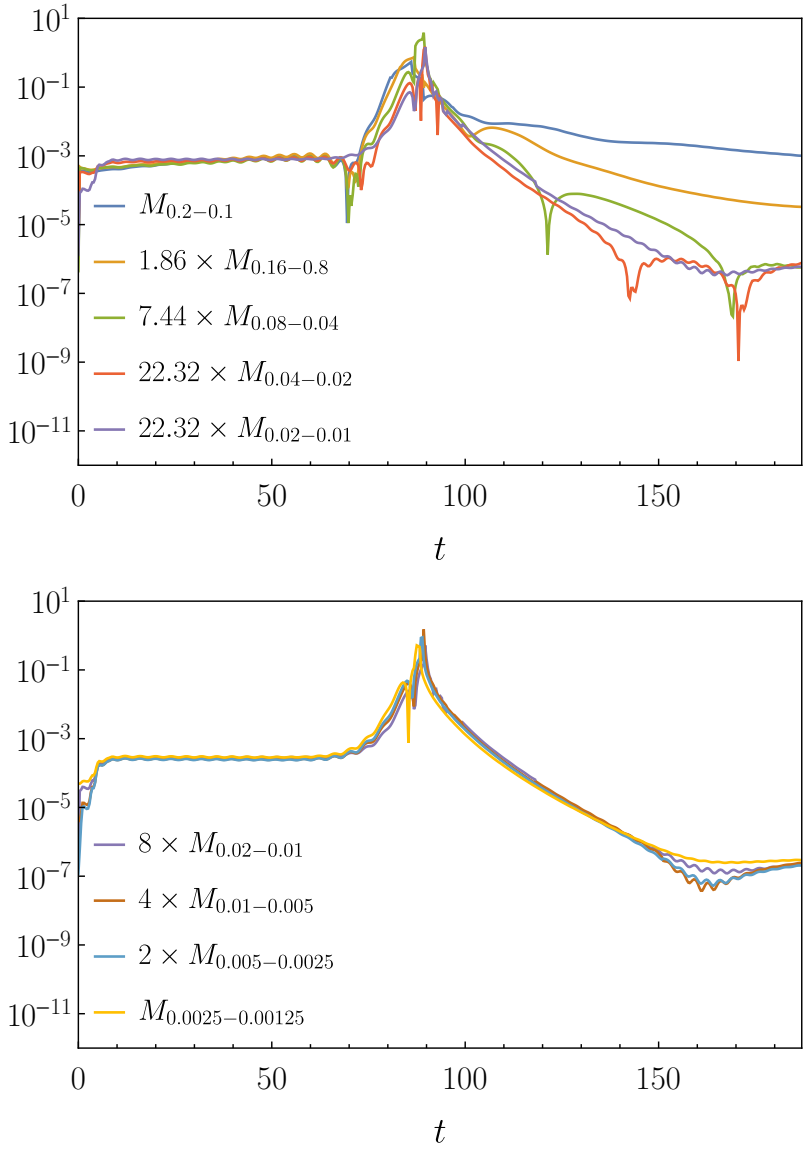

Figure A.4.: Comparison of the time evolution of the difference between total masses calculated for different isotropic grid resolutions with fixed polar-areal grid resolution $\Delta x_{\mathrm{pa}} = 0.0025$.

Further developments in this direction will be reported elsewhere. We also note that, similarly, first-order convergence is found for the polar-areal grid when the isotropic grid is fixed.

Appendix B.

RN-RN asymmetric wormhole parameter space

The orthographic projection is a common way to represent three dimensional objects in two dimensions. It is a representation of each side of an object as would be seen by an observer infinitely far away.

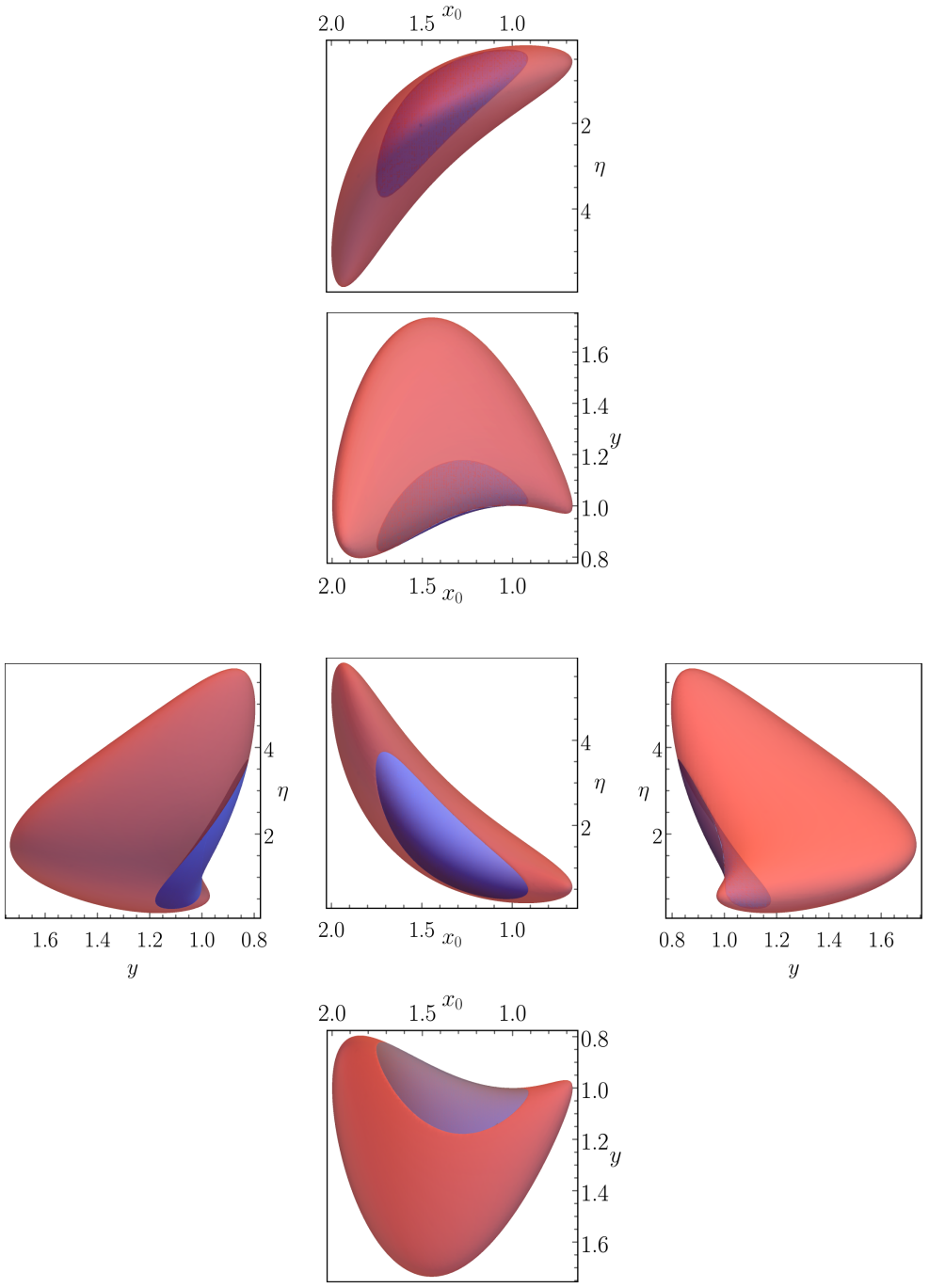

Figure B.1.: The six orthographic projections of the 3D plot shown in Fig. 7.1. The blue region represents the SPE space of parameters while the red region represents the SNE space of parameters. Transparency has been applied to the regions in order to make more noticeable that the SPE region (blue) is embedded onto the SNE region (red).

Thesis summary

The need for a well-behaved gravity theory at high energies demands a multidisciplinary approach, incorporating a wide range of viewpoints, from sophisticated mathematical tools and statistical techniques to ambitious experiments. Achieving this goal requires a deep understanding of our fundamental theories, their capabilities and limitations, as well as an improvement of the main roads in them are essential steps. This PhD thesis is situated within this context, with particular emphasis on investigating the existence and properties of exotic compact objects resembling black holes.

We begin this dissertation by introducing the concept of a boson star, which is a self-gravitating entity. A boson star represents a gravitationally bound configuration of bosonic particles that are minimally coupled to Einstein's theory of gravity. In essence, it can be thought of as a collection of particles whose dynamics are governed by the Klein–Gordon equation, resulting in dispersive behavior. To ensure stability, a crucial component is the presence of a locking mechanism. This mechanism is a consequence of the mass parameter μ associated with the bosonic field, which creates a potential barrier. Consequently, we can view boson stars as a macroscopic Bose–Einstein condensate.

Since boson stars can be considered as macroscopic quantum states, we can apply Heisenberg's uncertainty principle to estimate their maximum mass. It can be observed that the mass of a boson star is inversely related to the mass of the constituent scalar field. From this perspective, the mass and size of a boson star can vary widely, ranging from atomic scales to astrophysical scales, depending on the mass of the constituent bosons. Additionally, the inclusion of

a self-interaction term in the field potential can introduce further variations in the mass of the boson star.

Next, we will discuss modified gravity, the name given to theories that aim to extend Einstein's theory of gravity. Although General Relativity is the most widely accepted theoretical framework within the scientific community and has passed numerous experimental tests, including the recent detection of gravitational waves, Einstein's theory is unable to fully and satisfactorily explain certain phenomena, such as the rotation curves of spiral galaxies, the expansion and origin of the universe, or the singularity within black holes. Moreover, General Relativity remains incompatible with quantum theory. All these effects lead us to seek a gravitational framework that can explain, in a purely geometric way, all the observed phenomena.

Among the various ways to extend General Relativity, we highlight two. First, there is the consideration of an appropriate gravitational action, as Einstein-Hilbert action, upon which General Relativity is based, was chosen for its mathematical elegance and simplicity and has not been directly experimentally verified. In this context, we mention $f(R)$ theories, which are constructed from contractions of curvature tensors and offer significant simplicity and flexibility.

On the other hand, we emphasize the metric-affine formulation, in which it is considered that the connection is not the Levi-Civita connection, meaning that, it is not defined by the metric but is entirely independent of it. It is worth noting that when this formalism is applied to the Einstein-Hilbert action, the resulting equations of motion are exactly the same as if we considered the purely metric formalism. However, when the metric-affine formalism is applied to other gravitational actions, we do find substantial differences.

By combining these two modifications, we encounter Palatini $f(\mathcal{R})$ theories, which have an important feature compared to others. These can be rewritten in such a way that the nonlinearities of the gravitational sector of the action are transformed into nonlinearities of the matter sector. This allows us to transform a $f(\mathcal{R})$ gravity problem coupled to a certain matter sector into a General Relativity problem coupled to a modified matter sector. The significant

advantage of this approach is the ability to use techniques and mechanisms developed in the literature to address problems in General Relativity.

The tension between theory and observations does not allow us to dismiss the possible existence of compact objects beyond those known so far, namely, white dwarfs, neutron stars, and black holes. Thus, speculating about the possible existence of boson stars also leads us to observe the behavior of gravity in its strong field regime. It is of interest to explore how structural properties such as mass and radius of boson stars could be affected by a modification of the gravitational Lagrangian. Since $f(\mathcal{R})$ theories offer a high degree of freedom while maintaining field equations within reasonable limits of simplicity, we will explore the impact that high-energy modifications of the gravitational interaction of the $f(\mathcal{R})$ type can have on the astrophysical properties of boson stars.

The approach we will take is as follows. Starting from the action of the problem at hand, i.e., a static boson star in the context of $f(\mathcal{R}) = \mathcal{R} + \xi\mathcal{R}^2$ Palatini gravity, we will use the correspondence between this theory and that of Einstein to translate our system into a Lagrangian of nonlinear matter coupled to General Relativity. This will allow us to solve the equations formulated in this context and then reverse the transformation to observe the resulting outcome from the perspective of Palatini $f(\mathcal{R})$ gravity.

An important difference between boson stars in $f(\mathcal{R})$ and boson stars in General Relativity is the limited range of scalar field amplitudes allowed at the center of the star, which is much shorter than in General Relativity. For relatively small central field amplitudes ϕ_0, we find that the solutions do not significantly differ from those of General Relativity. Although one can achieve greater or lesser mass and compactness for a given ϕ_0 depending on whether $\xi < 0$ or $\xi > 0$, respectively. In the case of $\xi < 0$, new features arise regarding the dependence of the total mass and the number of particles of a solution on its oscillation frequency. In General Relativity coupled to a canonical matter Lagrangian, these curves exhibit a characteristic spiral pattern that is lost in the case of the aforementioned modified gravity theory. Therefore, an interesting

degeneracy is observed between boson stars in General Relativity and in $f(\mathcal{R})$, which is only broken at high values of the scalar field ϕ_0. It is also observed in this regard that the incorporation of self-interactions in the scalar field potential contributes to worsening this degeneracy.

Through the use of Numerical Relativity techniques, we can calculate the temporal evolution of boson stars using the static solutions discussed earlier. We study three different models for three values of the coupling parameter ξ: three stable models, An, Az, and Ap; three unstable models with negative binding energy, Bn, Bz, and Bp; and three unstable models with positive binding energy, Cn, Cz, and Cp. The lowercase letters, n, z, and p, indicate the value of the coupling parameter, $\xi = -0.1$, $\xi = 0$ (corresponding to General Relativity), and $\xi = 0.1$, respectively.

For the stable models An, Az, and Ap, we obtain stable time evolutions in which the parameters of the stars, such as mass or size, largely remain unchanged, except for minor oscillations caused by numerical errors from the discretization scheme. It is worth noting that in the case of model Az, i.e., in General Relativity, these oscillations are mainly attributed to the resolution of the initial data grid, and in the continuum limit, these oscillations vanish, as expected. However, for models An and Ap, in $f(\mathcal{R})$ Palatini gravity, the coordinate change from polar-areal to isotropic coordinates introduces a small source of numerical noise that contributes to the mentioned oscillation, which does not disappear when we increase the resolution of the initial grid. Further research is needed in this direction to obtain initial data in isotropic coordinates to carry out temporal evolution without the need for a change of coordinates.

Our simulations have also shown that the unstable models Bn, Bz, and Bp experience a migration towards stable branch configurations with the same mass when perturbed only by discretization errors. However, when these three models are perturbed beyond the discretization error, they undergo gravitational collapse. In the context of General Relativity, this leads to the formation of a black hole.

Regarding the perturbed model Bn, we found that the approach used in this work is not suitable for fully calculating its gravitational collapse due to the appearance of divergences, which could also indicate the appearance of naked singularities. This suggests the need for alternative approaches or refinements in computational techniques to properly analyze the behavior of gravitational collapse in this specific model (or models within a theory with a negative coupling parameter).

In contrast, for model Bp, we observed that a small portion of the spacetime inflates, leading to a finite universe that grows exponentially. In our model, this occurs concurrently with the development of an apparent horizon, making the internal process analogous to a cosmic bounce and preventing its electromagnetic observation by external observers. Our results are robust and persist for all values of the gravitational coupling parameter ξ and for other central scalar field amplitudes Φ_0 as long as they are on the unstable branch and the perturbation is high enough to trigger gravitational collapse. We observed that a portion of quasi-stationary scalar field remains outside the horizon, and the throat area decreases as the external scalar cloud is absorbed, suggesting that it will eventually close. However, numerical limitations challenge the analysis of this behavior at higher temporal values.

Finally, the unstable models Cn, Cz, and Cp are characterized by a rapid decrease in Φ_0, resulting in a drastic radial expansion of the boson stars and their complete dispersion.

The study conducted reveals significant differences compared to General Relativity models. These differences emphasize the profound influence of gravitational theory on the behavior and ultimate fate of self-gravitating compact objects such as boson stars.

The emergence of wormhole-like structures in the context of gravitational collapse in Palatini $f(\mathcal{R})$ gravity has captured our interest in these objects. Therefore, we will study the diverse descriptions that have been provided in the literature for wormholes, with particular emphasis on traversable wormholes and thin-shell wormholes.

We will then conduct an analysis of the observational signatures of a wormhole in $f(\mathcal{R})$ Palatini gravity, formed by two Reissner-Nordström (RN) spacetimes glued above their event horizons—in order to avoid them—using the thin-shell formalism. More specifically, we will examine the absorption spectrum of scalar wave excitations by these objects.

To investigate how the value of the throat location and the charge affects absorption, we analyze various configurations with thin-shell structures of both negative energy (violating the energy conditions) and positive energy (not violating the energy conditions). Regardless of the sign of the thin-shell energy, the wormhole can be constructed using a spacetime of two black holes, a spacetime of a black hole and a naked singularity, or two spacetimes with naked singularities. It is important to note that we are referring to the exterior of the black hole or naked singularity, so there are no actual event horizons or singularities present in the constructed solution.

If the effective potential has a well (either continuous or discontinuous), quasi-bound states emerge around the wormhole throat. These quasi-trapped modes create resonances in absorption spectra (sharp peaks in the absorption cross-section), causing the absorption profiles of asymmetric RN wormholes to be significantly different from those of RN black holes. These new peaks are heavily influenced by the symmetry of the potential well. If the effective potential exhibits symmetric well, resonances are noticeable across the entire frequency range. On the other hand, the presence of asymmetry in the effective potential leads to the damping of resonance peaks associated with quasi-bound states for higher modes ℓ. Thus, the high-frequency regime of the absorption cross-section is degenerate with that of the standard RN black hole, in contrast to symmetric wormhole configurations. Consequently, even minor deviations from symmetry in wormhole spacetimes can produce significant differences in observable characteristics associated with quasi-bound states.

If we attach a RN black hole (before its photon sphere) to a RN naked singularity spacetime, the wormhole can mimic the absorption of a standard RN black hole. This can be understood by the fact that the total absorption cross-

section depends on the dominant light ring (associated with the highest peak of the effective potential in the eikonal limit). Therefore, the dominant light ring will be that of the RN black hole, dictating the profile of the absorption cross-section in the eikonal limit.

An interesting absorption behavior arises when we cut-and-paste together two naked singularities. In these scenarios, the throat effectively acts as a photosphere. As a result, the total absorption cross-section will converge to the shadow area associated with the effective light ring. Interestingly, the oscillatory pattern of the absorption profile rapidly diminishes, and the absorption cross-section gradually approaches the shadow region associated with the null geodesics trapped at the throat.

Our results indicate that asymmetric wormholes may exhibit diverse observational signatures when compared to black holes or symmetric wormholes. These spacetime asymmetries can lead, for example, to significant features in the quasi-normal mode spectrum and the potential presence of echoes.

Throughout this thesis, we have studied various types of wormholes, ranging from the Einstein-Rosen bridge to the Reissner-Nordström thin-shell wormhole. One common feature among them is that they all connect one infinitely extended universe with another (or the same) infinitely extended universe. In contrast, the results obtained from the gravitational collapse of a boson star in $f(\mathcal{R})$ Palatini gravity presents a dynamically evolving wormhole structure that possesses a distinctive topology. One side of the wormhole is characterized by an infinitely extended universe, while the other side describes a finite universe in expansion. Thus, we aim to revisit this idea and analyze observables for possible signals that may indicate the presence of finite universes on the other side of a wormhole.

One of the simplest wormhole configurations in General Relativity is the Ellis solution. It consists of two asymptotically flat spacetime regions connected by a throat. In our study, we make modifications to one of these regions. Instead of being infinitely extended, we create a region with a bounded radius for the 2-spheres. We achieve this by using a modified radial function that smoothly transitions from the standard Ellis solution to the inner bounded 2-spheres on

the other side. Inside the finite universe of the modified Ellis wormhole, the radius of the 2-surface initially reaches a local maximum and then gradually decreases toward the asymptotic value R."

When the asymptotic value of the radius of the 2-spheres is less than the throat radius, $R < a$, there are light rays that, depending on their impact parameter, experience a bounce in the inner universe and propagate back outwards to the outer universe. For the scenario $R = 0$, all geodesics entering the inner universe scatter back to the outer universe, and the only null geodesic that can propagate forever in the inner region is that of the purely radial moving photon. Finally, for $R \geq a$, any photon crossing the throat propagates toward the asymptotic infinity with a bounded radius of the 2-spheres.

We have conducted an analysis of the evolution of scalar perturbations in the mentioned geometry. Once the perturbation is transmitted to the inner universe, it interacts with an unbounded potential barrier in the case of $R = 0$ or a step potential if $R \neq 0$. Consequently, some modes become trapped in a potential well and manifest as a series of echoes in the temporal profile of the scalar perturbation, with distinctive characteristics depending on the parameters used.

Our results suggest that the overall structure of wormholes can give rise to significant observational aspects even when the structure of the throat remains unchanged. The study of perturbations can, for example, be used to extract information about the possible compactness of the inner universe, which could be valuable for future spectroscopic experiments aimed at identifying new compact objects.

Resum de la tesi

L'absència d'una teoria ben entesa sobre la gravetat i les seues propietats a altes energies exigix un esforç global per construir una teoria quàntica viable per al camp gravitatori. La complexitat del problema requerix un enfocament multidisciplinari, que incorpore un espectre ampli de punts de vista: des de sofisticades eines matemàtiques i tècniques estadístiques fins a experiments ambiciosos. Cal una entesa profunda de les nostres teories bàsiques, de les seues capacitats i limitacions, així com una millora dels enfocaments principals per assolir, com a objectiu últim, el desenvolupament d'una teoria satisfactòria que combine gravetat i física quàntica. Aquesta tesi doctoral s'emmarca en aquest context, prestant especial atenció a l'existència i les propietats d'objectes compactes similars a forats negres.

Comencem la dissertació introduint el concepte d'estrela de bosons, una entitat autogravitant la qual és una configuració gravitacionalment lligada de partícules bosòniques mínimament acoblades a la gravetat d'Einstein. Una estrela de bosons es pot entendre com una col·lecció de partícules que seguixen la dinàmica dictada per l'equació de Klein-Gordon i com a resultat presenta un comportament dispersiu. Per tal de garantir l'estabilitat la presència d'un mecanisme de confinament esdevé crucial. Aquest mecanisme de confinament sorgix de la massa μ associada al camp bosònic, que genera una barrera de potencial. En conseqüència, les estreles de bosons es poden considerar com a condensats macroscòpics de Bose-Einstein.

Atés que les estreles de bosons es poden considerar com a estats quàntics macroscòpics, és possible aplicar el principi d'incertesa de Heisenberg per estimar la seua massa màxima. En conseqüència, la massa d'una estrela de bosons

presenta una relació inversa amb la massa del camp escalar constituent. Així des d'aquesta perspectiva, la massa i la mida d'una estrela de bosons poden variar des de l'escala atòmica fins a l'escala astrofísica, depenent de la massa del bosó constituent. A més, la inclusió d'un terme d'autointeracció en el potencial del camp pot introduir variacions en la massa de l'estrela de bosons.

Tot seguit tractarem la gravetat modificada, el nom que reben les teories que tracten d'estendre la gravetat d'Einstein. Encara que la relativitat general és el marc teòric més àmpliament acceptat per la comunitat científica i ha passat gran nombre de testos experimentals, incloent la recent detecció de les ones gravitacionals, la teoria d'Einstein no és capaç d'explicar de manera completament satisfactòria certs fenòmens com podrien ser les corbes de rotació de les galàxies espirals, l'expansió i origen de l'univers o la singularitat de dins dels forats negres. Tanmateix, la relativitat general roman irreconciliable amb la teoria quàntica. Tots aquests efectes ens conduïxen a buscar un marc gravitatori que puga explicar, de manera purament geomètrica, tots els fenòmens observats.

D'entre les diverses maneres que es poden plantejar per estendre la relativitat general en destaquem dues. Per una banda, la descripció d'una acció de gravetat adequada, ja que l'acció d'Einstein-Hilbert, sobre la que es definix la relativitat general, fou escollida per criteris d'elegància i simplicitat matemàtica i no ha estat comprovada experimentalment de manera directa. En aquest context mencionem les teories del tipus $f(R)$ les quals estan construïdes a partir de contraccions dels tensors de curvatura i oferixen una simplicitat i flexibilitat significant.

Per altra banda, destaquem la formulació mètric-afí, en la qual es considera que la connexió no és la de Levi-Civita, és a dir, no ve definida per la mètrica sinó que hi és completament independent. Cal mencionar que aquest formalisme quan és aplicat sobre l'acció d'Einstein-Hilbert les equacions del moviment resultants són exactament les mateixes que si considerarem el formalisme purament mètric. Malgrat això, quan el formalisme mètric-afí s'aplica a altres accions de gravetat sí que trobem diferències substancials.

Combinant aquestes dues modificacions trobem les teories $f(\mathcal{R})$ del tipus Palatini, les quals presenten una característica important respecte d'altres. Aquestes poden ser reescrites de tal manera que les no-linealitats del sector gravitatori de l'acció es transformen en no-linealitats del sector de matèria. Això ens permet transformar un problema de gravetat $f(\mathcal{R})$ acoblada a cert sector de matèria en un problema de relativitat general acoblada a aquest mateix sector de matèria però amb modificacions. El gran avantatge que presenta aquest procediment és la possibilitat d'emprar les tècniques i els mecanismes desenvolupats a la bibliografia per afrontar problemes de relativitat general.

La tensió entre teoria i observacions no ens permet descartar la possible existència d'altres objectes compactes més enllà dels coneguts fins ara, a saber, nanes blanques, estreles de neutrons i forats negres. Així, teoritzar sobre la possible existència d'estreles de bosons també ens porta a poder observar el comportament de la gravetat en el seu règim de camp fort. Resulta d'interés explorar com les propietats estructurals com la massa i el radi de les estreles de bosons podrien veure's afectades per una modificació del lagrangià gravitatori. Degut a que les teories $f(\mathcal{R})$ oferixen un alt grau de llibertat mentre mantenen les equacions de camp dins de límits raonables de simplicitat, explorarem l'impacte que les modificacions d'alta energia de la interacció gravitatòria del tipus $f(\mathcal{R})$ pot tindre sobre les propietats astrofísiques de les estreles de bosons.

El plantejament que farem és el següent. Partint de l'acció del problema en qüestió, és a dir, una estrela de bosons estàtica en el context de la gravetat $f(\mathcal{R}) = \mathcal{R} + \xi\mathcal{R}^2$ Palatini, farem ús de la correspondència entre aquesta teoria i la d'Einstein per traduir el nostre sistema a un lagrangià de matèria no lineal acoblat a la relativitat general. Això ens permetrà resoldre les equacions formulades en aquest context i després desfer la transformació per observar el resultat resultant des de la perspectiva de la gravetat $f(\mathcal{R})$ Palatini.

Una diferència important entre les estreles de bosons d'$f(\mathcal{R})$ i les estreles del bosó de la relativitat general és el rang limitat d'amplituds de camp escalar permeses al centre de l'estrela, que és molt més curt que en relativitat general. Per a amplituds de camp central ϕ_0 relativament menudes trobem que les

solucions no diferixen significativament de les de relativitat general. Tot i que es poden aconseguir masses i compacitat més/menys grans per a un ϕ_0 donat depenent de si $\xi < 0$ o $\xi > 0$, respectivament. En el cas $\xi < 0$ sorgixen noves característiques pel que fa a la dependència de la massa total i el nombre de partícules d'una solució amb la seua freqüència d'oscil·lació. En relativitat general acoblada a un lagrangià matèria canònic, aquestes corbes presenten un patró espiral característic que es perd en el cas de la mencionada teoria de gravetat modificada. Per tant, s'observa una degeneració interessant entre les estreles de bosons en relativitat general i en $f(\mathcal{R})$ que només es trenca en valors alts del camp escalar ϕ_0. Observem també, en aquest sentit, que la incorporació d'autointeraccions en el potencial del camp escalar contribuïx a empitjorar aquesta degeneració.

Mitjançant l'ús de les tècniques de la relativitat numèrica podem calcular l'evolució temporal d'estreles de bosons emprant les solucions estàtiques que hem comentat abans. Estudiem tres models diferents per a tres valors del paràmetre d'acoblament ξ: tres models estables An, Az i Ap; tres models inestables amb energia d'enllaç negativa Bn, Bz i Bp; i tres models inestables amb energia d'enllaç positiva Cn, Cz i Cp. Les lletres en minúscula, n, z i p, indiquen el valor del paràmetre d'acoblament, $\xi = -0.1$, $\xi = 0$ (relativitat general) i $\xi = 0.1$, respectivament.

Per als models estables An, Az i Ap, obtenim evolucions estables en les quals els paràmetres de les estreles, com ara la massa o la mida, romanen en gran mesura sense canvis, excepte per menudes oscil·lacions produïdes pels errors d'origen numèric provinents de l'esquema de discretització. Observem que en el cas del model Az, és a dir, en relativitat general, aquestes oscil·lacions són atribuïdes principalment a la resolució de la malla de les dades inicials de manera que en el límit al continu aquestes oscil·lacions s'esvairan, tal com s'espera. No obstant per als models An i Ap, en gravetat $f(\mathcal{R})$ Palatini, el canvi de coordenades de polar-areal a isòtropes introduïx una xicoteta font de soroll numèric que contribuïx a la mencionada oscil·lació que no desapareix quan incrementem la resolució de la malla inicial. Cal seguir investigant en aquesta direcció per tal d'obtenir les dades inicials en coordenades isòtropes

per tal de poder dur a terme l'evolució temporal sense necessitat de fer servir un canvi de coordenades.

Les nostres simulacions també han demostrat que els models inestables Bn, Bz i Bp experimenten una migració cap a les configuracions de la branca estable que tenen la mateixa massa, quan només són pertorbats per errors de discretització. Tanmateix, quan aquests tres models es pertorben més enllà de l'error de discretització, sofrixen un col·lapse gravitacional. En el context de relativitat general això conduïx a la formació d'un forat negre. Pel que fa al model pertorbat Bn, hem trobat que l'enfocament utilitzat en aquest treball no és adequat per calcular completament el seu col·lapse gravitacional, a causa de l'aparició de divergències, que al mateix temps podrien estar indicant l'aparició de singularitats nues. Això suggerix la necessitat d'enfocaments o perfeccionaments alternatius en les tècniques computacionals per analitzar correctament el comportament del col·lapse gravitacional d'aquest model específic (o models dins d'una teoria amb un valor negatiu del paràmetre d'acoblament). En canvi, per al model Bp hem vist que un petit tros d'espaitemps pot inflar-se donant lloc a un univers finit que creix exponencialment. En el nostre model, això passa paral·lelament al desenvolupament d'un horitzó aparent, fent que el procés intern siga anàleg a un rebot còsmic i, impedint la seua observació electromagnètica per part d'observadors externs. Els nostres resultats són robusts i persistixen per a tots els valors del paràmetre d'acoblament gravitatori ξ i per a altres amplituds centrals de camp escalar Φ_0 sempre que estiguin a la branca inestable i la pertorbació siga prou alta com per excitar el col·lapse gravitacional. Hem vist que una porció de camp escalar quasi estacionari queda fora de l'horitzó i que l'àrea de la gola es reduïx a mesura que s'absorbix el núvol escalar extern, cosa que suggerix que finalment es tancarà. Tanmateix, les limitacions numèriques desafien l'anàlisi d'aquest comportament a valors temporals més alts.

Finalment, els models inestables Cn, Cz i Cp, es caracteritzen per una ràpida disminució de Φ_0, mostrant una dràstica expansió radial de les estreles del bosó i donant lloc a la seua completa dispersió.

L'estudi dut a terme revelant diferències notables en comparació amb els models de relativitat general. Aquestes diferències emfatitzen la profunda influència de la teoria gravitatòria en el comportament i el destí final dels objectes compactes autogravitants com les estreles de bosons.

L'aparició d'estructures del tipus forats de cuc en el context de col·lapse gravitacional a gravetat $f(\mathcal{R})$ Palatini ha captat el nostre interés en aquests objectes. Així estudiarem les diferents descripcions que s'han donat al llarg de la literatura dels forats de cuc, prestant especial atenció als forats de cuc transitables i als del tipus *thin-shell*.

Seguint el nostre estudi plantejarem l'anàlisi de les empremtes observacionals d'un forat de cuc en gravetat $f(\mathcal{R})$ Palatini format per dos espaitemps del tipus Reissner-Nordström (RN) apegats mitjançant el formalisme *thin-shell* per sobre de l'horitzó d'esdeveniments per tal d'evitar-lo. Més concretament, estudiarem l'espectre d'absorció d'ones escalars d'aquests objectes.

Per tal d'investigar com la ubicació de la gola i els valors de càrrega influïxen en l'absorció, analitzem diverses configuracions amb *thin-shell* d'energia negativa (violant les condicions d'energia) i positiva (no violant les condicions d'energia). Independentment del signe de l'energia de la *thin-shell*, el forat de cuc es pot construir utilitzant un espaitemps de dos forats negres, un espaitemps de forat negre i una singularitat nua, o dos espaitemps de singularitat nua. Tingueu en compte que ens referim a l'exterior del forat negre o a la singularitat nua, de manera que no hi ha cap horitzó ni singularitat realment present a la solució construïda.

Si el potencial efectiu té una vall (continua o discontínua), emergixen estats quasilligats al voltant de la gola del forat de cuc. Aquests modes quasi atrapats creen ressonàncies en els espectres d'absorció (apareixen pics aguts a la secció eficaç d'absorció), que fan que els perfils d'absorció del forat de cuc asimètric de RN asimètrics siguen molt diferents dels corresponents als forats negres de RN. Aquests nous pics estan molt influenciats per la simetria del pou de potencial. Si el potencial efectiu presenta una vall simètrica, les ressonàncies es noten en tot el rang de freqüències. D'altra banda, la presència d'una asimetria en el

potencial efectiu dona lloc a l'atenuació dels pics de ressonància associats a estats quasilligats per a modes ℓ més alts. Així, el règim d'alta freqüència de la secció eficaç d'absorció és degenerat amb la del forat negre RN estàndard, en contrast amb les configuracions simètriques del forat de cuc. En conseqüència, fins i tot desviacions menors de la simetria en espaitemps de forat de cuc poden produir diferències significatives en les característiques observables associades als estats quasilligats .

Si apeguem un forat negre RN (abans de la seua fotosfera) amb un espaitemps de singularitat nua RN, el forat de cuc pot imitar l'absorció del forat negre RN estàndard. Això es pot entendre pel fet que la secció eficaç d'absorció total depén de l'anell de llum dominant (associat amb el pic més alt del potencial efectiu en el límit eikonal). Per tant, l'anell de llum dominant serà el del forat negre RN i dictarà el perfil de la secció eficaç d'absorció en el límit eikonal.

Apareix un comportament d'absorció interessant quan retallem i enganxem dues singularitats nues. En aquests escenaris, la gola actua de manera efectiva com una fotosfera. Com a resultat, la secció eficaç d'absorció total anirà a l'àrea de l'ombra associada a l'anell de llum efectiu. Curiosament, el patró oscil·latori del perfil d'absorció s'atenua ràpidament i la secció eficaç d'absorció va lentament a la zona d'ombra associada a les geodèsiques nul·les atrapades a la gola.

Els nostres resultats indiquen que els forats de cuc asimètrics poden portar associades diferents empremtes observacionals quan els comparem amb els forats negres o els forats de cuc simètrics. Aquestes asimetries en l'espaitemps poden conduir, per exemple, a característiques significatives en l'espectre del mode quasi normal i a la possible presència d'ecos.

Al llarg de la present tesi, hem estudiat diversos tipus de forats de cuc, que van des del pont Einstein-Rosen fins al forat de cuc de tipus *thin-shell* de Reissner-Nordström. Una característica que trobem en comú entre tots ells és que tots estan construïts de manera que connecten un univers infinit amb un altre (o el mateix) univers també infinit. Recordat el resultat obtingut del col·lapse gravitatori d'una estrella de bosó en gravetat $f(\mathcal{R})$ Palatini, on sorgeix

una estructura de forat de cuc en evolució dinàmica, vegem que en aquest cas el forat de cuc posseeix una topologia distintiva. Un costat es caracteritza per un univers infinit, mentre que l'altre descriu un univers finit en expansió. Així, pretenem revisar aquesta idea i analitzar observables per a possibles senyals que puguen indicar la presència d'universos finits a l'altre costat d'un forat de cuc.

Una de les configuracions de forat de cuc més simples de la Relativitat General és la representada per la solució d'Ellis. Consisteix en dues regions espaitemps asimptòticament planes, és a dir, l'espaitemps de Minkowski, connectades per una gola. Nosaltres prenem aquest model i en modifiquem una de les regions asimptòtiques infinites del forat de cuc substituint-la per una regió amb radi de les 2-esferes fitat, mitjançant una funció radial modificada, que interpola suaument des de la solució d'Ellis estàndard fins al nucli de 2-esferes fitades a l'altre costat. A la regió interna del forat de cuc d'Ellis modificat, el radi de les 2-àreea presenta un màxim local i després decau cap al valor asimptòtic R.

Quan el valor asimptòtic del radi de 2 esferes és inferior al radi de la gola, $R < a$, hi ha raigs de llum que, segons el seu paràmetre d'impacte, patixen un rebot a l'univers interior i es dispersen cap a l'univers exterior. Per a l'escenari $R = 0$, totes les geodèsiques que entren a l'univers interior es dispersen de nou a l'exterior, i l'única geodèsica nul·la que es pot propagar per sempre a la regió interior és la del fotó en moviment purament radial. Finalment, per a $R \geq a$, qualsevol fotó que travesse la gola es propaga cap a l'infinit asimptòtic amb un radi acotat de 2 esferes.

Hem dut a terme una anàlisi de l'evolució de pertorbacions escalars en la geometria mencionada. Després que la pertorbació siga transmesa a l'univers interior, aquesta interacciona amb una barrera de potencial no fitada en el cas $R = 0$ o un potencial esglaó si $R \neq 0$. Per tant, part dels modes queden atrapats en un pou de potencial i s'observen com una sèrie d'ecos en el perfil temporal de la pertorbació escalar, amb característiques distintives depenent del paràmetres emprats.

Els nostres resultats suggerixen que l'estructura global dels forats de cuc pot donar lloc a aspectes observacionals significatius inclús quan l'estructura de la gola no es varia. L'estudi de les pertorbacions es pot utilitzar per exemple per extreure informació sobre la possible compacitat de l'univers interior i, això podria ser útil per als futurs experiments d'espectroscòpia que tracten d'identificar nous objectes compactes.

Bibliography

[1] A. Masó-Ferrando, N. Sanchis-Gual, J. A. Font, and G. J. Olmo, "Boson stars in Palatini gravity," *Class. Quant. Grav.*, vol. 38, no. 19, p. 194003, 2021.

[2] A. Masó-Ferrando, N. Sanchis-Gual, J. A. Font, and G. J. Olmo, "Birth of baby universes from gravitational collapse in a modified-gravity scenario," *JCAP*, vol. 06, p. 028, 2023.

[3] R. B. Magalhães, A. Masó-Ferrando, G. J. Olmo, and L. C. B. Crispino, "Asymmetric wormholes in palatini $f(\mathcal{R})$ gravity: Energy conditions, absorption, and quasibound states," *Phys. Rev. D*, vol. 108, p. 024063, Jul 2023.

[4] A. Masó-Ferrando, N. Sanchis-Gual, J. A. Font, and G. J. Olmo, "Numerical evolutions of boson stars in palatini $f(\mathcal{R})$ gravity," Sep 2023. arXiv:gr-qc/2309.14912.

[5] R. B. Magalhães, A. Masó-Ferrando, F. Bombacigno, G. J. Olmo, and L. C. B. Crispino, "Echoes from bounded universes," Oct 2023. arXiv:gr-qc/2310.03727.

[6] J. A. Wheeler, "Geons," *Phys. Rev.*, vol. 97, pp. 511–536, Jan 1955.

[7] E. A. Power and J. A. Wheeler, "Thermal geons," *Rev. Mod. Phys.*, vol. 29, pp. 480–495, Jul 1957.

[8] T. Regge and J. A. Wheeler, "Stability of a schwarzschild singularity," *Phys. Rev.*, vol. 108, pp. 1063–1069, Nov 1957.

[9] D. J. Kaup, "Klein-gordon geon," *Phys. Rev.*, vol. 172, pp. 1331–1342, Aug 1968.

[10] R. Rufifini and S. Bonazzola, "Systems of self-gravitating particles in general relativity and the concept of an equation of state," *Phys. Rev.*, vol. 187, pp. 1767–1783, Nov 1969.

[11] G. H. Derrick, "Comments on Nonlinear Wave Equations as Models for Elementary Particles," *J. Math. Phys.*, vol. 5, pp. 1252–1254, Dec 2004.

[12] M. Colpi, S. L. Shapiro, and I. Wasserman, "Boson stars: Gravitational equilibria of self-interacting scalar fields," *Phys. Rev. Lett.*, vol. 57, pp. 2485–2488, Nov 1986.

[13] B. P. Abbott *et al.*, "GWTC-1: A Gravitational-Wave Transient Catalog of Compact Binary Mergers Observed by LIGO and Virgo during the First and Second Observing Runs," *Phys. Rev. X*, vol. 9, no. 3, p. 031040, 2019.

[14] R. Abbott *et al.*, "GWTC-2: Compact Binary Coalescences Observed by LIGO and Virgo During the First Half of the Third Observing Run," *Phys. Rev. X*, vol. 11, p. 021053, 2021.

[15] R. Abbott *et al.*, "GW190521: A Binary Black Hole Merger with a Total Mass of $150M_{\odot}$," *Phys. Rev. Lett.*, vol. 125, no. 10, p. 101102, 2020.

[16] J. Calderón Bustillo, N. Sanchis-Gual, A. Torres-Forné, J. A. Font, A. Vajpeyi, R. Smith, C. Herdeiro, E. Radu, and S. H. W. Leong, "Gw190521 as a merger of proca stars: A potential new vector boson of 8.7×10^{-13} eV," *Phys. Rev. Lett.*, vol. 126, p. 081101, Feb 2021.

[17] R. Brito, V. Cardoso, C. A. R. Herdeiro, and E. Radu, "Proca stars: Gravitating Bose–Einstein condensates of massive spin 1 particles," *Phys. Lett. B*, vol. 752, pp. 291–295, 2016.

[18] R. Abbott *et al.*, "Properties and Astrophysical Implications of the 150 $M_{\odot}$ Binary Black Hole Merger GW190521," *Astrophys. J. Lett.*, vol. 900,

no. 1, p. L13, 2020.

[19] V. De Luca, V. Desjacques, G. Franciolini, P. Pani, and A. Riotto, "GW190521 Mass Gap Event and the Primordial Black Hole Scenario," *Phys. Rev. Lett.*, vol. 126, no. 5, p. 051101, 2021.

[20] J. Calderon Bustillo, N. Sanchis-Gual, S. H. W. Leong, K. Chandra, A. Torres-Forne, J. A. Font, C. Herdeiro, E. Radu, I. C. F. Wong, and T. G. F. Li, "Searching for vector boson-star mergers within LIGO-Virgo intermediate-mass black-hole merger candidates," Jun 2022. arXiv:gr-qc/2206.02551.

[21] F. E. Schunck, "A Scalar field matter model for dark halos of galaxies and gravitational redshift," Feb 1998. arXiv:astro-ph/9802258.

[22] J.-W. Lee, "Is dark matter a BEC or scalar field?," *J. Korean Phys. Soc.*, vol. 54, p. 2622, 2009.

[23] R. Sharma, S. Karmakar, and S. Mukherjee, "Boson star and dark matter," Dec 2008. arXiv:gr-qc/0812.3470.

[24] A. Arvanitaki, S. Dimopoulos, S. Dubovsky, N. Kaloper, and J. March-Russell, "String axiverse," *Phys. Rev. D*, vol. 81, p. 123530, Jun 2010.

[25] R. M. Wald, *General Relativity.* The University of Chicago Press, 1984.

[26] C. A. R. Herdeiro, A. M. Pombo, and E. Radu, "Asymptotically flat scalar, Dirac and Proca stars: discrete vs. continuous families of solutions," *Phys. Lett. B*, vol. 773, pp. 654–662, 2017.

[27] S. Liebling and C. Palenzuela, "Dynamical boson stars," *Living Rev. Rel.*, vol. 15, Feb 2012.

[28] C. W. Misner and D. H. Sharp, "Relativistic equations for adiabatic, spherically symmetric gravitational collapse," *Phys. Rev.*, vol. 136, pp. B571–B576, Oct 1964.

[29] M. Alcubierre, *Introduction to 3+1 Numerical Relativity.* Oxford Univer-

sity Press, Apr 2008.

[30] L. Lehner, "Numerical relativity: A Review," *Class. Quant. Grav.*, vol. 18, pp. R25–R86, 2001.

[31] S. G. Hahn and R. W. Lindquist, "The two-body problem in geometrodynamics," *Annals of Physics*, vol. 29, pp. 304–331, 1964.

[32] G. Darmois, "Les équations de la gravitation einsteinienne," *Mémorial des Sciences Mathématiques*, vol. 25, 1927.

[33] A. Lichnerowicz, *Sur certains problèmes globaux relatifs au système des équations d'Einstein.* Hermann, Paris, 1939.

[34] A. Lichnerowicz, "L'intégration des équations de la gravitation relativiste et le problème des n corps," *Journal de Mathématiques Pures et Appliquées*, vol. 25, pp. 37–63, 1944.

[35] A. Lichnerowicz, "Sur les équations relativistes de la gravitation," *Bulletin de la Société Mathématique de France*, vol. 80, pp. 237–251, 1952.

[36] Y. Fourès-Bruhat, "Théorème d'existence pour certains systèmes d'équations aux dérivées partielles non linéaires," *Acta Mathematica*, vol. 88, no. none, pp. 141 – 225, 1952.

[37] Y. Fourès-Bruhat, "Sur l'intégration des Équations de la relativité générale," *Journal of Rational Mechanics and Analysis*, vol. 5, no. 6, pp. 951–966, 1956.

[38] R. L. Arnowitt, S. Deser, and C. W. Misner, "The Dynamics of general relativity. In: Witten L (ed) Gravitation: An Introduction to Current Research.," *Wiley*, p. 227–265, 1962.

[39] T. W. Baumgarte and S. L. Shapiro, "Numerical integration of einstein's field equations," *Phys. Rev. D*, vol. 59, p. 024007, Dec 1998.

[40] M. Shibata and T. Nakamura, "Evolution of three-dimensional gravitational waves: Harmonic slicing case," *Phys. Rev. D*, vol. 52, pp. 5428–5444,

Nov 1995.

[41] C. Bona, J. Massó, E. Seidel, and J. Stela, "New formalism for numerical relativity," *Phys. Rev. Lett.*, vol. 75, pp. 600–603, Jul 1995.

[42] F. Guzmán, "Introduction to numerical relativity through examples," *Revista Mexicana de Física*, vol. 53, Aug 2007.

[43] I. Cordero-Carrion and P. Cerda-Duran, "Partially implicit Runge-Kutta methods for wave-like equations in spherical-type coordinates," Nov 2012.

[44] I. Cordero-Carrión and P. Cerdá-Durán, *Partially Implicit Runge-Kutta Methods for Wave-Like Equations*, pp. 267–278. Cham: Springer International Publishing, 2014.

[45] P. J. Montero and I. Cordero-Carrion, "BSSN equations in spherical coordinates without regularization: vacuum and non-vacuum spherically symmetric spacetimes," *Phys. Rev. D*, vol. 85, p. 124037, 2012.

[46] J. D. Brown, "Covariant formulations of BSSN and the standard gauge," *Phys. Rev. D*, vol. 79, p. 104029, 2009.

[47] E. Seidel and W.-M. Suen, "Dynamical evolution of boson stars: Perturbing the ground state," *Phys. Rev. D*, vol. 42, pp. 384–403, Jul 1990.

[48] J. Balakrishna, E. Seidel, and W.-M. Suen, "Dynamical evolution of boson stars. 2. Excited states and selfinteracting fields," *Phys. Rev. D*, vol. 58, p. 104004, 1998.

[49] A. Escorihuela-Tomàs, N. Sanchis-Gual, J. C. Degollado, and J. A. Font, "Quasistationary solutions of scalar fields around collapsing self-interacting boson stars," *Phys. Rev. D*, vol. 96, no. 2, p. 024015, 2017.

[50] N. Sanchis-Gual, J. C. Degollado, P. J. Montero, and J. A. Font, "Quasistationary solutions of self-gravitating scalar fields around black holes," *Phys. Rev. D*, vol. 91, p. 043005, 2015.

[51] S. Yoshida and Y. Eriguchi, "Rotating boson stars in general relativity,"

Phys. Rev. D, vol. 56, pp. 762–771, Jul 1997.

[52] E. Mielke, *Rotating Boson Stars*, pp. 115–131. Springer, Apr 2016.

[53] F. E. Schunck and E. W. Mielke, "Rotating boson star as an effective mass torus in general relativity," *Physics Letters A*, vol. 249, no. 5, pp. 389–394, 1998.

[54] C.-W. Lai, *A Numerical study of boson stars*. PhD thesis, The University of British Columbia, Sep 2004.

[55] N. Sanchis-Gual, F. Di Giovanni, M. Zilhão, C. Herdeiro, P. Cerdá-Durán, J. A. Font, and E. Radu, "Nonlinear dynamics of spinning bosonic stars: Formation and stability," *Phys. Rev. Lett.*, vol. 123, p. 221101, Nov 2019.

[56] D.-I. Choi, *Numerical Studies of Nonlinear Schrodinger and Klein-Gordon Systems: Techniques and Applications*. PhD thesis, University of Texas, Austin, 1998.

[57] J. Balakrishna, *A Numerical Study of Boson Stars: Einstein Equations with a Matter Source*. PhD thesis, Washington University, St.Louis, 1999.

[58] D.-I. Choi, "Collision of gravitationally bound bose-einstein condensates," *Phys. Rev. A*, vol. 66, p. 063609, Dec 2002.

[59] E. Seidel and W.-M. Suen, "Formation of solitonic stars through gravitational cooling," *Phys. Rev. Lett.*, vol. 72, pp. 2516–2519, 1994.

[60] A. R. Liddle and M. S. Madsen, "The Structure and Formation of Boson Stars," *International Journal of Modern Physics D*, vol. 1, no. 1, pp. 101–143, 1992.

[61] F. Schunck and E. Mielke, "General relativistic boson stars," *Classical and Quantum Gravity*, vol. 20, p. R301, Sep 2003.

[62] A. Einstein, "The Field Equations of Gravitation," *Sitzungsber. Preuss. Akad. Wiss. Berlin (Math. Phys.)*, vol. 1915, pp. 844–847, 1915.

[63] C. M. Will, "The Confrontation between General Relativity and Experi-

ment," *Living Rev. Rel.*, vol. 17, p. 4, 2014.

[64] F. W. Dyson, A. S. Eddington, and C. Davidson, "A Determination of the Deflection of Light by the Sun's Gravitational Field, from Observations Made at the Total Eclipse of May 29, 1919," *Philosophical Transactions of the Royal Society of London Series A*, vol. 220, pp. 291–333, 1920.

[65] W. Rindler, *Relativity: Special, general, and cosmological*. Relativity: Special, General, and Cosmological, Oxford University Press, 2006.

[66] B. P. Abbott *et al.*, "Observation of Gravitational Waves from a Binary Black Hole Merger," *Phys. Rev. Lett.*, vol. 116, no. 6, p. 061102, 2016.

[67] A. Friedmann, "Über die Krümmung des Raumes," *Zeitschrift fur Physik*, vol. 10, pp. 377–386, 1922.

[68] G. Lemaître, "Un Univers homogène de masse constante et de rayon croissant rendant compte de la vitesse radiale des nébuleuses extra-galactiques," *Annales de la Société Scientifique de Bruxelles*, vol. 47, pp. 49–59, 1927.

[69] H. P. Robertson, "Kinematics and World-Structure," *apj*, vol. 82, p. 284, 1935.

[70] A. G. Walker, "On milne's theory of world-structure*," *Proceedings of the London Mathematical Society*, vol. s2-42, no. 1, pp. 90–127, 1937.

[71] P. J. E. Peebles and B. Ratra, "The cosmological constant and dark energy," *Rev. Mod. Phys.*, vol. 75, pp. 559–606, Apr 2003.

[72] E. Di Valentino, O. Mena, S. Pan, L. Visinelli, W. Yang, A. Melchiorri, D. F. Mota, A. G. Riess, and J. Silk, "In the realm of the Hubble tension—a review of solutions," *Class. Quant. Grav.*, vol. 38, no. 15, p. 153001, 2021.

[73] Y. Akrami *et al.*, *Modified Gravity and Cosmology: An Update by the CANTATA Network*. Springer, 2021.

[74] G. J. Olmo, *Introduction to Palatini theories of gravity and nonsingular*

cosmologies, ch. 7. IntechOpen, 2012.

[75] F. W. Hehl, J. McCrea, E. W. Mielke, and Y. Ne'eman, "Metric-affine gauge theory of gravity: field equations, noether identities, world spinors, and breaking of dilation invariance," *Physics Reports*, vol. 258, no. 1, pp. 1–171, 1995.

[76] J. Beltrán Jiménez, L. Heisenberg, and T. S. Koivisto, "The Geometrical Trinity of Gravity," *Universe*, vol. 5, no. 7, p. 173, 2019.

[77] J. M. Nester and H.-J. Yo, "Symmetric teleparallel general relativity," *Chin. J. Phys.*, vol. 37, p. 113, 1999.

[78] R. Aldrovandi and J. G. Pereira, *Teleparallel Gravity: An Introduction*. Springer, 2013.

[79] T. Clifton, P. G. Ferreira, A. Padilla, and C. Skordis, "Modified Gravity and Cosmology," *Phys. Rept.*, vol. 513, pp. 1–189, 2012.

[80] M. Ostrogradsky, "Mémoires sur les équations différentielles, relatives au problème des isopérimètres," *Mem. Acad. St. Petersbourg*, vol. 6, no. 4, pp. 385–517, 1850.

[81] C. Brans and R. H. Dicke, "Mach's principle and a relativistic theory of gravitation," *Phys. Rev.*, vol. 124, pp. 925–935, 1961.

[82] G. W. Horndeski, "Second-order scalar-tensor field equations in a four-dimensional space," *Int. J. Theor. Phys.*, vol. 10, pp. 363–384, 1974.

[83] C. Rovelli, "Loop quantum gravity," *Living Rev. Rel.*, vol. 1, p. 1, 1998.

[84] O. Aharony, S. S. Gubser, J. M. Maldacena, H. Ooguri, and Y. Oz, "Large N field theories, string theory and gravity," *Phys. Rept.*, vol. 323, pp. 183–386, 2000.

[85] A. De Felice and S. Tsujikawa, "f(R) Theories," *Living Rev. Rel.*, vol. 13, no. 1, p. 3, 2010.

[86] L. Amendola, R. Gannouji, D. Polarski, and S. Tsujikawa, "Conditions

for the cosmological viability of $f(r)$ dark energy models," *Phys. Rev. D*, vol. 75, p. 083504, Apr 2007.

[87] G. J. Olmo, "Limit to general relativity in $f(R)$ theories of gravity," *Phys. Rev. D*, vol. 75, p. 023511, Jan 2007.

[88] G. J. Olmo, "Palatini Approach to Modified Gravity: $f(R)$ Theories and Beyond," *Int. J. Mod. Phys. D*, vol. 20, pp. 413–462, 2011.

[89] V. I. Afonso, G. J. Olmo, E. Orazi, and D. Rubiera-Garcia, "Correspondence between modified gravity and general relativity with scalar fields," *Phys. Rev. D*, vol. 99, p. 044040, Feb 2019.

[90] G. J. Olmo and D. Rubiera-Garcia, "Junction conditions in Palatini $f(R)$ gravity," *Class. Quant. Grav.*, vol. 37, no. 21, p. 215002, 2020.

[91] A. Delhom, G. J. Olmo, and E. Orazi, "Ricci-Based Gravity theories and their impact on Maxwell and nonlinear electromagnetic models," *JHEP*, vol. 11, p. 149, 2019.

[92] V. I. Afonso, G. J. Olmo, E. Orazi, and D. Rubiera-Garcia, "Mapping nonlinear gravity into General Relativity with nonlinear electrodynamics," *Eur. Phys. J. C*, vol. 78, no. 10, p. 866, 2018.

[93] V. I. Afonso, G. J. Olmo, and D. Rubiera-Garcia, "Mapping ricci-based theories of gravity into general relativity," *Phys. Rev. D*, vol. 97, p. 021503, Jan 2018.

[94] V. I. Afonso, G. J. Olmo, E. Orazi, and D. Rubiera-Garcia, "New scalar compact objects in Ricci-based gravity theories," *JCAP*, vol. 12, p. 044, 2019.

[95] M. Guerrero, G. Mora-Pérez, G. J. Olmo, E. Orazi, and D. Rubiera-Garcia, "Rotating black holes in Eddington-inspired Born-Infeld gravity: an exact solution," *JCAP*, vol. 07, p. 058, 2020.

[96] W.-H. Shao, C.-Y. Chen, and P. Chen, "Generating Rotating Spacetime in Ricci-Based Gravity: Naked Singularity as a Black Hole Mimicker,"

JCAP, vol. 03, p. 041, 2021.

[97] G. J. Olmo, E. Orazi, and D. Rubiera-Garcia, "Multicenter solutions in Eddington-inspired Born–Infeld gravity," *Eur. Phys. J. C*, vol. 80, no. 11, p. 1018, 2020.

[98] A. Einstein, *The Meaning of Relativity*. United States: Princeton University Press, original edition ed., 1922.

[99] A. Pais, *Subtle is the Lord: The Science and the Life of Albert Einstein*. England, United States: Oxford University Press, 1st edition ed., 1982.

[100] A. Einstein, *Einheitliche Feldtheorie von Gravitation und Elektrizität*, pp. 267–273. John Wiley & Sons, Ltd, 2005.

[101] N. Dadhich and J. M. Pons, "On the equivalence of the Einstein-Hilbert and the Einstein-Palatini formulations of general relativity for an arbitrary connection," *Gen. Rel. Grav.*, vol. 44, pp. 2337–2352, 2012.

[102] H. A. Buchdahl, "Non-Linear Lagrangians and Cosmological Theory," *Monthly Notices of the Royal Astronomical Society*, vol. 150, pp. 1–8, Sep 1970.

[103] A. A. Starobinsky, "A New Type of Isotropic Cosmological Models Without Singularity," *Phys. Lett. B*, vol. 91, pp. 99–102, 1980.

[104] G. J. Olmo, "Post-Newtonian constraints on f(R) cosmologies in metric and Palatini formalism," *Phys. Rev. D*, vol. 72, p. 083505, 2005.

[105] G. J. Olmo, "The Gravity Lagrangian according to solar system experiments," *Phys. Rev. Lett.*, vol. 95, p. 261102, 2005.

[106] A. Delhom, A. Jiménez-Cano, and F. J. Maldonado Torralba, "Instabilities in field theories: Lecture notes with a view into modified gravity," Jul 2022.

[107] A. Bhadra, K. Sarkar, D. P. Datta, and K. K. Nandi, "Brans-Dicke theory: Jordan versus Einstein frame," *Mod. Phys. Lett. A*, vol. 22, pp. 367–376,

2007.

[108] T. Harko and F. S. N. Lobo, *Extensions of $f(R)$ Gravity: Curvature-Matter Couplings and Hybrid Metric-Palatini Theory*. Cambridge Monographs on Mathematical Physics, 2018.

[109] L. Lombriser and A. Taylor, "Breaking a Dark Degeneracy with Gravitational Waves," *JCAP*, vol. 03, p. 031, 2016.

[110] L. Lombriser and N. A. Lima, "Challenges to Self-Acceleration in Modified Gravity from Gravitational Waves and Large-Scale Structure," *Phys. Lett. B*, vol. 765, pp. 382–385, 2017.

[111] T. Baker, E. Bellini, P. G. Ferreira, M. Lagos, J. Noller, and I. Sawicki, "Strong constraints on cosmological gravity from GW170817 and GRB 170817A," *Phys. Rev. Lett.*, vol. 119, no. 25, p. 251301, 2017.

[112] J. Sakstein and B. Jain, "Implications of the Neutron Star Merger GW170817 for Cosmological Scalar-Tensor Theories," *Phys. Rev. Lett.*, vol. 119, no. 25, p. 251303, 2017.

[113] P. Creminelli and F. Vernizzi, "Dark Energy after GW170817 and GRB170817A," *Phys. Rev. Lett.*, vol. 119, no. 25, p. 251302, 2017.

[114] J. M. Ezquiaga and M. Zumalacárregui, "Dark Energy After GW170817: Dead Ends and the Road Ahead," *Phys. Rev. Lett.*, vol. 119, no. 25, p. 251304, 2017.

[115] J. M. Ezquiaga and M. Zumalacárregui, "Dark Energy in light of Multi-Messenger Gravitational-Wave astronomy," *Front. Astron. Space Sci.*, vol. 5, p. 44, 2018.

[116] G. J. Olmo, H. Sanchis-Alepuz, and S. Tripathi, "Dynamical Aspects of Generalized Palatini Theories of Gravity," *Phys. Rev. D*, vol. 80, p. 024013, 2009.

[117] C. Barragan and G. J. Olmo, "Isotropic and Anisotropic Bouncing Cosmologies in Palatini Gravity," *Phys. Rev. D*, vol. 82, p. 084015, 2010.

[118] G. J. Olmo, "Palatini Actions and Quantum Gravity Phenomenology," *JCAP*, vol. 10, p. 018, 2011.

[119] J. Beltran Jimenez, L. Heisenberg, G. J. Olmo, and D. Rubiera-Garcia, "Born–Infeld inspired modifications of gravity," *Phys. Rept.*, vol. 727, pp. 1–129, 2018.

[120] V. I. Afonso, G. J. Olmo, and D. Rubiera-Garcia, "Mapping Ricci-based theories of gravity into general relativity," *Phys. Rev. D*, vol. 97, no. 2, p. 021503, 2018.

[121] G. J. Olmo, D. Rubiera-Garcia, and A. Wojnar, "Stellar structure models in modified theories of gravity: Lessons and challenges," *Phys. Rept.*, vol. 876, pp. 1–75, 2020.

[122] D. Rubiera-Garcia, "From fundamental physics to tests with compact objects in metric-affine theories of gravity," *Int. J. Mod. Phys. D*, vol. 29, no. 11, p. 2041007, 2020.

[123] D. F. Torres, A. R. Liddle, and F. E. Schunck, "Gravitational memory of boson stars," *Phys. Rev. D*, vol. 57, pp. 4821–4825, 1998.

[124] Y. Brihaye, A. Cisterna, and C. Erices, "Boson stars in biscalar extensions of Horndeski gravity," *Phys. Rev. D*, vol. 93, no. 12, p. 124057, 2016.

[125] Y. Verbin and Y. Brihaye, "Charged boson stars and black holes with nonminimal coupling to gravity," *Phys. Rev. D*, vol. 97, no. 4, p. 044046, 2018.

[126] B. Hartmann, J. Riedel, and R. Suciu, "Gauss-Bonnet boson stars," *Phys. Lett. B*, vol. 726, pp. 906–912, 2013.

[127] Y. Brihaye and J. Riedel, "Rotating boson stars in five-dimensional Einstein-Gauss-Bonnet gravity," *Phys. Rev. D*, vol. 89, no. 10, p. 104060, 2014.

[128] V. Baibhav and D. Maity, "Boson stars in higher-derivative gravity," *Phys. Rev. D*, vol. 95, p. 024027, Jan 2017.

[129] A. A. Starobinsky, "Dynamics of Phase Transition in the New Inflationary Universe Scenario and Generation of Perturbations," *Phys. Lett. B*, vol. 117, pp. 175–178, 1982.

[130] D. H. Lyth and A. Riotto, "Particle physics models of inflation and the cosmological density perturbation," *Phys. Rept.*, vol. 314, pp. 1–146, 1999.

[131] S. M. Carroll, V. Duvvuri, M. Trodden, and M. S. Turner, "Is cosmic speed - up due to new gravitational physics?," *Phys. Rev. D*, vol. 70, p. 043528, 2004.

[132] C. Barragan, G. J. Olmo, and H. Sanchis-Alepuz, "Bouncing Cosmologies in Palatini f(R) Gravity," *Phys. Rev. D*, vol. 80, p. 024016, 2009.

[133] G. J. Olmo and D. Rubiera-Garcia, "Nonsingular Black Holes in $f(R)$ Theories," *Universe*, vol. 1, no. 2, pp. 173–185, 2015.

[134] C. Bejarano, G. J. Olmo, and D. Rubiera-Garcia, "What is a singular black hole beyond General Relativity?," *Phys. Rev. D*, vol. 95, no. 6, p. 064043, 2017.

[135] P. P. Avelino, "Eddington-inspired Born-Infeld gravity: nuclear physics constraints and the validity of the continuous fluid approximation," *JCAP*, vol. 11, p. 022, 2012.

[136] J. Naf and P. Jetzer, "On the 1/c Expansion of f(R) Gravity," *Phys. Rev. D*, vol. 81, p. 104003, 2010.

[137] S. Ilijić and M. Sossich, "Boson stars in $f(T)$ extended theory of gravity," *Phys. Rev. D*, vol. 102, no. 8, p. 084019, 2020.

[138] N. Siemonsen and W. E. East, "Stability of rotating scalar boson stars with nonlinear interactions," *Phys. Rev. D*, vol. 103, no. 4, p. 044022, 2021.

[139] C. Bambi, A. Cardenas-Avendano, G. J. Olmo, and D. Rubiera-Garcia, "Wormholes and nonsingular spacetimes in Palatini $f(R)$ gravity," *Phys. Rev. D*, vol. 93, no. 6, p. 064016, 2016.

[140] M. Guerrero and D. Rubiera-Garcia, "Nonsingular black holes in nonlinear gravity coupled to Euler-Heisenberg electrodynamics," *Phys. Rev. D*, vol. 102, no. 2, p. 024005, 2020.

[141] C. Bona, J. Masso, E. Seidel, and J. Stela, "First order hyperbolic formalism for numerical relativity," *Phys. Rev. D*, vol. 56, pp. 3405–3415, 1997.

[142] M. Alcubierre, B. Bruegmann, P. Diener, M. Koppitz, D. Pollney, E. Seidel, and R. Takahashi, "Gauge conditions for long term numerical black hole evolutions without excision," *Phys. Rev. D*, vol. 67, p. 084023, 2003.

[143] M. Alcubierre and M. D. Mendez, "Formulations of the 3+1 evolution equations in curvilinear coordinates," *Gen. Rel. Grav.*, vol. 43, pp. 2769–2806, 2011.

[144] P. J. Montero, J. A. Font, and M. Shibata, "NADA: A New code for studying self-gravitating tori around black holes," *Phys. Rev. D*, vol. 78, p. 064037, 2008.

[145] N. Sanchis-Gual, J. C. Degollado, P. J. Montero, J. A. Font, and V. Mewes, "Quasistationary solutions of self-gravitating scalar fields around collapsing stars," *Phys. Rev. D*, vol. 92, no. 8, p. 083001, 2015.

[146] J. Thornburg, "Event and apparent horizon finders for 3+1 numerical relativity," *Living Rev. Rel.*, vol. 10, p. 3, 2007.

[147] R. Penrose, "Gravitational collapse: The role of general relativity," *Riv. Nuovo Cim.*, vol. 1, pp. 252–276, 1969.

[148] S. W. Hawking and R. Penrose, "The Singularities of gravitational collapse and cosmology," *Proc. Roy. Soc. Lond. A*, vol. 314, pp. 529–548, 1970.

[149] J. M. M. Senovilla and D. Garfinkle, "The 1965 Penrose singularity theorem," *Class. Quant. Grav.*, vol. 32, no. 12, p. 124008, 2015.

[150] R. H. Brandenberger, V. F. Mukhanov, and A. Sornborger, "A Cosmological theory without singularities," *Phys. Rev. D*, vol. 48, pp. 1629–1642,

1993.

[151] J. Khoury, B. A. Ovrut, P. J. Steinhardt, and N. Turok, "The Ekpyrotic universe: Colliding branes and the origin of the hot big bang," *Phys. Rev. D*, vol. 64, p. 123522, 2001.

[152] M. Gasperini and G. Veneziano, "The Pre - big bang scenario in string cosmology," *Phys. Rept.*, vol. 373, pp. 1–212, 2003.

[153] M. Novello and S. E. P. Bergliaffa, "Bouncing Cosmologies," *Phys. Rept.*, vol. 463, pp. 127–213, 2008.

[154] A. Ashtekar and P. Singh, "Loop Quantum Cosmology: A Status Report," *Class. Quant. Grav.*, vol. 28, p. 213001, 2011.

[155] P. S. Joshi, ed., *Gravitational Collapse and Spacetime Singularities*. Cambridge Monographs on Mathematical Physics, Cambridge University Press, Sep 2012.

[156] J. R. Oppenheimer and H. Snyder, "On Continued gravitational contraction," *Phys. Rev.*, vol. 56, pp. 455–459, 1939.

[157] G. J. Olmo and P. Singh, "Effective Action for Loop Quantum Cosmology a la Palatini," *JCAP*, vol. 01, p. 030, 2009.

[158] A. Delhom, G. J. Olmo, and P. Singh, "A diffeomorphism invariant family of metric-affine actions for loop cosmologies," *JCAP*, vol. 06, p. 059, 2023.

[159] P. Diener, "A New general purpose event horizon finder for 3-D numerical space-times," *Class. Quant. Grav.*, vol. 20, pp. 4901–4918, 2003.

[160] N. Sanchis-Gual, C. Herdeiro, E. Radu, J. C. Degollado, and J. A. Font, "Numerical evolutions of spherical Proca stars," *Phys. Rev. D*, vol. 95, no. 10, p. 104028, 2017.

[161] M. Visser, *Lorentzian wormholes: From Einstein to Hawking*. American Inst. of Physics, 1995.

[162] O. James, E. von Tunzelmann, P. Franklin, and K. S. Thorne, "Visualizing

Interstellar's Wormhole," *Am. J. Phys.*, vol. 83, p. 486, 2015.

[163] J. B. Hartle, *Gravity: An Introduction to Einstein's General Relativity*. Benjamin Cummings, illustrate ed., 2003.

[164] J. Barranco, A. Bernal, J. C. Degollado, A. Diez-Tejedor, M. Megevand, M. Alcubierre, D. Nunez, and O. Sarbach, "Schwarzschild black holes can wear scalar wigs," *Phys. Rev. Lett.*, vol. 109, p. 081102, 2012.

[165] R. Gambini, J. Olmedo, and J. Pullin, "Spherically symmetric loop quantum gravity: analysis of improved dynamics," *Class. Quant. Grav.*, vol. 37, no. 20, p. 205012, 2020.

[166] A. Simpson and M. Visser, "Black-bounce to traversable wormhole," *JCAP*, vol. 02, p. 042, 2019.

[167] F. S. N. Lobo, M. E. Rodrigues, M. V. de Sousa Silva, A. Simpson, and M. Visser, "Novel black-bounce spacetimes: wormholes, regularity, energy conditions, and causal structure," *Phys. Rev. D*, vol. 103, no. 8, p. 084052, 2021.

[168] G. J. Olmo and D. Rubiera-Garcia, "Reissner-Nordström black holes in extended Palatini theories," *Phys. Rev. D*, vol. 86, p. 044014, 2012.

[169] G. J. Olmo, D. Rubiera-Garcia, and H. Sanchis-Alepuz, "Geonic black holes and remnants in Eddington-inspired Born-Infeld gravity," *Eur. Phys. J. C*, vol. 74, p. 2804, 2014.

[170] F. Cabral, F. S. N. Lobo, and D. Rubiera-Garcia, "Cosmological bounces, cyclic universes, and effective cosmological constant in Einstein-Cartan-Dirac-Maxwell theory," *Phys. Rev. D*, vol. 102, no. 8, p. 083509, 2020.

[171] J. Sakstein, "Hydrogen Burning in Low Mass Stars Constrains Scalar-Tensor Theories of Gravity," *Phys. Rev. Lett.*, vol. 115, p. 201101, 2015.

[172] G. J. Olmo, D. Rubiera-Garcia, and A. Wojnar, "Minimum main sequence mass in quadratic Palatini $f(R)$ gravity," *Phys. Rev. D*, vol. 100, no. 4, p. 044020, 2019.

[173] F. S. N. Lobo, "From the Flamm–Einstein–Rosen bridge to the modern renaissance of traversable wormholes," *Int. J. Mod. Phys. D*, vol. 25, no. 07, p. 1630017, 2016.

[174] F. S. N. Lobo, ed., *Wormholes, Warp Drives and Energy Conditions*. Fundamental Theories of Physics, Springer Cham, 1 ed., 2017.

[175] K. Schwarzschild, "On the gravitational field of a mass point according to Einstein's theory," *Sitzungsber. Preuss. Akad. Wiss. Berlin (Math. Phys.)*, vol. 1916, pp. 189–196, 1916.

[176] K. Schwarzschild, "On the gravitational field of a sphere of incompressible fluid according to Einstein's theory," *Sitzungsber. Preuss. Akad. Wiss. Berlin (Math. Phys.)*, vol. 1916, pp. 424–434, 1916.

[177] L. Flamm, "Republication of: Contributions to einstein's theory of gravitation," *General Relativity and Gravitation*, vol. 47, Jun 2015.

[178] G. W. Gibbons, "Editorial note to: Ludwig flamm, contributions to einstein's theory of gravitation," *General Relativity and Gravitation*, vol. 47, no. 6, p. 71, 2015. Gibbons2015.

[179] A. Einstein and N. Rosen, "The Particle Problem in the General Theory of Relativity," *Phys. Rev.*, vol. 48, pp. 73–77, 1935.

[180] M. D. Kruskal, "Maximal extension of Schwarzschild metric," *Phys. Rev.*, vol. 119, pp. 1743–1745, 1960.

[181] G. Szekeres, "On the singularities of a Riemannian manifold," *Publ. Math. Debrecen*, vol. 7, pp. 285–301, 1960.

[182] J. A. Wheeler, "On the Nature of quantum geometrodynamics," *Annals Phys.*, vol. 2, pp. 604–614, 1957.

[183] C. W. Misner and J. A. Wheeler, "Classical physics as geometry: Gravitation, electromagnetism, unquantized charge, and mass as properties of curved empty space," *Annals Phys.*, vol. 2, pp. 525–603, 1957.

[184] H. G. Ellis, "Ether flow through a drainhole - a particle model in general relativity," *J. Math. Phys.*, vol. 14, pp. 104–118, 1973.

[185] K. A. Bronnikov, "Scalar-tensor theory and scalar charge," *Acta Phys. Polon. B*, vol. 4, pp. 251–266, 1973.

[186] M. S. Morris and K. S. Thorne, "Wormholes in space-time and their use for interstellar travel: A tool for teaching general relativity," *Am. J. Phys.*, vol. 56, pp. 395–412, 1988.

[187] M. S. Morris, K. S. Thorne, and U. Yurtsever, "Wormholes, Time Machines, and the Weak Energy Condition," *Phys. Rev. Lett.*, vol. 61, pp. 1446–1449, 1988.

[188] M. Visser, S. Kar, and N. Dadhich, "Traversable wormholes with arbitrarily small energy condition violations," *Phys. Rev. Lett.*, vol. 90, p. 201102, 2003.

[189] F. S. N. Lobo, G. J. Olmo, E. Orazi, D. Rubiera-Garcia, and A. Rustam, "Structure and stability of traversable thin-shell wormholes in Palatini $f(\mathcal{R})$ gravity," *Phys. Rev. D*, vol. 102, no. 10, p. 104012, 2020.

[190] E. Gravanis and S. Willison, "'Mass without mass' from thin shells in Gauss-Bonnet gravity," *Phys. Rev. D*, vol. 75, p. 084025, 2007.

[191] T. Harko, F. S. N. Lobo, M. K. Mak, and S. V. Sushkov, "Modified-gravity wormholes without exotic matter," *Phys. Rev. D*, vol. 87, no. 6, p. 067504, 2013.

[192] P. H. R. S. Moraes and P. K. Sahoo, "Nonexotic matter wormholes in a trace of the energy-momentum tensor squared gravity," *Phys. Rev. D*, vol. 97, no. 2, p. 024007, 2018.

[193] O. Svitek and T. Tahamtan, "Nonsymmetric dynamical thin-shell wormhole in Robinson–Trautman class," *Eur. Phys. J. C*, vol. 78, no. 2, p. 167, 2018.

[194] M. Visser, "Traversable wormholes: Some simple examples," *Phys. Rev.*

D, vol. 39, pp. 3182–3184, 1989.

[195] M. Visser, "Traversable wormholes from surgically modified Schwarzschild space-times," *Nucl. Phys. B*, vol. 328, pp. 203–212, 1989.

[196] E. Poisson and M. Visser, "Thin shell wormholes: Linearization stability," *Phys. Rev. D*, vol. 52, pp. 7318–7321, 1995.

[197] C. J. S. Clarke and T. Dray, "Junction conditions for null hypersurfaces," *Classical and Quantum Gravity*, vol. 4, p. 265, mar 1987.

[198] W. Israel, "Singular hypersurfaces and thin shells in general relativity," *Nuovo Cim. B*, vol. 44S10, p. 1, 1966. [Erratum: Nuovo Cim.B 48, 463 (1967)].

[199] M. Mars and J. M. M. Senovilla, "Geometry of general hypersurfaces in space-time: Junction conditions," *Class. Quant. Grav.*, vol. 10, pp. 1865–1897, 1993.

[200] M. Ishak and K. Lake, "Stability of transparent spherically symmetric thin shells and wormholes," *Phys. Rev. D*, vol. 65, p. 044011, 2002.

[201] F. S. N. Lobo and P. Crawford, "Linearized stability analysis of thin shell wormholes with a cosmological constant," *Class. Quant. Grav.*, vol. 21, pp. 391–404, 2004.

[202] E. F. Eiroa and G. E. Romero, "Linearized stability of charged thin shell wormholes," *Gen. Rel. Grav.*, vol. 36, pp. 651–659, 2004.

[203] F. S. N. Lobo, "Energy conditions, traversable wormholes and dust shells," *Gen. Rel. Grav.*, vol. 37, pp. 2023–2038, 2005.

[204] T. P. Sotiriou and V. Faraoni, "f(R) Theories Of Gravity," *Rev. Mod. Phys.*, vol. 82, pp. 451–497, 2010.

[205] S. Krasnikov, "Electrostatic interaction of a pointlike charge with a wormhole," *Class. Quant. Grav.*, vol. 25, p. 245018, 2008.

[206] K. Jusufi and A. Övgün, "Gravitational Lensing by Rotating Wormholes,"

Phys. Rev. D, vol. 97, no. 2, p. 024042, 2018.

[207] D. Jafferis, A. Zlokapa, J. D. Lykken, D. K. Kolchmeyer, S. I. Davis, N. Lauk, H. Neven, and M. Spiropulu, "Traversable wormhole dynamics on a quantum processor," *Nature*, vol. 612, no. 7938, pp. 51–55, 2022.

[208] D.-C. Dai and D. Stojkovic, "Observing a Wormhole," *Phys. Rev. D*, vol. 100, no. 8, p. 083513, 2019.

[209] V. De Falco, E. Battista, S. Capozziello, and M. De Laurentis, "General relativistic Poynting-Robertson effect to diagnose wormholes existence: static and spherically symmetric case," *Phys. Rev. D*, vol. 101, no. 10, p. 104037, 2020.

[210] C. Bambi and D. Stojkovic, "Astrophysical Wormholes," *Universe*, vol. 7, no. 5, p. 136, 2021.

[211] J. H. Simonetti, M. J. Kavic, D. Minic, D. Stojkovic, and D.-C. Dai, "Sensitive searches for wormholes," *Phys. Rev. D*, vol. 104, no. 8, p. L081502, 2021.

[212] E. W. Mielke and F. E. Schunck, "Boson stars: Alternatives to primordial black holes?," *Nucl. Phys. B*, vol. 564, pp. 185–203, 2000.

[213] M. Visser and D. L. Wiltshire, "Stable gravastars: An Alternative to black holes?," *Class. Quant. Grav.*, vol. 21, pp. 1135–1152, 2004.

[214] T. Damour and S. N. Solodukhin, "Wormholes as black hole foils," *Phys. Rev. D*, vol. 76, p. 024016, 2007.

[215] R. A. Konoplya and A. Zhidenko, "Wormholes versus black holes: quasinormal ringing at early and late times," *JCAP*, vol. 12, p. 043, 2016.

[216] E. Di Grezia, E. Battista, M. Manfredonia, and G. Miele, "Spin, torsion and violation of null energy condition in traversable wormholes," *Eur. Phys. J. Plus*, vol. 132, no. 12, p. 537, 2017.

[217] J. a. L. Rosa, J. P. S. Lemos, and F. S. N. Lobo, "Wormholes in generalized

hybrid metric-Palatini gravity obeying the matter null energy condition everywhere," *Phys. Rev. D*, vol. 98, no. 6, p. 064054, 2018.

[218] V. De Falco, E. Battista, S. Capozziello, and M. De Laurentis, "Reconstructing wormhole solutions in curvature based Extended Theories of Gravity," *Eur. Phys. J. C*, vol. 81, no. 2, p. 157, 2021.

[219] J. a. L. Rosa and J. P. S. Lemos, "Junction conditions for generalized hybrid metric-Palatini gravity with applications," *Phys. Rev. D*, vol. 104, no. 12, p. 124076, 2021.

[220] R. A. Konoplya and A. Zhidenko, "Traversable Wormholes in General Relativity," *Phys. Rev. Lett.*, vol. 128, no. 9, p. 091104, 2022.

[221] J. P. S. Lemos and O. B. Zaslavskii, "Black hole mimickers: Regular versus singular behavior," *Phys. Rev. D*, vol. 78, p. 024040, 2008.

[222] C. A. R. Herdeiro, A. M. Pombo, E. Radu, P. V. P. Cunha, and N. Sanchis-Gual, "The imitation game: Proca stars that can mimic the Schwarzschild shadow," *JCAP*, vol. 04, p. 051, 2021.

[223] P. V. P. Cunha, C. A. R. Herdeiro, E. Radu, and H. F. Runarsson, "Shadows of Kerr black holes with scalar hair," *Phys. Rev. Lett.*, vol. 115, no. 21, p. 211102, 2015.

[224] M. Wielgus, J. Horak, F. Vincent, and M. Abramowicz, "Reflection-asymmetric wormholes and their double shadows," *Phys. Rev. D*, vol. 102, no. 8, p. 084044, 2020.

[225] X. Wang, P.-C. Li, C.-Y. Zhang, and M. Guo, "Novel shadows from the asymmetric thin-shell wormhole," *Phys. Lett. B*, vol. 811, p. 135930, 2020.

[226] M. Guerrero, G. J. Olmo, and D. Rubiera-Garcia, "Double shadows of reflection-asymmetric wormholes supported by positive energy thin-shells," *JCAP*, vol. 04, p. 066, 2021.

[227] S. Aneesh, S. Bose, and S. Kar, "Gravitational waves from quasinormal modes of a class of Lorentzian wormholes," *Phys. Rev. D*, vol. 97, no. 12,

p. 124004, 2018.

[228] N. K. Johnson-Mcdaniel, A. Mukherjee, R. Kashyap, P. Ajith, W. Del Pozzo, and S. Vitale, "Constraining black hole mimickers with gravitational wave observations," *Phys. Rev. D*, vol. 102, p. 123010, 2020.

[229] V. Cardoso, E. Franzin, and P. Pani, "Is the gravitational-wave ringdown a probe of the event horizon?," *Phys. Rev. Lett.*, vol. 116, no. 17, p. 171101, 2016. [Erratum: Phys.Rev.Lett. 117, 089902 (2016)].

[230] V. Cardoso, S. Hopper, C. F. B. Macedo, C. Palenzuela, and P. Pani, "Gravitational-wave signatures of exotic compact objects and of quantum corrections at the horizon scale," *Phys. Rev. D*, vol. 94, no. 8, p. 084031, 2016.

[231] R. A. Konoplya, Z. Stuchlík, and A. Zhidenko, "Echoes of compact objects: new physics near the surface and matter at a distance," *Phys. Rev. D*, vol. 99, no. 2, p. 024007, 2019.

[232] R. A. Matzner, "Scattering of Massless Scalar Waves by a Schwarzschild "Singularity"," *J. Math. Phys.*, vol. 9, pp. 163–170, Oct 2003.

[233] R. Fabbri, "Scattering and absorption of electromagnetic waves by a Schwarzschild black hole," *Phys. Rev. D*, vol. 12, pp. 933–942, 1975.

[234] W. G. Unruh, "Absorption Cross-Section of Small Black Holes," *Phys. Rev. D*, vol. 14, pp. 3251–3259, 1976.

[235] L. C. B. Crispino, A. Higuchi, and G. E. A. Matsas, "Low-frequency absorption cross section of the electromagnetic waves for the extreme Reissner-Nordstrom black holes in higher dimensions," *Phys. Rev. D*, vol. 82, p. 124038, 2010.

[236] E. S. Oliveira, L. C. B. Crispino, and A. Higuchi, "Equality between gravitational and electromagnetic absorption cross sections of extreme Reissner-Nordstrom black holes," *Phys. Rev. D*, vol. 84, p. 084048, 2011.

[237] L. C. B. Crispino, S. R. Dolan, A. Higuchi, and E. S. de Oliveira, "Inferring

black hole charge from backscattered electromagnetic radiation," *Phys. Rev. D*, vol. 90, no. 6, p. 064027, 2014.

[238] L. C. B. Crispino, S. R. Dolan, A. Higuchi, and E. S. de Oliveira, "Scattering from charged black holes and supergravity," *Phys. Rev. D*, vol. 92, no. 8, p. 084056, 2015.

[239] L. C. S. Leite, S. R. Dolan, and L. C. B. Crispino, "Absorption of electromagnetic and gravitational waves by Kerr black holes," *Phys. Lett. B*, vol. 774, pp. 130–134, 2017.

[240] L. C. S. Leite, S. Dolan, and L. Crispino, C. B., "Absorption of electromagnetic plane waves by rotating black holes," *Phys. Rev. D*, vol. 98, no. 2, p. 024046, 2018.

[241] C. L. Benone and L. C. B. Crispino, "Massive and charged scalar field in Kerr-Newman spacetime: Absorption and superradiance," *Phys. Rev. D*, vol. 99, no. 4, p. 044009, 2019.

[242] M. A. A. Paula, L. C. S. Leite, and L. C. B. Crispino, "Electrically charged black holes in linear and nonlinear electrodynamics: Geodesic analysis and scalar absorption," *Phys. Rev. D*, vol. 102, no. 10, p. 104033, 2020.

[243] R. B. Magalhães, L. C. S. Leite, and L. C. B. Crispino, "Schwarzschild-like black holes: Light-like trajectories and massless scalar absorption," *Eur. Phys. J. C*, vol. 80, no. 5, p. 386, 2020.

[244] R. B. Magalhães, L. C. S. Leite, and L. C. B. Crispino, "Parametrized black holes: scattering investigation," *Eur. Phys. J. C*, vol. 82, no. 8, p. 698, 2022.

[245] C. F. B. Macedo, T. Stratton, S. Dolan, and L. C. B. Crispino, "Spectral lines of extreme compact objects," *Phys. Rev. D*, vol. 98, no. 10, p. 104034, 2018.

[246] M. Cabero, J. Westerweck, C. D. Capano, S. Kumar, A. B. Nielsen, and B. Krishnan, "Black hole spectroscopy in the next decade," *Phys. Rev. D*,

vol. 101, no. 6, p. 064044, 2020.

[247] S. Chandrasekhar, V. Ferrari, and J. E. Enderby, "On the non-radial oscillations of a star. iii. a reconsideration of the axial modes," *Proceedings of the Royal Society of London. Series A: Mathematical and Physical Sciences*, vol. 434, no. 1891, pp. 449–457, 1991.

[248] V. Cardoso, L. C. B. Crispino, C. F. B. Macedo, H. Okawa, and P. Pani, "Light rings as observational evidence for event horizons: long-lived modes, ergoregions and nonlinear instabilities of ultracompact objects," *Phys. Rev. D*, vol. 90, no. 4, p. 044069, 2014.

[249] A. Delhom, C. F. B. Macedo, G. J. Olmo, and L. C. B. Crispino, "Absorption by black hole remnants in metric-affine gravity," *Phys. Rev. D*, vol. 100, no. 2, p. 024016, 2019.

[250] H. C. D. Lima, C. L. Benone, and L. C. B. Crispino, "Scalar absorption: Black holes versus wormholes," *Phys. Rev. D*, vol. 101, no. 12, p. 124009, 2020.

[251] M. S. Churilova, R. A. Konoplya, Z. Stuchlik, and A. Zhidenko, "Wormholes without exotic matter: quasinormal modes, echoes and shadows," *JCAP*, vol. 10, p. 010, 2021.

[252] J. M. M. Senovilla, "Junction conditions for F(R)-gravity and their consequences," *Phys. Rev. D*, vol. 88, p. 064015, 2013.

[253] P. T. Leung, Y. T. Liu, W. M. Suen, C. Y. Tam, and K. Young, "Perturbative approach to the quasinormal modes of dirty black holes," *Phys. Rev. D*, vol. 59, p. 044034, 1999.

[254] L. C. B. Crispino, S. R. Dolan, and E. S. Oliveira, "Scattering of massless scalar waves by Reissner-Nordström black holes," *Phys. Rev. D*, vol. 79, p. 064022, 2009.

[255] E. Barausse, V. Cardoso, and P. Pani, "Can environmental effects spoil precision gravitational-wave astrophysics?," *Phys. Rev. D*, vol. 89, no. 10,

p. 104059, 2014.

[256] C. F. B. Macedo, L. C. S. Leite, and L. C. B. Crispino, "Absorption by dirty black holes: null geodesics and scalar waves," *Phys. Rev. D*, vol. 93, no. 2, p. 024027, 2016.

[257] A. Higuchi, "Low frequency scalar absorption cross-sections for stationary black holes," *Class. Quant. Grav.*, vol. 18, p. L139, 2001. [Addendum: Class.Quant.Grav. 19, 599 (2002)].

[258] Y. Decanini, G. Esposito-Farese, and A. Folacci, "Universality of high-energy absorption cross sections for black holes," *Phys. Rev. D*, vol. 83, p. 044032, 2011.

[259] R. Shaikh, P. Banerjee, S. Paul, and T. Sarkar, "A novel gravitational lensing feature by wormholes," *Phys. Lett. B*, vol. 789, pp. 270–275, 2019.

[260] G. J. Olmo, J. L. Rosa, D. Rubiera-Garcia, and D. Saez-Chillon Gomez, "Shadows and photon rings of regular black holes and geonic horizonless compact objects," *Class. Quant. Grav.*, vol. 40, no. 17, p. 174002, 2023.

[261] G. Breit and E. Wigner, "Capture of Slow Neutrons," *Phys. Rev.*, vol. 49, pp. 519–531, 1936.

[262] H. Feshbach, D. C. Peaslee, and V. F. Weisskopf, "On the scattering and absorption of particles by atomic nuclei," *Phys. Rev.*, vol. 71, pp. 145–158, Feb 1947.

[263] H. C. D. Lima, Junior., L. C. B. Crispino, P. V. P. Cunha, and C. A. R. Herdeiro, "Can different black holes cast the same shadow?," *Phys. Rev. D*, vol. 103, no. 8, p. 084040, 2021.

[264] M. Guerrero, G. J. Olmo, D. Rubiera-Garcia, and D. S.-C. Gómez, "Light ring images of double photon spheres in black hole and wormhole spacetimes," *Phys. Rev. D*, vol. 105, no. 8, p. 084057, 2022.

[265] V. Cardoso and P. Pani, "Tests for the existence of black holes through gravitational wave echoes," *Nature Astronomy*, vol. 1, no. 9, pp. 586–591,

2017.

[266] P. Bueno, P. A. Cano, F. Goelen, T. Hertog, and B. Vercnocke, "Echoes of kerr-like wormholes," *Phys. Rev. D*, vol. 97, no. 2, p. 024040, 2018.

[267] K. A. Bronnikov and R. A. Konoplya, "Echoes in brane worlds: ringing at a black hole-wormhole transition," *Phys. Rev. D*, vol. 101, no. 6, p. 064004, 2020.

[268] Y. Yang, D. Liu, Z. Xu, Y. Xing, S. Wu, and Z.-W. Long, "Echoes of novel black-bounce spacetimes," *Phys. Rev. D*, vol. 104, no. 10, p. 104021, 2021.

[269] R. B. Magalhães, L. C. Crispino, and G. J. Olmo, "Compact objects in quadratic palatini gravity generated by a free scalar field," *Phys. Rev. D*, vol. 105, no. 6, p. 064007, 2022.

[270] V. Sharma and S. Ghosh, "Generalised ellis–bronnikov wormholes embedded in warped braneworld background and energy conditions," *The European Physical Journal C*, vol. 81, no. 11, p. 1004, 2021.

[271] S. Capozziello, T. Harko, T. S. Koivisto, F. S. N. Lobo, and G. J. Olmo, "Wormholes supported by hybrid metric-Palatini gravity," *Phys. Rev. D*, vol. 86, p. 127504, 2012.

[272] E. I. Guendelman, G. J. Olmo, D. Rubiera-Garcia, and M. Vasihoun, "Non-singular electrovacuum solutions with dynamically generated cosmological constant," *Phys. Lett. B*, vol. 726, pp. 870–875, 2013.

[273] A. Övgün, K. Jusufi, and I. Sakallı, "Exact traversable wormhole solution in bumblebee gravity," *Phys. Rev. D*, vol. 99, no. 2, p. 024042, 2019.

[274] J. R. Nascimento, G. J. Olmo, P. J. Porfirio, A. Y. Petrov, and A. R. Soares, "Global Monopole in Palatini $f(R)$ gravity," *Phys. Rev. D*, vol. 99, no. 6, p. 064053, 2019.

[275] Z. Fu, B. Grado-White, and D. Marolf, "A perturbative perspective on self-supporting wormholes," *Class. Quant. Grav.*, vol. 36, no. 4, p. 045006,

2019. [Erratum: Class.Quant.Grav. 36, 249501 (2019)].

[276] K. A. Bronnikov, "Spherically Symmetric Black Holes and Wormholes in Hybrid Metric-Palatini Gravity," *Grav. Cosmol.*, vol. 25, no. 4, pp. 331–341, 2019.

[277] C. Gundlach, R. H. Price, and J. Pullin, "Late time behavior of stellar collapse and explosions: 1. Linearized perturbations," *Phys. Rev. D*, vol. 49, pp. 883–889, 1994.

[278] K. Kokkotas, R. Konoplya, and A. Zhidenko, "Quasinormal modes, scattering, and hawking radiation of kerr-newman black holes in a magnetic field," *Phys. Rev. D*, vol. 83, no. 2, p. 024031, 2011.

[279] B. Turimov, B. Toshmatov, B. Ahmedov, and Z. Stuchlík, "Quasinormal modes of magnetized black hole," *Phys. Rev. D*, vol. 100, no. 8, p. 084038, 2019.

[280] C. Herdeiro, E. Radu, and H. Rúnarsson, "Kerr black holes with Proca hair," *Class. Quant. Grav.*, vol. 33, no. 15, p. 154001, 2016.